Forces in a microvessel-on-chip : system development,poroelasticity mechanics and cellular response

Claire Dessalles

INSTITUT POLYTECHNIQUE DE PARIS

ÉCOLE POLYTECHNIQUE

IP PARIS

NNT : 2021IPPAX082

Thèse de doctorat

Forces in a microvessel-on-chip: system development, poroelasticity mechanics and cellular response

Thèse de doctorat de l'Institut Polytechnique de Paris
préparée à l'Ecole polytechnique

École doctorale n°626 Ecole Doctorale de l'Institut Polytechnique de Paris (ED IP Paris)
Spécialité de doctorat: mécanique des fluides et des solides, acoustiques

Thèse présentée et soutenue à Palaiseau, le 15 septembre 2021, par

Claire Dessalles

Composition du Jury :

Pierre Sens Directeur de recherche, UMR CNRS 168, Institut Curie	Président
Benoit Ladoux Directeur de recherche, UMR CNRS 7592, Institut Jacques Monod	Rapporteur
Andries Van Der Meer Associate professor, Faculty of Science and Technology, University of Twente	Rapporteur
Guillaume Charras Professor, London Centre for Nanotechnology, University College London	Examinateur
Kristen Mills Assistant professor, Biomedical Engineering Department, Rensselaer Polytechnic Institute	Examinateur
Abdul Barakat Directeur de recherche, LadHyX, Ecole polytechnique	Directeur de thèse
Avin Babataheri Ingénieur de recherche, LadHyX, Ecole polytechnique	Co-Directeur de thèse

Summary

Endothelial cells (ECs) lining the inner surfaces of blood vessels sense and respond to the numerous mechanical forces present in the microvascular environment. Although the influence of wall shear stress, stiffness and curvature has been thoroughly investigated, the role of strain and wall tension remains less clear, most notably in the case of confluent monolayers. In vitro platforms such as organ-on-chips are ideal systems to investigate EC mechanobiology as they offer a controllable and well defined set of mechanical stimuli.

I started by developing a hydrogel-based microvessel-on-chip that encompasses both shear stress and circumferential strain in a pulsatile manner based on luminal flow actuation. The concept is the following: by imposing a given flow rate inside the channel, the luminal pressure is increased due to the channel's hydraulic resistance, which dilates the vessel. I then performed an extensive characterization of the mechanical behavior of the system and demonstrated that the shear and strain span the physiological ranges. Because both stresses derive from the luminal pressure, shear and strain are tightly coupled. To enable independent control of each stress, I explored three strategies: (1) adding a hydraulic resistance of variable length at the channel output, (2) changing the width of the hydrogel, and (3) tuning the hydrogel concentration. I also demonstrated the endothelial monolayer has an effect of flow shielding which explains the higher deformation obtained in endothelialized channels relative to cell-free channels.

The luminal flow actuation in the microvessel-on-chip can also be viewed as a hydraulic compression assay. The second part of my Ph.D. was devoted to the study of the dynamics of the poroelastic gel in this novel assay. Three major responses were investigated: the dynamics of the channel dilation after a pressure step, the strain distribution in the hydrogel and wave propagation. Each of these responses leads to complex dynamic behavior that can be exploited to derive the important poroelastic parameters of the hydrogel, most notably the Young's modulus and the permeability.

The final part of my Ph.D. was the investigation of the response of EC monolayers to static tensile stresses where I discovered a new behavior. ECs showed a strong reorganization, aligning their overall shape, cytoskeleton and nuclei in the stretch direction, and the effect was magnitude dependent. Associated with this overall reorientation, adherens junctions (AJs) remodeled into focal AJs (FAJs), a specialized structure that forms under tension. The cortical network of actin filaments also remodeled into thick bundles of central stress fibers. The association of the stress fibers and FAJs enabled the formation of circumferential transendothelial actin cables. In parallel, I proposed a hypothetical framework for the long term monolayer mechanics observed in this assay.

In summary, during my Ph.D. I developed a microvessel-on-chip that can subject cells to wall tension, characterized its mechanical behavior in detail, and investigated the response of the cells to the tensile stresses in this system, revealing a novel collective behavior.

Résumé

Les cellules endothéliales qui tapissent la paroi des vaisseaux sanguins sont capables de détecter et de répondre aux nombreuses forces mécaniques présentes dans le système microvasculaire. Bien que l'influence de forces dues au cisaillement, à la rigidité et à la courbure soit bien étudiée, le rôle de l'étirement et de la tension de la paroi vasculaire demeure peu compris, en particulier dans le cas des monocouches jointives. Les plateformes in vitro telles que les organes sur puce sont idéales pour l'étude de ces phénomènes, puisqu'elles offrent une panoplie de stimuli mécaniques contrôlables et caractérisables .

Le premier étape de ma thèse a été le développment d'un microvaisseau-sur-puce, constitué d'un hydrogel, permettant de générer à la fois le cisaillement et l'étirement circonférentiel de manière pulsatile, par l'actionnement par flux. Le concept est le suivant: en imposant un certain débit dans le microcanal, la pression luminale augmente à cause de la résistance hydraulique du canal, ce qui dilate le vaisseau. J'ai ensuite réalisé une caractérisation exhaustive du comportement mécanique du système et démontré que le cisaillement et l'étirement couvrent les plages de valeurs physiologiques. Puisque les deux contraintes découlent de la pression luminale, le cisaillement et l'étirement sont intrinséquement couplés. Pour contrôler chaque contraintes indépendemment, j'ai exploré trois stratégies: (1) l'ajout d'une résistance hydraulique de longueur variable à la sortie du microcanal, (2) le changement de la largeur de l'hydrogel, et (3) la variation de la concentration de l'hydrogel. J'ai également démontré que la monocouche endothéliales agit comme une barrière contre le flux, ce qui explique les déformations plus importantes obtenues dans les canaux endothélialisés par rapport aux canaux sans monocouche cellulaire.

L'actionnement par flux luminal peut également être vu comme un essai de compression hydraulique. La deuxième partie de ma thèse a été consacrée à l'étude de la dynamique du gel poroélastique dans ce nouvel essai. Trois réponses majeures ont été analysées : la dynamique de la dilatation du canal après une marche de pression, le champ de déformation et la propagation d'ondes dans le gel. Chacune de ces réponses conduit à des comportements dynamiques complexes, qui peuvent être exploités afin de calculer les paramètres poroélastiques de l'hydrogel, notamment le module d'Young et la permeabilité.

La dernière partie de ma thèse a consisté en l'étude de la réponse des monocouches endothéliales à des forces de tractions statiques, où j'ai mis en évidence un nouveau comportement. Les cellules endothéliales ont été fortement remodelées, alignant leur forme globale, leur cytosquelette et leur noyau dans la direction de l'étirement, et cet effet était dépendant de la magnitude de la tension. Les jonctions adhérentes se sont remodelées en jonctions adhérentes focales, une structure spécialisée qui se forme sous tension. Le réseau d'actine corticale s'est également réorganisé en fibres de stress et les jonctions adhérentes focales ont permis la formation de câbles d'actine transcellulaires circonférentiels. En parallèle, j'ai proposé un cadre hypothétique pour la mécanique au long terme des monocouches observées dans cette expérience.

En résumé, pendant ma thèse j'ai développé un microvaisseau-sur-puce qui peut soumettre les cellules à des forces de tension, caractérisé son comportement mécanique en détail, et

étudié la réponse des cellules aux forces de tractions dans ce système, révélant un nouveau comportement collectif.

Acknowledgements

No man is an island entire of itself

John Donne - 17th century

I want to thank first Abdul Barakat and Avin Babataheri, my PhD advisors. Abdul, thank you for believing in me and giving me autonomy and freedom. You gave me your trust, encouraging me to take ownership of my project and allowing me to go into whatever direction I was excited about. I am very grateful that I could grow from a student to a researcher during my PhD.

And Avin, thank you for being a great mentor. By believing in me and all that I could achieve, you gave me the confidence I needed to push through the darkest times. You shaped the scientist I am today and the one I aspire to be. You made me aware of my privilege to underscore my responsability, showed me my limitations so I could improve, and challenged me to be the best version of myself. The high standards you set for me are a gift and hope you will continue to do so in the future. Today, I stand proud as a woman and a doctor, wanting to change the world, and that is in big part thanks to you.

I was fortunate enough to have the opportunity to mentor five incredible young women: Clara, Clara, Elvire, Aude and Sara. You taught me more about myself that I could ever teach you about science. Thank you for your trust and all your help.

And an even bigger thank you to Clara and Sara, the awesome members of the microvessel team, for all your inputs on my work. Working alongside you was a great strength and a source of inspiration. I am grateful to you two for showing me that I am happier as part of team.

My PhD would not have been the same without the dream team, the amazing people of Building 65, past and present. I had a great time with the animated lunch breaks, various sports events, social activities and game evenings. But beyond the fun, I want to thank you all for the incredible spirit of kindness, empathy and assistance that each of you participated in creating. You guys changed everything.

I am grateful to everyone at LadHyX. The various research conducted in the lab is a testament to the wealth of multi-disciplinary work. And the organization of the lab, as a collective of independent researchers moving together towards great science, was an inspiration. And a big thank you to Caroline Frot, for all the help with the microfabrication molds, and to Emmanuel Delangre, for listening to us, helping us and caring about the struggles of the doctoral candidates.

As my project was at the intersection of multiple disciplines, collaborations were essential, and I learned so much from each of them. I want to thank Jean-Marc, for the OCT, Philippe, Céline and Mathieu, for the collaboration of poroelasticity modeling, Yanan, for the smoothest experients, Arthur, for all the beautiful laser ablation experiments, Suzie, for all the fun doing the permeability experiments and inspiring discussions, and Michael, for

your blunt criticism and all our tchats on science and life. I am also grateful to my teaching mentors, Olivier, Benjamin and Bruno, for all the discussion we had during the MODAL, on both science and academia. I also acknowledge all the scientific colleagues, for the tips, ideas, critics and help: everybody at CRRET, Chris McMinn, Stephan Huveneers, Dominique Chapelle, Arezki Boudaoud and Benoit Ladoux. I am very appreciative of the time you took for me out of your busy lives. A special thank you to Naïs, for all the inputs on the scientific illustration, that matter a lot to me.

I am grateful to the scientific community at conferences and to academic twitter, for the ideas, critics, comments, and for creating an exciting and stimulating environment. It is chance I will not take for granted to be able to work among passionate and hard working people. I also want to thank all my "twitter buddies" for their support and encouragement, and for creating an international network of ECR trying to make their way in the science world and change academia along the way.

Another big thank you to all my friends, for all the mental support, holidays, diners and chats, that made my life happier. I want to make a special mention to Thévy. You were there for me every time I needed you, for games, cake time, experiments or walks in the park to vent. It was a privilege to have you as a friend. You are an inspiration.

I am very lucky to have an amazing family and I am grateful to all you bring me. Thank you Alice, my larva, for all the moments we shared and for bringing fun into my life. Thank you Pierre, for all the ingenious gifts and our talks about science and life. And thank you Maman and Papai, for raising me to be an empathetic and well-adapted person. You saw beyond the academic smarts, and gave me everything I needed to be a successful contributing member of society. Thank you for teaching me that everyone has to give as much as they received. I am also very lucky to have fallen in a great new family. Thank you Jean-Pierre and Christianne, Karine and Romain for welcoming me and taking an interest in what I do.

And finally, I am deeply grateful to my husband, David. You are my rock, my balance, my home, my port in the storm. You were there through it all, the best and the worst, and I know I can always count on you. I also want to thank you for pushing me to be ambitious, to want more, to give it all, to be the best version of myself. There is no greater gift you could ever offer me.

Contents

Chapter 1

Introduction

If I have seen further it is by standing on the shoulders of Giants

Isaac Newton - 1675

1.1 Thesis overview

1.1.1 Context

Microvascular dysfunction has recently been shown to play a crucial role in several diseases including pulmonary and coronary microvascular diseases as well as neurodegenerative pathologies. Vascular dementia and Alzheimer's disease have been linked to hypertension, which is characterized by an increased pulse pressure. Hypervascularized organs, such as the brain and the kidneys, have low resistance and are more prone to penetration of pulsatility into the microvascular bed, leading to capillary dysfunction. The question of how the pulse pressure potentially damages microvessels remains to be elucidated. The increased stretch in microvessels caused by higher pressures is likely to be a major contributor to this process. The influence of stretch on vascular endothelial cell (EC) function has received much less attention than the effect of shear stress and remains poorly understood. The impact of stretch in combination with other mechanical cues present in the native microenvironment, such as substrate stiffness and/or shear stress, is even less thoroughly investigated.

1.1.2 Goal and rationale

The core idea of my PhD project is to understand how mechanical forces affect microvascular EC function. After a review of the literature on the existing systems, the choice of a microvessel-on-chip as a platform for the in vitro study of cellular response to controlled mechanical stimuli seemed quite natural. I planned on developing a novel microvessel-on-chip that would enable the application of circumferential strain and stress on the cells. The design also had to include shear stress and to allow pulsatility. I wanted to have a hydrogel-based system, which required a fine comprehension of the mechanical behavior of poroelastic materials. Exploring the dynamics of poroelasticity became quickly my second goal. The final step was to use the chip to investigate the response of ECs to tensile stresses. I chose cell shape and cytoskeletal organization as cellular readouts since both are involved in virtually all mechanical responses and are essential for regulating EC function.

1.1.3 Structure

The three years of my Ph.D. were spent accomplishing the four following main tasks: first, the development of a novel hydrogel-based microvessel-on-chip platform, which occupied the best part of the first year. Second, the characterization of the microvessel, and third, the exploration of the poroelastic behavior of the gel, which together occupied the second year. The fourth task, the investigation of the response of ECs to tensile stresses in the microvessel, was done during my third year. The various steps of of the technical development of the microfluidic system are presented in Chapter 2 alongside the chip characterization. The description of the poromechanics of the hydrogel, in particular its dynamics, with the mechanical contribution of the endothelium, are reported in Chapter 3. Finally, the response of ECs to tension and hypotheses on underlying mechanisms including the preliminary experiments to test them are discussed in Chapter 4. I conclude in Chapter 5 by describing the next steps for my project, ongoing collaborations, future projects using the microvessel-on-chip, and the current and expected outcomes of my Ph.D.

1.2 Biology of the microvasculature

1.2.1 The vasculature : a central organ

1.2.1.1 A brief history of the circulatory system

The closed and heart-centered circulatory system was first presented by William Harvey in De Motu Cordis in 1628 [1]. He described the double-sided circulation accurately, with the smaller side to the lungs and a larger one to the body. He also reported the hierarchy of vessels, with large vessels branching off into smaller ones when traveling away from the heart and small vessels merging into larger vessels back to the heart. Although he did not observe the capillaries, he postulated the existence of an anastomosis system or diffusion through the porous tissues to connect the arterial side to the venous side.

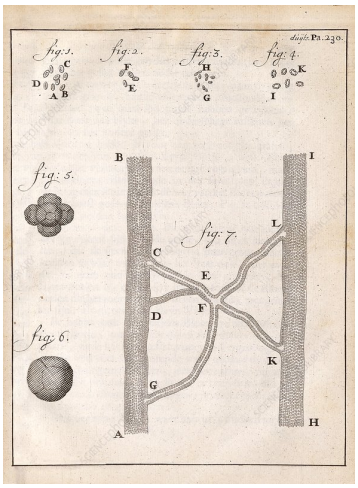

FIGURE 1.1: Drawings of RBCs and capillaries by Anton van Leeuwenhoek.

The first observation of capillaries was reported during the seventeenth century by Marcello Malpighi, who developed new microscopy approaches. He described the presence of tiny vessels wrapping around the alveolar structure in the lungs, connecting both the arterial and venous trees [1]. Later, Anton van Leeuwenhoek, who fabricated new lenses to improve microscopy techniques, noticed the presence of small roundish cells inside the capillaries, the red blood cells (RBCs). He was the first to image blood flow in the capillaries in 1674 thanks to the RBC movement.

1.2.1.2 Anatomy of the vasculature

The vasculature is a central organ in the human body and is in charge of tissue perfusion. It provides oxygen and nutrients and removes CO_2 and waste products from our tissues. To perform this vital mission, the vasculature is composed a highly dense double network of vessels throughout the body, named the vascular tree. One network is the arterial side, delivering blood from the heart to the organs, and the other network is the venous side, which brings blood from the organs back to the heart. Once blood reaches the heart, it flows

through a second loop to the lungs to be re-oxygenated before returning to the heart. The pulmonary arteries (heart to lungs) are the only arteries in the body transporting blood low in oxygen, and the pulmonary veins (lungs to heart) are the only veins in the body transporting oxygenated blood.

The complexity of the geometry of the vascular tree is reflected in the vessel dimensions, which vary drastically throughout the body, spanning four orders of magnitude. The aorta is the largest vessel, around three centimeters in diameter, followed by the vena cava at two centimeters. Both vessels have walls that are more than a millimeter thick. At the other end of the spectrum, the smallest capillaries in the human body are around three to four microns in diameter, and their walls are on average below a micron thick. Because of its highly branched organization, the total length of the vasculature is around 100,000 km, two and a half times the circumference of the planet earth, with the microvasculature accounting for 80 % of this total length. In hypervascularized organs, such as the brain, the average inter-capillary distance can be as small as 40 microns, close to the size of a single cell, illustrating the highly dense vascular mesh made by the capillaries.

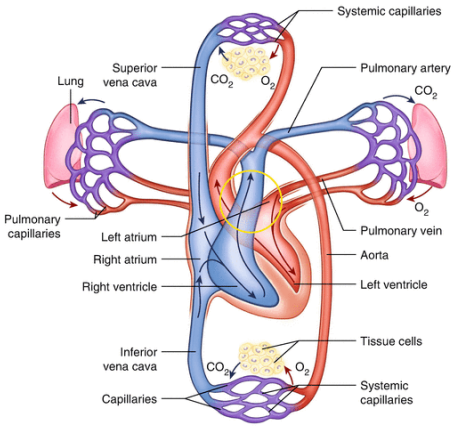

FIGURE 1.2: Illustration of the closed double-sided circulatory system.

1.2.2 The microvessel wall

1.2.2.1 A brief history of the endothelium

The composition of blood vessels, and more specifically that of the vessel wall, remained a mystery until the 19th century. The first vascular cells to be described were RBCs, by Jan Swammerdam in 1658 using one of the earliest microscopes. A decade later, Anton van Leeuwenhoek estimated RBC size to be "25,000 times smaller than a fine grain of sand". He also observed bacteria and protozoa with his microscope and called these tiny creatures "animalcules". Around the same time, in 1665, Robert Hooke discovered the first cells in a cork [1]. These little pores reminded him of prison cells, hence the name "cells".

After the discovery of single cells, scientists started to describe assemblies of cells, forming membranes. One example can be found in Virchow's writings: "A capillary vessel is a simple tube, in which we have, with the aid of our present appliances, hitherto only been able to discover a simple membrane, best at intervals with flattened nuclei. This is a membrane as simple as any that is ever met with in the body." [1]. The term endothelium was introduced in 1865 by Wilhelm His in his publication titled *Die Haute und Hohlen des Korpers* [1]. At the beginning of the 20th century, the famous reference book Gray's Anatomy reflected this now complete understanding about the membrane composing the capillary walls: "The nucleated endothelial cells which constitute the wall of a capillary are flat, irregular in outline, and are united by a cement material." [1].

1.2.2.2 Microvessel structure

The variety of vessel diameters found across the vasculature is reflected in the structure of the vessel walls, which have different cellular and matrix compositions depending on their location in the vascular tree. Capillaries have the thinnest walls, composed of only two elements: endothelial cells (ECs) and the vascular basement membrane (VBM). The VBM is

a thin layer (a few hundreds of nanometers) of extracellular matrix that serves as an adhesive substrate for the ECs [2]. The VBM is composed of two networks of laminin and collagen IV, cross-linked together by perlecans and nidogens.

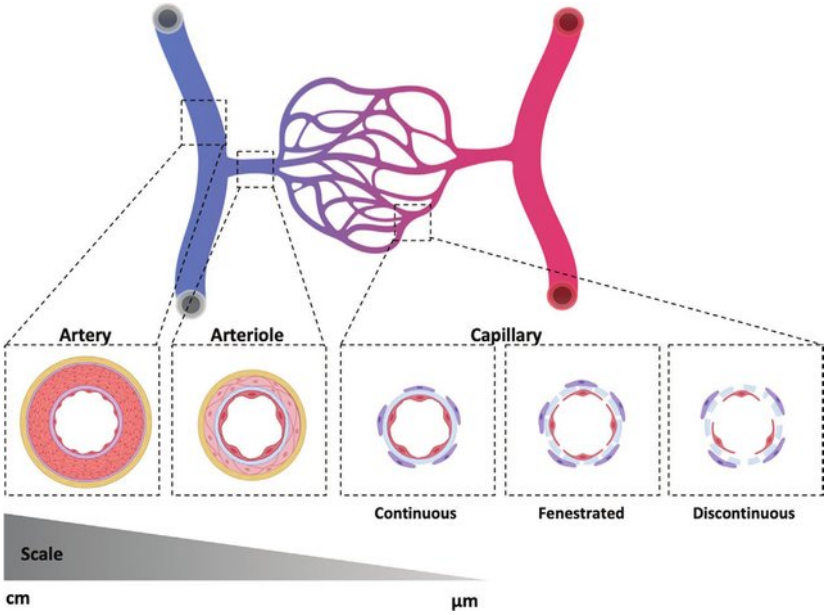

FIGURE 1.3: Illustration of the different vessel wall structure from arteries to capillaries [3].

This monolayer is reinforced by mural cells, pericytes or smooth muscle cells, when the vessel diameter increases (Figure 1.3). Pericytes cover the smallest vessels, those with diameters between three and twenty microns. They are embedded in the VBM, wrapping themselves around the vessel. Their morphology and vessel coverage varies significantly along the capillary bed. While the smallest capillaries have very sparse pericytes, the larger pre-capillary arterioles and post-capillary venules have an almost continuous layer of disjointed pericytes, which then switches abruptly to a continuous and connective layer of smooth muscle cells. Smooth muscle cells wrap circumferentially around the endothelium and are usually found in vessels with diameters above 15-20 microns.

1.2.3 EC biology

ECs are the primary cells of the microvasculature and the focus of my thesis. They have received considerable attention in the last 50 years, with the emergence of the field of EC mechanics in the past 30 years. Extensive literature exists on the molecular and biological aspects of ECs. I will focus here on the important notions in EC mechanobiology at the core of my project: the cytoskeleton, adhesion to the substrate and to neighboring ECs, and cell polarization.

1.2.3.1 Cell cytoskeleton

The cytoskeleton of most living cells is composed of three principal elements: actin filaments, microtubules, and intermediate filaments. The actin cytoskeleton is of major interest in this work because of its known role in forces generated by cells. Actin filaments are polymers made of successive actin mononers, i.e. G-actin, that come together to form a double strand, i.e. F-actin (or filamentous actin). F-actin is organized in different forms: branched and parallel bundles that can exert extensile forces and cortical actin and stress fibers, an arrangement of anti-parallel filaments that can exert contractile forces (Figure 1.4). In confluent ECs, actin is mostly found as cortical actin filaments or central stress fibers.

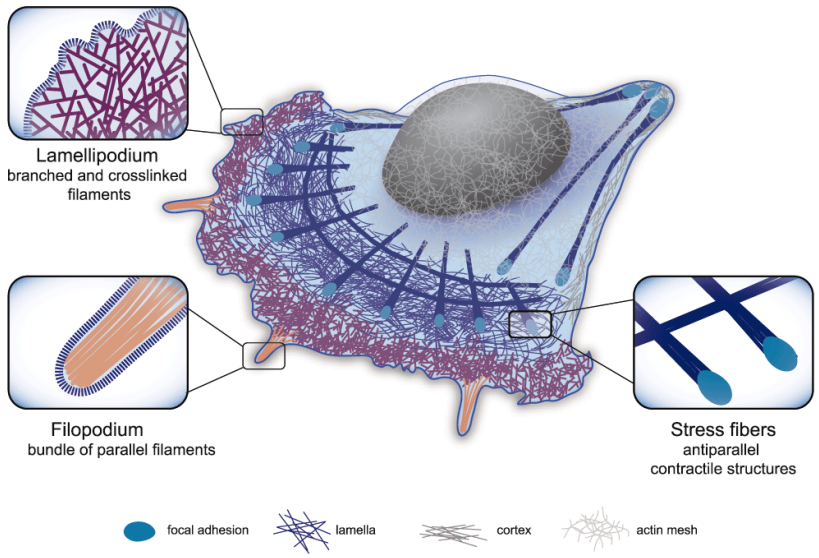

FIGURE 1.4: Illustration of the different actin networks found inside a migrating cell [4].

Extensile forces Branched, or tree like, actin networks rely on a protein complex named WASP-Arp2/3 that nucleates a new actin filament at a 60° angle from the original filament. This organization of actin is typically found in the lamellipodia, a fan-like structure at the front of migrating cells. Parallel bundles rely on the protein formin that nucleates new actin filaments without branching. They are found in filopodia, finger-like extensions at the front of migrating cells. In both structures, polymerization at the (+) end generates an extensile force, pushing against the membrane and enabling forward extension and migration.

Contractile forces Stress fibers are bundles of anti-parallel actin filaments running through the central part of the cell. They are associated with several proteins, such as myosins and alpha-actinin, and are capable of generating contractile forces through the acto-myosin machinery [5]. "Tension striae" or "stress fibers" were first detected by light microscopy as dark lines or fibrils crossing many types of cells growing in culture [6]. Stress fibers have also been noted in ECs, particularly those lining arteries exposed to high velocity flow such as the aorta [7]. Stress fibers appear to be more pronounced in ECs lining vessels from hypertensive animals [8].

Myosins and associated actin bundles form the acto-myosin complex which is responsible for cytoskeletal tension and cell contractility. Several myosin isoforms exist inside a cell and across cell types. In ECs, non-muscle myosin-II is the predominant isoform found in stress fibers. Myosins are composed of two heavy chains and two light chains, which associate to form a tail and a head. The head binds to the actin filament and "walks" on it in an ATP-dependent process, traveling toward the + end (actin filaments are polarized, with a + and a - end). In the anti-parallel arrangement, when the tails of two different myosins bind together, a sliding motion of the two actin filaments is generated, as each myosin walks toward the + end, located in opposite directions. This sliding motion creates the contraction, and as several asynchronized myosins and cross-linkers connect the two filaments, it also creates tension.

Finally, to transmit this pulling force, stress fibers need to be anchored at their ends to the substrate through focal adhesions (see below), to cell-cell junctions through focal ahderens junctions (see below), to other cytosolic elements such as transverse actin arcs through crosslinking foci, or to the nucleus through the Linker of Nucleoskeleton and Cytoskeleton (LINC) complex.

1.2.3.2 Cell-substrate adhesion

ECs are anchored to their substrate, the VBM, through focal adhesions (FAs). FAs are complex protein assemblies located at the cell membrane that bind actin filaments to the ECM (Figure 1.6). The proteins creating the transmembrane linking are the integrins, heterodimers whose head recognizes specific ECM proteins and whose cytosolic tail is the binding site for the rest of the complex. FAs are composed of several cytosolic proteins including paxilin, vinculin, talin and focal adhesion kinase. In immunostaining, FAs co-localize with the ends of stress fibers and appear as elongated dots. FAs are highly dynamic structures, assembled and disassembled by cells as needed. As FAs mature and grow, more and more proteins are recruited, creating a giant complex of parallel units, that can reach up to a couple microns in length.

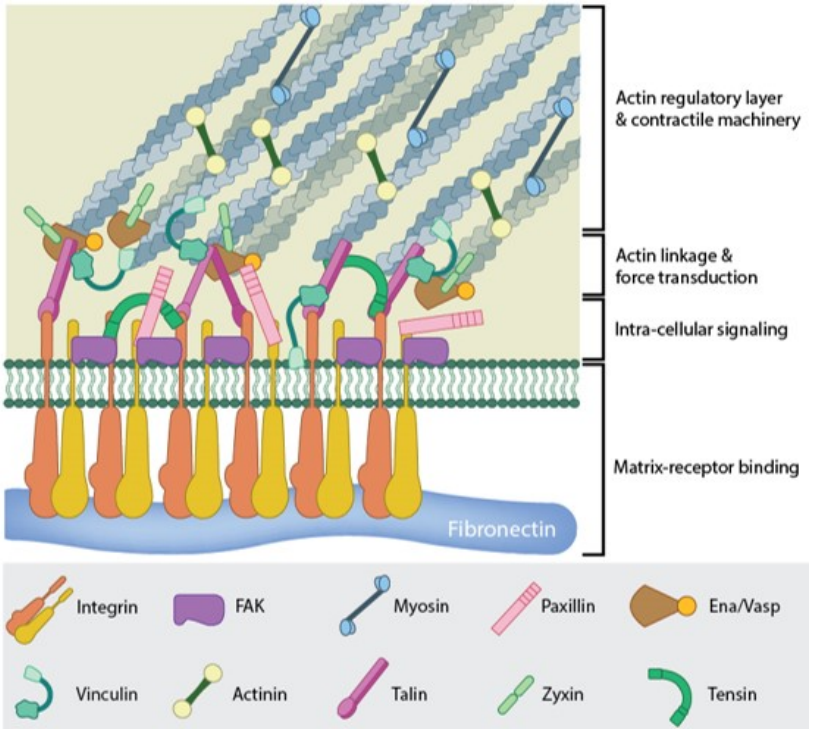

FIGURE 1.5: Schematic of the FA complex, detailing the constituting proteins and the role of each layer. https://www.mechanobio.info/what-is-mechanosignaling/what-is-the-extracellular-matrix-and-the-basal-lamina/what-are-focal-adhesions/what-are-mature-focal-adhesions-composed-of/

FAs are also known force transducers: they convey mechanical forces from the external substrate to the cytoskeleton, both mechanically and chemically. Their size and number depend on the cytoskeletal tension. For instance, FAs are smaller and less present in ECs on soft substrates, that are known to downregulate stress fibers (see above), compared to those on stiff substrates. FAs are also downregulated by cell-cell adhesions (see below), and are less present in confluent endothelium compared to single cells.

1.2.3.3 Cell-cell adhesion

ECs self-organize in monolayers and are attached to their neighbors through cell-cell junctions. Cell-cell junctions are complexes of transmembrane proteins binding together the two opposing cell membranes and ensuring the integrity of the monolayer. In ECs, they are predominantly divided into two types: adherens junctions (AJs) and tight junctions (TJs).

Adherens junctions AJs are also named zonula adherens, underlining the notion of 'adhesion', defined as the ability to stick. This underscores their importance in the mechanical integrity of the cell-cell contact and in force transmission. AJs are mostly composed of transmembrane cadherins, Vascular Endothelial Cadherins (VE-Cadherins) in ECs, and cytosolic catenins (p120, α and β), which link the cadherins to the actin cytoskeleton. AJs are highly dynamic structures, constantly remodeling with a time scale of minutes as cells migrate in the monolayer. AJs can have different morphologies, and defining clear nomenclature and understanding the origin of these various shapes is an ongoing effort. Currently, three main AJ types have been identified: linear AJs, focal AJs, and reticulated junctions. All three AJ types have been linked to the level of cytoskeletal tension.

- Linear adherens junctions are the most frequent type of junctions in healthy endothelia. They are described as straight thin lines with tangent actin filaments.
- Focal adherens junctions (FAJs) have been reported as discontinuous, punctate, dot-like or even zipper-like structures. In 2010, Millan et al. showed discontinuous AJ formation in correlation with stress fibers in ECs under the effect of inflammatory molecules [9]. Stress fibers from the two adjacent cells were shown to align orthogonal to the cell border and to be directly connected by these particular junctions independently of FAs. Two years later, Huveneers et al. reported that AJs were remodeled into discontinuous and punctate junctions when cytoskeletal and junctional tension increased [10]. They showed that vinculin was recruited to these junctions, which led them to propose the existence of a new type of junctions. Because of their similarities to FAs, with the insertion of the stress fiber ends, vinculin co-localization and their dot-like shape, they were named FAJs. FAJs are thought to be major force transmitting complexes in confluent endothelia.
- Reticulated junctions were first reported in 2012 by Fernandez-Martin et al. [11]. They were described as thick sponge-looking bands, with low levels of actin and co-localizing with regions where the two adjacent cells overlap. They are in fact three-dimensional structures. They were shown to ensure monolayer permeability in regions of low cytoskeletal tension in association with PECAM-1 [11].

Tight junctions TJs are also named zonula occludens, underlining the notion of 'occlusion', defined as the blocking or closing of a path. This nomenclature is consistent with their role in vascular homeostasis and barrier function. TJs are composed of strands of successive transmembrane complexes that seal the two cell membranes together, preventing paracellular transport of water, ions and solutes [12]. The three major transmembrane proteins present in TJs are occludin, claudins, and junction adhesion molecule (JAM) proteins. TJs are associated with the microtubule and actin cytoskeleton, and recent evidence suggests a possible role for them in EC mechanobiology [13].

1.2.3.4 Polarization

The last characteristic of ECs important in mechanobiology is their ability to polarize along the three orthogonal axes: z-axis with the baso-apical polarity, x-axis with the front-rear polarity, and y-axis with the left-right polarity.

Baso-apical polarity The endothelium's main function is to provide a physical barrier between blood and tissues. Like most monolayers, it separates two different biological compartments and therefore has a strong baso-apical polarity [14]. The basal surface is in contact with the VBM, while the apical surface is in direct contact with blood. Markers of baso-apical polarity include integrins, at the basal surface, and podocalyxin, found on the apical surface.

Front-rear polarity Planar cell polarization is the asymmetry between the cell "front" and "rear". The canonical example of this polarity is a migrating cell, with a lamelipodium at the front and a trailing rear. Planar cell polarization also exists in confluent monolayers, and can be visualized with the position of the microtubule organizing center (MTOC) relative to the cell nucleus [15]. The front-rear polarity can determine the vessel mitotic axis. For instance, in vessels, ECs are polarized along the vessel length in sprouts without flow and therefore divide along the vessel axis, contributing to the longitudinal extension of the sprout [16]. This polarization is mechanosensitive and is therefore affected by mechanical cues such as cell shape or flow patterns (see section 1.3). The flow can for instance reverse the planar cell polarization, both in vivo and in vitro, in a microtubule-dependent manner [15, 17].

Left-right polarity: chirality The last polarization axis is also in-plane, transverse to the cell front-rear axis, a "left-right" polarization, or chirality. Chirality is defined as the asymmetry of a molecule, object or cell. It is often used in the context of rotational movement, where the particle exhibits a preferred direction of rotation. Chirality has been demonstrated in cells as early as the 1920s and has attracted considerable attention in recent years [18–21]. Cell chirality has been linked to permeability of endothelial monolayers, with cellular neighbors of opposing chirality having poor cell-cell junctions, pointing to a novel player in our understanding of permeability regulation [21, 22]. The current hypothesis to explain the origin of cell chirality is based on actin chirality, which is thought to propagate to the cell level [**?**, 23], similar to the way cell polarity propagates to an organ or an embryo, creating tissue level polarity [24]. This hypothesis was tested and validated by Tee et al. in fibroblasts in a recent preprint [25]. In this work, the authors knocked down certain actin regulators to abolish (or reverse) actin chirality, which correlated with the disappearance (or reversal) of chirality at the cell and monolayer levels.

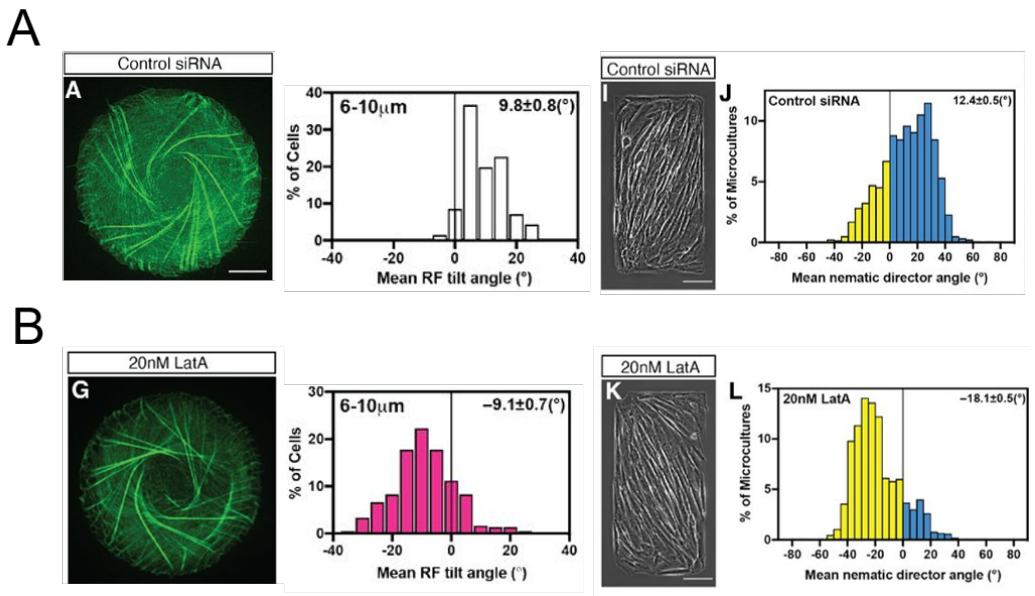

FIGURE 1.6: Propagation of chirality from the actin network to the cell monolayer. **A.** Control condition, with a right handed chirality, as shown with the clockwise rotation and the positive tilt angle of the actin (left panels) and monolayer (right panels). **B.** Treated condition, with a left handed chirality, as shown with the counter clockwise rotation and the positive tilt angle of the actin (left panels) and monolayer (right panels). [25].

1.3 Forces in the microvasculature

Physical interactions of cells with their substrate, with neighboring cells and with the surrounding fluid generate mechanical stresses on the cells. The study of cell behavior through the mechanical lens is relatively new. For instance, the term mechanobiology was coined in the 1990's. This approach is particularly important for vascular cells, whose environment is highly dynamic due to the pulsatile nature of blood flow. I will present here the hemodynamic forces exerted on ECs, which depend on the nature of the blood as a fluid, followed by a brief description of the important notions in fluid and solid mechanics necessary to appreciate the work presented here.

1.3.1 Hemodynamic forces on the endothelium

1.3.1.1 Properties of blood flow

Blood rheology Blood is a biological fluid composed mostly of plasma (54%) and RBCs (45%), and behaves as a complex non-Newtonian fluid. Plasma itself is 90% water and thus behaves as a Newtonian fluid with a viscosity very close to that of water, while RBCs, which are suspended particles that can aggregate and deform, are at the origin of the complex rheology of blood. Different models are used to describe blood flow depending on vessel diameter. In large vessels, blood is often modeled as a homogeneous (single-phase) fluid, from a mesoscopic perspective, where the RBCs' mechanical contribution is introduced as a shear-thinning behavior, i.e. the apparent viscosity of blood depends on the shear rate. In small vessels, such as in the microvasculature, blood can no longer be considered as a homogeneous fluid and is described as a suspension of deformable biconcave particles in a Newtonian fluid. At this scale, blood exhibits a diameter-dependent thinning behavior, called the Fahraeus-Lindqvist effect. As the vessel diameter decreases, RBCs concentrate towards the channel center, creating a "cell free" zone at the channel wall. This thin plasma layer has low viscosity and acts as a lubrication layer, fluidizing the overall blood flow. Microfluidics has been a revolutionary tool in the study of the Fahraeus-Lindqvist effect and of the single RBC behavior in capillaries, where RBCs deform into a parachute shape to squeeze through narrow vessels. In most *in vitro* studies focusing on the effect of stresses on ECs, blood is simplified to a water-based fluid, only aiming at replicating the stress applied on the endothelium at the wall.

Blood vessel hydraulics Fluids are driven forward by pressure gradients. In the body, the pressure gradient is created by the heart's contraction to pressurize the blood in the left ventricle. When the pressure passes a threshold, the aortic valve opens, releasing the pressurized blood into the aorta, which constitutes the beginning of the vascular tree. The blood is then pushed through the vascular network, traveling down the hydraulic pressure gradient present across the entire vasculature, due to hydraulic resistance of the different vessels. Indeed, the flow rate and pressure gradient in a vessel are linked through the vessel hydraulic resistance which depends on the vessel diameter and overall geometry. Indeed, vessel diameter, total vessel cross-sectional area, blood pressure and blood velocity are co-dependent and their variations throughout the vascular tree are orchestrated to optimize tissue oxygenation (see Figure 1.7). In the vasculature, arteries have large diameters to reduce resistance to blood flow and maintain an elevated pressure. In the microvasculature, the diameter of the vessels is reduced to maximize gas and nutrient exchange with the surrounding tissues, while the total cross-sectional area increases dramatically in order to optimize tissue perfusion and maintain the overall hydraulic resistance at reasonable levels, which together lead to a slow velocity with associated increased transit time which favors gas and nutrient exchange.

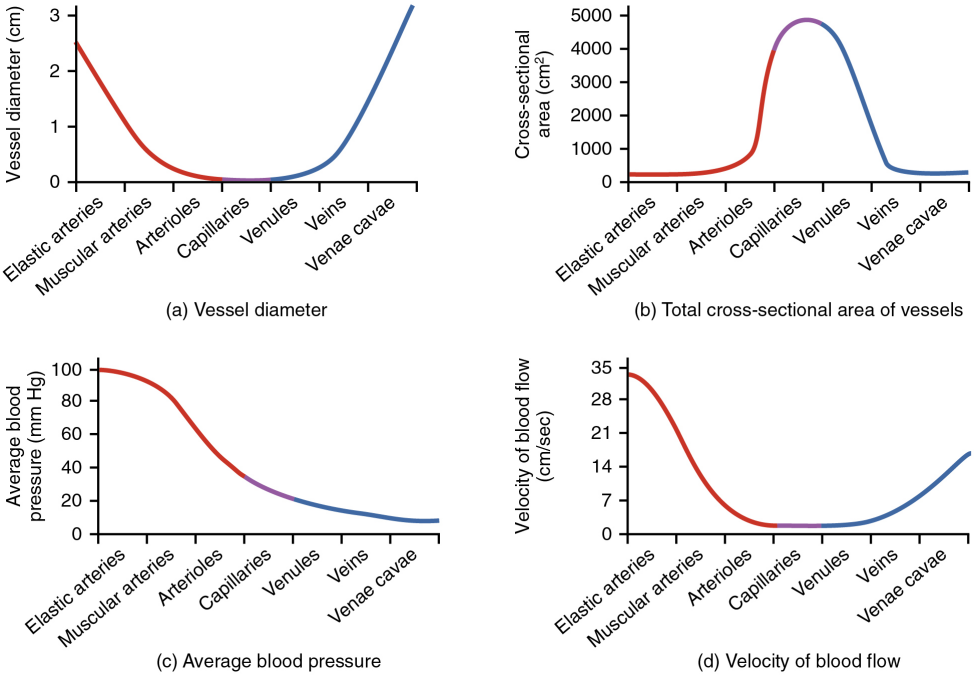

FIGURE 1.7: Schematics of the variation of hemodynamic quantities along the vascular tree: vessel diameter (top left), total area (top right), pressure (bottom left) and velocty (bottom right). https://opentextbc.ca/anatomyandphysiologyopenstax/chapter/blood-flow-blood-pressure-and-resistance/

1.3.1.2 Stresses on cells

Blood flow exerts various forces on ECs, listed in the next paragraph, along with the major candidates for mechanosensing pathways.

First, the luminal pressure generates a compressive force on the apical surface of ECs that might be sensed through direct nuclear deformation or mecanosensitive ion channels such as Piezzo-1 [26,27]. Next, the luminal viscous blood flow exerts a tangential force at the vessel wall, on the endothelial lining. This force exerted on the apical surface of the ECs is called shear stress. Numerous candidates are identified as potential mechanosensors for the luminal shear stress including the primary cilia, mechanosensitive ion channels, the nucleus, cadherins and integrins. Next is the transmural pressure difference which leads to transmural flow, outwards or inwards depending on the balance between luminal pressure and tissue pressure. Transmural flow passes primarly paracellularly, i.e. through cell-cell junctions, exerting a shearing force on them. Although the velocity and flow rate of transmural flow are relatively low, on the order of micrometers per second, the narrow spacing between cells leads to large shear stresses. VE-cadherins are known mechanosensors, and as the main component of adherens junction, they are prime candidates for transmural flow mecanosensing. Finally, the transmural pressure difference also leads to dilation of the vessel, stretching the compliant vessel wall and the cells lining it, leading to circumferential strain and tensile stresses.

Additionally, blood flow is pulsatile, i.e. has temporal oscillations, and it therefore generates pulsatile stresses at the heartbeat frequency. The pulsatility is mostly present on the arterial side of the vascular tree, is progressively dampened by the arteries, and vanishes during the passage through the high resistance microvasculature. The dynamic aspect is particularly important for the wall shear stress and the circumferential strain, both features of the arterial side. Before reviewing the response of ECs to these stresses (see next section), I will present the necessary basic notions of fluid and solid mechanics to understand, quantify and discuss the stresses at play.

1.3.2 Fluid mechanics

1.3.2.1 Steady flow

Different flow patterns Flows in nature can broadly be categorized as either laminar or turbulent, depending on the value of the flow Reynolds number. The Reynolds number is defined as the ratio of inertial forces to viscous forces:

$$Re = \frac{\rho U L}{\mu}$$

where U is the characteristic velocity, L the characteristic length, and ρ and μ the fluid density and dynamic viscosity, respectively. Laminar flows are characterized by smooth fluid motion with parallel streamlines, typically found at low Reynolds numbers when viscous forces dominate. Turbulent flows have chaotic pressure and fluid velocity fields, with cascades of vortices and flow instabilities. They are found when inertial forces dominate, which corresponds to high Reynolds number flows. The laminar-to-turbulent transition for steady pipe flow, i.e. flow in cylindrical channels, occurs at $Re \sim 2300$.

Assuming the homogeneous fluid model for blood, we can compute the cardiac cycle-average Reynolds number across the vasculature. The values are reported in Table 1.1. Flow in most of the vasculature lies clearly in the laminar regime, with the exception of the aorta which toes the transition threshold. Values for microvessels smaller than 30 microns in diameter are not reported as the vessel size starts to be comparable to the size of a RBC, challenging the validity of the homogeneous fluid model.

Vessel	Diameter (mm)	Velocity (cm/s)	Re	α
Aorta	25	40	2700	18
Arteries	4	10	105	3
Arterioles	0.03	5	0.4	0.02
Capillaries	0.008	0.03	x	0.006
Venules	0.02	1	0.05	0.01
Veins	5	5	66	3.6
Vena cava	30	15	1200	22

TABLE 1.1: Table of the hydrodynamic parameters across the vasculature.

Laminar flow in a pipe For steady laminar flow in a constant diameter cylindrical channel, the inertial term in the Navier-Stokes equation drops out, which transforms it into a simpler form that has an analytical solution, the Poiseuille flow solution. This was first described in 1846 by Jean-Louis Marie Poiseuille, a French doctor and physicist who studied blood flow in vessels, which until then was considered to have a flat velocity profile. Poiseuille flows have a parabolic velocity profile due to the no-slip condition at the wall, which propagates toward the center of the pipe due to friction in the fluid. The wall shear stress exerted on the cells, computed as the product of the fluid dynamic viscosity and the tangent of the velocity profile at the wall , can be determined directly from Poiseuille's parabolic velocity profile equation and is found to be

$$\tau = \frac{4\mu Q}{piR^3}$$

where μ is the dynamic viscosity of the fluid, Q the volumetric flow rate and R the pipe radius.

1.3.2.2 Pulsatile flow

An important dimensionless parameter in the case of pulsatile flow is the Womersley number, defined as the ratio of the transient inertial force to the viscous force. The Womersley number can be computed as

$$\alpha = R\left(\frac{\omega\rho}{\mu}\right)^{1/2}$$

, where ω is the angular frequency of the pulsatile flow, R the pipe radius and ρ and μ the fluid density and dynamic viscosity, respectively. When α is small (below 1), i.e. viscous forces are large, a parabolic profile has time to develop during each phase of the temporal oscillations, and the flow rate and pressure waveforms are mostly in phase. When α is large (above 10), the flow profile is flat (except within a narrow boundary layer near the wall), and the flow rate has a phase shift of nearly 90°relative to the pressure. In the intermediate α zone, the flow profile has a typical M shape, which increases the velocity tangent at the wall. When α is above 1, the parabolic approximation is not valid as already mentioned, and the wall shear stress expression presented above for Poiseuille flow does not apply (it strongly underestimates the actual peak shear stress). In the vascular tree, the Womersley number spans over four orders of magnitude, from 10^1 in the aorta down to 10^{-2} in the microvasculature. For all vessels with a diameter below 1 mm, α is below one, indicating the presence of a parabolic velocity profile at each time in the cardiac cycle and ensuring the validity of the wall shear stress expression given above for Poiseuille flow profiles.

1.3.3 Solid mechanics, stiffness, strain and tension

1.3.3.1 Passive materials

The deformability of a perfectly elastic passive or inert material is characterized by its Young's modulus, defined as the ratio of the tensile stress to the resulting strain. Therefore, the distribution of stresses in an elastic material can be calculated from the distribution of strains, with the Young's modulus acting as a proportionality constant. While the Young's modulus is an intrinsic property of a given material, the "stiffness" of the material is a measure of its deformability in a given configuration. For instance, the bending stiffness of a beam will depend not only on the Young's modulus of the beam material but also on the dimensions of the beam. Young's moduli of biological materials in the human body span across five orders of magnitudes (see Figure 1.8).

In addition, materials can be isotropic i.e. having the same Young's modulus in all directions, or anisotropic, i.e. having different Young's moduli in the different orthogonal directions. For instance, a hydrogel made of networks of parallel fibers would be anisotropic, as it would be stiffer in the fiber direction compared to the transverse directions.

1.3.3.2 Living materials

Uniform Young's modulus? Scientists have been trying to measure the Young's modulus of cells for decades, reporting a host of values across several orders of magnitude [29]. The variety of reported Young's moduli can be explained by the fact that cells are not composed of one homogeneous material. The Young's modulus is defined as an intrinsic property for a given material, and one can wonder how much sense it makes to talk about the Young's modulus of a cell. Is there really a unique Young's modulus that describes the mechanical properties of cells when they are highly heterogeneous structures? It is more likely that each intracellular component, such as the actin cortex, the cytoplasm, the nucleus, the cytoskeleton or even the cell membrane, have different and complex rheological behavior, and the overall

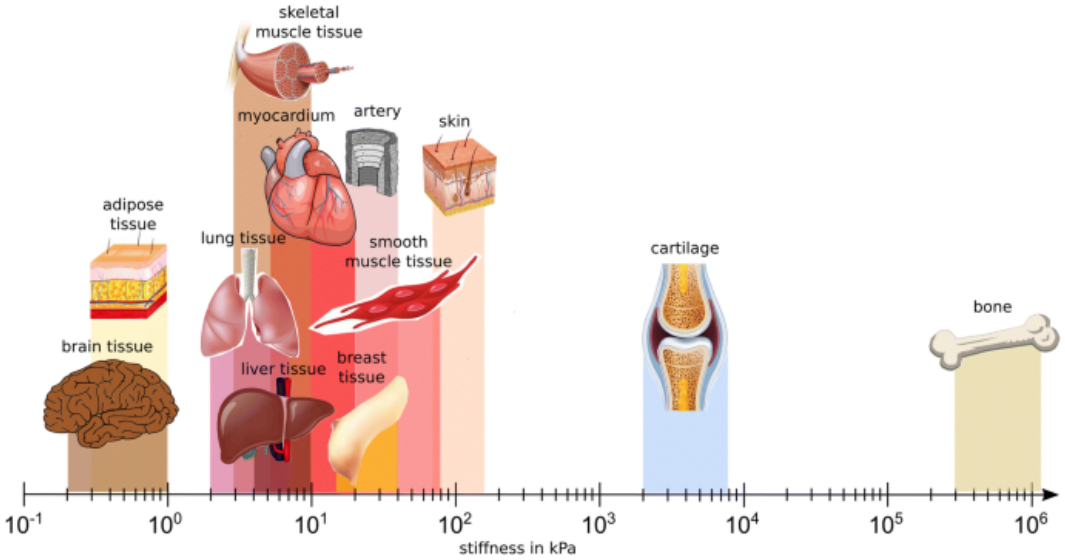

FIGURE 1.8: Distribution of various tissue Young's moduli inside the human body, spanning several orders of magnitude. [28]

"Young's modulus" would depend on the composition of the sub-region measured and on the measurement method.

Numerous techniques have been developed to probe live cells' Young's moduli [29–35]. They can be classified according to the length scale at which they probe the cells, which determines which intracellular structures contribute to the mechanical response. Atomic force microscopy and nano-indentation indent the cell surface locally, while micropipette aspiration pulls on the cell surface locally. The deformed cell region depends on the probe and pipette size and on the depth of indentation and aspiration length. On average, these three techniques are very sensitive to the mechanical contribution of the actin cortex and/or of the nucleus. Particle tracking microrheology measures the rheology of the intracellular space, composed of the cytoplasm, cytoskeleton and other proteins. Magnetic twisting cytometry, magnetic tweezers and optical tweezers mostly probe the cell surface, with the actin cortex likely contributing significantly to the measured signal. Optical stretching, optics-based noninvasive Brillouin microscopy method, microplates and parallel plates rheometers, microfluidic stretching and acoustoholographics all probe the entire cell, and the reported stiffnesses depend on all the internal organelles. Finally, cell monolayer rheometers measure the stiffness of cell monolayers, which also depends on intercellular contacts.

Constant Young's modulus? In addition to spatial heterogeneity, cells are living materials, constantly moving and adapting their shape and internal structure. Consequently, the Young's modulus is bound to vary in time. A principal manner by which cells tune their stiffness is via the actomyosin contractility, by altering the tension in their cytoskeleton. Classical examples include the stiffening of cells due to increased substrate stiffness or due to cyclic strain (see next section). In the case of stretch, cells actually undergo a biphasic stiffness modulation in a time frame of minutes, starting with fluidization, where they soften, followed by solidification, where they become stiffer than the controls. This example underscores the fine and fast dynamics of cellular stiffness.

Isotonic and isometric contractions, an analogy for cytoskeletal tension We have seen that cells cannot be described as simple elastic materials because of spatial and temporal variations. In addition to these two factors, the strain and tension in cells are not proportional, because of cell activity. A useful analogy to comprehend how the cytoskeleton tension can change independently of cell strain is muscle contraction. Indeed, actin stress fibers can be

seen as microscopic muscles capable of contraction inside the cell, thanks to myosin activity (see section 1.1.2). Muscles can perform both isotonic and isometric contractions. In isotonic contraction, the stress, i.e. tone, is maintained constant while the muscle shortens. For instance, when lifting a weight with a biceps curl, the weight determines the constant load and the muscle shortens as the weight is lifted. In isometric contraction, the strain, i.e. metric length, is maintained constant, while the muscle contracts. For instance, at the beginning of an arm wrestling match, the two players' hands do not move (constant strain), and both biceps contract to increase the force applied on the opposing hand.

The same phenomena are found in the actin cytoskeleton, where myosin activity can increase or decrease the tension in a fiber without shortening or lengthening it, i.e. an isometric contraction. Myosin activity can also shorten fibers without changing their tension when acting against a fixed load, i.e. an isotonic contraction. In both cases, one element of the strain-tension-stiffness triad is held constant, while the stiffness is increased through muscle contraction to vary the remaining elements. In living systems, and in particular in cells, the ability to infer stress from strain and strain from stress is lost, and the notion of "cell stiffness" becomes too intricate to interpret.

1.4 Endothelial cells and forces

My review of the literature on the response of ECs to the various mechanical forces present in the microvascular environment was formatted into a review article, co-authored with a post-doc from the group. This review was published as an open access paper in Communications Biology and is presented in Appendix 1.

Abstract Endothelial cells (ECs) lining all blood vessels are subjected to large mechanical stresses that regulate their structure and function in health and disease. Here, we review EC responses to substrate-derived biophysical cues, namely topography, curvature, and stiffness, as well as to flow-derived stresses, notably shear stress, pressure, and tensile stresses. Because these mechanical cues in vivo are coupled and are exerted simultaneously on ECs, we also review the effects of multiple cues and describe burgeoning in vitro approaches for elucidating how ECs integrate and interpret various mechanical stimuli. We conclude by highlighting key open questions and upcoming challenges in the field of EC mechanobiology.

1.5 Physiological *in vitro* systems for EC culture

1.5.1 A brief history of EC culture in vitro

The first report of cells being kept alive outside their host body was in the 19th century by Wilhelm Roux [36]. He extracted neural cells from chick embryos and cultured them in a saline solution. The first cell culture techniques were developed by Ross Harrison at the beginning of the 20th century [36]. By mounting his explanted tissues on glass coverslips, he could image the live tissue growth, reporting: "the development of the nerve fibers by independent growth from cells outside the body". After observing bacterial contamination of his tissues, he created a heat sterilization protocol, with a flame, boiling water and autoclave. A couple of years later, Burrows and Carrel made a plasma-based culture medium that maintained in vitro tissues alive for months [36].

Burrows and Carrel proposed the idea of "continuous culture" by using cancerous tissues instead of the primary culture of explants. The first cell line was created in 1912 by Carrel's team and was maintained for more than thirty years, with an annual birthday celebration in the New York World Telegram [36]. During the course of the 20th century, tens of new cell lines were isolated and protocols for in vitro cell culture were slowly improved [36].

Researchers developed culture substrate coatings, better culture media with adapted amino acids, ions, serum, sugar, antibiotics and growth factors, and controlled environmental conditions, with the right pH, temperature, oxygen and CO_2 levels, osmolarity and viscosity. Two important inventions to that end were the "safety cabinet" and the incubator, with commercial models being widely distributed beginning in the 1960s [36].

For the best part of the 20th century, endothelial cells were seen as inconsequential for vessel physiology, described as "a sheet of nucleated cellophane" or "the inner tube of a tire and, in fact, if you can grow them in culture, you will probably end up with nondescript fibroblasts" [37]. As a result, very few scientists turned their attention to the endothelium and attempted to isolate it, with only a handful of reports on EC culture with varying degrees of success. Issues included the identification of the cultured cells and transdifferentiation. Nachman's team was the first to isolate and carefully identify ECs in vitro, leading to an explosion of interest in them in vascular biology. They made their first successful isolation in 1971: "We had clearly cultured what appeared to be endothelial cells — a monolayer of very flat, polygonal-shaped cells.", and they characterized their phenotype with immunofluorescence labeling of the von Willebrand Factor, the accepted biochemical marker for EC identification at the time. ECs then became the point of focus of the vascular biology community, as reflected by the exponential growth of papers on ECs in the years following Nachman's first publication.

1.5.2 Improved in vitro platforms

For the first decades of cell culture, the efforts focused on mimicking the native biochemical environment of cells, with all the factors listed above. The physical and mechanical environment of cells was completely left out, and cells were cultured on simple glass or plastic flat surfaces, coated with an adhesion molecule. The human body is obviously not an assembly of flat plastic rectangles, and cells reside in a much more complex microenvironment. Important properties of this physiological niche include softness, curvature, nano- and microtopography as most matrices have a fibrillar structure, three-dimensionality, and the various mechanical cues listed in section 1.2. Towards the end of the 20th century, two major axes of improvement were in progress.

One direction explored by researchers was cell culture on or inside hydrogels [38]. Hydrogels are native or synthetic polymeric networks with high water content and excellent biocompatibility [39]. They can be polymerized on top of a glass substrate before cell plating or could be mixed with a cell suspension before polymerization to encapsulate the cells inside the biomaterial. One of the first reports of the decisive influence of hydrogels as culture substrate was in 1992 by Petersen et al. They showed that epithelial cells, displaying a tumorigenic phenotype on standard Petri dishes, assembled into multicellular spherical structures resembling healthy acini when encapsulated in a soft hydrogel [40].

The other endeavor, aiming at the introduction of relevant mechanical stresses in culture systems, was pioneered by the vascular community. Indeed, even in first studies on ECs, it was clear that blood flow was a key player in their physiology. For instance, atherosclerosis, a major cardiovascular disease, was linked very early on to shear stress patterns, with plaques developing more frequently in areas where the flow was disturbed and cells failed to elongate (see section 1.3). As a result, various platforms attempting to apply a controlled shearing force on the cells by motion of the fluid on top of the monolayer can be found in the literature beginning in the 1980's. The first device was the cone-and-plate viscometer [41–44]. A modified version, a disk-plate chamber, was published a few years later [45]. Finally, the parallel flow chamber, which is still one of the most popular platforms for shear application because of its simplicity and well-defined flow profile [46], was developed and used for EC flow studies.

1.5.3 Organ-on-chips

1.5.3.1 Concept and advantages

The new generation of in vitro systems, the organ-on-chips, bring together the two approaches described above. Organ-on-chips are miniaturized platforms for in vitro cell culture, and they lie at the interface of multiple scientific fields [47]. They were developed with two goals: culturing cells in a physiological microenvironment and facilitating in vitro culture. These microfluidic chips, made of mechanically and chemically relevant biomaterials, allow the culture of multiple cell types in 3D environments. They can furthermore encompass sensors for real-time monitoring of different parameters or mechanical stimulation to better mimic the native cellular environment [48]. One of the seminal works that helped launch this field is the lung-on-a-chip, designed by Ingber's group in 2010, which is a perfect illustration of the important concepts in organs-on-chip [49]. An epithelium is co-cultured with an endothelium, on either side of an elastic porous membrane (Figure 1.9 A). The two separate microfluidic channels allow physiological air and medium flow on top of the epithelial and endothelial cells, respectively. On the lateral side of the chip, a third channel, whose pressure can be controlled, allows stretching of the elastic membrane in order to mimic the cyclic strain experienced by the cells during lung inflation and deflation (Figure 1.9 A & B). This chip was made with standard microfabrication techniques, such as photolithography used to make a master mold followed by PDMS casting to obtain the chip housings; the two parts are then bound together by plasma activation (Figure 1.9 C & D). The final object is as big as a coin (Figure 1.9 E).

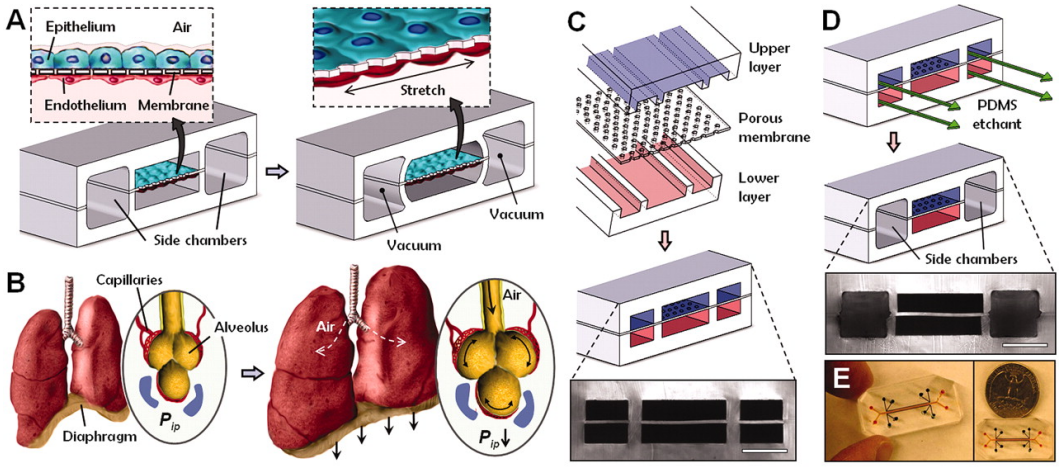

FIGURE 1.9: Ingber's lung-on-chip design and microfabrication process. [49].

Commercially available organs-on-chips, such as the ones from Emulate or Mimetas, have permitted the adoption of bioengineering technologies by laboratories that are not equipped for home-made and complex culture platforms. The miniaturization reduces the volume of medium, cells and reagents used, lowering costs and enabling high throughput screening [50–52]. Organs-on-chips have numerous applications; one of the most advanced ones today is drug testing [53, 54]. Thanks to the organ mimicking environment, cells have a more physiological reaction to drugs, leading to a better prediction of the effect of the tested drugs in vivo. An exciting direction is the body-on-chip, where multiple organs-on-chips are connected to one another to replicate the native organ interconnections via the vascular system [55, 56].

1.5.3.2 Microvessels-on-chip

The microfluidics aspect of organ-on-chip systems is particularly interesting for the study of vascular cells, particularly to apply flow on the cells. Through various fabrication methods, a plethora of vessel-on-chips has been published in the last decade [57,58]. I will present here the major geometrical configurations, all of which enable flow on ECs.

The oldest class of microvessel-on-chips are straight rectangular channels, made in PDMS. They are often used for drug testing and metabolic studies because of their fabrication robustness and high throughput [59, 60]. The second class are straight cylindrical channels, made inside soft hydrogels [61–65]. They are better mimics of the native microenvironment of the microvasculature and might become the new gold standard as fabrication techniques evolve. The third class are branched vessels, with a user defined geometry that can be rectangular in PDMS [66, 67] or cylindrical in soft gels [68, 69]. They are used to investigate the role of narrowing, branching or merging in EC function. The fourth and last class are capillary beds, a random network of thin endothelial tubes inside hydrogels. The hydrogel is usually placed between two lateral channels in a PDMS-based chip [70, 71]. The capillaries can then anastomose to the lateral channels, enabling perfusion. These systems have a much more realistic network geometry and the smallest lumen diameter, allowing the study of interactions between blood-borne cells and the endothelium [72]. Finally, co-culture of mural cells is possible in PDMS microvessels with the use of porous membranes [60, 73] and in all the hydrogel-based microvessel platforms [74–76].

1.6 Biofabrication for the vasculature

The biofabrication techniques to obtain the various platforms presented above are constantly evolving [77]. I will review here the state-of-the-art biofabrication techniques for the vasculature before discussing challenges and opportunities pushing the field towards new technological development. During the second year of my thesis, I had the opportunity to collaborate with a team from the University of New South Wales (UNSW) in Australia for a review article on 3D printing for cardiovascular applications [78]. The following section was synthesized into a few paragraphs as part of this review.

1.6.1 Current fabrication techniques for vascular platforms

1.6.1.1 3D bioprinting

Concept 3D bioprinting is conceptually similar to standard additive manufacturing (3D printing) of non-biological materials: successively adding different materials layer-by-layer to form precise geometries. The difference with bioprinting is that the materials are biologically-based including the possibility of living cells [79]. The biological dimension leads to specific challenges compared to traditional 3D printing, from the perspective of both the materials and the printing process [80]. In terms of the materials, the bioinks need to be biocompatible and to allow cell culture or implantation. They also need to have tailored mechanical properties to match those of the tissues being printed. Inclusion of cells in the printed material and the need to ensure cell viability dictate the permissible ranges of several parameters such as temperature, pH, chemical composition, and shear forces. Indeed, shear-induced cellular damage through bioprinter nozzles remains a major challenge [ref].

The technology of bioprinting for vascular applications has been the subject of several recent reviews [81–83]. The vascular geometry with its extensive curvature, numerous bifurcations, and elaborate tortuosity increases the complexity of the printing process. Blood vessels are hollow cylinders and need to be perfusable. The use of sacrificial materials allows the

fabrication of a continuous structure where the lumen is formed after printing by dissolution or melting of the sacrificial material. Because blood vessels have thin and compliant walls, printing a freestanding vessel is currently not possible; therefore, printed vascular structures can either be large and stiff or, in the case of small vessels, encased in a soft bulk material.

Technology Three technologies exist for 3D bioprinting: inkjet, micro-extrusion and laser-assisted (Figure 1.10 A) [80]. In inkjet bioprinters, liquid droplets containing the biological material are ejected out of the printer nozzle and deposited at controlled positions onto a substrate. Inkjet printing is fast and low cost, is associated with reasonably good cell viability, but has low spatial control and is only compatible with certain bioinks. In micro-extrusion, a continuous paste of material is mechanically pushed out. Micro-extrusion allows high cell density printing and is compatible with many bioinks but suffers from low cell viability and significant cost. In laser-assisted bioprinters, a laser is used to generate mechanical pressure that allows etching material out from a layer. Laser printing is extremely precise, is compatible with virtually all bioinks, and is associated high cell density and excellent cell viability; however, it is slow and very expensive. The differences in cost, precision, compatible materials, and cell viability among the three techniques suggest that the optimal choice of technique is application-specific [84].

Applications There are a number of recent reports of bioprinted vessels that have been used to address important biological questions. One example is extrusion printing of large vessels (1 mm in diameter) lined with endothelial cells and fibroblasts and encased in a bulk material that were subsequently used to study thombus formation and thombolysis [85]. A second example involved printing of agarose template fibers inside synthetic polymers which allowed generation of a network of endothelial cell-lined microvessels down to 250 μm in diameter [86]. A third example was the use of three different inks in one constructto fabricate a large vascularized tissue with co-culture of endothelial cells, tissue-specific cells, and ECM components [87]. Yet another example focused on inkjet printing of a 3D vascular network with bifurcations as well as tortuous vessels [88, 89]. A final example entailed the use of laser bioprinting for the formation of endothelial cell-lined microvascular networks that follow a large scale pattern [90, 91].

1.6.1.2 Casting and molding

Casting and molding are simple approaches that typically do not require expensive equipment; therefore, they are favored by many laboratories. The basis is very simple: a liquid polymer is cast in a mold around a cylindrical rod which is removed after solidification to form the vascular lumen (Figure 1.10 B). Cells are subsequently seeded in this lumen. This technique allows the rapid, cheap, and robust generation of straight vessels of various diameters and cellular composition.

Large vessels One study proposed using off-the-shelf laboratory supplies to readily create models of aneurysms, stenoses, and bifurcations while also allowing endothelial cell culture [mannino2015yourself]. The approach consisted of casting PDMS over an optical fiber, removing the fiber after PDMS polymerization to form the lumen, and then perfusing with endothelial cells. The experimental studies focused on platelet aggregation and were complemented with computational fluid dynamic (CFD) simulations. Using a biomaterial such as a collagen or fibrin hydrogel as the casting material increases the complexity and interest of the casting and molding technique. This allows cell seeding not only in the vascular lumen but also within the hydrogel as a model for mural cells that can subsequently be subjected to a more physiologically relevant environment. Casting and molding can be used to generate vessels of different sizes, thus modeling arteries and veins as well as microvessels.

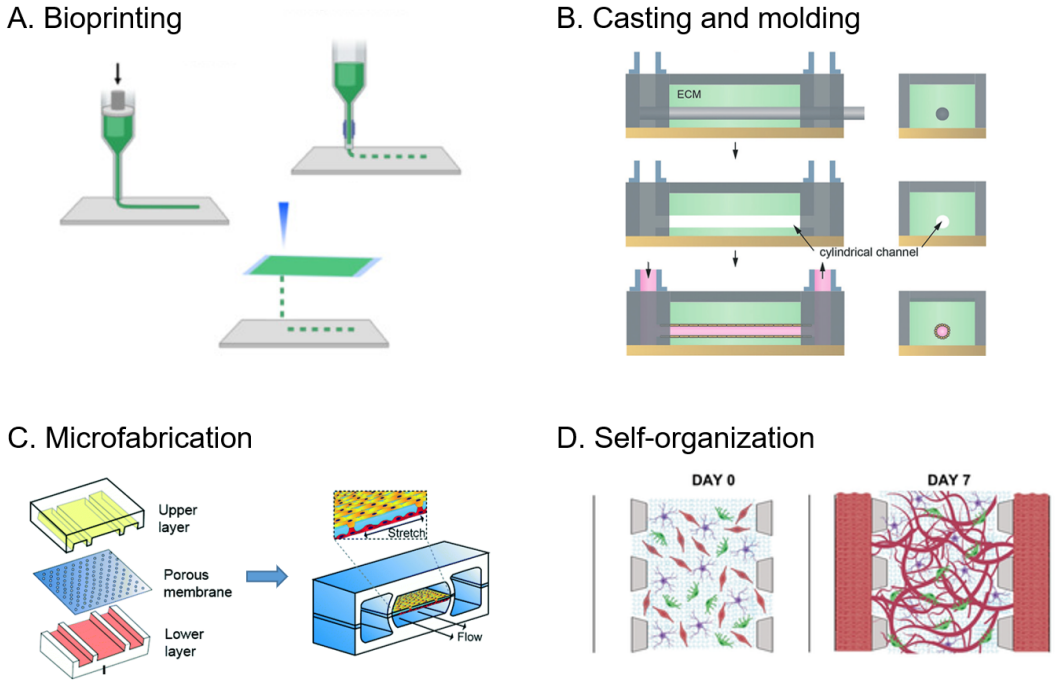

FIGURE 1.10: Schematics of the four major fabrication process. [73, 92–94]

In some cases, these more sophisticated models have been used to explore pathologically and clinically relevant scenarios. An example is work that has developed an in vitro artery containing both endothelial and smooth muscle cells and within which a stent can be deployed and the subsequent cellular responses to the stenting procedure monitored at high resolution in real time [95]. The arterial wall in this particular case consisted of a type 1 collagen hydrogel, a versatile material ideal as an engineered scaffold [96]. The study demonstrated the ability to track endothelial wound healing post stenting, to monitor smooth muscle cell migration within the hydrogel, and to characterize the extent of flow disturbance induced by the stent using particle image velocimetry (PIV). In addition, the experiments were complemented with CFD simulations that demonstrated close agreement between the computed flow fields and those measured by PIV. This in vitro artery is an example of a system that can serve broadly as a platform for various investigations including endovascular device development, toxicity testing of cardiovascular drugs, dynamic monitoring of leukocyte interaction with the arterial wall, and assessment of the effects of nanomaterials on the arterial wall.

Microvessels In a similar manner, templating a hydrogel around a thin needle allows the fabrication of microvessels with a diameter as small as 50 µm [refs]. Co-culture with mural cells, be they smooth muscle cells or pericytes, replicates the native physiology and provides a versatile system for studying microvascular physiology and pathology [refs]. Engineered microvessels are also of interest because they constitute one possible pathway towards vascularization of tissue engineered constructs. Finally, casting and molding can be combined with 3D printing for fast and relatively inexpensive fabrication of vessels with a complex geometry [97]. In this scenario, a 3D printer is used to generate a template of an entire vascular network, potentially derived from a real geometry, using a soluble material, and the scaffold is poured around it. After dissolution of the template, the remaining hollow tunnels representing the vessels can be seeded with cells.

1.6.1.3 Microfabrication

Microfabrication techniques initially derived from the microelectronics industry have spread to biological laboratories and have been adapted to fabricate high resolution patterns down to the micron scale (Figure 1.10 C). Two primary families of microfabrication can be distinguished: micropatterning and microfluidics [98].

Micropatterning In the case of micropatterning, photolithography is used to directly pattern a synthetic or biological material of interest or an intermediate stamp or mold that is then used to imprint the pattern on the material. Micropatterning has been used to fabricate extremely complex geometries, derived from images of real vessels, on the surface of a PDMS substrate [99, 100]. A glass slide or coverslip is used to provide a closed system within which fluid perfusion is possible. The micropatterning technique also allows fabrication of vessels on the surfaces of biomaterials such as hydrogels or synthetic biocompatible polymers [101, 102]. To embed the vessels deeper within the construct, the patterned free surface can then be bound to another gel layer [103–105].

Microfluidics In the case of microfluidics, vessels that are 10-100 μm in diameter that can be seeded with endothelial cells are produced by the flow of concentric fluid layers (the core and sheath approach) [106]. The flow focusing technique allows precise control of the thickness of each layer. Polymerization generates free-standing vessels with walls having two or three layers. When combined with extrusion printing, the microfluidics technique allows the printing of a multi-layered vessel inside another material that modes the extravascular matrix [85, 107, 108]. These microfabrication approaches generate vascular networks with high spatial control and that are compatible with incorporation of organ-specific cells in the bulk material. Ongoing efforts are targeting improved scaling and robustness.

1.6.1.4 Self-organization

Self-organization relies on the natural biological development processes to obtain physiologically relevant three-dimensional vascular constructs (Figure 1.10 D). The technique consists of applying controlled external chemical and mechanical cues to form a microenvironment that guides the cells of interest toward target tissue formation. Self-organization is very popular for vascular engineering as endothelial cells seeded in a bulk biomaterial and cultured with the appropriate mix of growth factors connect to each other and form networks of immature capillaries. The growth factors can either be added to the culture medium or secreted by co-cultured cells such as fibroblasts. The addition of mural cells (typically SMCs or pericytes) leads to narrower and longer capillaries and an overall more stable network. The field of organs-on-chip has explored several applications of self-organization such as tumor neovascularization, tumor or immune cell extravasation, blood-brain barrier modeling, and the impact of mechanical cues. Self-organization is advantageous for research applications as it does not require any specialized equipment. Vasculogenesis can be combined with 3D bioprinting to generate a vascular tree: large vessels are generated with inkjet printing and a capillary bed connecting these vessels is obtained by self-organization (vasculogenesis) [109].

1.6.2 Future of biofabrication

1.6.2.1 Challenges and opportunities

Many challenges remain in the field of biofabrication of vascular tissues, and some of these challenges have been highlighted elsewhere [110]. We focus here on the two most critical challenges: building complexity and improving the translational potential. Current constructs are highly simplified models of the native vasculature. There is a need for more elaborate

models that incorporate multiple cell types; most current in vitro vessels include only endothelial cells. Mural cells, such as pericytes or smooth muscle cells, are essential to mimic physiological functions, and fibroblasts, mesenchymal stem cells, and endothelial progenitor cells are also constituents of large vessel walls. Designing and developing vascular constructs that model the complex cellular cocktail will undoubtedly receive significant attention in the coming years. Another challenge stems from the marked hierarchy of the vasculature, characterized by a wide range of diameters and different wall structures. Including processes such as arteriogenesis, remodeling, and vessel maturation in engineered vascular constructs will be necessary to replicate the complex vascular tree. Finally, vessels in vivo are embedded deep within tissues to ensure proper vascularization. Separately fabricating blood vessels and the tissues they are intended to perfuse precludes efficient integration of these structures. Therefore, more physiologically relevant engineered tissues will require advances in co-fabrication.

Beyond research applications, the ultimate goal of biofabrication is to produce constructs with translational potential in order to improve patients' lives. The need to implant a tissue in a patient imposes significant demands on the fabrication process in terms of durability, robustness, and integration into surrounding tissues. Once implanted, artificial vessels will be subjected to prominent environmental cues that can induce remodeling and can accelerate the deterioration of the construct. Therefore, engineered vessels need to be able to not only withstand but also adapt to the dynamic chemical and mechanical environment in which they will reside. Finally, to allow transplantation, immunological matching is necessary: using patient-derived induced pluripotent stem cells (iPSCs) promises to ensure this biocompatibility, and several recent studies have focused on using these cells. More broadly, iPSCs are also very useful for research applications as they allow the study of patient-to-patient variability as well as exploration of the mechanisms governing genetic diseases.

1.6.2.2 Recent technical innovations

To overcome the challenges outlined above, many technical innovations have recently emerged. We review here the most promising such innovations. The use of organoids as building blocks in the bioink increases cell density to better match in vivo values and permits the quick fabrication of larger structures [111,112]. Building on this, modifying the material properties towards so-called self-healing gels allows the subsequent printing of a vascular network inside a bulk construct [refs]. In this technique, a condensed solution of organoids is poured into a mold after which a nozzle moves through the liquid condensate of organoids to print a bilayered vascular network. Finally, the bulk material is polymerized, and the lumens of the vessels are generated via dissolution of a sacrificial material. This is a significant step toward higher complexity and vascularization of bulk tissues. One study used this approach to generate a beating muscle of several centimeters with hiPSCs [refs].

Laser patterning of hydrogels is another relatively new and highly promising technique that allows carving lumens into a hydrogel with sub-micron resolution [113]. This technique has been used to generate endothelialized 5 μm-diameter capillaries of controlled geometry in a collagen hydrogel to study red blood cell stalling in malaria [114]. In all of these approaches, it will be critical to incorporate the ability for perfusion of large tissues in order to add the relevant mechanical forces which constitute important cues for remodeling and stabilization of immature vessels [112]. Finally, a recent study in the field of skin tissue engineering reported in situ printing in both mice and pigs of a construct consisting of dermal fibroblasts and epidermal keratinocytes in a hydrogel in order to directly deposit autologous skin cells and accelerate wound healing [115]. Exploring how this approach may be extrapolated to the case of the vasculature, at least for the case of superficial vessels, certainly merits future investigation.

1.7 *In vitro* platforms for stretching ECs

Most published studies using microvessels-on-chip focus on only one mechanical force, the steady shear stress, assuming that flow pulsatility and strain are absent in the microvasculature [116]. Indeed, shear stress is a feature found in many *in vitro* platforms to investigate vascular processes, as it can be generated simply by flowing medium over the cells. Although pulsatile shear stress is less common, it usually does not require design modifications but only a different type of flow generator. Strain, on the other hand, requires substrate deformation with an actuation system, which is difficult to achieve inside a microvessel-on-chip. I will review here the different types of existing stretchers and how they were adapted for the case of vascular ECs.

1.7.1 Traditional stretchers

1.7.1.1 Mechanical stretchers

Concept The first family of devices are based on mechanical actuation, where the displacement of an external solid frame by a servo or stepper motor stretches the substrate in plane. The first cell stretcher was reported in 1989 and was based on the mechanical and uniaxial stretching of a silicon membrane [117]. In uniaxial stretch, tensile strain is applied in only one direction, but compressive strains are also present in the transverse direction due to the material's Poisson's ratio. Two variations of this stretcher have been developed: purely uniaxial, by constraining the sample in the transverse direction, and biaxial, with two axes of mechanical stretching [118].

An interesting possible modification of mechanical stretchers is to replace the 2D membrane by a 3D gel. Cells can then be cultured on the surface of gels of various stiffnesses in order to investigate the combined effects of strain and stiffness and of strain and topography, and the cells can even embedded cells inside the gel to generate 3D strain fields [119–122]. In vascular applications, the 3D stretch is particularly interesting for the study of angiogenesis, a process during which cells leave the 2D vessel surface to invade the surrounding 3D tissue. Those tissues are often moving, generating strains, which can affect the structure of the resulting network of microvessels [123–125].

Pros and cons The main strengths of mechanical stretchers are the defined and controlled strain vector field they generate, thanks to the in-plane and homogeneous strain application and the stretching of 3D gels. Their major limitations are the high cost of equipment used and their large dimensions, both leading to a low throughput, with only a couple of systems possible in parallel. 3D printing has been used in the last few years to make mechanical stretchers more cost-effective and facilitate their adoption in both uniaxial [126] and biaxial [127] configurations.

1.7.1.2 Pneumatic stretchers

Concept The second family of devices are based on pneumatic actuation, where motion is generated through vacuum creation next to a deformable wall. Two main configurations of pneumatic actuation are found in the literature.

In the first configuration, the vacuum is formed directly beneath a thin membrane lined with cells, deforming the membrane and thus stretching the cell layer [128]. In this setup, the membranes are stretched through the bending of the membrane, either inward with negative pressure or outward with positive pressure, subjecting cells to a concave or convex curvature in addition to the strain. In most cases, the radius of curvature is large compared to cell size,

minimizing the effect of this additional mechanical cue. The strain field, however, is often complex and not homogeneous due to the geometry of the deforming membranes [129].

In the other design, the vacuum deforms a lateral wall, which in turn stretches the membrane bound to that moving wall. In this setup, the membranes are stretched in-plane, without curvature and in a homogeneous manner. The difficulty here is the complexity of the device, which requires separate lateral channels for pneumatic actuation, with thin deformable lateral wall or flexible posts, in addition to the thin deformable membrane acting as the cell substrate. An example of this design is the previously described lung-on-chip (Figure 1.9) [49].

Pros and cons The advantage of pneumatic stretchers is the possibility of parallelization, miniaturization and relatively low cost, which increase the system's throughput. The main drawbacks are the complex strain fields, the difficulty of generating independent bi-axial strain and only one option as the substrate type, PDMS rather than 2D or 3D hydrogels.

1.7.2 Stretchers for vascular studies: combining flow and stretch

An essential mechanical cue in the vasculature is the shear stress due to luminal blood flow, but flow is absent in all the stretchers presented above. Three classes of *in vitro* systems are used in the vascular field, which permit the application of strain in combination with flow and shear stress: inflatable vessels, flow chambers in mechanical stretchers and microfluidic pneumatic stretchers [130]. While the first one is an innovation by vascular scientists and is a perfect example of bioinspired design, the latter two are adaptations of the two traditional stretchers presented above with the goal of adding a flow component.

Inflatable vessels In the inflatable vessels, thin PDMS tubes are lined with endothelial cells and perfused with controlled flow to generate both shear stress and circumferential strain through the dilation of the soft tube [131–135]. The diameter of these model systems is around 5 mm, which mimics medium arteries or veins but poorly replicates the high curvature found in the microvasculature. Additionally, because both shear stress and stretch are generated by the luminal pressure, the two stresses are coupled in this type of system. A modified version of the inflatable vessel, decoupling the shear stress and the strain, was published by van Haaftern et al. The shearing flow is applied on the outside of the vessel and the stretch comes from actuation inside the cylinder with the luminal pressure [136].

Flow chambers on mechanical stretchers The oldest platforms for shear stress, the flow chambers, and for stretch, the mechanical stretcher, can be combined together to couple the two stresses [137–139]. The concept is simple: the flow chamber is made entirely in PDMS, without a bottom glass slide, and mounted on a mechanical stretcher. It has the advantages of both systems with well defined flow and strain fields, but it also maintains their drawbacks, being a flat, stiff, macroscopic and costly system.

Microfluidic pneumatic stretchers Pneumatic actuation is well suited for microfluidic systems, such as microfabricated vessel-on-chips, as it relies on controlled air pressure in tight channels. A multitude of microfluidic pneumatic stretchers were reported in the last two decades, either in plane [73, 140–143] or curved configurations [144, 145]. Because the floating membrane has to have a minimal thickness (typically tens of microns) to maintain its mechanical integrity, the small radii of curvature present in the microvasculature cannot be attained with microfluidic pneumatic stretchers.

Chapter 2

A flow-actuated microvessel-on-chip

> Science, though apparently transformed into pure knowledge, has yet never lost its character of being a craft; and that it is not the knowledge itself which can rightly be called science, but a special way of getting and of using knowledge.
>
> *William Kingdon Clifford - 1886*

The literature review presented in Chapter 1 reveals the existing gaps in available in vitro platforms, in particular for the study of stretch. Variations of microvessels encompassing shear stress have been developed to include substrate stiffness or curvature. Variations of stretchers have been similarly explored to include shear stress or substrate stiffness. However, to the best of my knowledge, a platform for the application of stretch on ECs in a microvessel configuration, i.e. on an endothelial lining a cylindrical vessel of micron-scale dimensions, does not exist, without even mentioning the combination with shear stress and substrate stiffness. Furthermore, many of the interesting platforms are accessible only to a small number of other laboratories because of their technical complexity and the expensive fabrication equipment they require. Only the simplest platforms such as the square PDMS-based vessels-on-chip, have become broadly accessible because they involve user-friendly designs and cheap fabrication processes. This current gold standard lacks many important mechanical cues such as curvature, stretch and adequate substrate mechanical properties. In sum, the development of a vessel-on-chip comprising all the relevant mechanical stimuli and made with a simple fabrication process would be a valuable contribution for the research community in the field.

That is the task I defined as the first goal of my Ph.D.: to develop a microvessel-on-chip allowing ECs to be subjected to stretch, shear, high curvature and substrate stiffness. I wanted a system that is readily adoptable by other laboratories, in particular biology groups with no access to expensive microfabrication techniques. The system needed to be simple and cheap and to require minimal microfabrication equipment in order to have a chance at becoming a new convenient, versatile and useful tool. It also needed to encompass a pulsatile mode for all the stresses. Finally, all these features had to be applicable within physiologically (and potentially pathologically) relevant ranges (see Chapter 1).

After a thorough review of the literature on existing systems, I chose to combine two types of stretchers (see section 1.7.2), the inflatable vessel and the microfluidic pneumatic stretcher, by creating an inflatable microvessel-on-chip. The technical development of the microfluidic chip, which took the better part of the first year of my Ph.D., is presented in Appendix 2. In this chapter, I will describe the characterization of the microvessel's mechanical behavior

and potentialities, presented in the format of a paper.

I finish this short preamble by mentioning two other projects in the group with helpful elements that guided my choice of certain experimental features. I used the preexisting expertise on microfluidic flow chambers in the choice of syringe pumps and connectors and the cell culture under flow. Colleagues working on the artificial artery platforms helped me with the collagen hydrogel fabrication.

Luminal Flow Actuation Generates Coupled Shear and Strain in a Microvessel-on-Chip

Claire A. Dessalles*, Clara Ramón-Lozano, Avin Babataheri#, Abdul I. Barakat#*

LadHyX, CNRS, Ecole polytechnique, Institut polytechnique de Paris, 91120, Palaiseau, France

# These authors contributed equally.
* Corresponding authors. claire.dessalles@ladhyx.polytechnique.fr, abdul.barakat@ladhyx.polytechnique.fr

Abstract

In the microvasculature, blood flow-derived forces are key regulators of vascular structure and function. Consequently, the development of hydrogel-based microvessel-on-chip systems that strive to mimic the in vivo cellular organization and mechanical environment has received great attention in recent years. However, despite intensive efforts, current microvessel-on-chip systems suffer from several limitations, most notably failure to produce physiologically relevant wall strain levels. In this study, a novel microvessel-on-chip based on the templating technique and using luminal flow actuation to generate physiologically relevant levels of wall shear stress and circumferential stretch is presented. Normal forces induced by the luminal pressure compress the surrounding soft collagen hydrogel, dilate the channel, and create large circumferential strain. The fluid pressure gradient in the system drives flow forward and generates realistic pulsatile wall shear stresses. Rigorous characterization of the system reveals the crucial role played by the poroelastic behavior of the hydrogel in determining the magnitudes of the wall shear stress and strain. The experimental measurements are combined with an analytical model of flow in both the lumen and the porous hydrogel to provide an exceptionally versatile user manual for an application-based choice of parameters in microvessels-on-chip. This unique strategy of flow actuation adds a dimension to the capabilities of microvessel-on-chip systems and provides a more general framework for improving hydrogel-based in vitro engineered platforms.

Keywords: Endothelial cells, hydrogel, shear stress, strain, pulsatility, flow actuation.

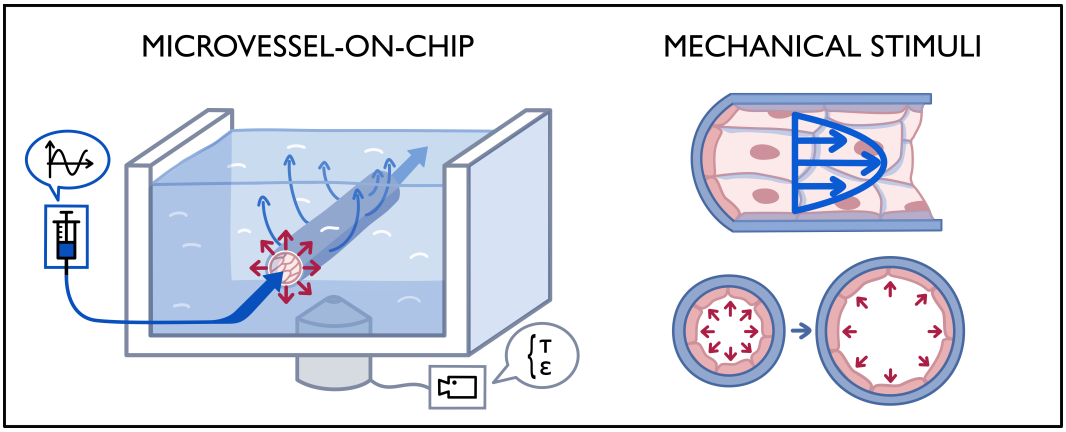

Introduction

In the vasculature, mechanical forces regulate blood vessel development, network architecture, wall remodeling, and arterio-venous specification [1,2]. Abnormalities in the mechanical environment play a critical role in the development of vascular diseases in both large and small vessels. In the specific case of the microvasculature, hemodynamic perturbations are associated with chronic pathologies such as hypertension as well as more acute events such as thrombosis [2–5]. Vascular responsiveness to mechanical stimulation is enabled in large part by the endothelium, the layer of cells at the interface between the bloodstream and the vascular wall. By virtue of their strategic position, endothelial cells (ECs) sense mechanical forces and transduce these

forces into signals that regulate vascular structure and function [6–8].

Elucidating the mechanisms governing endothelial mechanobiology requires the development of in vitro systems within which ECs experience a physiologically relevant mechanical environment [9, 10]. In vivo, the endothelium is principally subjected to two types of mechanical stresses that act in different directions: tangential shear stress due to the flow of viscous blood over the EC luminal surface [11] and circumferential (hoop) stress as a result of the transmural pressure difference which generates a circumferential strain that stretches the cells. Typical physiological shear stress values range from 0.5 to 5 Pa, depending on the location in the vasculature [4, 5, 12]. Strain magnitudes of 5-10% are considered physiological, whereas strains of 15-20% are characteristic of pathological situations [13–16]. Importantly, these mechanical forces are highly dynamic due to blood flow pulsatility. Although pulsatility has traditionally been assumed to be completely dampened by the time blood reaches the microvasculature, recent data challenge this consensus and have reported significant velocity and diameter oscillations even in the smallest capillaries [17–21]. Interestingly, in diseases such as hypertension, the higher pulse pressure penetrates deeper into the vascular tree, further increasing pulsatility in the microvasculature [7, 22].

Subjecting ECs to controlled levels of shear stress in vitro is readily accomplished in cone-and-plate systems, parallel plate flow chambers, and microfluidic channels [23]. However, these devices fail to stretch the cells. The effect of stretch on cells has traditionally been studied using planar uniaxial or biaxial stretching devices [24–26], but these systems do not incorporate flow and fail to capture the impact of substrate curvature, a particularly important consideration in the microvasculature. Microfluidic chips with pneumatic actuation in either planar [27–31] or curved [32, 33] configurations have been reported, but these systems require external actuation and do not mimic the native substrate in terms of curvature, fibrillar structure, or stiffness. One platform that has been used to study the combined effects of shear stress and stretch on ECs is the inflatable vessel, where PDMS tubes are pressurized to generate both flow and circumferential strain [34–38]; however, the tubes have diameters of 5 mm, too large for studies of the microvasculature and incompatible with high resolution cellular imaging.

More recently, there has been mounting interest in vessel-on-chip systems that enable the application of controlled shear stress while providing a biologically relevant substrate and a realistic geometry [39–43]. A popular design consists of an endothelialized perfusable channel inside a collagen or fibrin hydrogel [44–49]. However, current microvessel-on-chip systems do not allow stretch due to the difficulty of incorporating actuators into micron-scale channels inside soft hydrogels. The ability to actuate hydrogels in microvessels-on-chip in a simple and controlled manner would enable the application of strain and would thus allow exploration of the combined effects of flow and stretch in these systems. Such a capability would significantly expand the experimental toolbox in the field of endothelial mechanobiology.

Here, we present a novel collagen hydrogel-based flow-actuated microvessel-on-chip that produces shear and strain simultaneously and overcomes the limitations of previous systems. We fully characterize the mechanical performance of the system and demonstrate the inherent coupling between shear and strain that can be accurately described within the poroelasticity framework. We show the ability to subject a confluent and functional EC monolayer to physiological and pathological levels of shear stress and strain under both steady and pulsatile conditions. Finally, we illustrate how different aspects of the design of the system can be tuned to modulate the shear-strain coupling, thus providing a highly versatile platform for elucidating the effects of a physiologically relevant mechanical stress environment on ECs.

Materials and Methods

Microvessel-on-chip fabrication

As depicted in Figure 1 and Supplementary Figure S1, the microvessel-on-chip system consists of a chamber that houses a 120 µm-diameter endothelium-lined channel embedded in a soft collagen hydrogel. The different components of the system are next described.

Housing chamber fabrication and preparation. The rectangular (15x2x3 cm) housing chamber was fabricated by pouring liquid elastomer mixed with 10% curing agent (polydimethylsiloxane (PDMS); Sylgard 184; Dow Corning) on a custom mold micromachined in brass to specific dimensions (Figure S2). After curing for 15 min at 180°C, the PDMS chamber was unmolded, and inlet and outlet ports were punctured using a hole punch. A 120 µm diameter acupuncture needle (Seirin) was introduced into the chamber, and liquid PDMS was used to fix it in place. With the needle in place, the bottom surface of the chamber frame was then bound to a coverslip through plasma activation. Finally, two fluid reservoirs, cut and punched from blocks of PDMS, were sealed with liquid PDMS to the inlet and outlet ports of the chamber, and the entire chip was then cured again for 1 h at 180°C. A critical feature is that the top of the chamber was maintained open.

The PDMS housing chamber was sterilized in 70% ethanol, dried, and plasma-activated for 45 s to render its surface hydrophilic and improve subsequent coating steps. The chamber was then covered with sterile PBS and placed under vacuum to remove bubbles from the inlet and outlet ports followed by 20 min of UV

light exposure for final sterilization. To improve collagen adhesion to the PDMS walls, the chamber was coated with 1% polyethylenimine (PEI,an attachment promoter; Sigma-Aldrich) for 10 min followed by 0.1 % glutaraldehyde (GTA, a collagen crosslinker; Polysciences, Inc.) for 20 min.

Collagen hydrogel and microchannel fabrication. Collagen I was isolated from rat tail tendon as described previously [50]. Type I collagen solution was then prepared by diluting the acid collagen solution in a neutralizing buffer at a 1-to-1 ratio, pipetted into the housing chamber, and allowed to polymerize in a tissue culture incubator for 15 min for the baseline 6 mg/ml collagen concentration and for up to 4 h for lower collagen concentrations. The acupuncture needle was then carefully removed, and the needle holes were sealed with vacuum grease (Bluestar Silicones) to avoid leakage.

The hydrogel block formed inside the housing chamber was 15x2x3 mm (LxWxH); therefore, the length-to-diameter ratio of the 120 µm-diameter microchannel inside the chamber was 100. The microchannel was positioned far from all walls of the chamber: ∼400 µm from the bottom coverslip, 1 mm from the side walls, and more than 2 mm from the open top of the hydrogel (Figure 1.a, Figure S1).

Cell seeding and culture. Human umbilical vein ECs (HUVECs; Lonza) were cultured using standard protocols in Endothelial Growth Medium (EGM2; Lonza) and used up to passage 7. Upon confluence, HUVECs were detached from the flask using trypsin (Gibco, Life Technologies) and concentrated to 10^7 cells.ml^{-1}. 1 μL of the concentrated cell suspension was pipetted through the inlet port of the device. The level of both reservoirs was adjusted to allow a very small flow from inlet to outlet in order to infuse the cell suspension into the channel. After a 5 min incubation, non-adhering cells in the channel were gently flushed out. The addition of 500 µL of medium to the inlet reservoir generated a small flow, necessary for cell survival and spreading. After 1 h, a flow rate of 2 µL min^{-1} was applied via a syringe pump (PhD Ultra, Harvard apparatus). A confluent monolayer was obtained in 36 h.

Microvessel perfusion

Two different techniques were used to perfuse the microvessel at controlled flow rates: 1) a hydrostatic pressure head for the low flow (2 µL min^{-1}) used for medium replenishment and waste product removal during long-term cell culture, and 2) syringe pump-driven flow at 10 or 50 µL min^{-1} used for the mechanical characterization of the microvessel and for the application of mechanical stimuli on the confluent HUVEC monolayer. To generate the hydrostatic pressure head, a PDMS reservoir was created by punching a 5 mm-diameter hole in a PDMS cubic block (1 cm on a side) and gluing the block to the inlet. The reservoir was continuously replenished using a syringe pump (Nemesys, Centoni). Using the reservoir as an intermediary between the syringe pump and the microchannel was particularly useful for preventing air bubbles within the channel. For the syringe pump-driven flow, the pump was connected directly to the microchannel inlet.

Immunostaining

Cell-cell junctions were stained using a rabbit anti-VE-cadherin primary antibody (Abcam). Actin filaments and nuclei were stained using Alexa Fluor phalloidin (Invitrogen, Thermo Fisher Scientific) and DAPI (Sigma-Aldrich), respectively. Immunostaining was performed by slow infusion of reagents into the microchannel. Cells were fixed in 4% paraformaldehyde (PFA; Thermo Fisher Scientific) for 15 min, rinsed with phosphate-bufered saline (PBS), and then permeabilized with 0.1% Triton in PBS for another 15 min. The channel was then perfused with a 3% bovine serum albumin (BSA) solution in PBS for 1 h to block non-specific binding. Cells were incubated with the VE-cadherin primary antibody (1:400) in PBS for 1 h at room temperature and then rinsed with PBS for an additional 1 h. The channel was then perfused with an anti-rabbit secondary antibody (1:400), phalloidin (1:200), and DAPI (1:1,000,000) solutions. Finally, the cells were incubated overnight in PBS at 4°C. Samples were imaged using the NIS-Elements software on an epifluorescence inverted microscope (Nikon Eclipse Ti) and/or a Crest X-Light confocal system mounted on an inverted microscope (Nikon Eclipse Ti).

Permeability measurement

After monolayer formation, HUVECs were maintained in culture for an additional 24 h under a 2 µL min^{-1} flow to allow cell-cell junction maturation. Rhodamine-dextran (10 and 70 kDa molecular weight; Life technologies) was used as a fluorescent tracer to assess monolayer macromolecular permeability. The cells were maintained at 37°C during permeability measurements by using a microscope equipped with a stage-top incubator.

50 µL of medium containing 2 µL of dextran was added to the inlet reservoir. The fluid volume in the outlet reservoir was adjusted to 50 µL to avoid the creation of a hydrostatic pressure difference. The open top of the chip was covered with PBS during image acquisition to avoid evaporation in the hydrogel.

Images of dextran diffusion into the hydrogel were acquired at 4 frames.min^{-1} for 2 h and at several positions along the length of the channel using a Flash 4.0 CCD camera (Hamamatsu) mounted on an inverted fluorescence microscope (Nikon eclipse Ti) equipped with a 10x objective. The intensity profiles from the images were extracted using ImageJ. The evolution of dextran intensity over time was measured in the channel lumen

and in the gel at a radial position 15 µm from the microvessel walls.

As in previous work [51], the hydraulic conductivity (which is directly proportional to permeability) (K) of endothelialized channels to dextran was calculated as follows:

$$K = \frac{1}{\Delta I_{channel}} \left(\frac{\mathrm{d}I_{gel}}{\mathrm{d}t} \right)_{out} \frac{R}{2}$$

where $\frac{\mathrm{d}I_{gel}}{\mathrm{d}t}$ is the rate of change of fluorescence intensity in the hydrogel, $\Delta I_{channel}$ is the increase in fluorescence intensity within the lumen (due to luminal filling with dextran), and R is the microvessel radius.

For bare (non-endothelialized) channels, dextran (both 10 and 70 kDa) diffuses virtually instantaneously into the gel after entering the channel. Therefore, hydraulic conductivity values in that case cannot be computed using this same approach.

Particle tracking velocimetry

Particle tracking velocimetry (PTV) was used to determine the velocity profile within the microvessel.

The channel was perfused with a suspension of (1.7 µm-diameter microbeads (Polysciences, Inc.) in PBS ($1.8\text{x}10^9$ beads.mL^{-1}) at controlled flow rates ranging from 10 to 50 µL min^{-1}. Images were acquired with a high speed camera (Proton Fastcam SA3) and a 40x objective at 5,000 to 20,000 frames per second (fps). The camera's field of view was sufficiently large to include the entire channel diameter and 50 µm of channel length. The acquisition rate was enough for more than 500 beads (on average) to pass through, allowing precise velocity profile reconstruction. The images were pre-processed to remove the stationary background (by subtracting the average image) and inverted to make beads white. The tracking was performed using TrackMate, a free ImageJ plugin [52]. The beads (7 pixels in diameter) were detected automatically and linked in a continuous track by a linear motion tracker. Finally, erroneous tracks were removed with two low pass filters: velocity standard deviation and mean velocity.

For steady flow, the mean radial position and mean axial velocity were computed for each particle track. Because the illumination plane had a certain thickness (estimated to be 40 µm), the velocities at each radial position were dispersed. Because the particles of interest are the ones in the channel mid-plane, only beads having velocities within 5-10% of the maximum value at each radial position were used for velocity profile reconstruction. The experimental points were fitted to a parabola, in accordance with the Poiseuille flow profile for fully developed steady flow in a cylindrical channel at low Reynolds number (Re $\sim$ 10).

For pulsatile flow, the processing was adapted to access the instantaneous flow profile (Movie 1). The recorded movie was cut into hundreds of short time segments to ensure a nearly constant velocity during each segment. The mean axial velocity was computed for individual tracks in each segment. The highest velocities representing the particles passing close to the channel centerline were selected to obtain the maximum velocity as a function of time. At this stage, the reconstructed profile was not sufficiently precise to yield the flow rate directly since very few particles were present in each time segment (and usually none close to the channel walls), leading to a large uncertainty in the measured channel radius. The instantaneous radius was therefore extracted from the live recording of channel wall movement during the pulsatile cycle. Assuming a time-dependent parabolic flow profile, expected to be accurate for the low Womersley number present here

$$\alpha = R \left(\frac{\omega \rho}{\mu} \right)^{1/2}$$

$$\alpha \sim 0.15$$

and verified to be the case by plotting instantaneous velocity profiles (Movie 1), the mean flow rate and wall shear stress were computed for each time segment based on the maximum velocity (from PTV) and the radius (from channel wall tracking) using Poiseuille's equation for flow in a circular cross-section channel.

Stretch measurement

An increase in the luminal pressure leads to a pressure difference across the wall and subsequent channel dilation and circumferential strain. The circumferential strain was defined as the ratio of the increase in perimeter of the cross section of the channel to the initial perimeter. Because the perimeter depends linearly on diameter, the circumferential strain (when homogeneous) is equal to the normalized diameter increase. The circumferential strain was therefore obtained directly from the diameter change. Two methods were used to compute the strain: manual measurement of the diameter change for the case of constant strain and automated diameter tracking for cyclic strain. The manual measurements of channel diameter were performed in ImageJ, first on an image of the channel before the pressure increase and then on an image taken a few seconds after the pressure increase. The automated tracking of channel diameter was conducted using Clickpoints, an open-source tracking software [53].

Optical coherence tomography imaging

To visualize the channel cross section, Optical coherence tomography (OCT) images were acquired using a Ganymede OCT system (Thorlabs). The acquisition speed was 37 fps.

Statistical analysis

For Figures 1-4, all data are plotted as mean ± SD. An unpaired Student t-test was used for significance testing between two conditions. Statistical tests were performed using Matlab. For each condition, at least three independent microvessel systems (5 regions per system) were used for the imaging and data analysis. **** denotes $p < 0.0001$, *** denotes $p < 0.001$, ** denotes $p < 0.01$, and * denotes $p < 0.05$.

Results

Cellular coverage and monolayer integrity

Human umbilical vein ECs (HUVECs) seeded in the microvessel-on-chip and subjected to a low flow of $2\,\mu L\,min^{-1}$ for 48 h develop into a confluent monolayer with clearly delineated adherens junctions as demarcated by VE-cadherin staining (Figure 1a). Despite the softness of the collagen hydrogel within which it is embedded, the microvessel lumen has a circular cross-section as determined by 3D reconstruction of confocal microscopy images (Figure 1aii, Movie 2) and OCT imaging (Figure S1). Consistent with the size of microneedle used in its fabrication (nominal diameter of 120 µm), the microchannel prior to cell seeding has a diameter of 125±5 µm. Interestingly, this diameter increases to 134±5 µm after endothelial monolayer formation (Figure 1b).

Fluorescently labeled dextran infused into the microvessel lumen results in dextran transport across the endothelial monolayer and into the collagen hydrogel over a period of minutes (Figure 1c). The hydraulic conductivity (proportional to the permeability) of the microvascular wall is computed (see Methods) for dextran of two different molecular weights (10 and 70 kDa) and using HUVECs from two commercial sources (Lonza and Sciencell). For cells from both sources, the hydraulic conductivity to 70 kDa dextran is significantly lower than that for 10 kDa dextran (Figure 1c), demonstrating the ability of the endothelium to discriminate among molecules of different sizes and thus to act as a selective permeability barrier. At each molecular weight, there is a 2 to 3-fold difference in computed hydraulic conductivity between the cells from the different sources, underscoring the importance of carefully characterizing the cells and the potential perils of mixing cells from different commercial sources. The hydraulic conductivity values obtained here are consistent with measurements published in other in vitro microvessels [54–56].

Wall shear stress in the microvessel: interplay between luminal flow and gel porosity

Particle tracking velocimetry (PTV) measurements (Figure S3, Movie 3) confirm that for steady flow, the velocity profile inside the microvessel is parabolic, consistent with the Poiseuille flow expected for the range of Reynolds numbers studied (2 to 10) (Figure 2a,b). Adjusting the inlet flow rate allows fine tuning of the wall shear stress magnitude from 0.1 to 2 Pa (Figure 2c), spanning the physiological range in the microvasculature.

The measured flow rate in the microvessel averaged over the entire length Q_{ch} is lower than the imposed flow rate at the inlet Q_i: 8.4 vs. $10\,\mu L\,min^{-1}$ and 44 vs. $50\,\mu L\,min^{-1}$ (Figure 2d). This difference is attributable to a progressive decrease in luminal flow rate with axial position (Figure 2e). This luminal flow loss is due to the hydrogel porosity whereby part of the flow seeps into the gel surrounding the channel towards the open top which acts as a low pressure outlet. Interestingly, the wall shear stress does not exhibit a similar decrease (Figure 2f) due to the axial variations in channel diameter (see next section) that compensate the flow loss.

Understanding the division between luminal and transmural flow based on electrical circuit analogy

A useful analogy to understand the competition between the two flow paths, flow in the lumen and flow through the gel, is the equivalent electrical circuit (Figure 2g). In this analogy, the electrical current and the potential difference driving this current are analogous to the flow rate and pressure gradient, respectively. Because the channel here is much longer than wide, it can be modeled by an infinite number of elementary units along the axial position. At any axial position x, the flow splits between two paths: a microchannel path with resistance R_{ch} that depends on the channel radius and a gel path with resistance R_{gel} that depends on hydrogel dimensions and concentration. Thus, the remaining flow rate in the channel at $x+dx$ is smaller than that at x. From this equivalent electrical circuit, an analytical model of the free and porous medium flow through the microvessel is derived (see Appendix A) and is shown to accurately predict the flow drop in the channel for a bare (no cells) gel (Figure 2hi, red line).

Cell monolayer acts as a flow barrier

To investigate the role the endothelium might play in altering the microchannel flow loss, Q_{ch} is also measured in bare channels containing no ECs. The flow loss is significantly larger in bare gels than in endothelialized channels (Figure 2h), indicating the confluent monolayer acts as a semi-permeable membrane that reduces

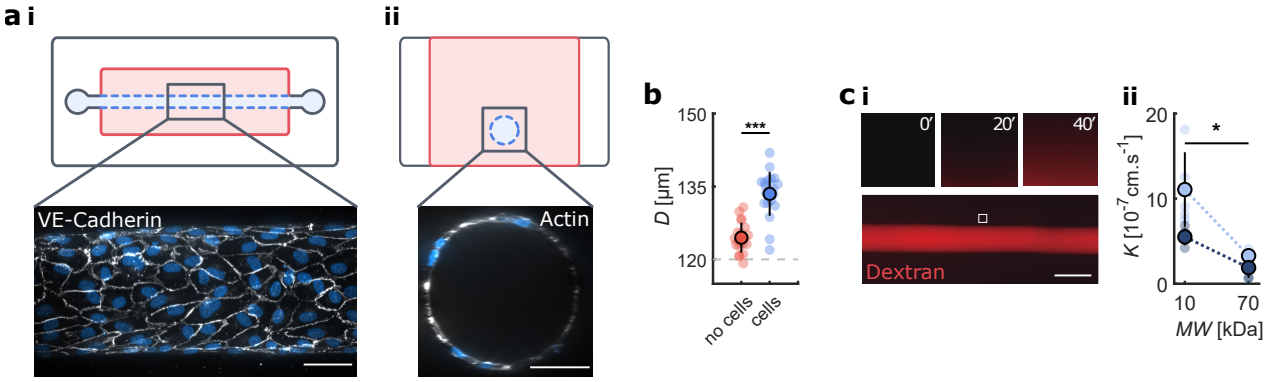

Figure 1. Endothelialization of the microvessel-on-chip. (**a**) Illustration of the microfluidic device (top view **i** and side view **ii**), showing the hydrogel (red), the channel (blue), and the PDMS housing (white). (**i**) Immunostaining of adherens junctions (VE-Cadherin, white) and cell nuclei (DAPI, blue), demonstrating the confluent monolayer lining the microvessel lumen. Scale bar 50 µm. (**ii**) Cross-section of the channel with actin staining in white (phalloidin) and cell nuclei in blue (DAPI), demonstrating the circularity of the endothelialized lumen. Scale bar 50 µm. (**b**) Microvessel diameter for bare gels (red) and with cells (blue). (**c**) **i** Diffusion of fluorescent dextran across the monolayer to quantify permeability. The three small panels show the progressive increase in dextran fluorescence intensity in the hydrogel at 0, 20, and 40 min. **ii** Quantification of monolayer hydraulic conductivity for two cell lines (Lonza, light blue; ScienCell, dark blue) and for two dextran molecular weights (MW), demonstrating barrier selectivity. Scale bar 150 µm. Dotted lines are guides for the eyes.

fluid leakage into the porous gel. The equivalent circuit model can also account for the contribution of the endothelium by modeling the monolayer as an additional resistance between the channel and gel. To this end, the gel permeability is first obtained by fitting the analytical flow drop to experimental data from bare channels (Figure 2hi, red line). The additional hydraulic resistance due to the cell monolayer is then obtained by fitting the analytical flow drop to experimental data from endothelialized channels using the gel permeability found above. The model correctly captures the decrease in flow loss due to the presence of the cell monolayer (Figure 2hi, blue line). These results confirm the validity of a simple equivalent circuit analysis and underscore the importance of taking porous medium flow into account to understand the mechanical environment inside hydrogel-based microvessel-on-chip systems.

Circumferential strain and gel elasticity

A principal novelty of the system presented here is its ability to produce controlled and physiologically relevant circumferential strains. This is accomplished through luminal flow actuation whereby increasing the flow rate in the microchannel increases luminal pressure, which compresses the soft hydrogel, dilates the channel, and stretches the endothelial monolayer (Figure 3a, Movie 4). OCT imaging demonstrates that the channel remains nearly circular during dilation, leading the cells to experience a circumferentially uniform strain field (Figure 3aii). When the flow is arrested, the luminal pressure rapidly drops, and the channel relaxes back to its original diameter. The hydrogel deformation is perfectly reversible, characteristic of elastic solids (Figure 3a), an essential feature to ensure controllable and robust actuation. The circumferential strain ε, quantified as the ratio of change in diameter to the initial diameter, reflects this reversible behavior (Figure 3aiii). The changes in luminal flow rate that drive wall strain also lead to changes in wall shear stress (Figure 3aiii), demonstrating the coupling between shear and strain in our system. As the strain ensues from luminal pressure, changing the imposed flow rate at the microvessel inlet Q_i modulates the level of applied strain. Average strains of 4% and 12%, spanning the relevant physiological range, are obtained as Q_i is increased from 10 to 50 µL min^{-1} (Figure 3bi).

For a given Q_i, the microvessel strain ε depends on the axial position. The deformation is small close to the two ends of the microvessel because the gel is chemically bound to the PDMS housing, imposing a zero displacement at the wall (Figure 3bii). Away from the microvessel ends, ε decreases axially as a result of the hydraulic pressure drop created by the flow. To investigate the possible impact of the endothelial monolayer on microvessel strain, the average strains are also measured in bare (no cells) channels at flow rates of 10 and 50 µL min^{-1}. Strain levels are significantly higher in the presence of an endothelium (Figure 3c). Although somewhat counter-intuitive, the increased deformation is explained by the flow barrier effect of the cell monolayer and the poroelastic properties of the hydrogel. More specifically, the presence of the EC monolayer decreases fluid seepage into the gel which leads to a lower gel pressure (while the pressure in the channel remains virtually unchanged). In poroelastic materials, pore de-

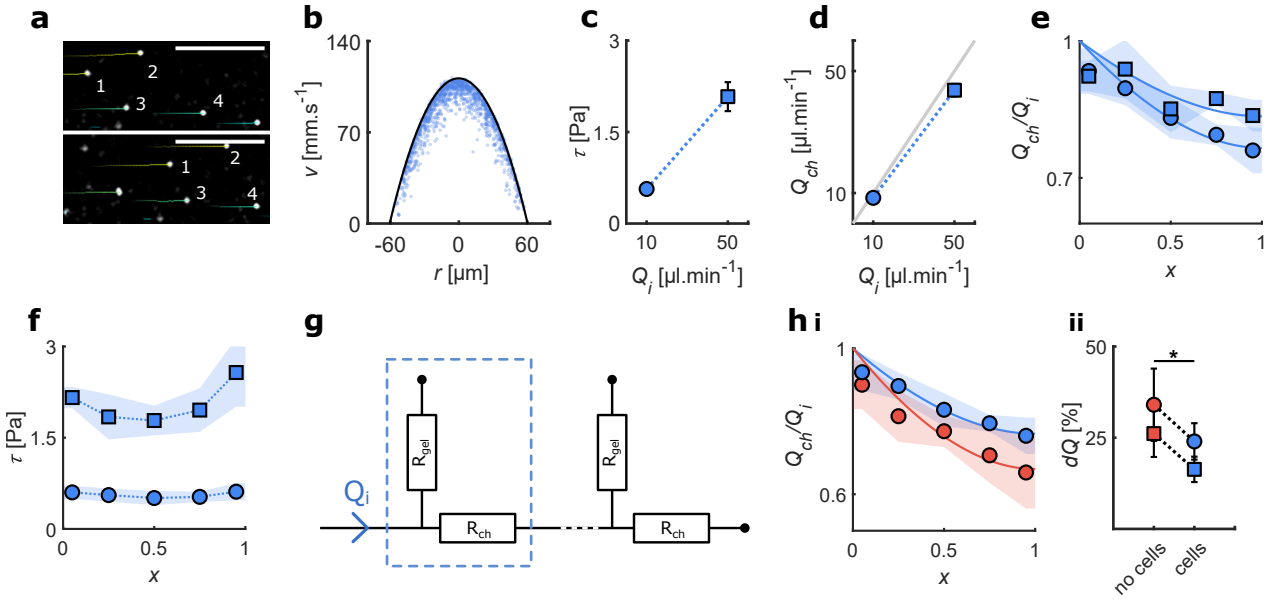

Figure 2. The imposed flow rate controls the wall shear stress. Blue represent data from endothelialized channels and red from bare channels. (**a**) Particle tracking velocimetry at two successive time points. (**b**) Velocity profile in the channel midplane; each dot represents the average velocity of one microbead. A parabola is fitted to the 5% fastest beads to measure the flow rate and wall shear stress. (**c**) Measured wall shear stress increases with flow rate. (**d**) The measured flow rate in the channel (symbols) is smaller than the imposed flow rate (solid gray line) due to fluid seepage into the gel. (**e**) Normalized flow rate in the channel at different axial positions for the two different imposed flow rates. The solid line is the best fit of the analytical model. (**f**) Wall shear stress as a function of position for the two different imposed flow rates. (**g**) Schematic of the equivalent electrical circuit used for the analytical modeling. R_{gel} is the hydraulic resistance of the porous gel and R_{ch} is the hydraulic resistance of the cylindrical channel. (**h**) **i** Flow loss is larger in bare channels (red) compared to channels with an endothelial monolayer (blue); $Q_i = 10\,\mu\text{L}\,\text{min}^{-1}$. Solid lines indicate the predictions of the analytical model. **ii** Flow loss in a bare gel G (red) and with cells C (blue), measured at the two different imposed flow rates. In all panels circles correspond to $Q_i = 10\,\mu\text{L}\,\text{min}^{-1}$ and squares correspond to $Q_i = 50\,\mu\text{L}\,\text{min}^{-1}$. Dotted lines are guides for the eyes.

formation is coupled to pore pressure, with increased pore pressure leading to reduced material compression. Thus, the lower gel pressure in the presence of an endothelium allows increased gel deformation and higher strains. This phenomenon illustrates the coupling between the flow rate and strain due to gel poroelasticity.

Tuning the shear-strain coupling

As mentioned in previous sections, the luminal flow rate Q_{ch} and the channel strain ε are coupled through pressure. Additionally, the wall shear stress τ depends not only on Q_{ch} but also on channel radius, which is modified by the strain ε. As a result, the shear stress τ and the strain ε are tightly coupled and vary as functions of the imposed flow rate Q_i, the hydraulic resistances, and the spring constant of the gel. To tune the coupling between shear stress and strain, three different strategies are explored.

Strategy 1: Modifying outlet resistance to control channel pressure

The simplest method to increase the channel pressure is to add hydraulic resistance to the outlet, R_{out}. Tubing of increasing length connected to the outlet is used to progressively increase the outflow resistance R_{out} (Figure 4a.i). Flow loss, strain and shear stress are then measured for each R_{out} in the same chip for $Q_i = 10\,\mu\text{L}\,\text{min}^{-1}$. As R_{out} is increased from 0 to $12\text{x}10^{12}$ N.s.m^{-5} (corresponding to outflow tubing length increasing from 0 to 9 cm), luminal pressure also increases, leading to an increase in average flow loss into the hydrogel (Figure 4a.ii) as well as an increase in average channel strain (Figure 4a.iii). These two effects lead to a reduction in average wall shear stress (Figure 4a.iv). These results demonstrate a strong coupling between channel strain and wall shear stress (Figure 4a.v). As for the axial variations (Figure S4a), the larger flow loss into the gel at high R_{out} translates into significantly larger axial gradients of wall shear stress. Interestingly, the strain slope remains fairly constant with R_{out} and is simply offset for the different outflow resistance values.

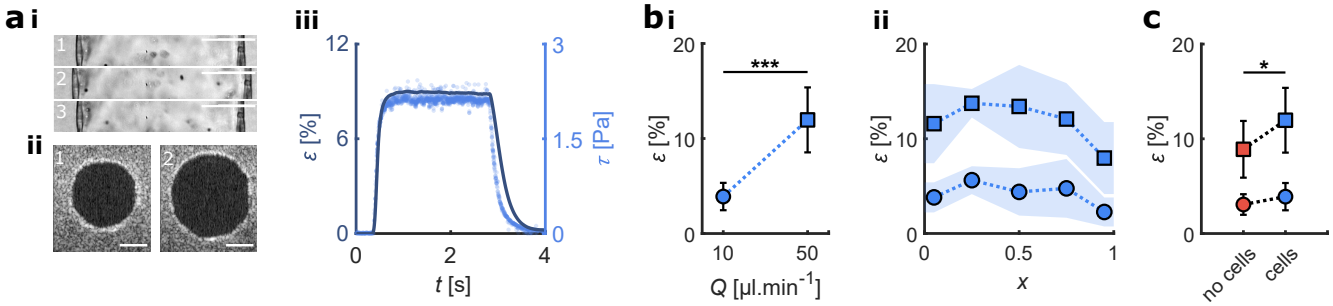

Figure 3. The imposed flow rate controls the circumferential strain. (**a**) Channel dilation following a step in flow rate. **i** Brightfield image of the channel's midplane before (1), during (2) and after (3) the step. **ii** OCT image of the channel cross-section before (1) and during (2) the step. **ii** Dynamics of channel dilation: strain ε (dark blue, solid line) and wall shear stress τ (light blue, dots) as a function of time during a flow step. Scale bars 50 µm. (**b**) Strain as a function of the imposed flow rate. **i** Average strain for two imposed flow rates. **ii** Strain as a function of position along the length of the channel for two imposed flow rates. (**c**) Strain for a bare gel (red) and a channel lined with an EC monolayer (blue) for two imposed flow rates. In panels b and c, circles correspond to $Q_i = 10\,\mu\text{L}\,\text{min}^{-1}$ and squares correspond to $Q_i = 50\,\mu\text{L}\,\text{min}^{-1}$. Dotted lines are guides for the eyes.

Strategy 2: Modifying gel width to change its hydraulic resistance and spring constant

Another strategy to tune the shear stress-strain coupling is to change the width of the chamber housing the hydrogel, which modulates both the hydraulic resistance and spring constant of the gel. Flow loss, strain, and wall shear stress in the channel are measured for chamber widths of 1, 2, and 4 mm at Q_i values of 10 and $50\,\mu\text{L}\,\text{min}^{-1}$ (Figure 4b). Although hydrogel width does not change the diameter of bare channels, endothelialized channels in narrower hydrogels have larger diameters (Figure 4b.i). Because wider hydrogels have smaller R_{gel}, increasing gel width leads to significantly increased flow loss (Figure 4b.ii). The smaller spring constants in wider hydrogels lead to higher gel deformation and thus to larger strains (Figure 4b.iii). Interestingly, the average wall shear stress remains relatively constant because of the smaller initial diameter found in wider hydrogels that compensate both the increased flow loss and increased strain (Figure 4b.iv). Therefore, this strategy provides a pathway for largely decoupling wall strain from wall shear stress (Figure 4b.v). As for the axial variations (Figure S4b), the strain slope is again maintained fairly constant and is simply offset for the different gel widths, while the wall shear stress does not exhibit significant axial variations.

Strategy 3: Modifying gel concentration to change its permeability and stiffness

The third strategy to tune the coupling between shear stress and strain is to modify hydrogel concentration which determines both gel permeability and stiffness. The flow rate, strain and wall shear stress in the channel are measured for the three collagen densities of 4, 6 and $8\,\text{mg}\,\text{mL}^{-1}$ and at the two Q_i values of 10 and $50\,\mu\text{L}\,\text{min}^{-1}$. Hydrogel concentration does not change the baseline diameter of either bare or endothelialized channels (Figure 4c.i). Because denser gels are less permeable and stiffer, channels exhibit smaller flow loss and smaller average strain (Figure 4c.ii & iii). The two effects combine to significantly increase the average wall shear stress in denser gels (Figure 4c.iv). Thus, using this strategy preserves the coupling between wall strain and wall shear stress (Figure 4c.v), although this coupling is somewhat weaker than that associated with strategy 1. The shape of the axial variations of both the strain and the wall shear stress are unchanged by varying gel concentration and are simply offset as gel concentration changes (Figure S4c).

The quality and homogeneity of the collagen hydrogel impacts its mechanical characteristics. The difference between two collagen batches of the same concentration was investigated. Batch #1 was visibly less homogeneous than batch #2: dissolution required a longer time, fibers were observed under the microscope, and numerous holes and defects were visible with OCT imaging. Predictably, batch #1 led to significantly higher flow loss and average strain than batch #2 (Figure S5), a behavior similar to that of a lower gel concentration, underscoring the sensitivity of the actuation to the quality of the gel. Consequently, throughout the present study, all the chips used in one experiment were fabricated with the same batch of collagen in order to ensure that only the tested parameter is changed among replicates.

Comparing strategies: an operating manual for the microvessel-on-chip

Integrating the information gleaned from the three different strategies described above provides a form of "operating manual" for the microvessel-on-chip system studied here, as schematically illustrated in Figure 5 which depicts the relative change in strain and wall shear stress afforded by each strategy. From a prac-

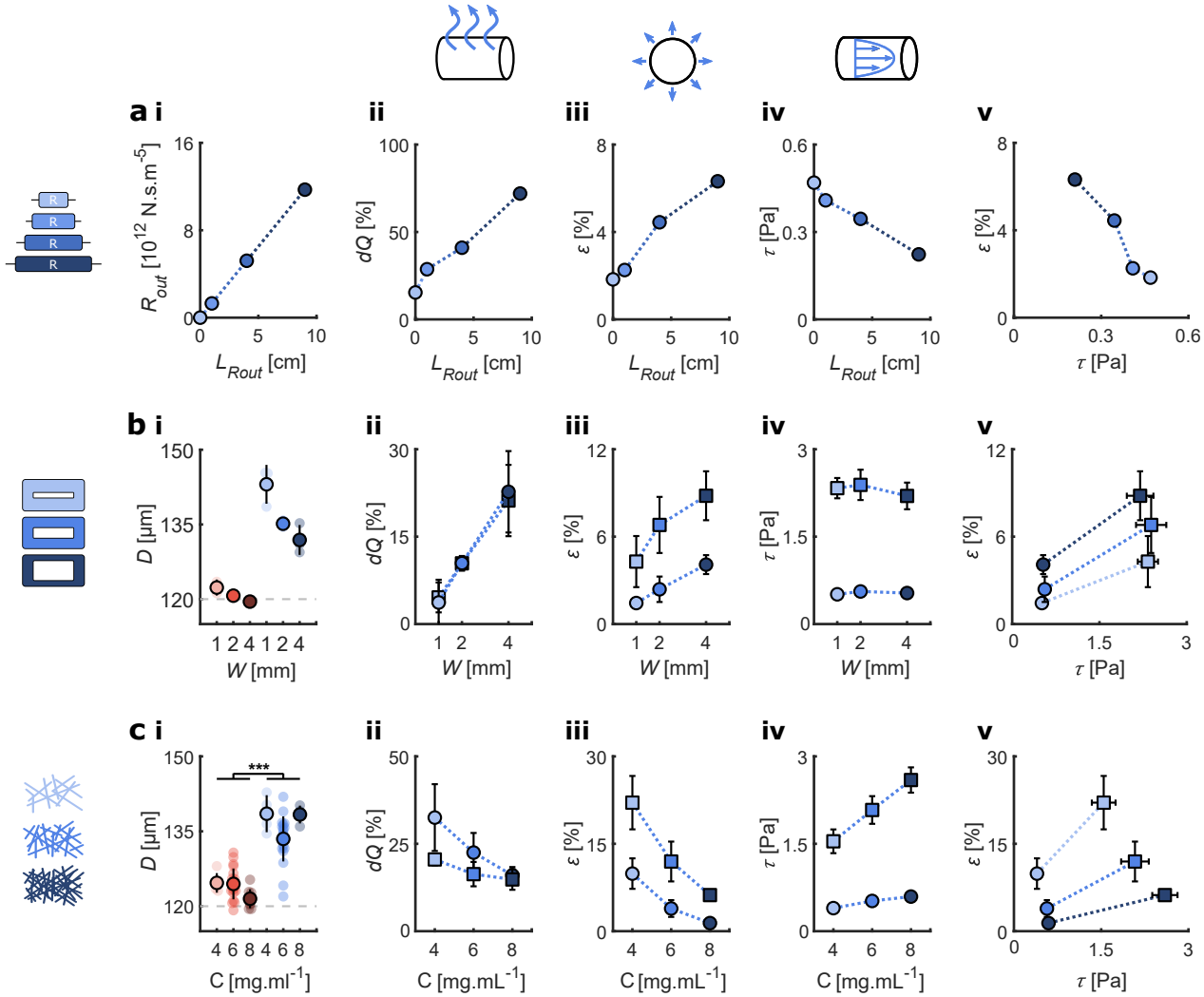

Figure 4. Three strategies to modulate the shear-strain coupling: outlet resistance, gel width and gel concentration. (**a**) Increasing the outlet resistance by increasing the length of the outlet tubing L_{Rout}. All results are for $Q_i = 10\,\mu L\,min^{-1}$. **i** Average outlet resistance. **ii** Average flow loss in the channel dQ. **iii** Average wall strain ε. **iv** Average wall shear stress τ. **v** Strain-wall shear stress coupling. (**b**) Changing the gel width. All results are repeated for two imposed flow rates. **i** Average channel diameter D. **ii** Average flow loss in the channel dQ. **iii** Average wall strain ε. **iv** Average wall shear stress τ. **v** Strain-wall shear stress coupling. (**c**) Changing the gel concentration. All results are repeated for two imposed flow rates. **i** Average channel diameter D. **ii** Average flow loss in the channel dQ. **iii** Average wall strain ε. **iv** Average wall shear stress τ. **v** Strain-wall shear stress coupling. In all panels, circles correspond to $Q_i = 10\,\mu L\,min^{-1}$ and squares to $Q_i = 50\,\mu L\,min^{-1}$. Red indicates bare gels and blue endothelialized channels. Dotted lines are guides for the eyes.

tical standpoint, changing the outlet resistance is by far the simplest strategy since it is straightforward, highly reproducible, and can be implemented in the same chip. Contrarily, changing hydrogel concentration and gel width require modifications to the fabrication and thus different chips.

How can the information from the different tuning strategies be exploited as an operating manual and when might each of these strategies be most useful? Because modifying the outlet resistance has opposite effects on strain and wall shear stress (Figure 5), it constitutes an effective strategy for elucidating if a particular cellular response is driven more by strain or by shear stress. Furthermore, because manipulating outlet resistance dramatically impacts the amount of flow loss into the gel, it generates significant gradients in wall shear stress along the channel length. Therefore, this strategy would also be particularly useful for studies that aim to elucidate the effect of spatial gradients of shear stress on the endothelium. Modulating the gel width allows a wide range of strains while maintaining the wall shear stress relatively constant (Figure 5), thereby provid-

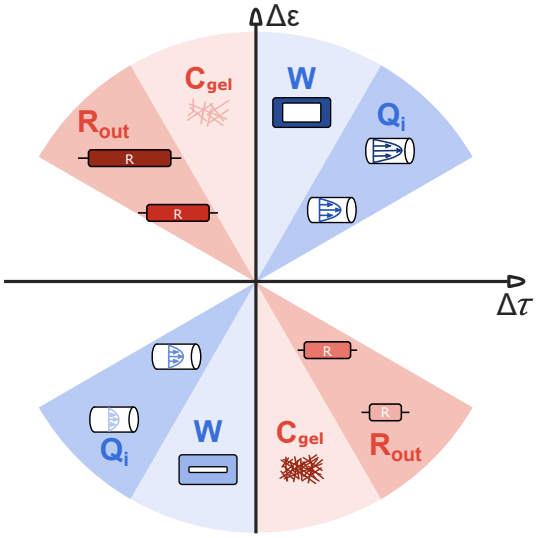

Figure 5. Schematic depiction of the relative effects of changing the outlet resistance (R_{out}), gel concentration (C_{gel}), gel width (W), and imposed flow rate Q_i on the coupling between wall strain and wall shear stress. The origin denotes the baseline conditions. Positive values of Δε and Δτ respectively denote increases in strain and wall shear stress relative to the baseline, while negative values correspond to decreases relative to the baseline. The colored wedges describe each of the tuning strategies with the blue and pink colors respectively indicative of strategies that have a similar or opposite effect on strain and wall shear stress. The position of each wedge describes the relative effect of the strategy it represents on strain and wall shear stress. For instance, changing gel width or gel concentration has a larger effect on channel strain than on wall shear stress, whereas changing outlet resistance or inlet flow rate has relatively similar effects on both strain and wall shear stress.

ing a roadmap for separating the effects of shear stress and strain. Finally, changing gel concentration allows a wide range of strains and shear stresses in a manner similar to manipulating outflow resistance, with smaller effect on the wall shear stress (Figure 5). An additional consideration, however, is that gel concentration has a significant impact on gel stiffness; therefore, in comparison to controlling outflow resistance, manipulating gel concentration would also provide the capability of studying EC responses to changes in substrate stiffness. In addition to the effects of these three strategies, Figure 5 also illustrates the effect of simply changing the imposed flow rate. Increasing the inlet flow rate increases both wall strain and wall shear stress and thus provides the full coupling that might be most representative of the situation encountered in vivo.

Model of the channel and gel flow

The analytical model derived from the equivalent electrical circuit analogy is detailed in Appendices A and B. This model, which considers free fluid flow within the channel and porous medium flow governed by Darcy's law within the hydrogel, can be used to demonstrate how the shear-strain coupling is impacted by the three tuning strategies and to guide the decision making process of microvessel-on-chip users. As detailed in the following section, modifications of the experimental system are implemented in the model by varying the constitutive parameters.

To model the impact of the added outlet resistance R_{out}, the boundary condition for the outlet pressure is modified to the following:

$$P_{out} = R_{out} \cdot Q_{out} \tag{1}$$

First, the gel permeability, the only unknown parameter of the system, is obtained by fitting the model to the experimental flow drop measured for $R_{out} = 0$. Then, the flow rate Q_{ch} and the pressure P at the different axial positions are calculated for different values of R_{out}. Our model correctly predicts the larger flow loss dQ for increasing R_{out} and matches the experimental data closely (Figure 6a.i). It is important to note that dQ saturates at high R_{out}. Indeed, when R_{out} is large, Q_{out} is small due to the large flow loss, leading in turn to a reduced effect of R_{out} on the luminal pressure. Additionally, the ratio of experimental strain to computed channel pressure is found to be constant (Figure 6a.ii). This proportionality constant is related to the Young's modulus of the gel which, by definition, relates stress to strain.

To elucidate the effect of variations in gel width and concentration, the layer of cells is not taken into account. Only the gel is modeled, and the experimental data from bare gels are used. Theoretical curves of Q_{ch}

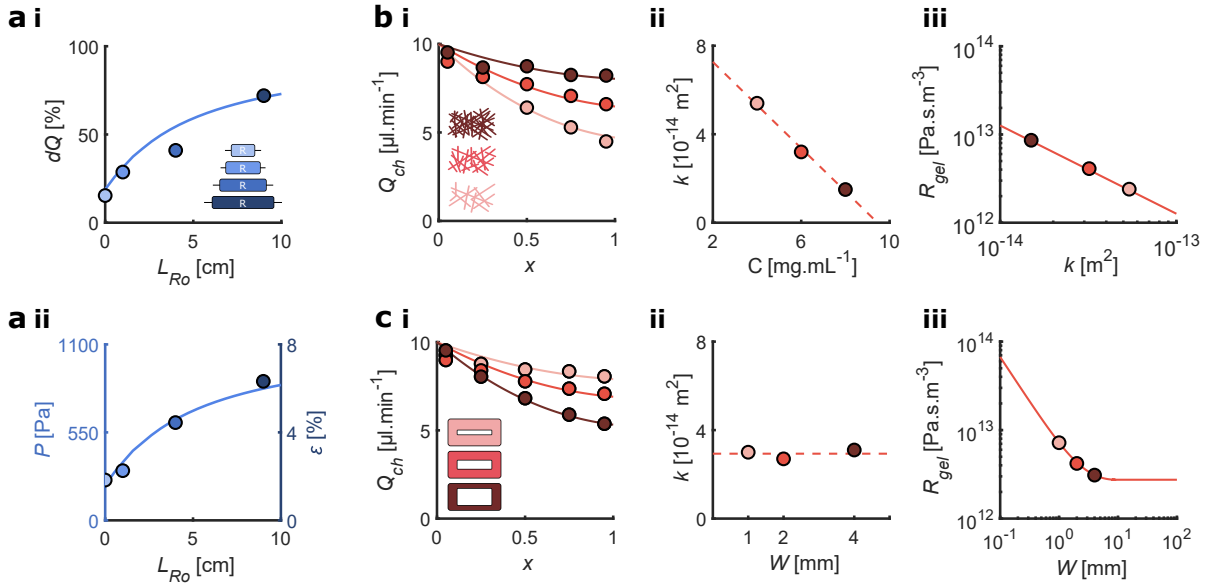

Figure 6. Analytical model of the porous medium flow based on the equivalent electrical circuit. (**a**) Modeling the impact of outlet resistance (darker colors correspond to increasing resistances, the cell monolayer is included in all cases). **i** Predicted flow loss and measured flow loss as a function of outlet resistance length. The model curve (solid line) is based on the permeability fitted to the baseline condition (R_{out}=0). **ii** Predicted luminal pressure (solid line) and measured strain (dots) as a function of outlet resistance. The model curve (solid line) is based on the permeability fitted to the experiment with no outlet resistance. (**b**) Modeling the impact of hydrogel width (light, medium and dark red correspond to 1, 2, and 4 mm-wide bare gels, respectively). **i** Channel flow as a function of the axial position: visualization of the least squares fitted curve to the experimental data for the optimal hydrogel width. **ii** Dotted line shows hydrogel permeability found through the fit as a function of hydrogel width. Circles represent experimental data (darker colors correspond to increasing width). **iii** Hydraulic resistance of the hydrogel as a function of hydrogel width. (**c**) Modeling the impact of hydrogel concentration (light, medium and dark red correspond to 4, 6, and 8 mg.mL^{-1} bare gels, respectively). **i** Channel flow as a function of the axial position: visualization of the least squares fitted curve to the experimental data for the optimal hydrogel concentration. **ii** Hydrogel permeability, found through the fit, as a function of hydrogel concentration. **iii** Hydraulic resistance of the hydrogel as a function of hydrogel permeability. In all panels, circles correspond to experimental data or values inferred from experimental data. Solid lines are the predictions of the model and dashed lines are linear fits.

as a function of axial position are fitted to the experimental flow drop for the three gel densities (Figure 6b.i). The optimal gel permeability k_{gel} for each condition is found by least squares fitting. The fitted gel permeability values are 5.4, 3.2, and 1.6 x 10^{-14} m^2 for gel densities of 4, 6, and 8 mg mL^{-1}, respectively. The model thus correctly predicts a smaller permeability for the denser gels. The permeability of other gels can be estimated by extrapolating the empirical linear k_{gel} - C_{gel} relationship (dashed line), provided their concentration is of the same order of magnitude (Figure 6b.ii). The gel resistance R_{gel} is inversely proportional to the gel permeability, as predicted by Darcy's law (Figure 6b.iii). As such, denser gels have larger resistances, leading to smaller flow losses.

The same approach is used to understand the role of gel width on porous medium flow in the system. Gel resistance R_{gel} depends not only on gel permeability but also on its dimensions. The geometry is defined by the cross-section of the system: a large rectangle with a small circular hole inside of it, in which fluid transport occurs from the hole towards the open top (zero pressure). Because the transport does not take place only in one dimension, there is no analytical expression for the gel resistance. The gel is therefore modeled as two resistances in series, assuming first radial flow across a torus, then longitudinal flow across a rectangle (see Appendix). Defined as such, the total gel resistance can be expressed analytically using Darcy's law as a function of the three relevant length scales: the radius of the channel and the width and height of the gel. The analytical solution is fitted to experimental data for the three different gel widths to obtain the permeability values, all found to be around 3x10^{-14} m^2 (Figure 6c.i,ii). Indeed, as the gel concentration is identical for all widths, the permeability is expected to remain unchanged. The model thus correctly predicts the different flow drops only through the change in gel width, included in the expression for R_{gel} (Figure 6c.i,iii). Plotting the analytical R_{gel} as a function of gel width W shows two

regimes (Figure 6c.iii). The three experimental designs (dots) are in the transition zone. When the gel is narrow, most of the resistance comes from the longitudinal transport: R_{gel} is inversely proportional to the width W. When the gel is wide, the resistance becomes constant: all the flow crosses the torus whose thickness is the constant height of the gel. In the transition zone, the contribution of the torus is significant, and R_{gel} varies logarithmically with gel width.

The analytical model of the free and porous medium flow, based on the equivalent electrical circuit, correctly replicates the experimental observations for three sets of variations: boundary conditions (outlet resistance), geometrical parameters (gel width), and constitutive parameters (gel concentration). Flow drop variations are reproduced and interpreted, and the computed luminal pressure, which cannot be measured experimentally, explains the observed strains. Although not presented here, wall shear stress can also be computed from the analytical flow values by substituting the deformed geometries based on the experimental measurements of strain into the model. The model can predict the behavior of new experimental designs, useful to tailor the system response for a specific need.

Pulsatile shear and strain

The present microvessel-on-chip also allows for the application of pulsatile shear stress and strain, which better mimics the in vivo mechanical environment. Pulsatile strain requires rapid and reversible gel deformation. Because hydrogels are poroelastic materials, they are ideal candidates for pulsatile stimulus generation. To impose pulsatility, a sinusoidal inlet flow rate Q_i with the following waveform is imposed:

$$Q_i = Q_{mean} + Q_{amp} \cdot sin(2\pi f t) \qquad (2)$$

Setting both the mean flow rate Q_{mean} and the amplitude Q_{amp} to $10\,\mu L\,min^{-1}$ and the frequency f to 1 Hz leads to significant oscillations of the channel diameter (Movie 5,6). The flow rate, wall shear stress, and channel strain all follow a sinusoidal waveform at the same frequency as Q_i, with a small phase shift due to gel viscosity (Figure 7a, Movie 1). As expected, the cycle-averaged Q_{ch} oscillates; however, the amplitude of the oscillation is smaller than that of the imposed Q_{amp} (data not shown). While the amplitude of the oscillations in strain is virtually equal to that of the mean value, the oscillations in wall shear stress are considerably damped and are approximately half of the mean value (Figure 7a).

Impact of the imposed waveform

To explore the extent of possible modulation of the amplitude of the pulsatile waveform for a given mean flow, Q_{amp} is set successively to 10, 20, and $50\,\mu L\,min^{-1}$ while maintaining Q_{mean} at $10\,\mu L\,min^{-1}$ and a 1 Hz frequency (Figure 7b.i). The amplitudes of the wall shear stress and the channel strain increase with increasing Q_{amp} as expected (Figure 7b.ii,iii). The mean wall shear stress increases slightly from 0.5 to 0.6 Pa and the mean strain increases from 2% to 4%, even though Q_{mean} is maintained constant (Figure 7b.ii,iii). Surprisingly, no negative values of wall shear stress or strain are observed. Additionally, the time behavior of both quantities deviates significantly from a sinusoidal waveform, with fast up and down phases followed by a short plateau phase at the end of the cycle. Tuning Q_{amp} allows control of the amplitude of the oscillations for both wall shear stress and strain. Interestingly, the cycle-average wall shear stress is less sensitive to Q_{amp} than the cycle-average strain.

Impact of the imposed frequency

The frequency of the imposed flow rate controls the frequency of the response for both wall shear stress and strain. Shear stress and strain are recorded as functions of time for three physiologically relevant frequencies: 0.5, 1, and 2 Hz, with Q_{mean} and Q_{amp} held constant. The observed waveforms for both shear stress and strain remain sinusoidal, and the frequencies match those of the imposed signals (Figure 7c,d). The mean wall shear stress and strain are largely independent of frequency, while their amplitudes decrease with frequency (Figure 7c,d). Although the amplitudes of the oscillations decrease with frequency, significant amplitudes are obtained for the range of physiological frequencies studied, demonstrating the capabilities of the present system.

Axial variations of the sinusoidal shear and strain

The mean value of pulsatile wall shear stress does not vary significantly along the channel length and remains around 0.46 Pa, whereas the amplitude of the shear stress oscillations decreases from 0.3 Pa to 0.1 Pa, characteristic of the progressive oscillation damping as described previously (Figure 7e). In contrast, both the mean and the amplitude of oscillation of strain decrease nearly linearly from 2.5% to 0.4% along the channel axis, with the amplitude equal to the mean value, as imposed through Q_i (Figure 7f). Strain results from compression of the hydrogel by the luminal pressure, and pressure exhibits a negative linear gradient from inlet to outlet for all time points. Therefore, the strain follows the same linear decrease along the channel length at each time point in accordance with the sinusoidal waveform.

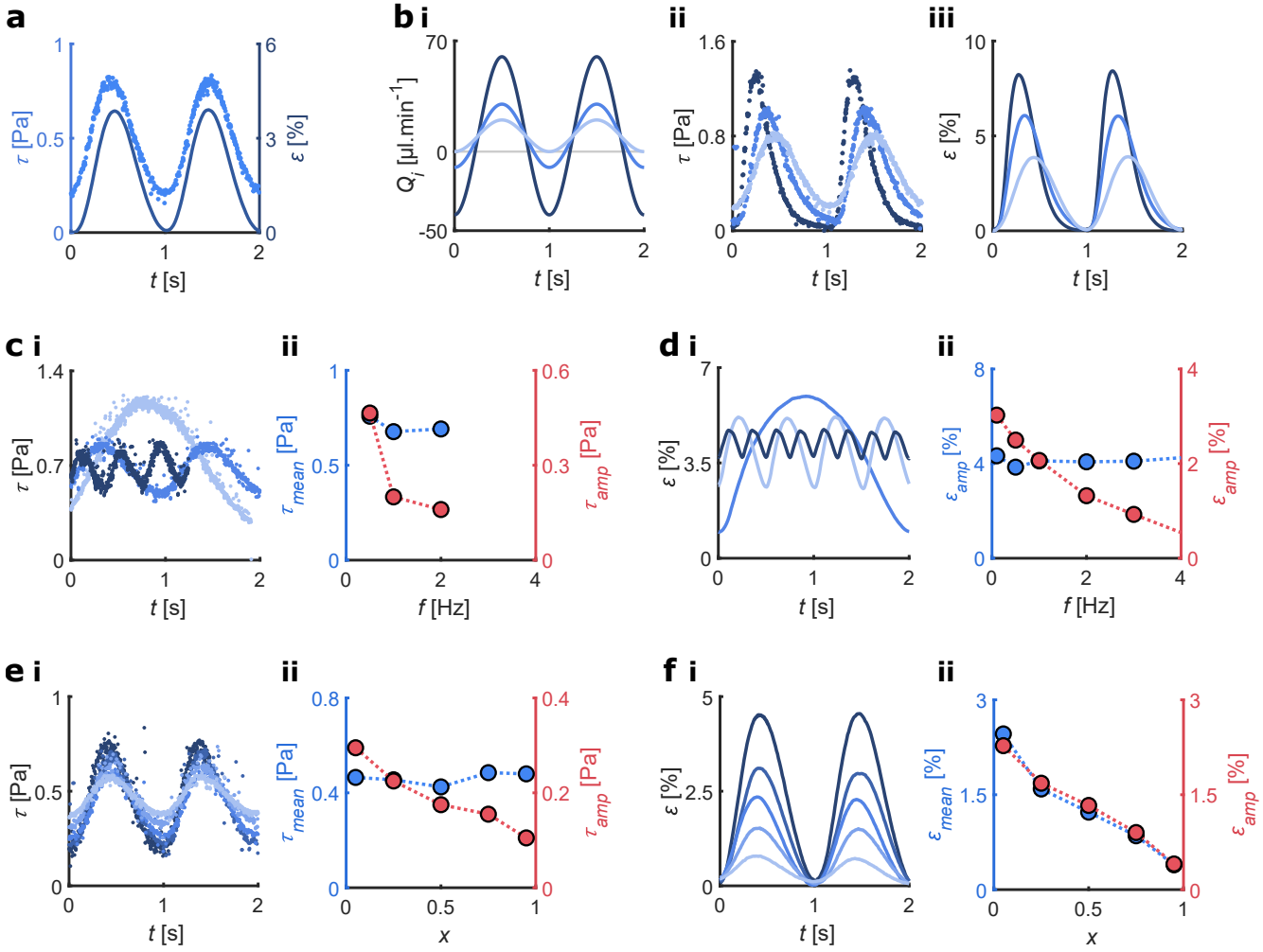

Figure 7. Response of the microvessel-on-chip to sinusoidal pulsatile flow. (**a**) Pulsatile stresses in the channel: mean wall shear stress τ (light blue, dots) and mean strain ε (dark blue, solid line) as a function of time for a sinusoidal imposed flow rate. (**b**) Impact of the amplitude of the imposed flow on channel response. Measured waveforms of the imposed flow rates (**i**), the resulting mean wall shear stress (**ii**), and mean strain (**iii**) (line colors match those of the corresponding imposed flow rate). (**c**) Wall shear stress waveform as a function of the sinusoidal frequency. **i** Measured waveforms for 0.5 Hz (light blue), 1 Hz (blue), and 2 Hz (dark blue). **ii** Measured mean (blue) and amplitude (red) of the wall shear stress oscillations as a function of frequency. (**d**) Strain waveform as a function of sinusoidal frequency. **i** Measured waveforms for 0.5 Hz (light blue), 2 Hz (blue), and 4 Hz (dark blue). **ii** Measured mean (blue) and amplitude (red) of the strain oscillations as a function of frequency. (**e**) Wall shear stress waveform as a function of position. **i** Measured waveforms from inlet (dark blue) to outlet (light blue). **ii** Measured mean (blue) and amplitude (red) of the wall shear stress oscillations as a function of position. (**f**) Strain waveform as a function of axial position. **i** Measured waveforms from inlet (dark blue) to outlet (light blue). **ii** Measured mean (blue) and amplitude (red) of the strain oscillations as a function of axial position. Dotted lines are guides for the eyes.

Discussion

In vivo, microvascular cells are subjected to both shear forces due to blood flow and stretch forces due to the transmural pressure difference. There is mounting evidence that when subjected simultaneously to multiple biophysical cues, cells integrate the information from the different cues and respond differently compared to cells subjected to one of the cues alone [57, 58]. Therefore, the ability to generate physiologically relevant shear and strain levels in the same system is particularly important. The microvessel-on-chip presented here accomplishes this objective via the novel approach of luminal flow actuation. While most existing microvessel-on-chip systems generate physiological shear stress levels, none are able to attain the strain levels reported here. Two unique features of our design,

namely the dimensions of the hydrogel within which the microchannel is embedded and the open top of the chamber housing the gel, enable large strains. In current microvessel-on-chip systems, the thickness of the gel surrounding the channel is typically not more than a hundred microns, which greatly limits gel deformation. Here, the channel is positioned several hundred microns from all walls, thereby generating large strains in response to a relatively small increase in intraluminal pressure. Furthermore, most current systems are encased in closed chambers; therefore, an increase in intraluminal pressure translates into pressurization of the poroelastic hydrogel, where pore pressure and pore deformation are coupled, which resists deformation and limits strain. Opening the top of the hydrogel housing chamber is therefore essential for pressure release, thereby allowing large strains.

The experiments on the flow-actuated microvessel-on-chip are complemented with a simple analytical model based on an electrical circuit analogy combined with calculations of the hydraulic resistance of the porous media. The model employs an inverse problem approach whereby a comparison of the analytical results to the experimental data enables deducing otherwise unknown material properties of the system. Although the current model captures the principal experimental tendencies, incorporating additional complexity would further improve the predictive capabilities of the model. For instance, an equivalent mechanical circuit with a series of parallel springs, potentially non-linear, could be coupled to the equivalent electrical circuit to predict gel deformation. To this end, additional experimental data would be required to empirically determine the non-linear stress-strain relationship exhibited by the hydrogel. In the present model, the deformation is injected into the equations simply as a geometrical parameter.

Our experimental results indicate that the presence of an endothelium amplifies strain in the collagen hydrogel, an outcome explained by the barrier effect of the confluent monolayer to fluid transport. However, the cell monolayer is also an additional material with a certain stiffness, which would resist stretching. A more complete description of the mechanical contribution of the endothelium would therefore include its elasticity. Even though the dominant effect is the barrier effect, careful modeling of the non-linear poroelastic deformation of the gel would shed light onto a possible stiffening contribution of the ECs. Future modeling of the fluid-poroelastic structure interaction would also clarify the origin of the observed dynamic effects, most notably the modification of the sinusoidal waveform observed under pulsatile flow.

Previous in vitro platforms used to study the effect of strain on microvascular cells are poor mimics of the native environment, principally because they lack the coupling between strain and other biophysical factors such as flow-derived shear stress or substrate-derived cues including curvature, stiffness, and topography. The system presented here overcomes these limitations, enabling pulsatile shear and strain in a microvessel inside a soft fibrillar hydrogel. The extensive characterization presented demonstrates the complexity of the mechanical behavior of hydrogel-based in vitro microvessels and the inherent coupling that exists among the different mechanical stresses in these systems. The current study, which complements previous work on the use of hydraulic pressure for deforming hydrogels [59–61], establishes luminal flow actuation as a novel mechanism for generating physiologically and pathologically relevant strain levels in hydrogel-based microfluidic systems. The extensive investigation of different parameters provides a detailed operating manual that we hope will facilitate the adoption of flow actuation in future in vitro platforms.

In vivo, two additional mechanical stresses are present in the microvasculature: compressive stress due to the luminal pressure and shear stress on intercellular junctions due to transmural fluid flow. Both of these stresses have been shown to play important roles in EC mechanobiology [10, 58]. Generating these stresses requires porous medium flow through a hydrogel as well as control of the pressure gradient [62–64], features of which very few in vitro systems are capable. Although not detailed in this study, these two stresses are indeed present in the flow-actuated microvessel-on-chip presented here. The luminal pressure is around a few mmHg, corresponding to venous pressure levels. The transmural shear stress magnitude is difficult to evaluate as it depends on the exact geometry of cell-cell junctions [64]; it is nevertheless proportional to the flow loss, which we have characterized in detail here.

With the recognition of the critical importance of mechanical factors in regulating vascular structure and function, in vitro systems used in vascular biology research have evolved over the past two decades from simple flat petri dishes to microfluidic channels and most recently to vessel-on-chip systems where cells are subjected to controlled levels of shear stress. Accounting for wall deformation, however, requires more complex designs and has therefore remained largely elusive. We show that relatively simple design modifications of current microvessel-on-chip systems enable the use of luminal flow actuation as a novel strategy for attaining large wall deformations. The templating technique employed in the present work for producing microchannels in hydrogels is similar to that used elsewhere [46, 49] and has been applied to study the effects of flow on angiogenesis [47, 65], atherosclerosis [66], tumor vascularization and cancer cell dissemination [67, 68], mural cell interactions [69], and blood-brain barrier function [70]. Adopting the flow actuation paradigm proposed here would enable the investigation of the role that wall strain plays in these important events and would thus add a new

dimension to the ability of vessel-on-chip systems to mimic the in vivo mechanical environment.

Conclusions

Although hydrogel-based microvessel-on-chip systems are increasingly popular mimics of the microvasculature, a major limitation of current systems is the inability to generate physiologically relevant levels of wall strain. In the present work, we show that combining specific design features with luminal flow actuation of a poroelastic collagen hydrogel constitutes a novel and highly effective strategy for overcoming these limitations. ECs lining the wall of this perfusable microvessel-on-chip can be subjected to a wide range of shear stresses and strains, steady or pulsatile, mimicking the native mechanical environment. Flow shear stress and wall strain in this system are strongly coupled, through the luminal pressure and the poroelastic nature of the hydrogel. We also show that a portion of the luminal flow seeps into the hydrogel, generating transmural flow that is associated with progressive luminal flow loss along the microvessel length. A key advantage of the flow actuation strategy described here is its simplicity and the fact that it obviates the need for external actuation.

Microvessel-on-chip systems have been shown to be excellent platforms for investigating the effect of flow-derived shear stress on a host of important phenomena such as endothelial-mural cell interactions, immune cell extravasation, tumor vascularization, and angiogenesis. Incorporating flow actuation into these systems provides the ability to also investigate the effects of wall circumferential stretch and thus greatly expands the mechanobiological toolbox. Beyond its application to the microvasculature, the concept of flow actuation of poroelastic hydrogels provides a general framework that promises to help unravel important open mechanobiological questions in many settings where cells are simultaneously subjected to mechanical stretching and interstitial shear.

Acknowledgments

The authors thank Prof. Jean-Marc Allain for access to the OCT imager. The authors also acknowledge all members of the Barakat group for their constructive input during the project and the preparation of the manuscript. This work was funded in part by an endowment in Cardiovascular Bioengineering from the AXA Research Fund (to AIB) and an AMX doctoral fellowship from Ecole Polytechnique (to CAD).

Conflict of interest

The authors declare no competing or financial interests.

Contributions

CAD Conceptualization, Methodology, Investigation, Writing; **CRL** Investigation; **AB** Conceptualization, Methodology, Review & Editing; **AIB** Conceptualization, Review & Editing, Funding Acquisition.

Appendices

Appendix A: Model of the free and porous medium flow

As shown below, a system of two first order coupled differential equations is obtained by using an Ohm's law analogy across R_{ch} and Kirchhoff's current law at a node combined with Ohm's law across R_{gel}. R_{ch} is given by the hydraulic resistance for Poiseuille flow in a pipe and R_{gel} by Darcy's law with a small modification to take the particular geometry of this system into account (see Appendix B). The two necessary boundary conditions are imposed by the experiment: the inlet flow rate is the imposed flow rate Q_i and the gauge pressure at the outlets is set to zero.

The hydraulic resistance R_{ch} for fully developed laminar flow in a cylindrical channel (Poiseuille flow) is given as:

$$R_{ch} = \frac{8\eta L}{\pi a^4}$$

where η is the dynamic viscosity of the fluid, L the channel length, and a the channel radius.

As the channel deforms due to the luminal pressure and the pressure decreases axially, a is not constant. We assume a linear dependence on the axial position x: if a_{mean} denotes the average radius and assuming a 10% difference (based on the experimental measurement of strain, shown in Figure 3) between inlet and outlet, we express $a(x)$ as:

$$a(x) = a_{mean} \cdot (1 - 0.1 \cdot (x - \frac{L}{2}))$$

Consequently, the infinitesimal R_{ch}, the resistance of a portion of the channel of length dx at position x, also depends on x and can be expressed as:

$$R_{ch}(x) = \frac{8\eta dx}{\pi \cdot [a_{mean} \cdot (1 - 0.1 \cdot (x - \frac{L}{2}))]^4}$$

$$R_{ch}(x) = \bar{R}_{ch}(x) \cdot dx$$

where

$$\bar{R}_{ch}(x) = \frac{R_{ch}}{L} \cdot \frac{1}{[1 - 0.1 \cdot (x - \frac{L}{2})]^4}$$

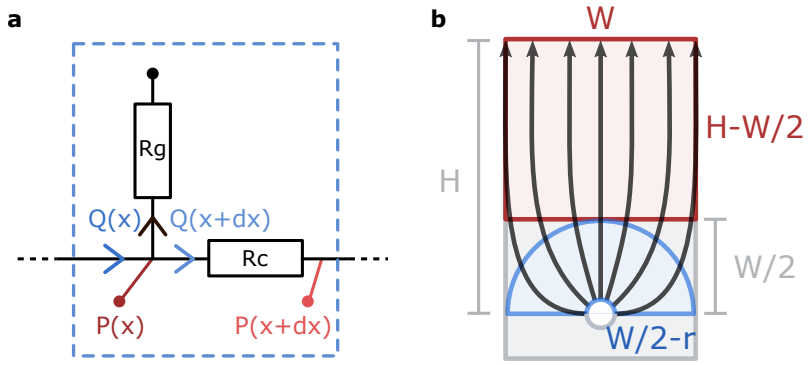

Figure 8. (**a**) Schematic of the equivalent electrical circuit. (**b**) Schematic of the equivalent geometries used to calculate the hydrogel hydraulic resistance showing the half torus in blue and the rectangle in red.

The flow resistance in the porous gel is given by Darcy's law (see Appendix B). As the variations of channel diameter are small and the channel radius is an order of magnitude smaller than the gel dimensions, R_{gel} is assumed to be independent of x.

Applying Ohm's law to one infinitesimal channel resistance (Figure 8a) yields:

$$P(x+dx) - P(x) = -R_{ch}(x) \cdot Q(x) \tag{3}$$

$$\Rightarrow P'(x) = -\bar{R}_{ch}(x) \cdot Q(x) \tag{4}$$

Using Kirchhoff's current law at a node (Figure 8a), we obtain:

$$Q(x) = Q(x+dx) + P(x) \cdot \frac{dx}{R_{gel} \cdot L} \tag{5}$$

$$\Rightarrow Q'(x) = -\frac{P(x)}{R_{gel} \cdot L} \tag{6}$$

Combining equations (4) and (6) and the boundary conditions gives the following system of coupled differential equations:

$$\begin{cases} Q'(x) = -P(x)/(R_{gel} \cdot L) \\ P'(x) = -Q(x) \cdot \bar{R}_{ch}(x) \end{cases} \qquad BCs: \begin{cases} Q(0) = Q_0 \\ P(L) = 0 \end{cases}$$

Normalizing the axial position by L leads to:

$$\begin{cases} Q'(x) = -P(x)/R_{gel} \\ P'(x) = -R_{ch} \cdot (1 - 0.1 \cdot (x - \frac{1}{2}))^{-4} \cdot Q(x) \end{cases}$$

$$BCs: \begin{cases} Q(0) = Q_0 \\ P(1) = 0 \end{cases}$$

This system of coupled nonlinear differential equations is then solved numerically using the bvp4c Matlab solver.

To account for the cell layer in the case of an endothelialized channel, R_{gel} is replaced by $R_{gel} + R_{cell}$, R_{cell} being the unknown resistance of the cell layer to be determined by fitting the experimental data.

To account for the additional outlet resistance R_{out}, the boundary conditions are changed to the following:

$$BCs: \begin{cases} Q(0) = Q_0 \\ P(1) = R_{out} \cdot Q(1) \end{cases}$$

Appendix B: Analytical expression for R_{gel}

For simple geometries where diffusion occurs along only one dimension, Darcy's law can be integrated to calculate the resistance of the porous medium in terms of the fluid viscosity η, the permeability k, and geometrical parameters. For diffusion across a rectangle of length H, width W, and thickness L:

$$R_{gel} = \frac{\eta}{Lk} \cdot \frac{H}{W}$$

For diffusion across half a torus of inner radius a, outer radius $a+\Delta a$, and thickness L:

$$R_{gel} = \frac{\eta}{Lk} \cdot log(\frac{\Delta a}{a})$$

To derive an analytical expression, R_{gel} is approximated as two resistances in series: R_{gel1} models the initial radial diffusion through a torus and R_{gel2} models the final longitudinal diffusion through a rectangle (Figure 8b). As such, both resistances can be expressed as functions of the geometrical parameters of the system:

$$R_{g1} = \frac{\eta}{Lk} \cdot \frac{H - W/2}{W}$$

$$R_{g2} = \frac{\eta}{Lk} \cdot log(\frac{W}{2a})$$

References

[1] F. Boselli, J. B. Freund, and J. Vermot, "Blood flow mechanics in cardiovascular development," 7 2015.

[2] C. Hahn and M. A. Schwartz, "Mechanotransduction in vascular physiology and atherogenesis," *Nature Reviews Molecular Cell Biology*, vol. 10, pp. 53–62, 1 2009.

[3] N. F. Jufri, A. Mohamedali, A. Avolio, and M. S. Baker, "Mechanical stretch: physiological and pathological implications for human vascular endothelial cells," *Vascular Cell*, vol. 7, p. 8, 12 2015.

[4] Y. S. Chatzizisis, A. U. Coskun, M. Jonas, E. R. Edelman, C. L. Feldman, and P. H. Stone, "Role of Endothelial Shear Stress in the Natural History of Coronary Atherosclerosis and Vascular Remodeling," *Journal of the American College of Cardiology*, vol. 49, pp. 2379–2393, 6 2007.

[5] K. S. Cunningham and A. I. Gotlieb, "The role of shear stress in the pathogenesis of atherosclerosis," *Laboratory Investigation*, vol. 85, pp. 9–23, 1 2005.

[6] M. F. O'Rourke and M. E. Safar, "Relationship between aortic stiffening and microvascular disease in brain and kidney: cause and logic of therapy.," *Hypertension (Dallas, Tex. : 1979)*, vol. 46, no. 1, pp. 200–204, 2005.

[7] O. de Montgolfier, A. Pinçon, P. Pouliot, M. A. Gillis, J. Bishop, J. G. Sled, L. Villeneuve, G. Ferland, B. I. Lévy, F. Lesage, N. Thorin-Trescases, and E. Thorin, "High Systolic Blood Pressure Induces Cerebral Microvascular Endothelial Dysfunction, Neurovascular Unit Damage, and Cognitive Decline in Mice," *Hypertension (Dallas, Tex. : 1979)*, vol. 73, no. 1, pp. 217–228, 2019.

[8] D. Wu and K. Birukov, "Endothelial Cell Mechano-Metabolomic Coupling to Disease States in the Lung Microvasculature," *Frontiers in Bioengineering and Biotechnology*, vol. 7, 7 2019.

[9] E. Ergir, B. Bachmann, H. Redl, G. Forte, and P. Ertl, "Small force, big impact: Next generation organ-on-a-chip systems incorporating biomechanical cues," 10 2018.

[10] E. Gordon, L. Schimmel, and M. Frye, "The Importance of Mechanical Forces for in vitro Endothelial Cell Biology," *Frontiers in Physiology*, vol. 11, 6 2020.

[11] E. Roux, P. Bougaran, P. Dufourcq, and T. Couffinhal, "Fluid Shear Stress Sensing by the Endothelial Layer," *Frontiers in Physiology*, vol. 11, 7 2020.

[12] R. S. Reneman and A. P. G. Hoeks, "Wall shear stress as measured in vivo: consequences for the design of the arterial system," *Medical & Biological Engineering & Computing*, vol. 46, pp. 499–507, 5 2008.

[13] T. M. Morrison, G. Choi, C. K. Zarins, and C. A. Taylor, "Circumferential and longitudinal cyclic strain of the human thoracic aorta: Age-related changes," *Journal of Vascular Surgery*, vol. 49, pp. 1029–1036, 4 2009.

[14] A. Wittek, K. Karatolios, C. P. Fritzen, J. Bereiter-Hahn, B. Schieffer, R. Moosdorf, S. Vogt, and C. Blase, "Cyclic three-dimensional wall motion of the human ascending and abdominal aorta characterized by time-resolved three-dimensional ultrasound speckle tracking," *Biomechanics and Modeling in Mechanobiology*, vol. 15, pp. 1375–1388, 10 2016.

[15] P. B. Dobrin, "Mechanical properties of arteries," *Physiological Reviews*, vol. 58, no. 2, pp. 397–460, 1978.

[16] K. L. Wedding, M. T. Draney, R. J. Herfkens, C. K. Zarins, C. A. Taylor, and N. J. Pelc, "Measurement of vessel wall strain using cine phase contrast MRI," *Journal of Magnetic Resonance Imaging*, vol. 15, no. 4, pp. 418–428, 2002.

[17] F. Atry, R. C.-H. Chen, J. Pisaniello, S. Brodnick, A. J. Suminski, J. Novello, J. Ness, J. C. Williams, and R. Pashaie, "Optogenetic interrogation of neurovascular coupling in the cerebral cortex of transgenic mice," *Journal of Neural Engineering*, vol. 15, p. 56033, 9 2018.

[18] Y. Li, W. J. Choi, W. Wei, S. Song, Q. Zhang, J. Liu, and R. K. Wang, "Aging-associated changes in cerebral vasculature and blood flow as determined by quantitative optical coherence tomography angiography," *Neurobiology of Aging*, vol. 70, pp. 148–159, 10 2018.

[19] F. Schmid, P. S. Tsai, D. Kleinfeld, P. Jenny, and B. Weber, "Depth-dependent flow and pressure characteristics in cortical microvascular networks," *PLOS Computational Biology*, vol. 13, p. e1005392, 2 2017.

[20] M. Hahn, T. Heubach, A. Steins, and M. Jünger, "Hemodynamics in Nailfold Capillaries of Patients with Systemic Scleroderma: Synchronous Measurements of Capillary Blood Pressure and Red Blood Cell Velocity," *Journal of Investigative Dermatology*, vol. 110, pp. 982–985, 6 1998.

[21] B. Gu, X. Wang, M. D. Twa, J. Tam, C. A. Girkin, and Y. Zhang, "Noninvasive in vivo characterization of erythrocyte motion in human retinal capillaries using high-speed adaptive optics near-confocal imaging," *Biomedical Optics Express*, vol. 9, no. 8, p. 3653, 2018.

[22] J. Stone, D. M. Johnstone, J. Mitrofanis, and M. O'Rourke, "The mechanical cause of age-related dementia (Alzheimer's Disease): The brain is destroyed by the pulse," *Journal of Alzheimer's Disease*, vol. 44, no. 2, pp. 355–373, 2015.

[23] S. E. Shelton and R. D. Kamm, "In vitro, primarily microfluidic models for atherosclerosis," in *Biomechanics of Coronary Atherosclerotic Plaque*, pp. 299–313, Elsevier, 1 2021.

[24] G. Helmlinger, R. V. Geiger, S. Schreck, and R. M. Nerem, "Effects of pulsatile flow on cultured vascular endothelial cell morphology," *Journal of Biomechanical Engineering*, vol. 113, pp. 123–131, 5 1991.

[25] N. Caille, Y. Tardy, and J. J. Meister, "Assessment of Strain Field in Endothelial Cells Subjected to Uniaxial Deformation of Their Substrate," *Annals of Biomedical Engineering*, vol. 26, pp. 409–416, 5 1998.

[26] A. S. Zeiger, F. D. Liu, J. T. Durham, A. Jagielska, R. Mahmoodian, K. J. Van Vliet, and I. M. Herman, "Static mechanical strain induces capillary endothelial cell cycle re-entry and sprouting," *Physical Biology*, vol. 13, p. 046006, 8 2016.

[27] W. Zheng, B. Jiang, D. Wang, W. Zhang, Z. Wang, and X. Jiang, "A microfluidic flow-stretch chip for investigating blood vessel biomechanics," *Lab on a Chip*, vol. 12, pp. 3441–3450, 9 2012.

[28] R. Sinha, S. Le Gac, N. Verdonschot, A. van den Berg, B. Koopman, and J. Rouwkema, "Endothelial cell alignment as a result of anisotropic strain and flow induced shear stress combinations," *Scientific Reports*, vol. 6, p. 29510, 7 2016.

[29] D. Meza, B. Musmacker, E. Steadman, T. Stransky, D. A. Rubenstein, and W. Yin, "Endothelial Cell Biomechanical Responses are Dependent on Both Fluid Shear Stress and Tensile Strain," *Cellular and Molecular Bioengineering*, vol. 12, pp. 311–325, 8 2019.

[30] N. C. A. van Engeland, A. M. A. O. Pollet, J. M. J. den Toonder, C. V. C. Bouten, O. M. J. A. Stassen, and C. M. Sahlgren, "A biomimetic microfluidic model to study signalling between endothelial and vascular smooth muscle cells under hemodynamic conditions," *Lab on a Chip*, vol. 18, no. 11, pp. 1607–1620, 2018.

[31] D. Meza, L. Abejar, D. A. Rubenstein, and W. Yin, "A Shearing-Stretching Device That Can Apply Physiological Fluid Shear Stress and Cyclic Stretch Concurrently to Endothelial Cells," *Journal of Biomechanical Engineering*, vol. 138, 3 2016.

[32] L. Bernardi, C. Giampietro, V. Marina, M. Genta, E. Mazza, and A. Ferrari, "Adaptive reorientation of endothelial collectives in response to strain," *Integrative Biology*, vol. 10, no. 9, pp. 527–538, 2018.

[33] K. Sato, M. Nitta, and A. Ogawa, "A Microfluidic Cell Stretch Device to Investigate the Effects of Stretching Stress on Artery Smooth Muscle Cell Proliferation in Pulmonary Arterial Hypertension," *Inventions*, vol. 4, p. 1, 12 2018.

[34] J. E. Moore, E. Bürki, A. Suciu, S. Zhao, M. Burnier, H. R. Brunner, and J.-J. Meister, "A device for subjecting vascular endothelial cells to both fluid shear stress and circumferential cyclic stretch," *Annals of Biomedical Engineering*, vol. 22, pp. 416–422, 7 1994.

[35] A. Benbrahim, G. J. L'Italien, B. B. Milinazzo, D. F. Warnock, S. Dhara, J. P. Gertler, R. W. Orkin, and W. M. Abbott, "A compliant tubular device to study the influences of wall strain and fluid shear stress on cells of the vascular wall," *Journal of Vascular Surgery*, vol. 20, pp. 184–194, 8 1994.

[36] Y. Qiu and J. M. Tarbell, "Interaction between Wall Shear Stress and Circumferential Strain Affects Endothelial Cell Biochemical Production," *Journal of Vascular Research*, vol. 37, no. 3, pp. 147–157, 2000.

[37] H. Guo, J. D. Humphrey, and M. J. Davis, "Effects of biaxial stretch on arteriolar function in vitro," *American Journal of Physiology-Heart and Circulatory Physiology*, vol. 292, pp. H2378–H2386, 5 2007.

[38] Z. H. Syedain, L. A. Meier, J. W. Bjork, A. Lee, and R. T. Tranquillo, "Implantable arterial grafts from human fibroblasts and fibrin using a multigraft pulsed flow-stretch bioreactor with noninvasive strength monitoring," *Biomaterials*, vol. 32, pp. 714–722, 1 2011.

[39] W. J. Polacheck, R. Li, S. G. M. Uzel, and R. D. Kamm, "Microfluidic platforms for mechanobiology," *Lab on a Chip*, vol. 13, no. 12, p. 2252, 2013.

[40] A. Cochrane, H. J. Albers, R. Passier, C. L. Mummery, A. van den Berg, V. V. Orlova, and A. D. van der Meer, "Advanced in vitro models of vascular biology: Human induced pluripotent stem cells and organ-on-chip technology," *Advanced Drug Delivery Reviews*, vol. 140, pp. 68–77, 2 2019.

[41] K. Haase and R. D. Kamm, "Advances in on-chip vascularization," *Regenerative Medicine*, vol. 12, pp. 285–302, 4 2017.

[42] A. M. Pollet and J. M. den Toonder, "Recapitulating the Vasculature Using Organ-On-Chip Technology," *Bioengineering*, vol. 7, p. 17, 2 2020.

[43] S. Pradhan, O. A. Banda, C. J. Farino, J. L. Sperduto, K. A. Keller, R. Taitano, and J. H. Slater, "Biofabrication Strategies and Engineered In Vitro Systems for Vascular Mechanobiology," *Advanced Healthcare Materials*, p. 1901255, 2 2020.

[44] K. M. Chrobak, D. R. Potter, and J. Tien, "Formation of perfused, functional microvascular tubes in vitro," *Microvascular Research*, vol. 71, no. 3, pp. 185–196, 2006.

[45] J. S. Miller, K. R. Stevens, M. T. Yang, B. M. Baker, D. H. T. Nguyen, D. M. Cohen, E. Toro, A. A. Chen, P. A. Galie, X. Yu, R. Chaturvedi, S. N. Bhatia, and C. S. Chen, "Rapid casting of patterned vascular networks for perfusable engineered three-dimensional tissues," *Nature Materials*, vol. 11, pp. 768–774, 7 2012.

[46] G. M. Price and J. Tien, "Subtractive Methods for Forming Microfluidic Gels of Extracellular Matrix Proteins," *Methods in Bioengineering: Microdevices in Biology and Medicine*, pp. 235–248, 2009.

[47] D.-H. T. Nguyen, S. C. Stapleton, M. T. Yang, S. S. Cha, C. K. Choi, P. A. Galie, and C. S. Chen, "Biomimetic model to reconstitute angiogenic sprouting morphogenesis in vitro," *Proceedings of the National Academy of Sciences*, vol. 110, no. 17, pp. 6712–6717, 2013.

[48] E. E. Antoine, F. P. Cornat, and A. I. Barakat, "The stentable in vitro artery: An instrumented platform for endovascular device development and optimization," *Journal of the Royal Society Interface*, vol. 13, 12 2016.

[49] W. J. Polacheck, M. L. Kutys, J. B. Tefft, and C. S. Chen, "Microfabricated blood vessels for modeling the vascular transport barrier," *Nature Protocols*, vol. 14, pp. 1425–1454, 5 2019.

[50] E. E. Antoine, P. P. Vlachos, and M. N. Rylander, "Tunable Collagen I Hydrogels for Engineered Physiological Tissue Micro-Environments," *PLOS ONE*, vol. 10, p. e0122500, 3 2015.

[51] V. H. Huxley, F. E. Curry, and R. H. Adamson, "Quantitative fluorescence microscopy on single capillaries: α-lactalbumin transport," *American Journal of Physiology - Heart and Circulatory Physiology*, vol. 252, no. 1, 1987.

[52] J. Y. Tinevez, N. Perry, J. Schindelin, G. M. Hoopes, G. D. Reynolds, E. Laplantine, S. Y. Bednarek, S. L. Shorte, and K. W. Eliceiri, "TrackMate: An open and extensible platform for single-particle tracking," *Methods*, vol. 115, pp. 80–90, 2 2017.

[53] R. C. Gerum, S. Richter, B. Fabry, and D. P. Zitterbart, "ClickPoints : an expandable toolbox for scientific image annotation and analysis," *Methods in Ecology and Evolution*, vol. 8, pp. 750–756, 6 2017.

[54] G. Adriani, D. Ma, A. Pavesi, R. D. Kamm, and E. L. K. Goh, "A 3D neurovascular microfluidic model consisting of neurons, astrocytes and cerebral endothelial cells as a blood-brain barrier," *Lab on a Chip*, vol. 17, no. 3, pp. 448–459, 2017.

[55] T.-E. Park, N. Mustafaoglu, A. Herland, R. Hasselkus, R. Mannix, E. A. FitzGerald, R. Prantil-Baun, A. Watters, O. Henry, M. Benz, H. Sanchez, H. J. McCrea, L. C. Goumnerova, H. W. Song, S. P. Palecek, E. Shusta, and D. E. Ingber, "Hypoxia-enhanced Blood-Brain Barrier Chip recapitulates human barrier function and shuttling of drugs and antibodies," *Nature Communications*, vol. 10, 12 2019.

[56] S. Bang, S. R. Lee, J. Ko, K. Son, D. Tahk, J. Ahn, C. Im, and N. L. Jeon, "A Low Permeability Microfluidic Blood-Brain Barrier Platform with Direct Contact between Perfusable Vascular Network and Astrocytes," *Scientific Reports*, vol. 7, no. 1, pp. 1–10, 2017.

[57] E. Gordon, L. Schimmel, and M. Frye, "The Importance of Mechanical Forces for in vitro Endothelial Cell Biology," 6 2020.

[58] F. W. Charbonier, M. Zamani, and N. F. Huang, "Endothelial Cell Mechanotransduction in the Dynamic Vascular Environment," *Advanced Biosystems*, vol. 3, p. 1800252, 2 2019.

[59] P. P. Partyka, G. A. Godsey, J. R. Galie, M. C. Kosciuk, N. K. Acharya, R. G. Nagele, and P. A. Galie, "Mechanical stress regulates transport in a compliant 3D model of the blood-brain barrier," *Biomaterials*, vol. 115, pp. 30–39, 2017.

[60] J. Tien, L. Li, O. Ozsun, and K. L. Ekinci, "Dynamics of interstitial fluid pressure in extracellular matrix hydrogels in microfluidic devices," *Journal of Biomechanical Engineering*, vol. 137, 9 2015.

[61] D. Maity, Y. Li, Y. Chen, and S. X. Sun, "Response of collagen matrices under pressure and hydraulic resistance in hydrogels," *Soft Matter*, vol. 15, pp. 2617–2626, 3 2019.

[62] E. Akbari, G. B. Spychalski, K. K. Rangharajan, S. Prakash, and J. W. Song, "Flow dynamics control endothelial permeability in a microfluidic vessel bifurcation model," *Lab on a Chip*, vol. 18, no. 7, pp. 1084–1093, 2018.

[63] Y. Abe, M. Watanabe, S. Chung, R. D. Kamm, K. Tanishita, and R. Sudo, "Balance of interstitial flow magnitude and vascular endothelial growth factor concentration modulates three-dimensional microvascular network formation," *APL Bioengineering*, vol. 3, p. 36102, 9 2019.

[64] P. A. Galie, D.-H. T. Nguyen, C. K. Choi, D. M. Cohen, P. A. Janmey, and C. S. Chen, "Fluid shear stress threshold regulates angiogenic sprouting," *Proceedings of the National Academy of Sciences*, vol. 111, no. 22, pp. 7968–7973, 2014.

[65] E. Lee, H. Takahashi, J. Pauty, M. Kobayashi, K. Kato, M. Kabara, J. I. Kawabe, and Y. T. Matsunaga, "A 3D in vitro pericyte-supported microvessel model: Visualisation and quantitative characterisation of multistep angiogenesis," *Journal of Materials Chemistry B*, vol. 6, no. 7, pp. 1085–1094, 2018.

[66] X. Zhang, M. Bishawi, G. Zhang, V. Prasad, E. Salmon, J. J. Breithaupt, Q. Zhang, and G. A. Truskey, "Modeling early stage atherosclerosis in a primary human vascular microphysiological system," *Nature Communications*, vol. 11, 12 2020.

[67] V. L. Silvestri, E. Henriet, R. M. Linville, A. D. Wong, P. C. Searson, and A. J. Ewald, "A Tissue-Engineered 3D Microvessel Model Reveals the Dynamics of Mosaic Vessel Formation in Breast Cancer," *Cancer Research*, vol. 80, pp. 4288–4301, 10 2020.

[68] G. Offeddu, C. Hajal, C. Foley, Z. Wan, L. Ibrahim, M. Coughlin, and R. Kamm, "Glycocalyx-Mediated Vascular Dissemination of Circulating Tumor Cells," *bioRxiv*, p. 2020.04.28.066746, 4 2020.

[69] S. Alimperti, T. Mirabella, V. Bajaj, W. Polacheck, D. M. Pirone, J. Duffield, J. Eyckmans, R. K. Assoian, and C. S. Chen, "Three-dimensional biomimetic vascular model reveals a RhoA, Rac1, and N-cadherin balance in mural cell–endothelial cell-regulated barrier function," *Proceedings of the National Academy of Sciences of the United States of America*, vol. 114, no. 33, pp. 8758–8763, 2017.

[70] A. Herland, A. D. Van Der Meer, E. A. FitzGerald, T. E. Park, J. J. F. Sleeboom, and D. E. Ingber, "Distinct contributions of astrocytes and pericytes to neuroinflammation identified in a 3D human blood-brain barrier on a chip," *PLoS ONE*, vol. 11, no. 3, pp. 1–21, 2016.

Chapter 3

Dynamics of poroelastic hydrogels

> Pourquoi faire simple quand on peut faire compliqué...
>
> *Jacques Rouxel - Les shadoks*

3.1 Introduction

3.1.1 Collagen hydrogels, a popular biomaterial

Hydrogels are networks of polymers with high water content, which makes them ideal biomaterials. The first hydrogels were developed in the 1960's with the professed goal of ultimately implanting them in patients [146]. Three generations of hydrogels came after the early trials: gels with chemical crosslinkers, stimuli-responsive (such as pH- or temperature-sensitive) gels , and stereo-complexed gels. Since then, hydrogels have attracted an exponentially growing interest in the scientific community in several areas including drug delivery, tissue engineering, organoid studies and organs-on-chip development.

Hydrogels can be natural, such as collagen or fibrin gels, or synthetic, such as polyethylene glycol (PEG) or acrylamide gels. Naturals hydrogels have the advantages of being biocompatible, biodegradable and non-toxic. Collagen hydrogels are one of the most popular options, in particular collagen type I [96]. The main sources of collagen type I are rat tendons and bovine dermis. They are mostly used at concentrations of around 1 mg/mL. Gels of lower concentrations tend to have poor mechanical integrity and are highly heterogeneous, whereas higher concentrations lead to very dense structures that have poor cell viability and are difficult to dissolve fully. The final micron-scale network structure is also determined by the pH and polymerization temperature, to which collagen hydrogels are very sensitive.

3.1.2 Hydrogel mechanics

Hydrogels are also popular materials because of their mechanical properties. They form a network of cross-linked thin stiff filaments immersed in water, creating a self sustaining, very soft and highly porous material. The characterization of their mechanical behavior remains a highly active field of study, with different models competing. While the elastic portion of hydrogels' mechanical behavior is a consensus, there is ongoing debate around which model best describes their dynamics: viscoelastic, poroelastic, visco-poroelastic or even visco-elasto-plastic.

3.1.2.1 Elasticity

Elastic materials are characterized by a proportionality between the force applied on them and their deformation, i.e. stress and strain are proportional. The ratio of stress to strain is therefore constant and is called the Young's modulus, a constitutive property of the material. In a purely elastic material, there are no dynamics: the material instantaneously deforms proportionally to the stress. The important parameter is the Young's modulus, and typical values for collagen hydrogels are 0.5-5 kPa, depending on the gels' density, pH and polymerization temperature [96, 147].

When the Young's modulus does not remain constant with loading, elasticity is non-linear. A classic example is the strain stiffening exhibited by fibrous networks such as hydrogels. Taking the example of a single fiber being pulled, the fiber will initially straighten out. During this period, the fiber appears very soft. However, when all the bends disappear, it will stretch and thus appear much stiffer. A network of fibers behaves similarly, with an additional degree of freedom due to fiber reorientation.

3.1.2.2 Different models beyond elasticity

Two main models are used to describe hydrogel deformation at intermediate time scales: viscoelasticity and poroelasticity [148,149]. Although these two models are the most prevalent in the literature, one study also reported visco-elasto-plasticity in hydrogels when considering longer time scales. I will present here the three models and their important features.

Viscoelasticity Viscoelasticity describes materials that exhibit a combination of elastic and viscous behavior depending on the time scale of observation. Most biomaterials exhibit viscoelastic behavior. When a stress is applied to a viscoelastic material, it exhibits an immediate elastic deformation followed in the longer term by gradual time-dependent deformation whose dynamics are determined by the material's viscosity.

Poroelasticity Poroelasticity describes porous deformable materials in which the porous fibrillar scaffold behaves as an elastic solid while the fluid is allowed to flow within the porous medium. In poroelastic materials, pore pressure is coupled to pore deformation. For instance, a hydrogel placed at the bottom of a water column, i.e. subjected to an increased fluid hydrostatic pressure, would swell and the scaffold would undergo extension. An important parameter to consider is the permeability, with typical values for collagen hydrogels ranging from 10^{-15} to $10^{-13}\,\mathrm{m}^2$ depending on gel density, pH and polymerization temperature [96, 150–152].

An interesting property specific to poroelastic materials is the fact that the characteristic response time depends on the material's length scale. The deformation of a solid generates a change in the fluid pressure inside the material, which dissipates with a characteristic speed. This characteristic speed is constant, as it is defined by the material permeability. As a result, the characteristic time is proportional to the characteristic length.

Visco-elasto-plasticity When considering longer time scales, tens of minutes to several hours, plasticity can also be observed in the response of collagen hydrogels to mechanical loading. Plasticity is defined as "the ability of a solid material to undergo permanent deformation, a non-reversible change of shape in response to applied forces" [153]. The standard test for plasticity is the creep-and-recovery test, where samples are subjected to a stress step of fixed duration and their strain is measured over time. Plasticity is then measured as the remaining deformation after the recovery.

One study investigated in detail the plasticity of collagen hydrogels through creep-and-recovery tests [154]. The authors quantified plasticity through the ratio of the final strain to the maximum strain. They showed that collagen gels can exhibit significant plasticity, up to

60 % irreversible strain for a creep time of one hour. The degree of plasticity depended on the creep time and stress magnitude. At the microscopic level, the authors attributed the plasticity to the detachment/reattachment of weak bonds, which allows the material to flow. To support this hypothesis, they showed that (1) covalent crosslinking decreased plasticity and (2) plasticity was nonlinear, i.e. it varied with the magnitude of stress or strain, as the probability of weak bond detachment depends on the externally applied force.

Choosing a rheological framework An effective approach for choosing the rheological model best suited to the problem at hand is to consider the characteristic times. If these times are on the order of seconds or minutes, plasticity can usually be neglected, as it typically enters into play only after tens of minutes or hours. However, the choice between the viscous and porous component remains, and here again, considering the characteristic times can help: while the characteristic time for viscoelasticity depends solely on the viscosity, the characteristic time for poroelasticity depends not only on the permeability but also on the characteristic length.

This difference can be used in one of two ways to help select the most appropriate model. The first is to vary the characteristic length to probe the impact on the response. If the relaxation time changes, then that would favor a poroelastic model, whereas if the relaxation time remains constant, then that suggests a viscoelastic model would be more appropriate. The second method is to compute the poroelastic, viscoelastic and experimental time scales and to compare them, assuming the permeability and viscosity of the hydrogel are known. For instance, the viscoelastic description is predominant in the biomechanics field because cell-scale deformations, such as the ones generated by cells migrating in a 3D matrix, result in a small poroelastic times.

Interestingly, the notion that viscoelasticity is the most appropriate framework for studying cells is being increasingly challenged. Indeed, viscoelasticity neglects the mechanical contribution of the fluid flowing inside the porous matrix, which was recently suggested to be the origin of the major forces exerted on cells inside a hydrogel [155]. This underscores the complex rheology of hydrogels and the importance of poroelasticity at both the micro- and macroscopic scales.

3.1.3 Classical assays for characterizing hydrogel rheology

Characterization of the rheology of hydrogels is an active field of study, with several different assays being used to extract permeability and Young's modulus values. I will present here three classical assays and their relative advantages and disadvantages.

3.1.3.1 Hydraulic perfusion assays

The oldest existing assay to test porous materials is the hydraulic perfusion assay. This actually is how Darcy investigated flow in porous media, in his case sand, and defined permeability. The concept is simple: a porous medium of known length and cross-sectional area is placed inside a tube, and a pressure difference is applied across the sample. This creates flow through the sample, with a flow rate that depends on the length, area and hydraulic conductivity. The hydraulic conductivity itself depends on the fluid properties (density and viscosity) and the permeability of the sample. Despite being one of the easiest tests in the field of hydrogeology, performing a hydraulic perfusion assay in hydrogels is challenging. In fact, due to their relatively low permeability (very small pore size) and softness, the pressure difference necessary to push a measurable volume of fluid through a gel is typically sufficient to cause large deformations and gel rupture. Measuring the permeability of hydrogels through such a direct method is very difficult and to the best of my knowledge, has never

been published. The current approach is to extract permeability from the dynamics of a gel under mechanical loading, as permeability dictates the poroelastic relaxation time.

3.1.3.2 Compression assays

Macroscopic The oldest assay to characterize elastic materials is the macroscopic compression assay, where a sample is placed between two plates and squeezed. A compression test can have an imposed stress and measured strain or an imposed strain and measured stress. For a purely elastic material, the proportionality between the strain and the stress will yield the Young's modulus of the material. However, most materials are either viscoelastic or poroelastic, exhibiting time-dependent regimes. The two most frequent tests are the step and the ramp. In the step test, if a constant strain is imposed, then the result is a relaxation test due to the stress relaxation of the material. Conversely, imposing a constant stress results in a creep test where the material deforms progressively in time. In the ramp test, the strain (or stress) rate determines the relative contribution of the viscous or porous component to the overall response. In both tests, viscosity and/or permeability values can be computed by fitting the dynamic response to the corresponding mechanical model. As long range motion, such as that generated by compression, tends to be dominated by porous effects, the macroscopic method is best suited for measuring poroelasticity.

Microscopic The microscopic versions of the compression assay, such as atomic force microscopy (AFM) or micro/nano indentation, are very popular in the field of biomaterial mechanics, in particular for hydrogels. In the indentation test, a probe of a given radius is pushed down onto the material, with fixed displacement (or load), and the evolution of the load (or displacement) with time is recorded. Once again, the test can be a step (relaxation and creep) or a ramp, and the dynamics provide viscosity or permeability values. As short range motion, such as that generated by indentation, tends to be dominated by viscous effects, the microscopic method is best suited for measuring viscoelasticity.

3.1.3.3 Shearing assays

The last class of mechanical testing assays is the shearing assay, most often implemented using a rheometer. This method measures the storage and loss moduli of a material, i.e. G' and G", as a function of the applied loading frequency. Rheometers are best suited for the study of viscoelasticity, do not give access to permeability and cannot be used for poroelasticity estimation. Although commonly used because of its simplicity, this method yields dynamic parameters that are impossible to compare to the values obtained with the other techniques.

3.1.4 Goal and rationale

In the work presented in this chapter, my goal was to understand the mechanical behavior of the gel, and in particular its poroelastic properties. Indeed, the microvessel-on-chip I developed is based on luminal flow actuation and can also be used as a mechanical testing platform. The assay would then be a hydraulic radial compression assay. I therefore explored several types of tests possible in the microvessel and collected data for both bare gels and endothelialized channels. To validate my hypotheses and investigate whether the framework of poroelasticity was sufficient to explain the experimental observations, I used numerical simulation using the multi-physics finite element-based commercial code COMSOL. These various tests should all provide measures of the Young's modulus and the permeability independently, enabling the comparison between the obtained values. With the experiments on bare gels, the focus was on the hydrogel mechanics, while with the addition of cells, I was able to not only investigate the monolayer mechanics but also to further characterize the

hydrogel mechanics thanks to the flow shielding effect of the endothelium. The presence of cells is expected to decrease the contribution of the porous medium flow, as shown in the previous chapter.

The present chapter started as a couple of side projects, which slowly became a full part of my thesis as interesting scientific questions emerged from the data. I thus made an excursion into biomaterial mechanics between the two main steps of my Ph.D. (chapters 2 and 4), a field quite different from the research expertise of the laboratory. As a result, this work was done in close collaboration with student interns and other colleagues. Interestingly, this poroelasticity project ended up being crucial to understand the response of the cells to stretch (see next chapter). The bulk of the data is made of preliminary results and exploratory experiments, which would need to be repeated before submission for publication.

3.2 Estimating hydrogel stiffness using a smartphone

3.2.1 Introduction

Goal I wanted to assess the elastic properties of the collagen hydrogel, namely its Young's modulus, before delving into the gel's complex poroelastic behavior. Indentation tests are frequently used to measure the stiffness of hydrogels (see section 3.1.3), typically at large scales and using millimeter-sized probes. The largest probe that can be used with the nanoindenter system available in the laboratory has a radius of 50 µm, which is only one or two orders of magnitude larger than the pore size in the gel. Had I used this probe, the measured stiffness would have been highly influenced by the local topography and gel microstructure. Furthermore, nanoindentation is a time consuming and delicate technique which requires days of optimization for a given material and experimental configuration.

I decided to pursue an alternative route. I developed a DIY macroscopic mechanical testing platform in the laboratory with the help of a student intern, Elvire Fauchet. This mechanical testing platform can also be used for systematic measurement of the properties of samples and for quantification of the reproducibility of the gel fabrication process. I had observed a large variability of hydrogel deformation among chips (see Chapter 2), which may have been a consequence of sample heterogeneity. Being able to confirm the origin of the variability and to measure the Young's modulus easily would enable us to optimize the fabrication protocol and establish an acceptable level of sample heterogeneity.

Elvire's internship The task of developing this new mechanical assay was the goal of the 3-month internship of Elvire Fauchet, a Polytechnique student. Elvire came up with the great idea of adapting the traditional two-point bending test for soft biological samples (Figure 3.1 A). I will not describe all the details of her work, but it can be found in her internship report. I present broadly the experimental approach and the results it generated in the next section and discuss the pertinence of this assay for my thesis and the scientific community.

3.2.2 Methods

3.2.2.1 Experimental measurement

Sample fabrication To fabricate samples of identical dimensions, Elvire used the same PDMS housing as for the microvessel. This dimensions of this housing are 15x3x2 mm (see Chapter 2 for more detail). Collagen hydrogels of varying concentrations (4, 6 and 8 mg mL^{-1}) were prepared using the same protocol as for the microvessel by mixing an acid collagen suspension in a pH-controlled solution. The solution was then pipetted into mutiple housings and polymerized at 37°C. A batch refers to all samples fabricated with one collagen solution. After solidification, hydrogels were gently pulled out of the housing with tweezers and

maintained in PBS for hydration until mechanical testing. During polymerization, collagen hydrogels tend to contract. Images of each sample from the top and the side were therefore acquired to measure their final dimensions.

Setup PDMS cubes were placed 10 mm apart in front of a black screen. Samples were gently positioned with tweezers between the two PDMS cubes. To avoid internal tension or compression in the final state, after positioning one end, the central part and free end were lifted with tweezers and then lowered slowly until the free end touched the opposite PDMS cube. The central part was then released and was free to bend under its own weight (Figure 3.1 B). A phone was placed on a tripod at exactly the same height as the sample and a picture of the deformed sample was acquired. Each sample was tested three consecutive times with the following protocol repeated after each test: the sample was removed after image acquisition, rehydrated and repositioned before a new test.

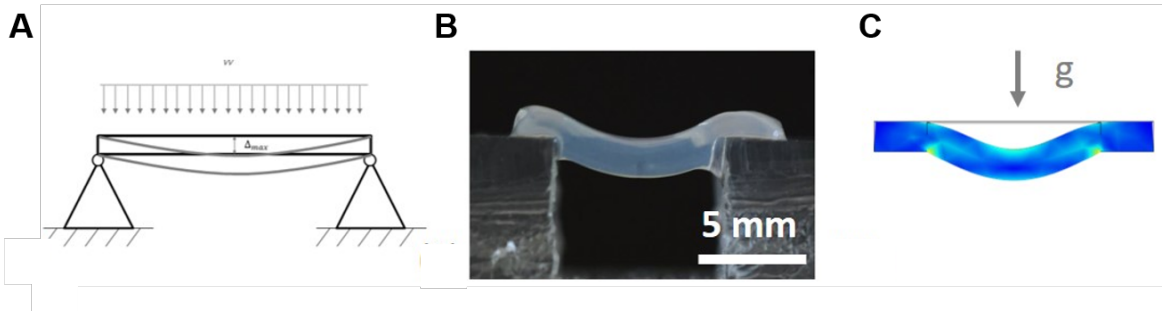

FIGURE 3.1: **A.** Schematic of the two point bending beam assay. **B.** Picture of the hydrogel sample suspended between two PDMS bloc, bending under its own weight. **C.** Illustration of the numerical simulation.

Image analysis Parameters of interest, i.e. the sample's free length, height and width, as well as the length of the sample under bending and the bending distance, were measured manually from the images using ImageJ.

3.2.2.2 Mechanical framework

To infer intrinsic material properties from the deformation and the forces, a mechanical framework is needed. The Young's modulus is the ratio of stress to strain, which should be calculated from the measured deformation and the sample weight. Two models could be used, either the bending beam theory in 1D or a 3D model based on numerical simulations.

1D bending beam theory In this 1D approximation, the sample is considered as a beam of length L, thickness a and height e, fixed at its extremities and bending under a uniform load w corresponding to its weight per unit length (Figure 3.1 A). The maximum deflection Δ_{max} can be expressed as a function of the geometric parameters and the Young's modulus E as follows:

$$\Delta_{max} = \frac{wL^4}{384EI}, \text{ where } w = \rho gae \text{ and } I = \frac{ae^3}{12} \tag{3.1}$$

3D COMSOL modeling To apply the 1D bending beam theory to our experiment, two broad approximations are necessary: the thickness and the length of the sample are similar, but we consider that the sample is a beam, and the contact points between the sample and the PDMS are considered punctual although they cover the top surface of the PDMS cube. To draw on a better mechanical framework, we conducted COMSOL simulations of a linear elastic solid sample deforming under its own weight, with a given length and fixed at both

ends (Figure 3.1 C). The maximum deflection Δ_{max} as a function of the Young's modulus E for various given geometries (L, e and a) can be calculated to serve in an inverse problem analysis (i.e. the deflections that match experiments are used to extract the correct value of the Young's modulus).

Comparison To estimate the error generated by the bending beam approximation, the ratio of the numerical Δ_{max} and the theoretical Δ_{max} are plotted as a function of sample thickness a and as a function of the ratio of the free suspended length over the total length. When a is below 1 mm, the ratio is equal to 1, as the bending beam theory applies fairly well, while for increasing a the Δ_{max} ratio diverges and is equal to 100 when a equals to 1 cm. In our case, a is around 2 mm, where the Δ_{max} ratio is around 2, introducing a significant error in the Young's modulus calculation. If more than half of the total length is free, the Δ_{max} ratio is close to 1. For free lengths below half the total length, the Δ_{max} ratio diverges rapidly. In our experiments, the free length to total length ratio were above 0.75, so the error was relatively small. Based on this comparison, we decided to use the COMSOL computed table to calculate Young's moduli based on the exact sample geometry.

3.2.3 Results

3.2.3.1 Measurement robustness

The first step before adopting the new home-made mechanical assay was defining its robustness. Three consecutive test repeats on the same sample were performed for this purpose to assess the reproducibility of the estimated Young's modulus. Ideally, the inferred value would be identical among the three tests. To our surprise, despite the home-made nature and simple design and setup, the bending assays generated extremely consistent values for a given sample (Figure 3.2 A). If we normalize all the measured samples by their mean E to display the dispersion of the triplicate measurements, we can see that the triplicate dispersion is well within 10%.

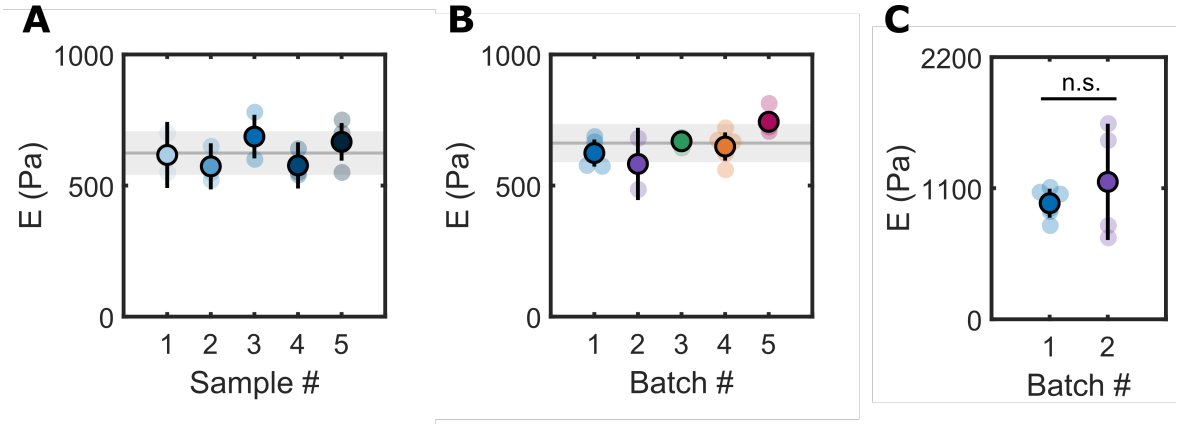

FIGURE 3.2: Estimated Young's moduli E based on the bending beam assay. **A.** Variability among samples of one batch (6 mg/mL). **B.** Variability among batches of the same concentration (6 mg/mL). **C.** Variability between a well-mixed (1) and poorly mixed (2) batch of the same concentration (8 mg/mL).

3.2.3.2 Sample homogeneity, an evaluation of fabrication reproducibility

Because the assay was fairly reproducible, we were able to use it to investigate sample-to-sample and batch-to-batch variability, as an assessment of fabrication robustness. Indeed, the dispersion of the triple measurements on each sample was smaller than the dispersion

among samples or between batches. Batches made of carefully mixed collagen solutions had homogeneous E values among samples (Figure 3.2 A) and had similar stiffness values among them (Figure 3.2 B). In contrast, batches that were not thoroughly mixed generated heterogeneous samples with large standard deviations, and sample stiffnesses could vary by a factor 2 (see batch 2 in Figure 3.2 C). Smaller batches, with three or four samples, were often more heterogeneous. Thoroughly mixing small volumes of a highly viscous solution without introducing air bubbles is notoriously difficult.

3.2.3.3 Varying collagen concentration to vary the Young's modulus

The Young's modulus of a collagen hydrogel is known to vary with the collagen concentration. The deformability of a hydrogel stems from the network of elastic fibers whose microstructure determines the overall stiffness. To assess the capacity of our novel assay to detect variations of Young's modulus with collagen concentration, we tested samples with three different collagen concentrations: 4, 6 and 8 $\mathrm{mg\,mL^{-1}}$. As expected, the estimated Young's modulus increased with collagen concentration, with a small standard deviation in any one sample group compared to the differences among groups (Figure 3.3). The precision and reproducibility of the results for such a simple technique were rather surprising and underscored the potential of this DIY assay.

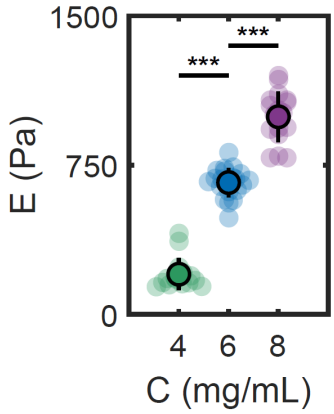

FIGURE 3.3: Young's modulus as a function of collagen concentration.

3.2.4 Discussion and conclusions

Validation of the Young's modulus Literature values of Young's modulus for collagen hydrogels span a large range depending on the measurement method (see Section 3.1.2). Our values, on the order of kPa, fall well within the range of previously reported values. Nevertheless, it would be useful to validate the results by measuring the Young's modulus of our samples using a traditional mechanical assay. This work has been started in collaboration with Sara Barrasa-Ramos, and we are currently exploring uniaxial traction and compression as macroscopic assays. Preliminary results show the same order of magnitude for the E measured with the different techniques.

Impact on the field When validated, our proposed method could be a much simpler method to assess the stiffness of soft biological materials. The possibility to estimate the stiffness with a phone camera is a perfect example of frugal science and could make mechanical testing available for less well funded laboratories across the world. The possibility to routinely test samples could help researchers improve their fabrication process, as demonstrated by our

mixing quality example, and measure the stiffness of their material instead of having to rely on literature values.

Conclusions As soon as the estimated Young's moduli are validated, I plan on publishing this simple DIY method in order to make hydrogel stiffness measurements accessible to all. As the crucial role of mechanics on cells becomes clearer, more and more laboratories are incorporating soft substrates into their experiments. This method would be a helpful tool to popularize mechanical testing and to gain an appreciation for contradictory literature results that might stem from poorly characterized homemade hydrogels or soft materials.

3.3 Poroelasticity: hydraulic pressure step

During the characterization of the microvessel presented in Chapter 2, I performed numerous recordings of the channel dilation during a pressure step. The strain values reported in that chapter were measured in the steady state. I will present here the transient regime, which revealed the poroelastic nature of the hydrogel. The typical response that I describe in the following paragraphs is actually how I "discovered" the poroelasticity of hydrogels.

3.3.1 Methods

3.3.1.1 Deformation measurement

To quantify the dynamic deformation of the gel, I used the same approach as described in Chapter 2. I recorded the channel dilation during a flow step (or a flow ramp) applied with a syringe pump in brightfield using a 40X objective. The edges of the channels were tracked with Clickpoints at multiple positions. The average diameter as a function of time was extracted using a custom-made Python code from the detected tracks.

3.3.1.2 Poroelastic simulations of the 2D cross-section

2D simulations of the cross-section of the microvessel were conducted in COMSOL. The gel was modeled as a poroelastic material with a hole at the channel position. A time-dependent load was imposed on the gel at the channel border, creating a double boundary condition: on the solid and on the fluid. The open top of the gel was maintained at zero pressure and was free to move. The bottom and lateral walls were considered as no flow and fixed constraint boundaries. Loads were imposed as steps (up) or ramps starting at t = 1 s, followed by a smoothed step (down). The outputs of interest were the gel displacement at the channel border and the pressure distribution in the gel.

3.3.2 Results and discussion

3.3.2.1 Overshoot and characteristic poroelastic time

Bare channels subjected to a pressure step exhibited a quick increase in diameter followed by a slow decrease toward the steady state equilibrium diameter (Figure 3.4). Similarly, after the load was removed, the diameter quickly decreased to below the initial value before showing a slow increase back to the original diameter (Figure 3.4). Two "overshoots" could be observed, one after the load increase and another after load removal. To distinguish between the two, I will call "overshoot" the one after load increase and "undershoot" the one after load removal. The "overshoot" and "undershoot" constitute the transient response of the hydrogel to an increase and decrease in the applied pressure.

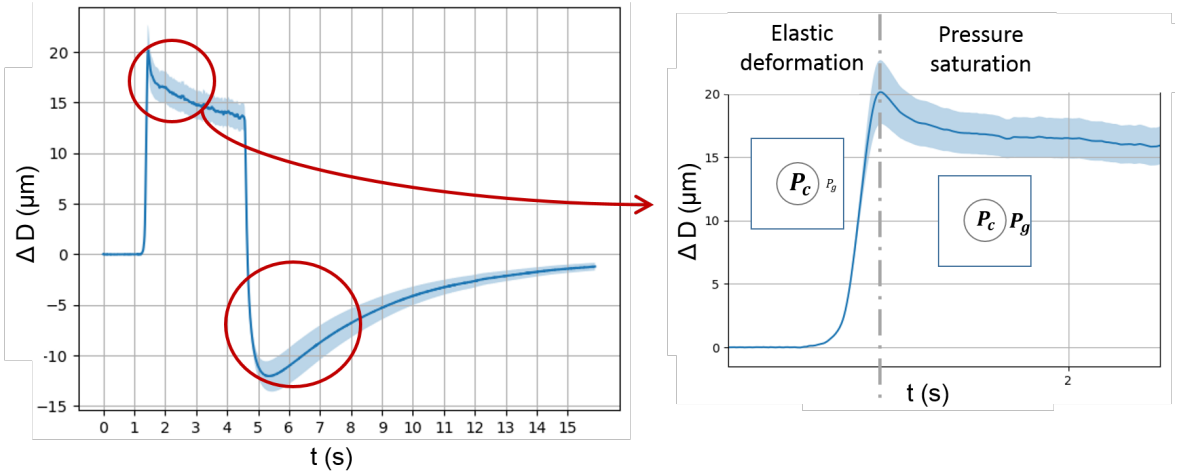

FIGURE 3.4: Representative trace of the variation of the channel diameter as a function of time during a pressure step (left), with the overshoot and undershoot circled in orange. The two regimes, elastic and poroelastic, are indicated in the zoomed graph (right), with schematics of the lumen and gel pressures (insets).

Poroelastic time The deformation sequence can be described from the point of view of the hydrogel to better highlight the underlying physics and the presence of two regimes (Figure 3.4). During the increase in pressure, the gel first decreases in volume due to the compression; it then slowly increases in volume as it undergoes swelling due to the increasing gel pressure. During the decrease in pressure, the gel first increases in volume as the compressive load is removed, and its volume exceeds the original volume because of the previous swelling; it then decreases in volume as it shrinks backs to its initial volume due to the decreasing gel pressure. The first regime is elastic while the second is poroelastic. The movement of fluid inside the porous material equilibrates the lumen and gel pressure, creating poroelastic effects in the gel. The transition from one regime to the other is therefore dictated by the characteristic poroelastic time, which depends on the gel permeability and dimensions.

Numerical simulations Numerical simulations were run to evaluate whether the poroelastic framework was capable of reproducing the experimental observations. The gel Young's modulus was set to 2 kPa, the gel permeability to $2\text{x}10^{-14}$ m^2 and the luminal pressure to 300 Pa, corresponding to a flow rate of 10 µL min^{-1}. The results of a time dependent simulation for a pressure step are shown in Figure 3.5. The channel diameter exhibits the same "overshoot" and "undershoot" (Figure 3.5 panel A, green curve). The pressure distribution in the gel at two different time points, one at the end of the elastic phase (t = 100 ms) and one in the plateau (t = 7 s), reveals two strikingly different profiles (Figure 3.5 B). At t = 100 ms, the high pressure is localized in a thin ring near the channel border, while the bulk of the gel is at low pressure (panel Bi). At t = 7 s, the pressure has increased throughout the gel (panel Bii), leading to gel swelling and a decrease in channel diameter (panel A). The simulations validated the hypothesis of poroelasticity to explain the diameter dynamics and offered the possibility of visualizing the pressure distribution inside the gel, a quantity impossible to measure experimentally.

Influence of axial position The absolute amplitude of the "overshoot" decreased along the channel axis (Figure 3.9). The luminal pressure is higher close to the inlet because of the hydraulic pressure gradient, leading to higher gel pressure and swelling compared to positions closer to the outlet. Normalizing the curves by their maximum values showed that the relative amplitude of the "overshoot" was constant along the channel. Similarly, the amplitude of the "undershoot", i.e. gel swelling, depends on the axial position and is higher close to the inlet

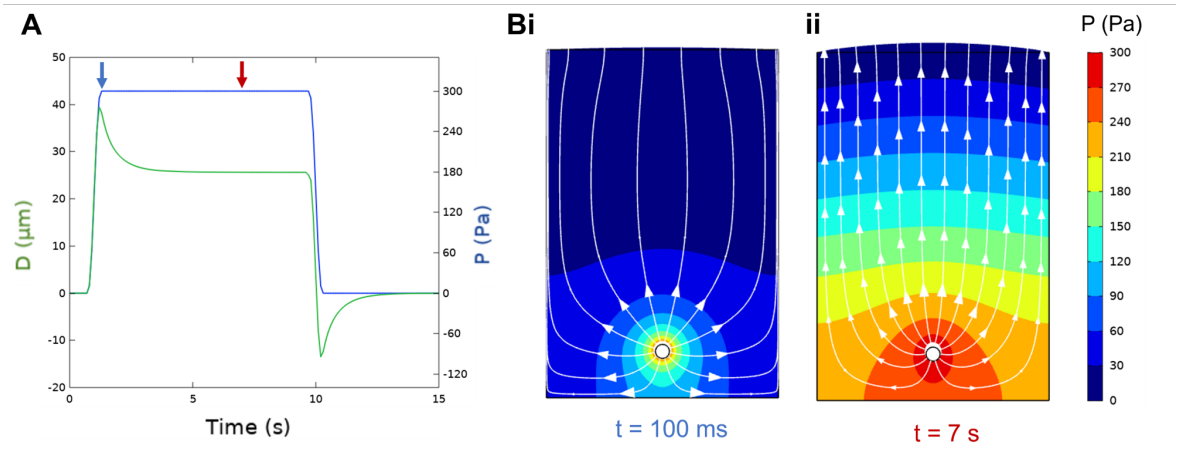

FIGURE 3.5: COMSOL numerical simulation of a poroelastic gel matching the microvessel cross-section. **A.** Channel diameter (green) as a function of time for a pressure step (blue). **B.** Pressure maps (rainbow coloring) at t = 100 ms (i) and t = 7 s (ii), with the porous flow streamlines overlayed in white.

(red and purple) and lower close to the outlet (blue and green, Figure 3.6). The gel pressure follows the same axial gradient as the lumen pressure, leading to different axial swelling and thus reduction of the channel diameter after unloading.

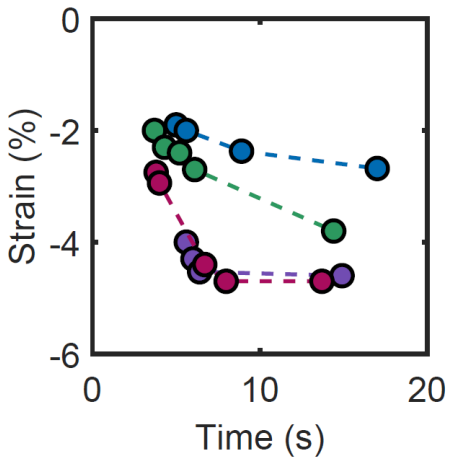

FIGURE 3.6: Amplitude of the undershoot as a function of load time for two different axial positions: close to the inlet (red and purple) and close to the outlet (blue and green). Dashed lines are guides for the eyes.

Gel pressurization Varying the duration of the step should alter the dynamics, in accordance with the gel swelling theory. For longer steps, the pressure can reach complete equilibrium, while for shorter steps, the gel pressure might not have the time to increase to its final equilibrium value. As a result, the "undershoot", i.e. the gel swelling is expected to be smaller for short pressure steps because the gel pressure is lower. This was observed experimentally by plotting the maximum negative strain (the height of the "undershoot") as a function of the step length. The results indeed showed higher negative strains for longer steps (Figure 3.6).

3.3.2.2 Ramps

I decided to change the loading rate, i.e. the experiment's characteristic time, to further test the idea that the "overshoot" was due to poroelasticity. Because the load increase in the step experiment was fast, with a characteristic time well below the poroelastic time, I was able to observe the quick elastic response. The gel was still at low pressure during the compression before the pressure had propagated into the gel. In contrast, if the load is increased slowly, the lumen pressure and gel pressure should be constantly equilibrated, and the gel would thus progressively deform in a quasi-steady state manner.

Experiments The results from the ramp assay are shown in figure 3.7 and confirm the poroelastic hypothesis. The height of the "overshoot" decreased with decreasing loading rate until it completely disappeared for the slowest ramp. The steady-state equilibrium position was independent of the loading rate. The diameter decrease due to the poroelastic swelling followed the same exponential curve for all loading rates. Fitting the decrease with a simple exponential gave the same characteristic time as the single step test, a couple of seconds.

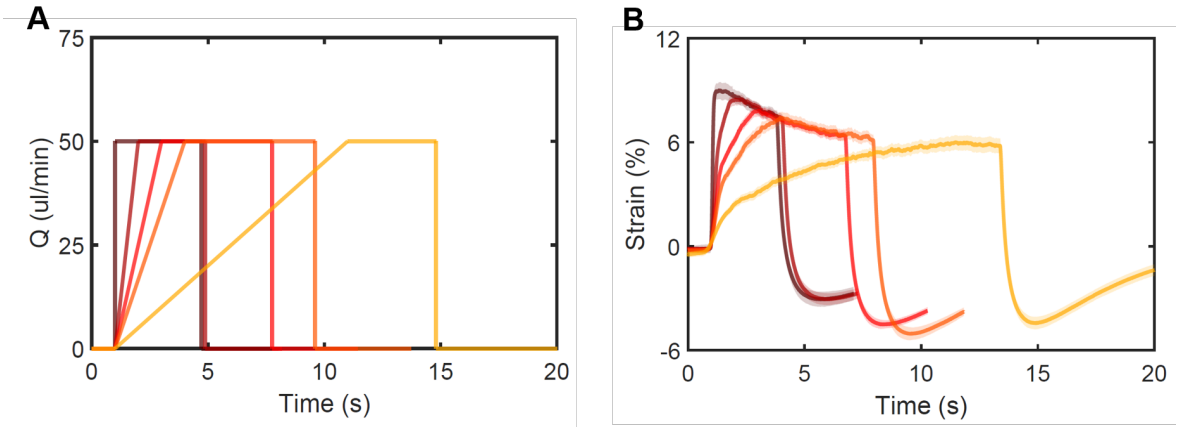

FIGURE 3.7: Deformation of the channel as a function of time for different loading rates (color coded). The imposed flow rate is shown in panel A. The loading is progressively slower while the unloading is kept instantaneous. The response of the channel is shown in panel B, with a disappearing overshoot and an increasing undershoot.

Numerical simulations Once again, numerical simulations were run to evaluate whether the poroelastic framework was capable of reproducing the experimental observations. The numerical parameters were set to the same values as for the step simulation. The results of a time dependent simulation for a pressure ramp are shown in Figure 3.8. The channel diameter exhibits a linear increase with no "overshoot" and a sharp decrease with an "undershoot" (Figure 3.5 panel A, green curve). These two features match the experimental curves (Figure 3.7). The pressure distributions in the gel at two different time points, one in the middle of the ramp (t = 4 s) and one at the end of the ramp (t = 7 s), reveal two identical profiles (Figure 3.5 B). In both cases, a pressure gradient spans the gel, with different maximum values due to the ramp. As expected, the pressure in the gel is constantly equilibrated to the luminal pressure, with a well established porous medium flow and progressive gel swelling. Because the load was removed instantaneously to mimic the experiments, we can still see the undershoot due to the remaining gel swelling at the end of the experiment.

3.3.2.3 Effect of gel concentration: permeability

Collagen gels with lower collagen concentrations are expected to be more permeable, leading to shorter characteristic poroelastic times. Indeed, for a given pressure gradient, permeability

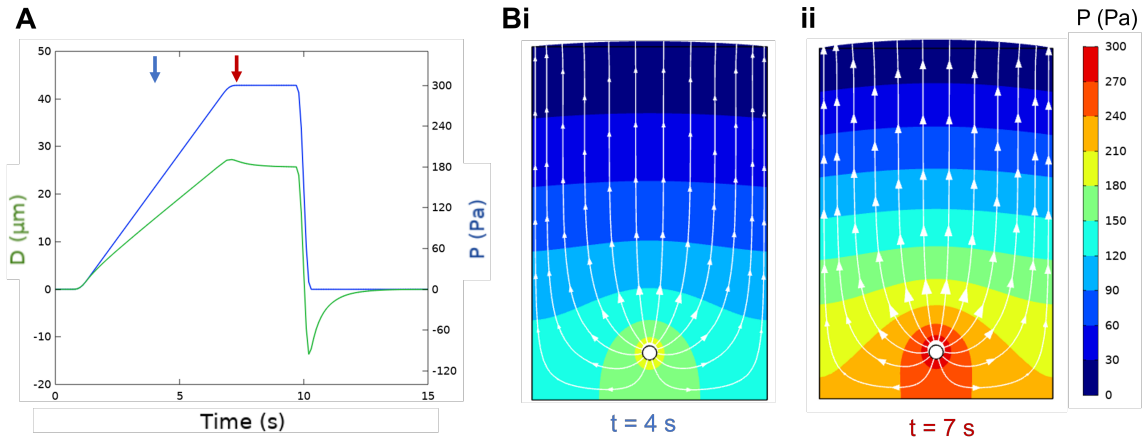

FIGURE 3.8: Numerical simulation with COMSOL of a poroelastic gel matching the microvessel cross-section. **A.** Channel diameter (green) as a function of time for a pressure ramp (blue). **B.** Pressure maps (rainbow coloring) at t = 4 s (i) and t = 7 s (ii), with the porous flow streamlines overlayed in white.

regulates the velocity of a given fluid through a porous medium, thereby affecting the time it takes to travel a given distance. Fitting the ramp experiments for a hydrogel with a collagen concentration of 4 mg/mL and a hydrogel with a collagen concentration of 6 mg/mL showed a two-fold difference in characteristic poroelastic times (Figure 3.9). The two-fold difference is consistent with the two-fold difference in gel permeability computed in Chapter 2 by fitting the flow loss to the analytical solution calculated with the analogy to an electrical circuit. This comparison confirms the validity of using the hydraulic compression assay to measure hydrogel permeability through the channel "overshoot".

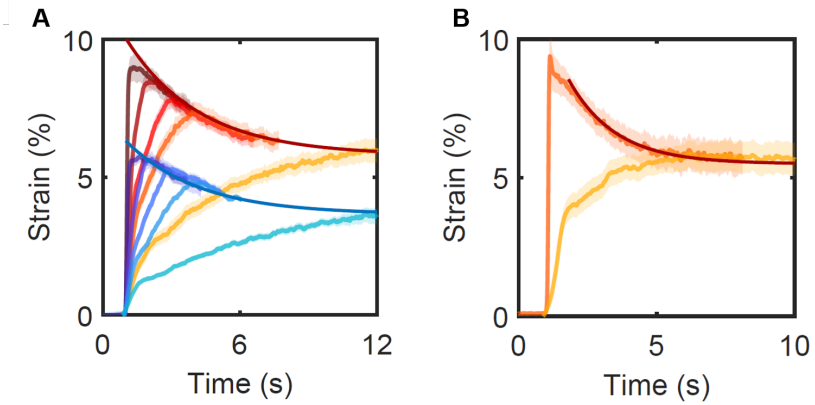

FIGURE 3.9: Exponential fits of the ramp experiments to extract gel permeability for hydrogels with a collagen concentration of 6 mg/mL (A) and 4 mg/mL (B). Warm colors indicate measurements close to the inlet, and blue colors are measured close to the outlet.

3.3.2.4 Effect of the cell monolayer

As discussed in Chapter 2, the cell monolayer acts as a semi-permeable membrane, creating a flow shielding effect. The reduced flow into the gel had important consequences for the pressure distribution, with the gel pressure being much lower in the presence of cells (Figure 3.10). Consequently, the gel did not undergo swelling, and the second poroelastic regime was not observed (Figure 3.10). The system exhibited instead a viscoelastic behavior, with a

quick increase in diameter followed by a slower exponential-like increase toward the maximum diameter. This steady-state diameter was much larger because of the absence of gel swelling.

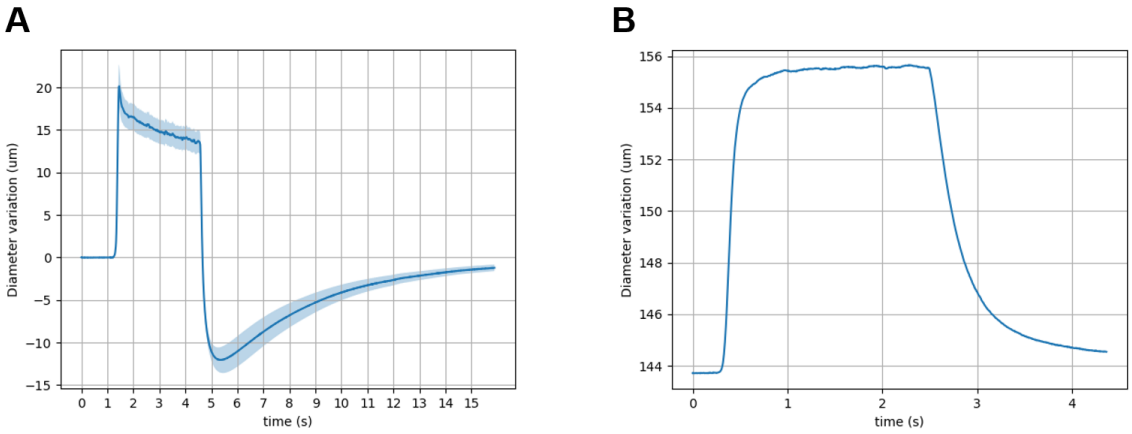

FIGURE 3.10: Representative traces of the channel diameter as a function of time without cells (A) and with cells (B).

The elastic contribution of the monolayer which would tend to reduce the channel deformation was completely concealed by the flow shielding effect. Hypothetically, if one could impose the same pressure load on a bare gel while preventing the porous flow and swelling, the channel dilation would follow the same viscoelastic response with a steady-state diameter larger than that with the cells. The difference between the two would give a measure of the monolayer stiffness. Using a fluid with a higher viscosity would increase the poroelastic time significantly, allowing the full elastic response to take place before the swelling. I plan on trying this experiment to measure the equilibrium position of the bare gel and therefore estimate the stiffness of the monolayer.

3.3.3 Discussion

The two regimes I observed constitute a well-studied characteristic of poroelastic deformations, which so far has only been investigated in compression or traction assays. If we consider the constant load compression case, after the load is applied, the poroelastic sample deforms quickly which increases the gel pressure abruptly by compressing the water in the pores. As the pressure "diffuses" out of the sample, with the characteristic poroelastic time, the sample deforms further. To illustrate the potential future studies enabled by my platform, I discuss briefly the two main differences between the compression assay and my hydraulic compression assay. First, the poroelastic effect contributes in opposite manners in the two assays. In the compression, the pressure equilibrium increases sample deformation. In contrast, in the hydraulic compression, the pressure equilibrium opposes sample compression through swelling. The second difference is the moment when we can measure the "true" Young's modulus of the gel. In the compression assay, this would occur after a longer time period when the gel pressurization has been dissipated, while in the hydraulic compression, it would be at the very beginning of the experiment before the gel has been pressurized by porous medium flow. Overall, hydraulic compression as described in a couple of analytical studies can now be tested experimentally with this novel platform [156–158]. Complex dynamics due to the double boundary load, both solid and fluid, are expected to appear, and if unraveled would further our understanding of poroelasticity.

3.4 Strain distribution in the hydrogel

Once it became clear that the hydrogel itself exhibited a complex mechanical deformation pattern, I decided to investigate the distribution of strain in the whole gel and not only at the channel border. One observation that remained unexplained by my project so far was the axial displacement of the channel after a pressure step. Indeed, from the experiments presented in Chapter 2, I was able to see a small shift in the channel's axial position, in particular close to the inlet. After I verified that it was not due to partial gel delamination from the PDMS wall, I identified two possible sources for this displacement: an anisotropic poroelastic gel swelling due to the luminal pressure gradient, or a fluid-structure interaction due to the shearing forces of the fluid flow.

3.4.1 Methods

3.4.1.1 Mapping the gel displacement field

Polystyrene beads, 1.7 microns in diameter, were suspended in the collagen solution at very low density to serve as displacement trackers. The polymerization encased the beads, which were too big to pass through the gel pores, thereby ensuring a precise displacement field reconstruction. A live movie was recorded in a large field of view using a 10X objective to include both the channel edges and a gel portion close to the lateral PDMS wall. After a similar image processing step as the one described in Chapter 2 (removing the background and inverting the images to have white beads), the beads were automatically detected and tracked using the ImageJ plugin Trackmate (Figure 3.11) [159]. The individual bead trajectories can be overlayed on the original movie, and average displacement curves can be computed from these trajectories. I divided the image into axial stripes and calculated the radial displacements as a function of the radial position. The same was done in radial stripes to compute the axial displacement as a function of the axial position.

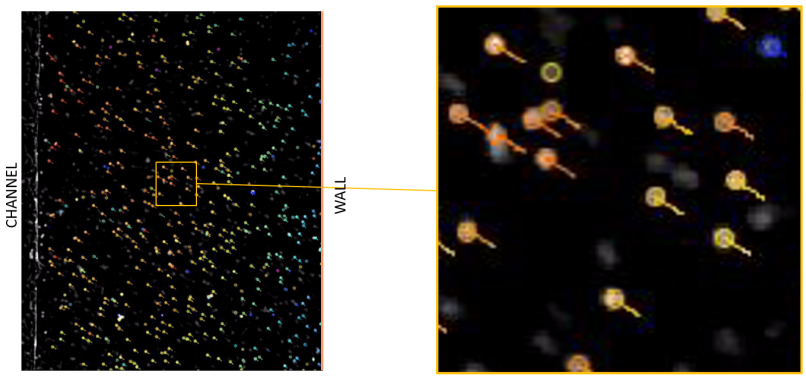

FIGURE 3.11: Illustration of the tracking process showing detected tracks for each bead, color coded for their total displacement.

3.4.1.2 OCT for cross-sectional view

Brightfield imaging is limited to the deformation in the horizontal plane. To assess vertical deformations and visualize the channel cross-section during deformation, I used optical coherence tomography (OCT) imaging (also presented in Chapter 2). The channel deformation was recorded during a flow step at 37 fps. The images were then processed using a custom-made MATLAB code to extract the channel outline for each time point. Briefly, the code performed image pre-processing, binarization and ellipse detection. From the outline,

the horizontal and vertical diameters were plotted as a function of time, in addition to the channel circularity and center position.

3.4.2 Results

3.4.2.1 Radial displacement

The first question I had was whether the gel deformation was present throughout the gel, as expected for an elastic material, or localized only close to the channel. Tracking the bead displacement showed that the entire gel was compressed, with detectable bead motion even close to the PDMS wall (Figure 3.12 A). Although the radial displacement decreases with axial position (see Chapter 2), the decline was not significant in these recordings due to the short length of the channel that was imaged (determined by the field of view of the microscope objective). Consequently, the movements of the beads could be averaged axially to interpolate the displacement as a function of the radial position (Figure 3.12 B). The radial displacement decreased with radial position from the channel edge to the PDMS wall, following a hyperbolic curve, as predicted in a cylindrical geometry (Figure 3.12 B, top line).

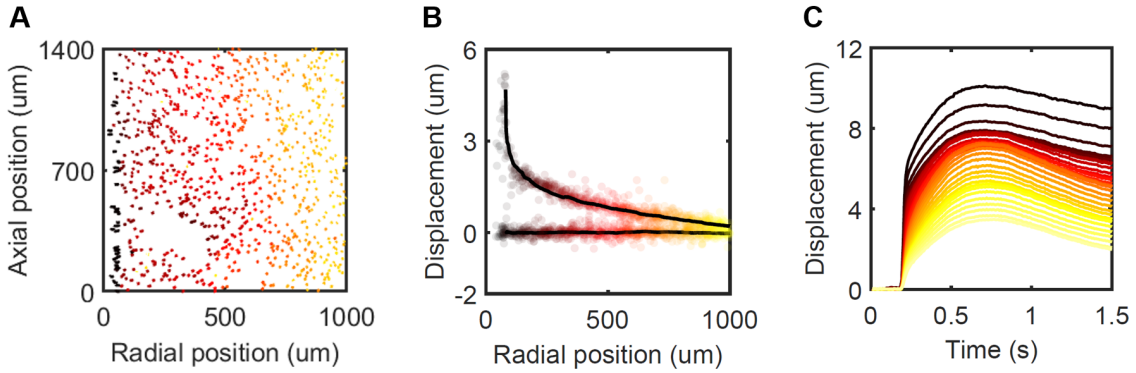

FIGURE 3.12: **A.** Map of the hydrogel strain derived from the individual bead displacement tracks, color coded for their total displacement. The channel axis is vertical, with the channel on the left and PDMS wall on the right. **B.** Examples of the interpolation on the instantaneous radial strain as a function of the radial position, averaged along the axial direction. **C.** Radial displacement as a function of time for various radial positions inside the gel (color map). In all panels, black is close to the channel and yellow close to the gel fixed boundary.

Interestingly, the radial displacement showed three regimes exhibited by the channel dilation (Figure 3.12 C): (1) an instantaneous hyperbolic compression (beads move toward the wall), (2) a fast propagation of the pressure wave into the gel, creating swelling of the gel and compression of the unpressurized gel (beads move further toward the wall), and (3) overall swelling of the whole gel with increasing pressure once the wave reaches the wall (beads move back toward the channel). Steps (1) and (3) correspond to the two regimes observed in the channel described in the previous section.

3.4.2.2 Axial displacement

The second question I had was the origin of the axial displacement of the gel. A longitudinal movement of the gel was clearly visible (although not quantified) in the channel dilation experiments and in the diagonal trajectories of the beads in the strain distribution experiment (Figure 3.13 A).

Axial gradient of the gel pressure Plotting the axial displacement as a function of time for different radial positions showed a single displacement curve (Figure 3.13 B). In contrast, plotting the axial displacement as a function of time for different axial positions showed gradually increasing displacement curves (Figure 3.13 C). As discussed in the previous section, the pressure gradient present in the lumen creates an axial pressure gradient in the gel and therefore a gradient in gel swelling. The portion of the gel close to the inlet swells more than the gel close to the outlet, creating a macroscopic longitudinal displacement of the gel toward the outlet, explaining the increasing displacement curves shown in panel C. Finally, the pressure is constant for all radial positions at a given axial position, which explains the single displacement curve shown in panel B.

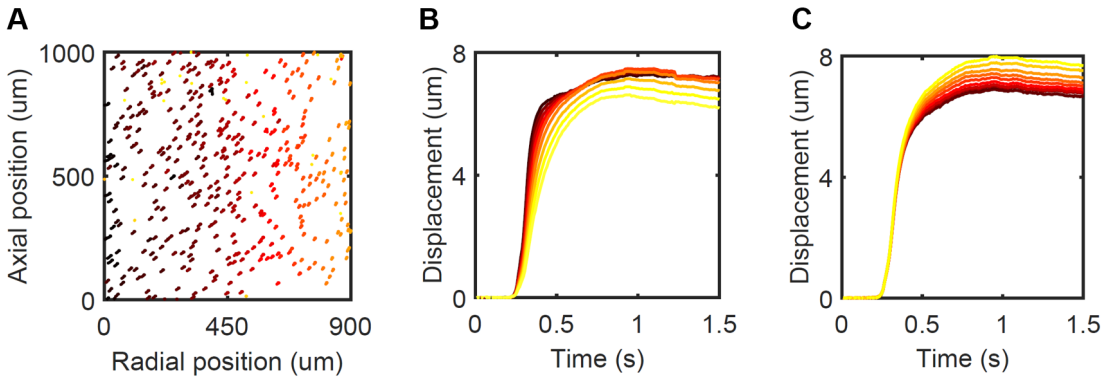

FIGURE 3.13: **A.** Map of the hydrogel strain derived from the individual bead displacement tracks, color coded for their total displacement. The channel axis is vertical, with the channel on the left and PDMS wall on the right. **B.** Axial displacement as a function of time for various radial positions inside the gel (color map, black is close to the channel, yellow close to the gel fixed boundary). **C.** Axial displacement as a function of time for various axial positions inside the gel (color map, black is toward the inlet, yellow towards the outlet).

Numerical simulations During this project, I supervised another student intern, Clara Deslypere, on the numerical aspects of the problem. Clara investigated whether fluid-structure interactions, namely viscous friction of the fluid on the gel, or poroelasticity, could explain the axial displacement. Her results showed that viscous shearing only moved a thin layer of the gel, and the amplitude and characteristic time were not compatible with the experimental measurements. In contrast, a gradient of poroelastic swelling of the gel (due to the hydraulic pressure gradient in the lumen) matched the behavior observed in the channel. Amplitudes of displacements due to poroelasticity were ten times larger than those generated by fluid-structure interactions, showing the importance of taking poroelasticity into account when investigating hydrogels, especially for large scale movements.

3.4.2.3 Vertical displacement

Another consequence of the gel poroelasticity is the vertical motion of the channel, visible with OCT (Figure 3.14 left and center panels). Because pressure is higher below the channel than above the channel (due to the closed boundary at the bottom vs. the open top), the gel under the channel swells considerably, pushing the channel upward. The fact that this motion is slow, with the same characteristic time as the "overshoot", shows that it is due to poroelastic effects and not a simple boundary effect in an elastic material. Numerical simulations with COMSOL recapitulated the same slow upward motion (Figure 3.14, right panel). Fitting the vertical trajectory of the channel center would be another method to

calculate gel permeability.

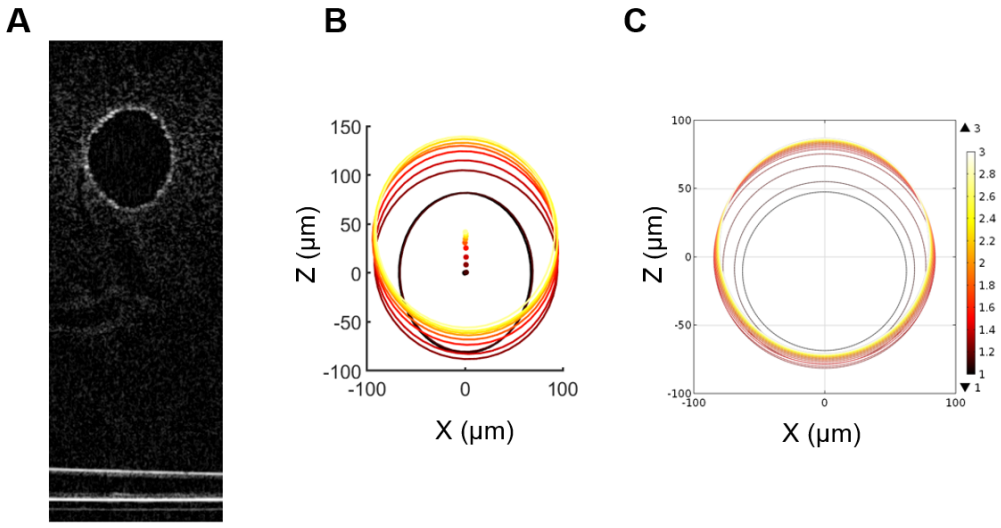

FIGURE 3.14: **A.** Typical image obtained with OCT showing the channel cross section (fuzzy white contour) and bottom glass slide (straight white line). **B.** Experimental channel cross section and position of its center as a function of time (color code), obtained from the OCT imaging. **C.** Simulated channel cross section and position of its center as a function of time (color code), obtained from COMSOL calculations.

Similarly, when the channel was not centered horizontally but instead positioned one-third/two-third from the walls, I was able to observe a horizontal movement of the entire channel away from the closest wall. The movement followed the same time course as the vertical movement, with the characteristic poroelastic time. The movement was due to increased swelling of the gel on the side closest to the wall, with higher pressure compared to the gel on the other side.

3.5 Wave propagation

Pulse wave propagation has faster dynamics than the phenomena presented above, on the scale of milliseconds, whereas the poroelastic time is on the orders of seconds. The propagation of waves in hydrogels is rarely studied, and several questions remain unanswered. Does poroelasticity intervene in wave propagation? Or do hydrogels behave as elastic materials?

3.5.1 Longitudinal waves in the poroelastic channel

The longitudinal propagation of waves has been extensively described in the case of an elastic thin wall to model pulse wave propagation in blood vessels. The pulse wave velocity (PWV) has been shown to depend on vessel stiffness, which is proportional to the square root of the vessel's Young's modulus. Measuring the PWV has even been used as a method to compute vessel wall compliance. How the PWV is affected by poroelasticity remains unclear. I decided to do a couple of preliminary tests in the microvessel as a proof-of-concept of the possibilities offered by the platform.

3.5.1.1 Methods

To detect the longitudinal wave propagation, I recorded the channel dilation with 4X and 10X objectives to image a long section of the channel. Channels walls were first saturated with beads (by flowing beads in the channels for a couple minutes) to improve edge detection at low flow rates. Then, a flow step was applied with the syringe pump, leading to channel dilation. Replaying the movie revealed a transient conical shape along the length of the channel when the inlet had already dilated and the outlet had not. To quantify the propagation, I used Clickpoints and automatically tracked the position of the channel edges at several regularly spaced points along the channel's longitudinal axis (Figure 3.15, top image). Plotting all the dilations showed a clear spread of the onset times, correlating with the axial position (Figure 3.15, left and center panels). Dilation curves were then normalized by their maximum value. By setting a threshold displacement, I detected the onset time for each curve, which was then plotted as a function of position. Onset time was linearly dependent on position (Figure 3.15, right panel). The velocity of the propagating wave, i.e. the pulse wave velocity (PWV), was equal to the inverse of the fitted slope's coefficient.

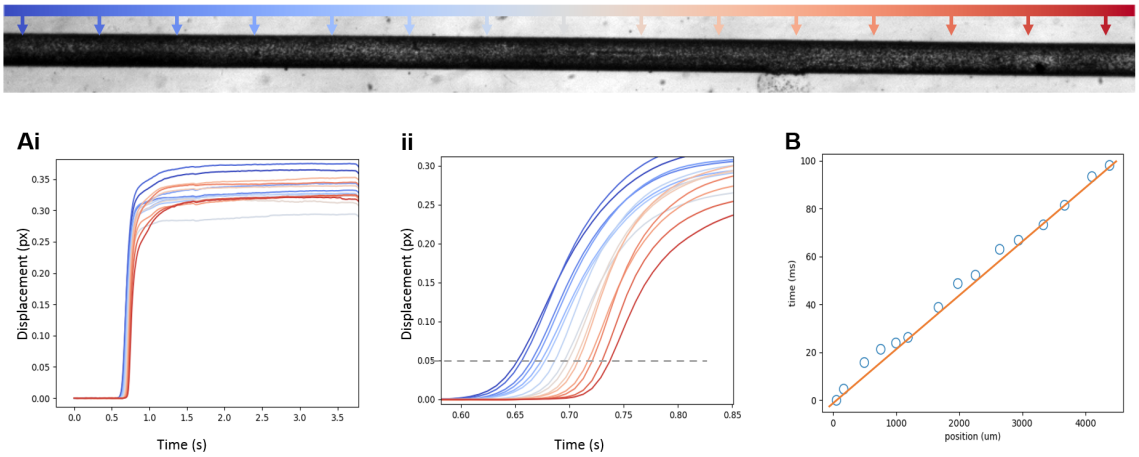

FIGURE 3.15: Illustration of the process of PWV calculation. The top image shows a typical bright-field image used for automated tracking, with the different tracked position (colored arrows). **A.** Channel displacement as a function of time for different axial positions (i), with a zoom on the earliest time points to show the clear time shift among positions (ii), with the threshold value used to detect the onset time (dashed gray line). The colormap denotes the axial position, blue being toward the inlet and red towards the outlet, as shown in the top image. **B.** Onset time as a function of the axial position (dots) showing a linear dependence (orange line).

3.5.1.2 Results

The linear relationship between onset time and axial position was quite consistent across experiments, and the fitted slope was not too sensitive to the threshold value. The PWV was found to be on the order of 0.1-1 m/s, around 10 times smaller than PWV in the blood vessels (typically around 5-10 m/s).

Amplitude dependence The PWV was strongly dependent on the amplitude of the pressure step, in contradiction to the elastic wave propagation theory. Waves of high amplitude propagated significantly faster than those with lower amplitudes (Figure 3.16 A). It is important to note what "amplitude" refers to. Indeed, plotting the PWV as a function of the flow rate showed a bilinear dependence (Figure 3.16 Bi), whereas plotting the PWV as a function of the deformation amplitude showed a linear dependence (Figure 3.16 Bii).

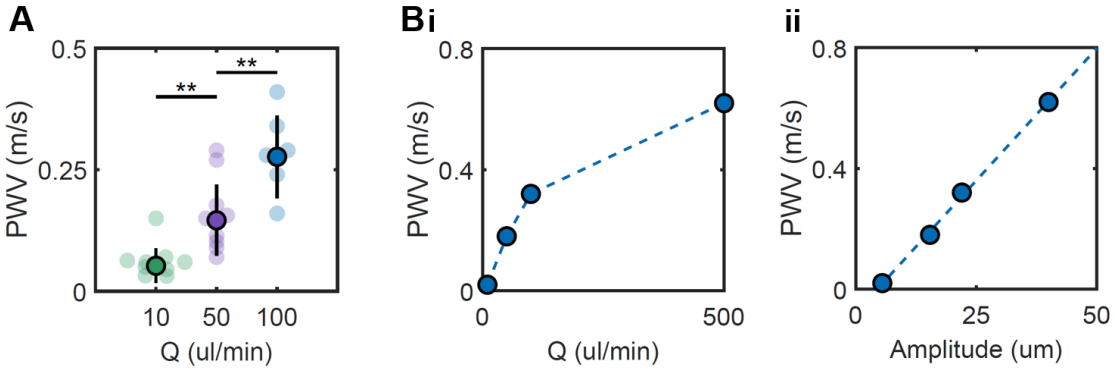

FIGURE 3.16: **A.** PWV as a function of the imposed flow rate. **Bi.** PWV as a function of the imposed flow rate. **Bii.** PWV as a function of the amplitude of the deformation.

Gel stiffness As the gel microstructure affects both the Young's modulus and permeability, it is expected to modify the PWV. Stiffer hydrogels (purple), i.e. ones that showed smaller strain for the same luminal pressure, had on average higher PWV than softer hydrogels (blue, Figure 3.17 A). This result is consistent with the elastic wave propagation theory that postulates that velocity increases with stiffness. The role of permeability is still unclear, as there is no theoretical framework for the propagation of a pulse inside a poroelastic material.

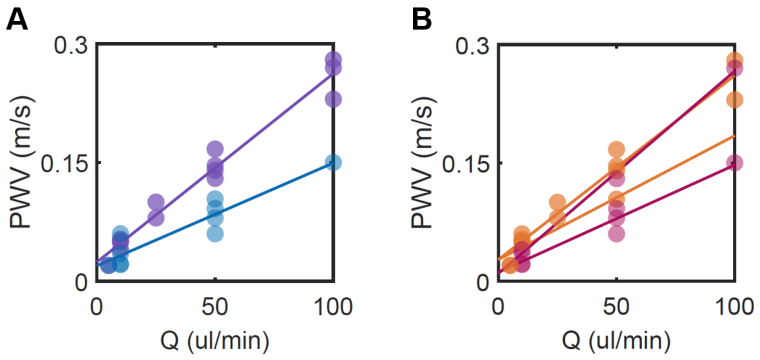

FIGURE 3.17: **A.** PWV as a function of the imposed flow rate for two different collagen batches of the same concentration but one stiffer (purple) than the other (blue). **B.** PWV as a function of the imposed flow rate with (orange) and without (pink) cells.

Effect of cells The contribution of the cellular monolayer was more difficult to anticipate. The addition of a stiff thin film would be expected to accelerate wave propagation, while the flow shielding effect would decrease gel pressure and thus decrease the apparent gel stiffness, reducing the wave propagation speed. PWV of endothelialized channels (orange) had largely similar values to that in bare channels (pink) (Figure 3.17), possibly because the two effects roughly balance one another. Interestingly, the linear relationship between onset times and axial position was consistently more noisy for endothelialized channels. This could be due to heterogeneity of the monolayer, creating local heterogeneities in the stiffness and thus in the PWV.

3.5.1.3 Discussion

My current working hypothesis for the amplitude dependence, based on a poroelastic effect, is as follows: larger wave amplitudes generate higher strain rates, under which poroelastic materials are known to have a higher apparent stiffness. This effect is due to the pore pressure and deformation coupling, when the fluid in the pores becomes highly pressurized (due to its incompressibility). The fluid-pressurized pores would resist deformation until the fluid has time to flow out, with a characteristic time that depends on the material's permeability. In a purely elastic tube, higher stiffness is associated with faster waves. To sum up, large amplitudes increase the effective stiffness of the gel through a poroelastic effect, which increases wave velocity.

One of the aims of the collaboration with the group at Inria (see Chapter 5) is to elucidate the mechanism behind the amplitude dependence and to validate the experimental observations and hypothesis. Extending the framework of pulse wave propagation from simple elastic vessels to poroelastic vessels is one of our goals.

3.5.2 Radial compressive waves in the poroelastic hydrogel

Another type of waves that could be detected in the channel, and that constitute an active field of research, are radial compressive waves. As the pressure propagates radially from the channel into the gel, it creates a deformation wave. Compressive wave velocity could be measured by analyzing the dynamics of the strain field in the gel.

3.5.2.1 Methods

The velocity of the compressive wave propagation in the gel can be extracted from the averaged radial displacement curves described in section 3.5. After normalizing the displacement curves, a threshold can be set to calculate the onset time for each radial position (Figure 3.18 Ai). By plotting the onset time as a function of the radial position, we show a linear dependence, as expected (Figure 3.18 Aii).

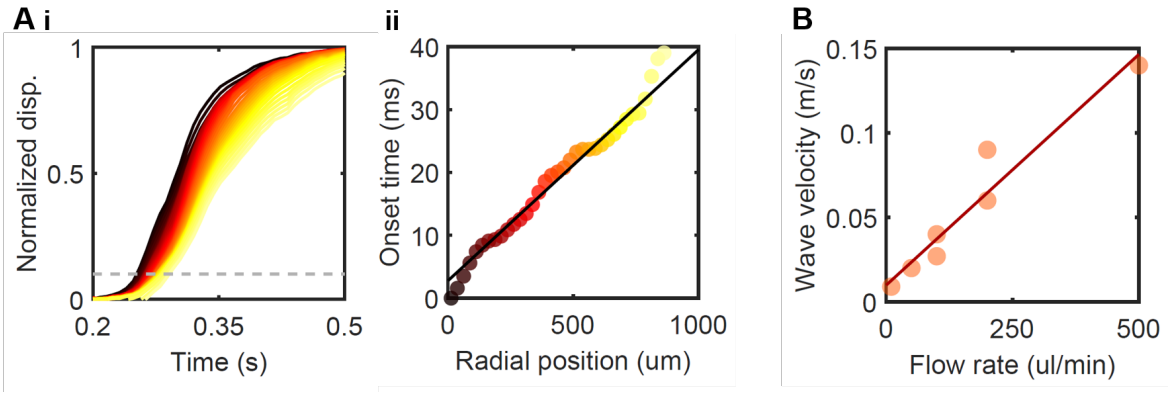

FIGURE 3.18: Illustration of the process of wave velocity calculation. **A.** Normalized displacement as a function of time for different radial positions, with the threshold value used to detect the onset time (dashed grey line). **B.** Onset time as a function of the radial position (dots) showing a linear dependence (black line). In panels A and B, the colormap denotes the radial position, black being close to the channel and yellow close to the wall. **C.** Wave velocity as a function of flow rate of the imposed step (dots) showing a linear dependence (red line).

3.5.2.2 Preliminary results and discussion

The radial or compressive wave velocity was of the same order of magnitude as the PWV. Interestingly, it also seemed to depend on the amplitude of the wave (Figure 3.18 B). These results remain preliminary and need to be validated in repeat experiments before drawing definitive conclusions. However, they already demonstrate the feasibility of the experiment. Wave propagation is an ongoing field of research in poroelastic materials and has yet to be applied to soft hydrogels. The impact of defects on the wave propagation is of particular interest in this field and could readily be investigated in this setup by suspending air bubbles, hard beads or even soft spheroids of various sizes within the gel.

3.6 DMA, viscoelastic or poroelastic?

The last proof-of-concept experiment I want to present is this chapter is that on dynamic mechanical analysis (DMA). DMA consists of imposing a sinusoidal stress (or strain) on a sample at a given frequency and measuring the resulting strain (or stress) as a function of time. For a viscoelastic material, the ratio of the amplitudes would be proportional to the Young's modulus, while the phase shift would be proportional to the viscosity.

3.6.1 Methods and preliminary results

The methods for the DMA experiment have already been presented in Chapter 2, as it is based on channel dilation recording, automated diameter tracking and PTV. The circumferential strain was computed from the channel diameter changes by normalizing the instantaneous diameter by its initial diameter. The stress, in this case the applied pressure, was assumed to be proportional to the flow velocity in the channel. By overlaying the strain and velocity sinusoidal tracks and adjusting the left and right y-scales so the amplitudes of each sinusoid match, a clear phase shift appeared (Figure 3.19). This phase shift is proportional to the viscosity of the gel. This semi-quantitative approach permits comparison of viscosity among different conditions by measuring the increase or decrease of the phase shift.

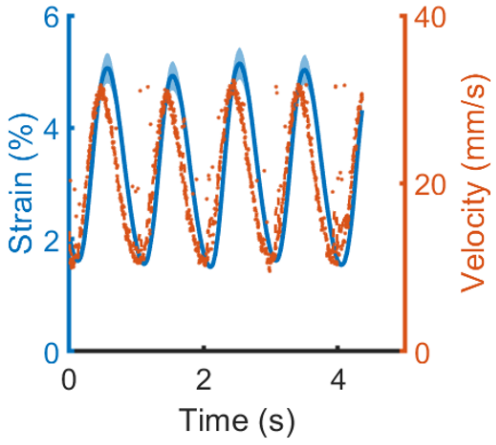

FIGURE 3.19: Channel strain (blue curves) and flow velocity (red dots) as a function of time showing a phase shift.

3.6.2 Discussion

The preliminary test shown above demonstrates the feasibility of the DMA experiment. By repeating it under different conditions, such as with and without cells or for different amplitudes, gel concentrations and gel widths, we should be able to measure the influence of these various parameters on the viscosity. Of note, the DMA framework was developed for a viscoelastic material. Whether it can still be used in the case of viscoporoelasticity, or even if poroelasticity would alter the material response and dominate over viscoelasticity, warrants further investigation.

3.7 Discussion and conclusions

In this chapter, I presented a catalog of different mechanical tests that all underscore the poroelastic behavior of the hydrogel. Each assay can be used to derive the poroelastic parameters of the hydrogel. Although preliminary, these results demonstrate the versatility of the microvessel-on-chip as a mechanical testing platform and the numerous applications of the hydraulic compression assay. In various discussions, researchers from the fields of poromechanics and biomaterials expressed interest for this system. The level of control and simple geometry were particularly attractive to theoretical and numerical researchers and were considered very useful for validating new models and predictions. Finally, I would like to highlight the importance of poroelasticity to understand the mechanics and dynamics of hydrogels, as evident from all the results presented above. This exploratory work that started as a side project ended up being crucial for understanding the cellular response to stretch presented in the next chapter, which links complex materials mechanics to monolayer behavior and cell mechanobiology.

Chapter 4

Endothelial cell response to tensile stresses

> The important thing is not to stop questioning. Curiosity has its own reason for existence. One cannot help but be in awe when he contemplates the mysteries of eternity, of life, of the marvelous structure of reality. It is enough if one tries merely to comprehend a little of this mystery each day.
>
> *Albert Einstein - 1995*

4.1 Introduction

4.1.1 Cells & stretch

This chapter begins with a review of the literature on cell response to stretch. In the following sections, I will first discuss the response of ECs to cyclic strain, followed by the response of epithelial monolayers to tensile stresses, because little information on this topic is available for ECs. I will close by presenting the cellular mechanisms involved in these processes and the theory of tensional homeostasis.

Before delving into cellular responses, it is essential to be clear on the definition of the three key terms: "stretch", "strain" and "tension". The term "stretch" refers to the action of pulling on a sample. The term "strain" refers to the normalized change in length of the sample. The term "tension", or "tensile stresses", refers to the force field present in the sample. Consequently, stretch systematically generates both strain and tension inside a sample. In most of the stretch experiments in the literature, the stretch imposes a given strain by controlling the sample length, which creates internal stresses whose magnitudes depend on the sample's Young's modulus. This is in a sense equivalent to the relaxation test described in Chapter 2. However, stretch can also impose a given tension level, by controlling the applied force, which creates a level of strain that once again depends on the sample's Young's modulus. This is in essence equivalent to the creep test described in Chapter 2.

Stretch at imposed tension is mostly found in the field of morphogenesis, when studying cell behavior in embryos. In the embryo, there is very little ECM [160], and tension on the tissue can be relatively easy to infer from the strain field through the tissue stiffness. In the adult, in contrast, there is extensive ECM which complicates the link between strain

and tension as the tension is distributed between the stiff ECM and the cells. For instance, in the case of the vasculature, circumferential (hoop) stress due to the transmural pressure difference that dilates the vessel is linked to circumferential strain through wall stiffness. Although circumferential strain is measured by simply recording diameter changes, assessing vessel wall stiffness remains a challenge [161, 162]. Moreover, separating the contribution of each layer of the vessel wall to isolate the tension in the endothelium is virtually impossible. Consequently, most studies on ECs focus on strain, where the goal is to match physiological levels.

4.1.1.1 ECs & strain

Mechanism Cytoskeletal reorganization in cells under cyclic strain precedes changes in overall cell orientation: after only 15 minutes of cyclic stretch, the cytoskeleton exhibits an alignment perpendicular to the direction of strain [163–166], whereas several hours are necessary to reach whole cell reorientation [167,168]. Disrupting the cytoskeleton or preventing its reassembly using pharmacological reagents abrogates cell reorientation in response to stretch [163,169]. Furthermore, cell contractility was shown to be necessary for the cytoskeletal reorientation that precedes cell reorientation [168].

To reorient, actin stress fibers disassemble prior to reassembling in the new direction [165, 170]. The dynamics of stress fiber remodeling are mirrored by the cell traction forces measured by traction force microscopy: after a sudden increase due to the stretch, traction forces decrease to almost zero, then increase again, transverse to the stretch direction [168]. ECs have been shown to sense stretch through ECM deformation: integrins are part of the mechanosensing pathway [171] and focal adhesions are necessary to induce cell and cytoskeleton reorganization [172]. Additionally, a release of tension, as occurs following stress fiber disassembly, is known to cause focal adhesions to disassemble [173], consistent with traction forces vanishing.

Stretching the cell substrate increases tension in the actin cytoskeleton [174]. When the tension is stress fibers exceeds a "stability threshold", existing stress fibers are disassembled and new stress fibers are prevented from forming [175]. Stretch has also been reported to increase cell stiffness [174, 176], and cell stiffness has been shown to depend on cytoskeletal tension [177].

Tensional homeostasis The dominant theoretical framework to explain the transverse alignment in the literature is that stress fibers respond to stretch by orienting in the direction that minimizes tension (Figure 4.1, green arrows) [178]. The tent-like structure of stress fibers observed under biaxial stretch [167] is consistent with this model since the minimum tension orientation in this case is the out-of-plane orientation [179]. Interestingly, another framework has been proposed to model the same experimental observation. This model postulates that stress fibers exist only if their strain does not exceed a 5% threshold, which effectively prevents fiber orientation in the stretch direction (Figure 4.1, purple crosses) [178]. This description is based on strain instead of stress and is consistent with experiments showing the initial orientation of single cells modulates their response: cells oriented at 45°were shown to not reorient under stretch [180].

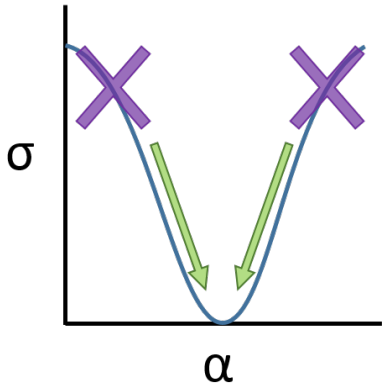

FIGURE 4.1: Schematics of the two theoretical framework modeling EC orientation transverse to the strain direction, through tension minimization (green arrows) or the stress fiber stability threshold (purple crosses).

The theory of tension minimization has been evoked
to explain the effect of strain waveform as well as the effect of pharmacological agents that interfere with cytoskeletal contractility. Tension modeling predicts that high rates of substrate lengthening generate greater average stress fiber tension than fast shortening [181]. This would explain the amplified cell response to physiological waveforms that exhibit fast lengthening and slow shortening. Inhibition of cytoskeletal contractility leads to impaired cell reorientation [180], presumably because it reduces cytoskeletal tension. In contrast, increased contractility amplifies EC reorientation, with a response even for strains as small as 1% [182].

4.1.1.2 Monolayers & tensile stresses

Because traction forces play an essential role in morphogenesis, the study of epithelia under tension has attracted significant attention. Conversely, much less research has focused on the effect of traction forces on ECs. In the developing embryo, tissue mechanics are driven principally by the cell contribution. As a result, stretch studies on epithelia focus on tension rather than strain (see the preamble). Because tension is of particular interest for this chapter, I will briefly review the literature on epithelia and tensile stresses in what follows.

Maintenance of monolayer physical integrity A critical feature of cellular monolayers is the presence of cell-cell junctions, which are absent in the case of single cells. The response of ECs to stretch in all the studies presented above was postulated to occur through FAs and the cytoskeleton. In contrast, cell-cell junctions, and in particular adherens junctions, have been shown to be essential in monolayer response to stretch [160, 183, 184]. Tension has been shown to regulate the size of adherens junctions in epithelial cells [185]. Adherens junction remodeling is thought to occur in order to protect the physical integrity of monolayers against external tensile stresses [9, 10, 186]. Interestingly, the force to break cell-cell junctions has been estimated to be around 2 µN in monolayers, 9 times higher than in cell doublets [187], illustrating the role of junction remodeling in monolayer mechanics.

Stress dissipation The concept of tensional homeostasis has also been applied to monolayers, although it has been formalized differently. The classical hypothesis for monolayers is the notion of stress dissipation via two mechanisms: (1) elongation of the cells in the direction of the strain, and (2) a directional proliferation. Both end in reducing the tension in the tissue. The elongation happens at shorter time scales (few hours) compared to proliferation (tens of hours).

(1) In tissues, the application of stretch induces elongation of cells in the strain direction [160], in contrast to the transverse alignment found in single cells. Indeed, because adherens junctions enable the propagation of tension from one cell to another [188], the strategy of perpendicular orientation does not reduce cellular tension. Instead, by elongating in the strain direction, cells redistribute the available material and reduce the tension [160]).

(2) Stretch also increases proliferation [189], with the cell divisions being oriented in the direction of the strain [190, 191]. Interestingly, it has been shown that the stretch itself, but also the cell elongation (induced by the stretch) are capable of orienting cell division. When there is a competition between the direction of the cell elongation and the strain direction, the direction of cell division will be dictated by the direction of the cell [190]. The resulting increase in cell mass in the stretch direction reduces tissue tension and restores cells back to a cuboidal shape [160].

4.1.2 Open questions

Endothelium & tension Most of the studies on ECs to date have been conducted on single cells plated on stiff membranes. The very few studies that use confluent ECs report differences

compared to single cell studies (see Section 1.4), underscoring the importance of collective behavior in mechanobiology. Similarly, the few reports on stretch on soft substrates show different responses depending on substrate stiffness. The tensile stresses in the monolayer can be expected to depend on the substrate properties: as the substrate gets softer, the load is progressively transferred to the cells. Would endothelia behave similarly to epithelia under high tension? How similar are their underlying mechanisms, both junctional and cytoskeletal?

Imposing constant tension In all the aforementioned studies, the mechanical constraint imposed on the cells in vitro is the strain induced by changing the length of the system. Even in the monolayer studies that discuss monolayer "tension" and "external tensile stresses", the imposed constraint is the strain. The only system that enables direct application of constant tension on cells is the suspended monolayer by Charras' team [187]. However, as the cells are suspended and do not have an underlying BM, they lose their polarity after a few hours [192]. Studying long term monolayer remodeling, adaptation under tension, and the mechanism(s) underlying stress dissipation are, to the best of my knowledge, impossible in today's in vitro platforms. How would cells under constant stress behave? What mechanism of minimization would they employ when tension is imposed and cannot be dissipated? How would our current understanding of tissue mechanics and the theory of tensional homeostasis evolve with these new data?

4.1.3 Objective & Rationale

I focused on tackling these open questions in the microvessel-on-chip during my last year. Indeed, my system is the first one to allow the direct application of tension on a confluent endothelium, thanks to flow actuation. Because the monolayer is grown on a soft hydrogel, it can be viewed as "a thin stiff film bound to a soft elastic substrate", as perfectly described by Harris et al. for an epithelium on a hydrogel [188]. The collagen hydrogel in my chip has a Young's modulus of around 1 kPa, while the Young's modulus of a monolayer (of epithelial cells) has been reported to be around 20 kPa [187]. The monolayer, which has a thickness of around 2 microns, is therefore an order of magnitude stiffer than the hydrogel, lending support to the stiff film on soft substrate analogy. As a result, we can expect the stress to be concentrated in the stiff thin film, which will become the load bearing layer. The tensile stress in the tissue will be imposed by the luminal pressure, which can be maintained constant, ensuring constant monolayer tension.

Based on these considerations, my plan was to subject endothelia to static tension and to investigate their response over time, both from the point of view of monolayer mechanics and cell mechanobiology. I aimed at (1) exploring the temporal dynamics of the cell response, (2) explaining this response within the framework of the mechanical minimization theory, analogous to the tensional homeostasis approach, and (3) unraveling the underlying cellular processes that cause monolayer remodeling.

A description of the detailed methods for this chapter is provided in Appendix 3. The important notion to keep in mind is that two methods were used to apply the static stretch: "flow based" and "outlet pressure based". The first method applies stretch by controlling the flow rate through the microvessel, and creates a large pressure gradient from inlet to outlet and increases the shear stress at the same time. The second method applies stretch by controlling the microvessel outlet pressure, and creates a nearly constant pressure profile, enables higher pressure values, and maintains the shear stress constant.

4.2 Results

4.2.1 Preliminary note

Although the study of endothelial response to static tensile stresses ended up being the focus of my Ph.D. (see section 4.1.3), I had initially set out to study EC response to strain. I chose to follow a chronological approach in this chapter to best present the iterative thinking process that led me to focus on tension as the key player instead of strain. As experiments unfolded and surprising results appeared, I progressively understood the mechanics at play and the fact that what I was imposing on the monolayer was a constant monolayer tensile stress and not a strain. This chronological approach also has the advantage of presenting the evidence in support of this strain-to-tension shift.

4.2.2 Channel structure under control condition

Cell shape and cytoskeletal organization result from the integration of numerous physical cues including cell density, substrate curvature and stiffness, shear stress, pressure and tensile stresses (see Chapter 1). All of these cues are present in the microvessel-on-chip, even in its baseline configuration, and they influence the cell state under control conditions. As the initial monolayer state was likely to influence the cell response and to better delineate which effect is due to the tested stimulus, I decided to first perform a careful characterization of the initial monolayer state.

4.2.2.1 Influence of cell density

Sources of experimental variability Cell density is known to affect many cellular processes including proliferation, migration, monolayer jamming, spreading area and elongation. Easy to control in 2D experiments, cell density is much more difficult to adjust in the microvessel and is one of the principal sources of chip-to-chip variability. Channel seeding was accomplished by flowing a concentrated suspension of cells into the channel and then allowing the cells to adhere to the walls for a couple of minutes. The channel was subsequently flushed to wash out any non-adhering cells (see Chapter 2 for protocol details). The outcomes of this seeding process was fairly unpredictable: a small variation in cell density in either direction would lead to either an overconfluent channel full of cellular aggregates or a sub-populated channel with so few cells that it would take days to attain confluence. Acceptable channels thus had a wide range of initial density just after seeding, which led to a wide range of cell density in the confluent monolayers at the onset of mechanical stimulation.

Characterization of the resulting cellular structure To establish a baseline for the control conditions, 6 channels were analyzed for their initial cell orientation. The cellular density was estimated by manual counting of cells from brightfield images. The results are shown in figure 4.2. Overall, low density correlated with higher elongation and cell alignment along the axial direction, while high density correlated with more round and randomly oriented cells (Figure 4.2 top images and center graphs). The actin cytoskeleton was organized in a cortical network of thin filaments in the case of dense monolayers and as a network of thin longitudinal stress fibers in the lower density case (Figure 4.2 bottom images). Nuclei were randomly oriented in dense monolayers and biased toward the longitudinal axis in lower density monolayers.

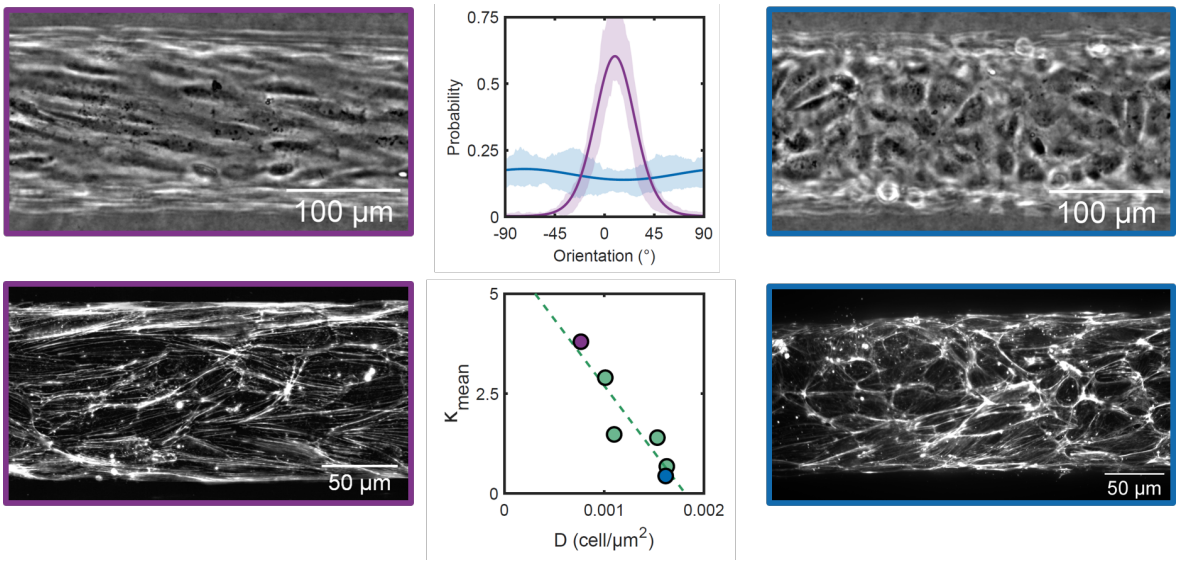

FIGURE 4.2: Influence of cell density on the initial monolayer state. Left panels (purple) show an example of low density monolayer exhibiting cell elongation and longitudinal orientation (top, brightfield) and longitudinal stress fiber orientation (bottom, phalloidin staining). Right panels (blue) show an example of high density monolayer displaying round and randomly oriented cells (top, brightfield) and a random network of cortical actin (bottom, phalloidin staining). Central panels show the quantification of the actin orientation. Top graph shows the fitted von Mises distribution to the mean distribution (solid line) and the standard deviation of the distributions from the different axial positions (shadows). Bottom graph shows the concentration parameter K as a function of cell density D (dots), with a linear fit (dashed line). The purple and blue dots correspond to the two cases shown in the other panels.

4.2.2.2 Basis for preferred monolayer orientation

In low density channels cell alignment and elongation are prominent. A key question is what drives these preferred orientations. Among all elongated monolayers, two major orientations could be distinguished: a purely longitudinal alignment and a helicoidal pattern (Figure 4.3 A & B). I will first discuss the longitudinal alignment because it is easier to understand in light of previous results in the literature. I will subsequently describe my hypothesis on the origins of the helicoidal alignment and the experiments that I performed to test this hypothesis.

Combined influence of curvature and shear stress ECs are known to avoid high curvature and to align in the direction of an applied shear stress (see Chapter 1). Both of these cues are present in the microvessel. Qualitatively, cells are expected to avoid the circumferential orientation due to curvature and favor the axial orientation due to the luminal shear stress. Quantitatively, these effects of course depend on the magnitudes of these stresses. Lowering the shear stress magnitude in the microvessel was not possible as cells are lost at smaller flow rates (presumably due to insufficient delivery of nutrients and removal of waste products). Increasing the diameter of the channel to lower curvature is feasible by using a larger diameter needle as the templating scaffold. Indeed, an earlier version of the channel had a diameter of 200 µm as already described. Although I did not repeat those experiments using the final protocols because of time constraints, I went back and analyzed a couple of preliminary experiments I had previously conducted to explore the role of curvature and shear stress on the longitudinal alignment.

ECs in the larger channels were round and randomly oriented, while in the narrower channels at similar cell densities, they were elongated and aligned. As the wall shear stress is inversely proportional to the cube of the channel diameter, the same flow rate of 2 µL min^{-1}

which generates a wall shear stress of 0.2 Pa in the smaller channel leads to a shear stress of 0.04 Pa in the large channel. Thus, both the curvature and shear stress were changed between the large and small channels. This analysis confirmed that curvature and shear stress play a role in the longitudinal alignment found in narrow channels but did not permit the distinction between the two. Interestingly, when doubling the flow rate in the large channel, ECs were found to switch from a random alignment to a weak longitudinal alignment and to elongate, as quantified by a smaller shape index. This finding, which requires confirmation in further experiments, suggests once again that shear stress can align the cells axially.

4.2.2.3 Helicoidal pattern

Phenomenon In a significant fraction of the chips, a helicoidal alignment was observed, where the cells were highly elongated and collectively aligned at an angle that varied between 15°and 45°relative to the channel axis (Figure 4.3 A ii, B purple). To process the images associated with this type of pattern, it was essential to keep in mind the cylindrical geometry and to flip the angle distribution of images coming from the top of the channel. If not, the orientation distribution appeared as bimodal, with one peak at around +30°and another at around -30°, when it was in fact a geometrical effect. The helical pattern could be either fully developed, i.e. extending over the entire channel length, or partial, with local helicoidal patterns alternating with disorganized regions.

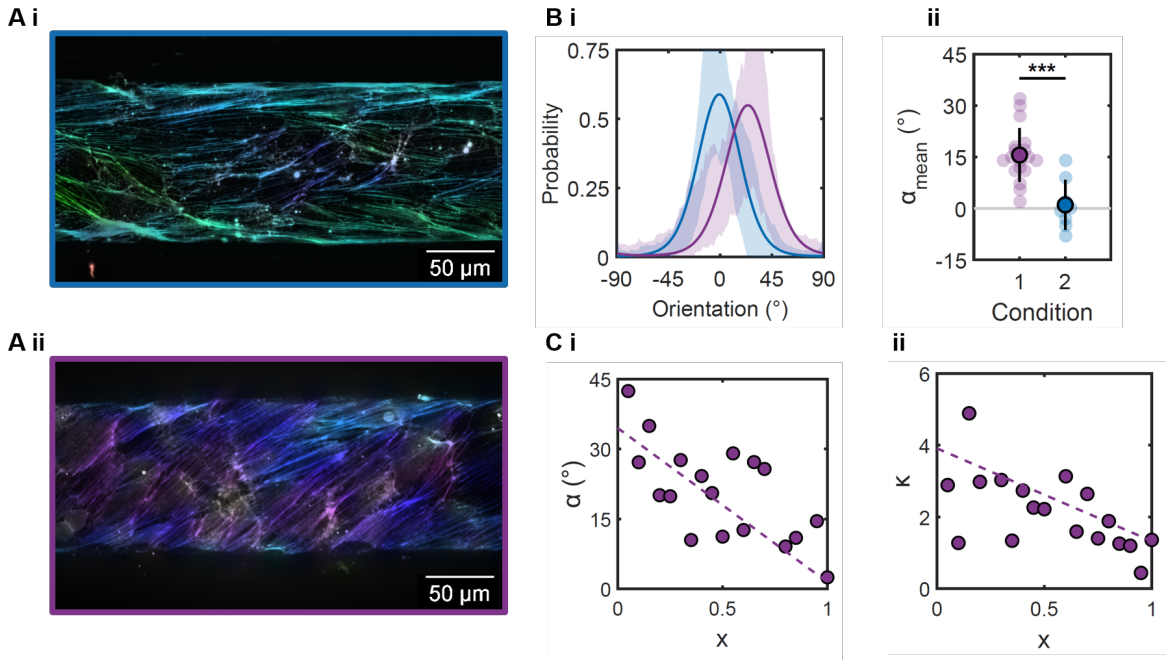

FIGURE 4.3: Comparison of the longitudinal and helicoidal patterns. **A.** Representative phalloidin staining of a longitudinal (**i**) and helicoidal (**ii**) pattern, color coded for actin stress fiber orientation. **B.** Quantification of the orientation direction of the monolayer from brightfield images through the location parameter α. **i** Two examples of the fitted von Mises distribution (solid line) for a longitudinal (blue) and a helicoidal (purple) channel, overlayed on the standard deviation of the axial distributions (shadow). **ii** Location parameter α as a function of the two experimental conditions: 1 is without inlet straws, 2 is with inlet straw. **C.** Variation of the helicoidal pattern along the channel axis, with a decreasing angle and elongation. **i** Location parameter α as a function of axial position x. **ii** Concentration parameter K as a function of axial position x. Each dot represents the parameters obtained from fitting the local orientation distribution, with a linear fit to indicate the decreasing trend (dashed line).

Chirality The quantification of numerous chips revealed that the helicoidal pattern was consistently in the clockwise direction relative to the channel axis with its direction defined by the flow direction (Figure 4.3 B purple). This robust behavior is a textbook example of cell chirality (see Chapter 1).

Origin As mentioned in the paragraphs above, both shear stress and curvature have been reported to promote axial cell alignment. Neither of these two stimuli was expected to promote diagonal or helicoidal cell orientation. To explain the helicoidal pattern, I hypothesized that two additional factors might potentially be involved: a nematic collective behavior based on spatial packing and/or the influence of a third heretofore unaccounted for mechanical stress.

Hypothesis 1: Cellular monolayers can behave as extensile or contractile tissues. The longitudinal alignment of nematic particles is an equilibrium position as it minimizes both the shear stress and curvature cues. The stability of this equilibrium point depends on the monolayer behavior. In the case of an extensile tissue, if a particle deviates from the 0°orientation, the axial forces exerted on it by the neighboring cells would tend to straighten the particle and rotate it back to the 0°orientation; thus, the equilibrium position is stable. On the other hand, in the case of a contractile tissue, if a particle deviates from the 0°orientation, the axial forces exerted on it by the neighboring cells would compress it further and rotate it away from the 0°orientation; therefore, the equilibrium position would be unstable. The stable equilibrium position would then depend on the curvature and shear stress levels.

Hypothesis 2: Although I present this second hypothesis here, I only formulated it after I saw that tensile stresses in the microvessel led to circumferential alignment. The presence of small tensile stresses in the microvessel even in the control conditions may therefore be the heretofore unaccounted for stress that would favor the circumferential direction. Upon examining the experimental setup of the control case more closely, I realized that the inlet reservoirs used during the initial monolayer growth were a couple of millimeters short to impose the correct hydrostatic pressure head. As a result, the equilibrium height dictated by the imposed flow rate was above the reservoir height, causing periodic overflow when the drop of medium was too big and surface tension could not hold it in place any longer. At that point, the entire drop would fall off the reservoir, leading to a small jump in inlet pressure. The pressure thus slowly increases (drop filling) and falls abruptly (drop falling over) periodically, inducing periodic tensile stresses on the cell monolayer.

The pressure within the channel decreases axially because of viscous dissipation (see Chapter 2). If the helix is pressure driven, its structure should differ along the channel axis. Consistent with this pressure hypothesis, both the helix angle, as quantified by the location parameter (Figure 4.3 Ci), and helix elongation, as quantified by the concentration parameter (Figure 4.3 Cii), tended to decrease with axial position. Finally, to test the hypothesis, I increased the height of the inlet reservoir by adding a straw. The resulting monolayer no longer exhibited a helicoidal pattern (Figure 4.3 A,B). I therefore changed the protocol for the monolayer growth to systematically have an inlet straw, guaranteeing a true control condition without tensile stress oscillations.

4.2.3 Preliminary study of shear and stretch

Once the control condition was properly characterized, I wanted to investigate the response of the channel to luminal shear stress, expecting to observe a strong longitudinal alignment. I increased to flow rate to $10\,\mu L\,min^{-1}$, five times higher than the baseline level used for monolayer growth. Under that flow rate and in light of the resulting change in channel diameter, the shear stress felt by the ECs was around 0.5 Pa, a a sufficiently high level to elicit cell elongation according to the literature (see Chapter 1.3). The increased flow rate also increases the luminal pressure and creates an axial gradient of static strain of around 3 to

5 % (see Chapter 2). As the strain magnitude was small and constant, I initially conjectured that the cell response would be dominated by the shear stress. Furthermore, as the strain is circumferential and the shear stress axial, they are thought to act in a synergistic manner and would therefore reinforce one another. In a nutshell, everything pointed toward a strong longitudinal alignment.

4.2.3.1 Overall cellular response

To my surprise, the cells elongated and aligned in the circumferential direction, in a robust and repeatable fashion. The whole cell response was mirrored intracellularly, with cytoskeletal reorganization and nuclear reshaping. After 7 h of mechanical stimulation, the actin cytoskeleton was composed of thick central stress fibers with a prominent circumferential orientation, and nuclei were broadly aligned around the 90°direction, albeit with significant dispersion.

4.2.3.2 Dynamics

To capture the dynamics of the cell response, monolayers under high flow rate were imaged for 24 h in brightfield, and cell shapes were analyzed over the channel length as a function of time. The time evolution for one position is shown in Figure 4.4, with time denoted in the rainbow coloring of both the graphs and the contours of the brightfield snapshots. Two distinct phases were discernible: a first phase where ECs elongated circumferentially and a second where ECs rounded up (Figure 4.4 right images). The orientation distribution analysis showed the same effect, with a progressive shift of the curve peak toward 90 °, followed by a progressive decrease in peak height (Figure 4.4 top left graph). To precisely quantify the dynamics, von Mises distribution fits were applied to the experimental probability densities to extract the location and the concentration parameters as a function of time (Figure 4.4 bottom graphs). The same two phases can be observed: EC orientation initially shifted with an exponential speed toward 90°and EC elongation increased linearly, and then EC elongation decreased linearly while the orientation angle no longer changed. The peak monolayer elongation was found after 11 h. The final state after 24 h was a randomly oriented monolayer of cuboidal ECs.

The different positions along the channel axis showed a similar two-phase dynamic, as shown by the mean location and mean concentration as a function of time (Figure 4.5, blue). The same dynamics were observed in a second experiment (Figure 4.5, purple), where the peak response was also found around t = 10 h.

4.2.3.3 Shear stress vs. strain

As the curvature is essentially constant within the microchannel, the mechanical cues that change are the shear stress, the strain, the absolute pressure, the transmural pressure gradient and the transmural shear stress. ECs are known to respond to all of these stresses (see Chapter 1.3), but only the first two are directional stresses capable of inducing in plane cell alignment. As a colleague in the group who was also studying HUVECs had observed cell alignment orthogonal to the flow direction in parallel flow chambers, one possibility I considered was that I was observing a similar response. This hypothesis was in contradiction with the gradient of cell alignment observed along the channel axis because the shear stress is fairly constant along the length (with only a 10% decrease, see Chapter 2). The strain, however, has a strong axial gradient, with a negligible magnitude close to the outlet, making it a good candidate for inducing the circumferential cell alignment.

I decided to focus the rest of my project on only stretch, a mechanical cue much less thoroughly investigated than shear stress, particularly in the case of confluent endothelium

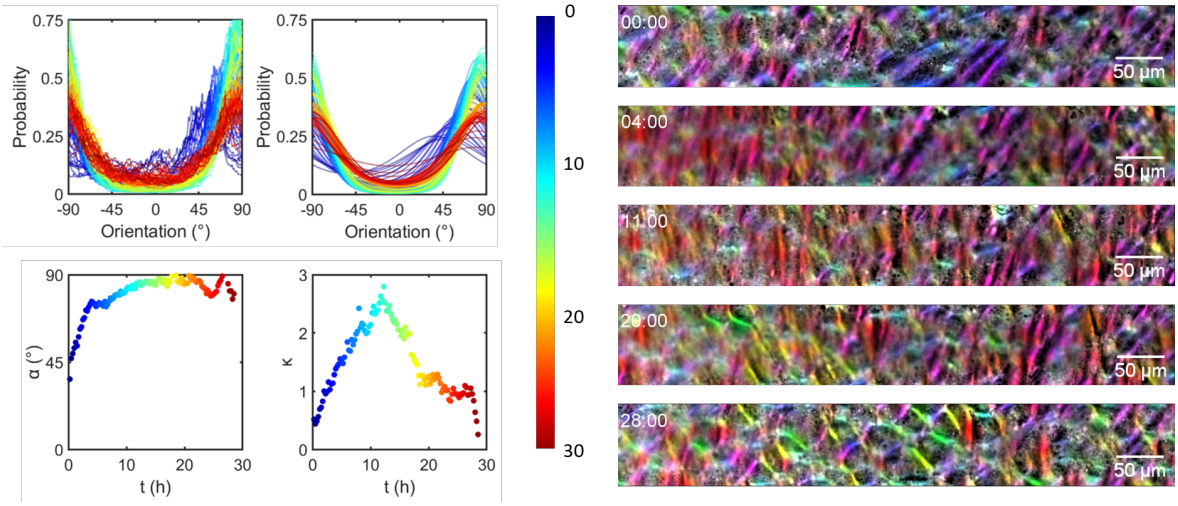

FIGURE 4.4: Dynamics of monolayer response after a static stretch at a fixed axial position. Experimental orientation distributions of cells (top left) obtained with brightfield imaging are fitted with von Mises distributions (top right) to extract location (bottom left) and concentration (bottom right) parameters as a function of time. Rainbow coloring in the graphs denotes time (color bar). Brightfield snapshots of the monolayer at five different time points (0, 4, 11, 20 and 28 h), color coded for cell-cell junction orientation, from the movie quantified in the graphs.

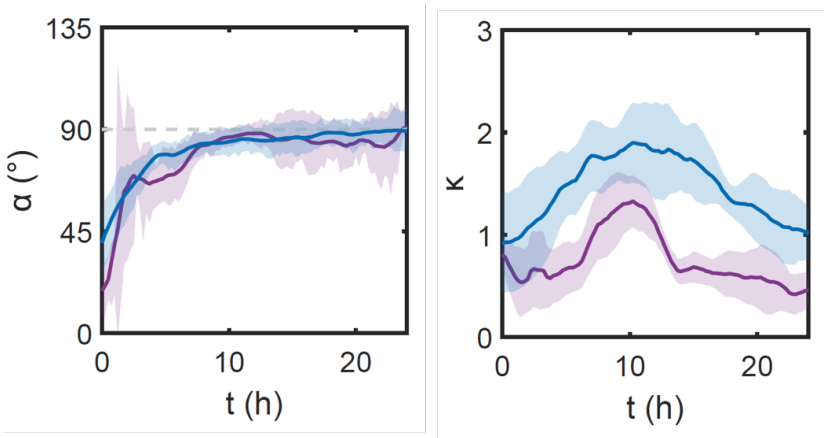

FIGURE 4.5: Dynamics of the monolayer response after a static stretch. Location α (left) and concentration K (right) parameters as a function of time for two different stretch experiments (blue and purple). The location and concentration were first extracted at each axial position in a given channel to then compute their average (solid line) and standard deviation (shadows) along the length.

in a complex microenvironment as is the case in the microvessel. The cherry on top, in my opinion, was the apparent contradiction with the literature, with the cells aligning in the strain direction instead of perpendicular to it, which, if explained, promised to bring novel mechanistic insight into EC mechanobiology.

4.2.4 Cellular response to stretch

4.2.4.1 Quantification of the applied stress

The stretching of the channel is created by the compressive force applied on the gel by the luminal pressure. Therefore, the most direct way to apply stretch is to control the lumenal pressure. To impose the desired pressure levels, water columns of different heights could be used at the channel ends (see Chapter 4.2). The bulk of the mechanical characterization of

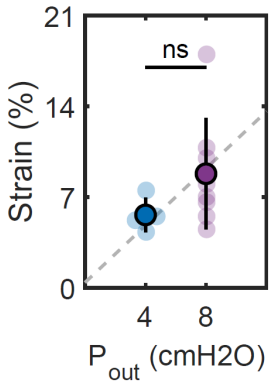

FIGURE 4.6: Strain as a function of outlet pressure, with a linear fit (dashed line) to show the increasing trend.

the microvessel was flow-based with an axial gradient of strain (see Chapter 2), providing an estimate of the strain exerted on the cells. In the new pressure-based configuration, the strain in endothelialized channels was measured for varying outlet pressures. Plotting the strain for different channels as a function of pressure reveals the expected increasing linear trend, with significant dispersion (Figure 4.6). I chose two pressure levels of 400 and 800 Pa to generate average strains of 5.6 ± 1.4 % and 8.8 ± 4.3 %, respectively. It is important to emphasize that with this new experimental configuration, the shear stress was maintained constant between the control and stretched microvessels. Thus, cell response was attributable only to stretch.

4.2.4.2 Main features of cellular response

EC response to stretch was qualitatively similar to EC response to high flow rates. However, it was different quantitatively as it was constant along the channel length and more marked as the stress magnitude increased. The three cellular components of interest, namely adherens junctions, actin cytoskeleton and nuclei, exhibited strong reorganization and alignment in response to stretch (Figure 4.7). Cells were more elongated and oriented at 90°, the actin cytoskeleton exhibited thick central stress fibers at 90°, and nuclei were also oriented at 90°.

4.2.4.3 Magnitude dependence of the stretch response

Low vs high I varied the magnitude of the stretch by changing the outlet pressure. First, two different pressure levels were tested: low corresponding to a column height of 4 cm (400 Pa), and high corresponding to 8 cm (800 Pa). As a point of comparison, these match the pressures imposed at the inlet by a flow of 13 and 26 $\mu L\,min^{-1}$. As a reminder, the low flow condition led on average to 5.6 ± 1.4 % initial strain and the high flow condition to 8.8 ± 4.3 % (Figure 4.6). EC response to stretch was magnitude-dependent, with stronger alignment observed for higher pressures (Figure 4.8 A,B,Ci). The extent of cell and cytoskeletal alignment, as quantified with the respective K values, were significantly higher for the high pressure case (Figure 4.8 ii). Cell elongation increased, correlating with a more pronounced nuclear alignment and elongation. Interestingly, although the strains (due to the pressure step) sometimes were similar between the low and high pressure conditions, the cell responses were very different. Cell response had a better correlation with the pressure value than with the initial strain.

Linear dependence To explore the existence of possible thresholds or optimal value effects, I measured the response of ECs to various lumenal pressures, from 0 to 800 Pa, with

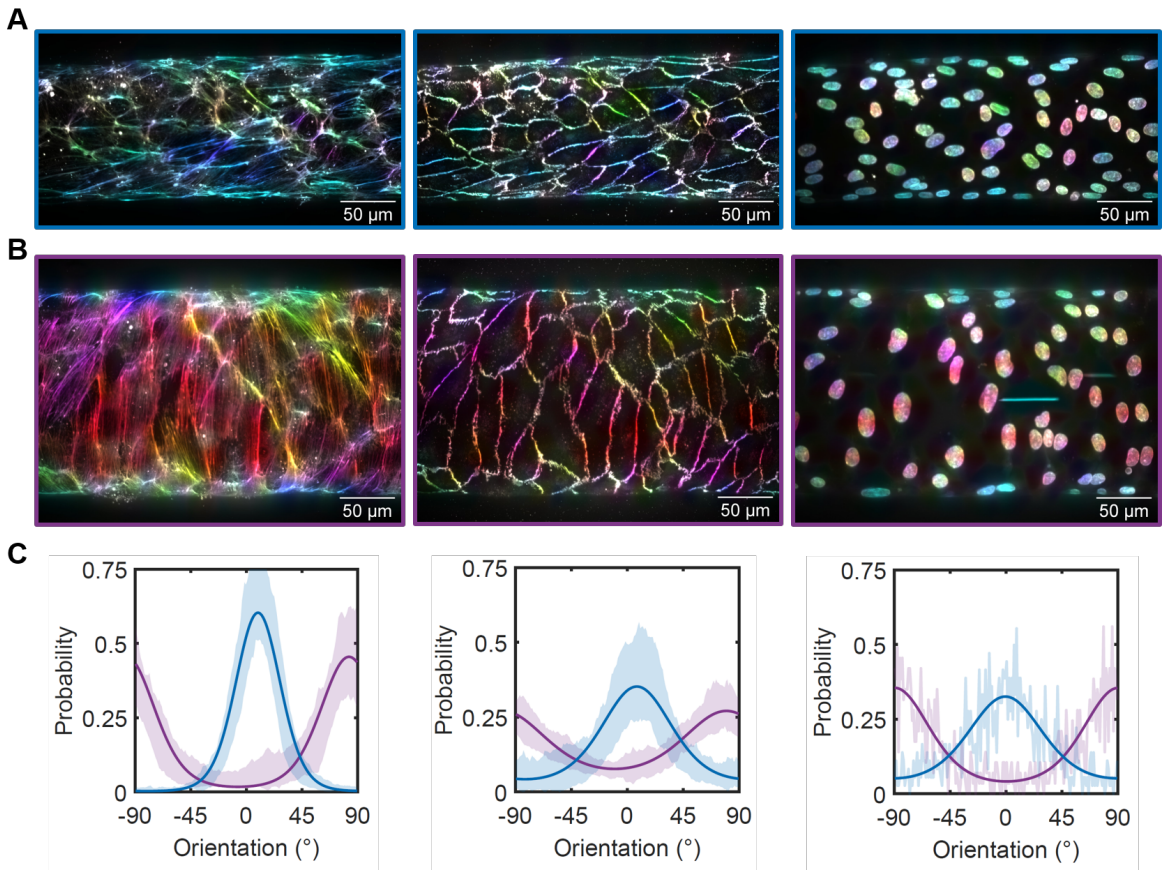

FIGURE 4.7: Effect of 7 h of static stretch on EC monolayers. Representative 40X maximum intensity projection (MIP) images of a control (**A**, blue) and stretched (**B**, purple) channel for actin (left, phalloidin), cell-cell junctions (center, VE-cadherin) and nuclei (right, DAPI). Images are color coded by element orientation. **C.** Von Mises distribution fit of the channel-averaged orientation (solid line) for actin (left), cell-cell junctions (center) and nuclei (right) in the control (blue) and stretched (purple) channels. In the left and center panels, shadows are the standard deviations of the orientation distributions at different axial locations. In the right panel, the line denotes the channel-averaged experimental curve.

incremental steps of 200 Pa. The same effect on elongation and alignment as with low and high pressure was observed, with the different parameters varying linearly (Figure 4.8 C iii). No threshold or optimal stretch level was observed.

4.2.4.4 Effect of the initial density

4.2.4.5 Dynamics

Similar to the shear and strain experiment, the response of ECs to stretch should be dynamic. I did not replicate the same live recording experiment as for the shear and strain case because of two experimental difficulties. First, the straight straws did not fit under the microscope. Second, the microscope incubator was maintained at 37 degrees for cell survival, but the flow rates were too small to compensate for the evaporation in the gel. With some time spent on optimization, the experiment is definitely possible, but I decided to instead study the dynamic behavior through time lapse staining. By comparing different microvessels stained at different time points, I was able to reconstruct the dynamics of the response.

7 h vs 24 h The live imaging of the flow-based stretch had indicated a two-phase response, with peak elongation and alignment around 10 h. I therefore decided on a simple two time

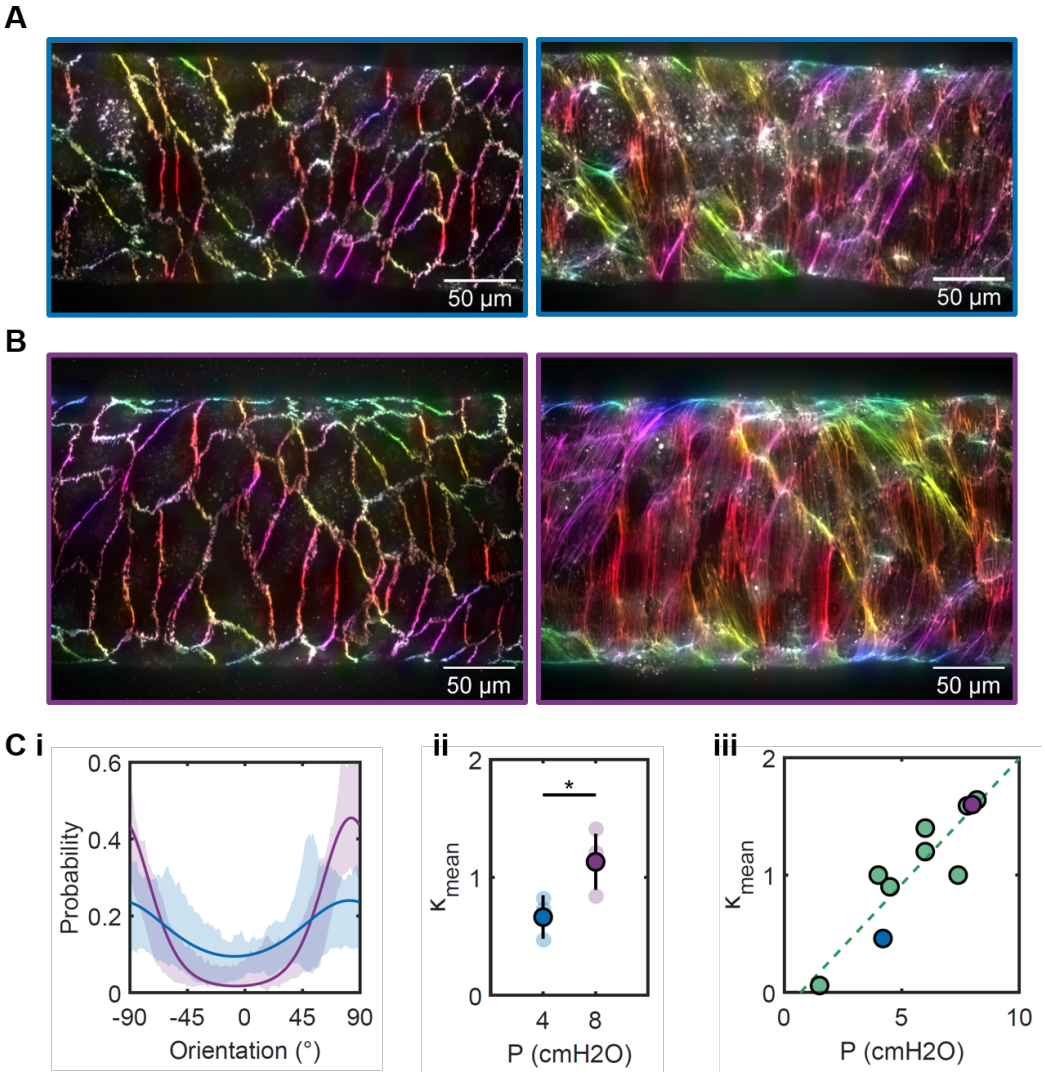

FIGURE 4.8: Pressure magnitude-dependent cell response. Representative 40X MIP images of a stretched channel with outlet pressures of 4 cmH_2O (**A**, blue) and 8 cmH_2O (**B**, purple) for cell-cell junctions (left, VE-cadherin) and actin (right, phalloidin). Images are color coded by element orientation. **C.** Quantification of the pressure magnitude dependence. **i** Von Mises distribution fit of the channel-averaged orientation (solid line) for outlet pressures of 4 cmH_2O (blue) and 8 cmH_2O (purple). Shadows are the standard deviations of the orientation distributions at different axial locations. **ii** Intensity of the monolayer response, quantified with the mean concentration parameter K of three experiments for the two different outlet pressures. **iii** Concentration parameter K as a function of outlet pressure (dots), with a linear fit (dashed line) to show the increasing trend. The blue and purple dots correspond to the monolayer shown in panels A, B and Ci.

point experiment for the first time lapse. A time lapse approach had the advantage of enabling the imaging of the intracellular components with fluorescence staining, whereas brightfield movies only gave access to cell shape. Cells, actin stress fibers and nuclei oriented in both cases toward 90°, as quantified with the location parameter. Surprisingly, however, the extent of alignment and elongation, as quantified with the concentration parameter K, did not exhibit the same two phase response. The mean K values for whole cells at 7 h (green) and 24 h (orange) were similar (Figure 4.10 A). The mean K values for actin stress fibers doubled from 7 h (green) to 24h (orange). Since stress fibers cannot elongate, this increased K can be interpreted as a more pronounced alignment. Finally, the mean K for the nuclei was slightly higher after 24 h (Figure 4.10 C) although not significantly.

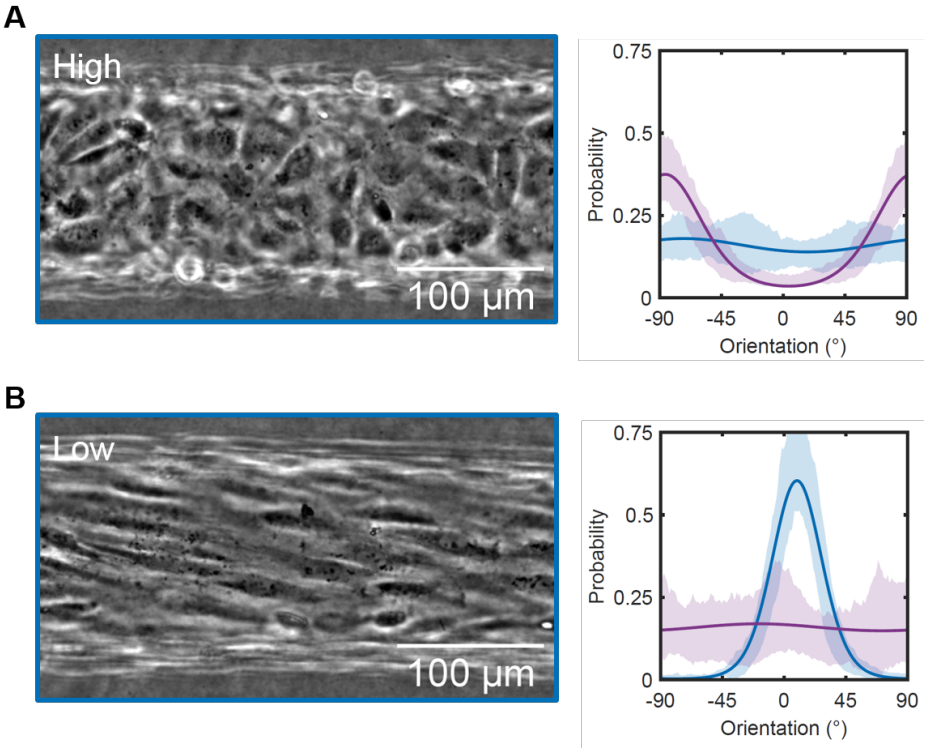

FIGURE 4.9: Influence of the initial monolayer density on the response to stretch. Representative brightfield images of a channel of high (**A**) and low (**B**) initial density. Quantification of the initial (blue) and final (purple) cell orientation for the two initial densities. Solid line indicates the von Mises distribution fit, and shadows denote the standard deviations of the distributions at the different positions.

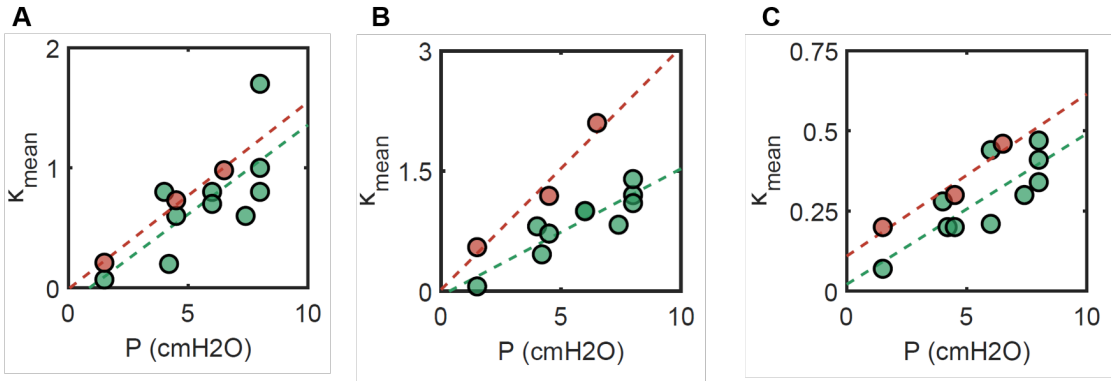

FIGURE 4.10: Dynamics of the cell response to stretch. Comparison of the concentration parameter K after 7 h (green) and 24 h (orange) of static stretch for the cell-cell junctions (**A**), actin (**B**) and nuclei (**C**). Each dot is a channel average, and the dashed lines are linear fits to show the increasing trends.

In my mind, the fact that I could not observe the same two phase dynamics as in the flow-based stretch had two possible explanations.

HYPOTHESIS 1 The monolayers under outlet pressure-based stretch do not have the same dynamics and remain oriented and elongated. This would be very surprising because of the tensional homeostasis that postulates that cells tend to normalize their tension and return to a steady state after a mechanical perturbation. Additionally, the idea that a monolayer could have an infinite memory is unlikely.

HYPOTHESIS 2 The monolayers under outlet pressure-based stretch have the same dynamics with a second rounding phase, but I had not imaged for sufficiently long periods of time to capture this second phase. I find this hypothesis much more likely and plan on testing it with longer time lapses. Two mechanical stresses were changed between the flow-based and outlet pressure-based stretch: the shear stress is smaller, and the strain and tensile stresses are higher in the outlet pressure-based stretch case. The hypothesized altered phase duration could be caused by either, and addressing this question would be a necessary step toward elucidating the mechanism behind this phenomenon.

Time-lapse The literature indicates that cytoskeletal reorganization in response to strain occurs in minutes up to an hour, whereas whole cell realignment requires several hours (see Section 1.3). I therefore designed a time lapse experiment with shorter time points spaced pseudo-logarithmically to match interesting time scales suggested by the literature. The selected time points after the onset of stretch were 1 min, 15 min, 1 h, 4 h, 8 h and 24 h, in addition to the control before stretch (t=0) (Figure 4.11 & 4.12).

It is important to note here that the ECs in the channels used in this set of experiments were the ones with a "strange" phenotype (see Section 4.3.9.2). These results have to thus be taken with grain of salt and should be repeated with "healthy" ECs before drawing definitive conclusions. Nevertheless, some trends emerged from these experiments, presented in the following paragraphs, and they seem to confirm that the time lapse approach is a valid method to study EC dynamics.

Phalloidin staining showed progressive reorganization of the actin cytoskeleton from a prominent longitudinal alignment to a circumferential alignment through an intermediate and almost random alignment, accompanied by a switch from cortical actin to central thick stress fibers (top images). Stress fibers were already visible after 1 h but with very disperse orientation, then distributed around 90°after 4 h with some level of noise, after which the whole network slowly sharpened its fiber orientation toward 90°over the next 20 h. To quantify the dynamics, location and concentration parameters were extracted by fitting von Mises distributions to the orientation distributions (Figure 4.11 A-C). The shift in mean actin orientation seemed to follow an exponential curve with a characteristic time of 1.5 h. After a couple of hours, the fibers stayed on average oriented at 90°, matching the preliminary visual observations in the staining. The concentration K, a measure of the intensity of orientation, increased linearly from 1.5 h to 24 h (Figure 4.11 Ci, dashed line), confirming the visual observation of a sharpening of fiber alignment. Finally, the concentration K during the initial fiber orientation (until 1.5 h) was low, below 1, indicating a network with no preferential direction (Figure 4.11 C ii).

Of note, I still have no clear explanation for the rapid drop in actin concentration, reflecting the switch from longitudinal stress fibers to random cortical actin between the control and the first two time points. This may correspond to the rapid actin remodeling reported in the literature, or it may simply be a coincidence, the control channel might have had a lower cell density and a more pronounced longitudinal alignment than the other channels. To clarify this effect and have a finer and more precise view of actin dynamics, I plan on imaging fiber structure and orientation in the same channel during a stretch experiment. This is possible using LifeAct ECs (see Section 4.3.7).

The same analysis was run on the VE-cadherin staining to analyze cell orientation (Figure 4.12 A) and on the DAPI staining to analyze nuclear orientation (Figure 4.12 B). Cells had no preferential alignment until 8 h after which they aligned at 90 °with a concentration parameter K around 1 (Figure 4.12 A). The alignment intensity did not increase further after 24 h. Nuclei had no preferential alignment until 24 h, then they aligned at 90 °with a concentration parameter K around 0.75 (Figure 4.12 B).

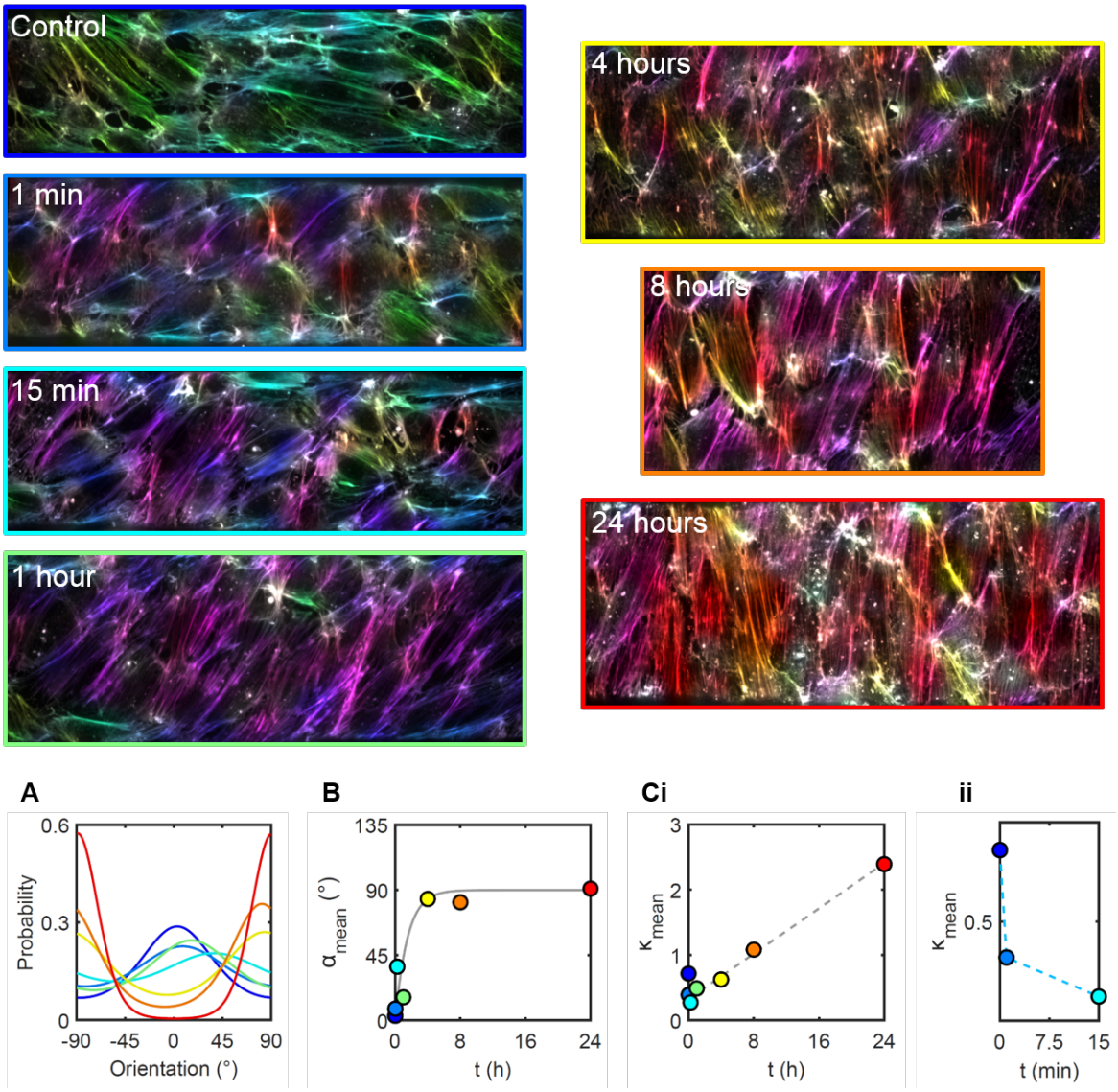

FIGURE 4.11: Time lapse of the cytoskeletal response to stretch. Representative 40X MIP images of the actin cytoskeleton of different channels after varying the duration of static stretch. von Mises distributions were fitted to the average channel actin orientation distribution for each time point (**A**), to extract the location (**B**) and concentration (**C**) parameter as a function of time. In all panels, rainbow coloring denotes time.

4.2.5 Stretch, strain and tensile stresses

After I had enough repeats of the stretch experiment to be convinced that it was not an artefact and that ECs do indeed orient in the direction of stretch in the microvessel, I wanted to build a framework based on hypotheses that would explain the apparent contradictions between my experiments and the literature. I present here my thought process and its results, a conjecture on the underlying mechanism based on simple considerations. I started by asking myself what is different between my experiments and those in the literature. The answer is that there are at least three differences: substrate stiffness, confluence and imposing tension instead of strain (see Section 1.3 and 4.1 for more details on the literature on EC and strain).

Substrate stiffness: tension distribution In most experiments in the literature, even when cells are plated on a deformable substrate, the stiffness of the substrate is several orders of magnitude higher than that of the cells. The distribution of stresses in two elastic layers

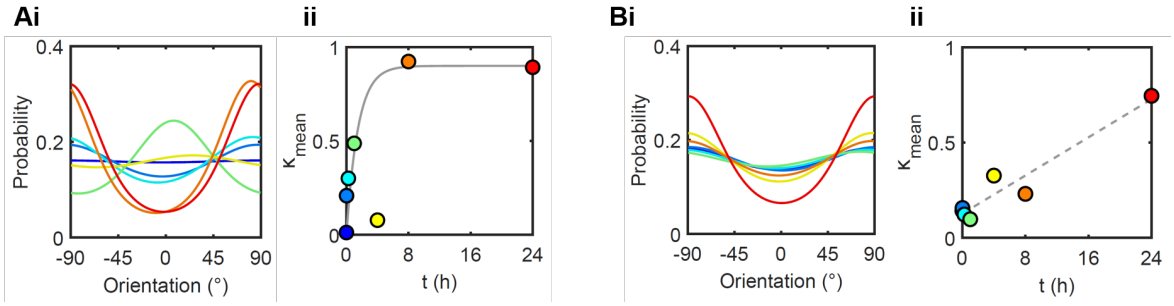

FIGURE 4.12: Time lapse of the cell and nuclear response to stretch. Von Mises distributions (**i**) were fitted to the average channel cell (**A**) and nuclear (**B**) orientation distributions for each time point to extract the concentration (**ii**) parameter as a function of time. In all panels, rainbow coloring denotes time.

placed in parallel for a given strain magnitude depends on their relative stiffnesses: the stiffer layer will concentrate the stress and will be the principal load-bearing structure. In my system where the collagen hydrogel is very soft, the cell monolayer is the load-bearing layer.

Cells have been reported to reduce their adhesions to the substrate, through focal adhesion remodeling and reduction of the actomyosin contractility, thus minimizing stress transmission from the stiff strained layer to the cells. In my system, cells cannot do that.

Confluence In most experiments in the literature, stretch is applied on single cells, even in studies on ECs. The few studies that do investigate the collective response of endothelial monolayers report varying alignment results. The confluence in my system has biological implications, by possibly changing the mechanosensing pathways, but also mechanical implications for the distribution of stresses in the cells by enabling direct stress propagation between contiguous cells, physically bound together by cell-cell junctions.

Imposing stress Once again, in most experiments in the literature, the imposed physical parameter is the strain through experimental platforms that generate controlled displacement (see Section 1.4). The corresponding stress felt by the cells depends on many parameters, such as cell stiffness, which can be actively altered by the cells. For instance, cells under stretch have been reported to reduce actomyosin contractility, which decreases cytoskeletal tension and leads to cell softening. For the same amount of strain, a softer cell would feel smaller tensile stresses. Cells also remodel their shape by elongating to the minimum strain direction which minimizes both stress propagation and cytoskeletal tension.

4.2.6 Diameter increase

A second major response of the microvessel to stretch was a marked increase in channel diameter which persisted even after load removal. Indeed, channels subjected to several hours of stretch did not relax back to their original diameter after the luminal pressure was lowered to zero, suggesting a plastic or fluid-like behavior of either the gel or the cell monolayer.

Once I realized that mechanical forces could lead to slow and long-lasting channel remodeling, I reanalyzed the collected data on channel diameter after monolayer growth presented in Chapter 2. Now that I suspected a mechanical origin, these measurements revealed several interesting clues that I will present in the next section, after which I will present the data from the stretch experiments.

4.2.6.1 Initial monolayer formation at small pressure

Cell dependent As presented previously, endothelialized channels had an average diameter of around 135 µm, wheres all the bare channels fabricated and tested during the three years of my Ph.D. had the same baseline diameter, around 125 µm (Figure 4.13 A). These findings indicate that cells are necessary for the process of channel enlargement.

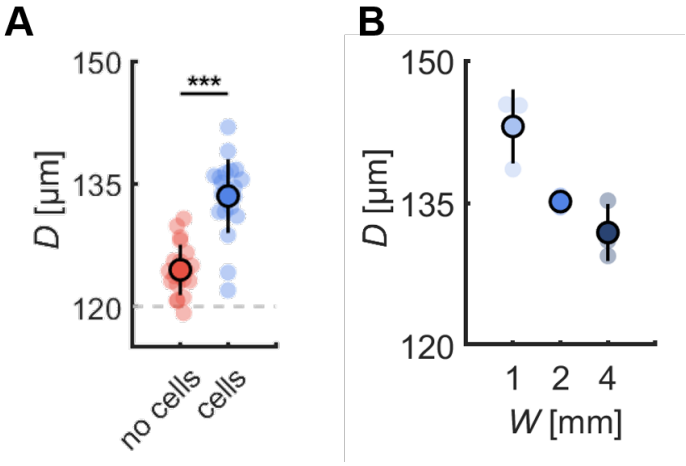

FIGURE 4.13: Increase in luminal diameter during initial monolayer formation with and without cells (**A**) and as a function of gel width (**B**).

Gel width dependence, i.e. pressure dependence? The width of the gel surrounding the channel influenced the diameter of the channel after monolayer formation, with narrow gels leading to larger diameter channels (Figure 4.13 A, see Chapter 2 for details). Narrow gels are associated with a higher hydraulic resistance, and as the channel is initially identical for the difference gel widths, the overall resistance of the microvessel (gel plus channel) is larger for the narrower gels. The constant flow rate imposed at the inlet leads to higher luminal pressure in the microvessels of higher resistance, i.e. the ones with narrower gels. This correlation suggests that pressure could be the driving force for the increased channel diameter.

Axial position dependence, i.e. pressure dependence? The data presented in the previous graph represent an average of five positions along the channel length. By plotting the channel diameter as a function of axial position, a clear dependence appeared (Figure 4.14). Overall, channel diameter decreased from inlet to outlet with a boundary effect, visible by the diameter drop close to the channel inlet. This pattern is similar to the strain pattern in the channel (Figure 4.14), which stems from the axial pressure drop in the channel lumen combined with boundary effects (see Chapter 2). This correlation suggests once again that pressure may be the driving force for the increased channel diameter.

Outlet pressure dependence To explore the idea of pressure-dependent remodeling, I varied the channel pressure during the initial monolayer formation by changing the height of the outlet PDMS reservoir to 1 cm. The final diameter increase after two days of culture was significantly higher when the outlet pressure was increased, lending further support for the hypothesis that increased lumenal pressure drives the increase in luminal diameter (Figure 4.15 A).

Time dependence Monolayers seeded at similar densities and cultured for 48 to 72 h (confluence was typicaly reached after 24h) had different average diameters (Figure 4.15 B). Channels cultured for an extra day had even larger diameters than the control channels,

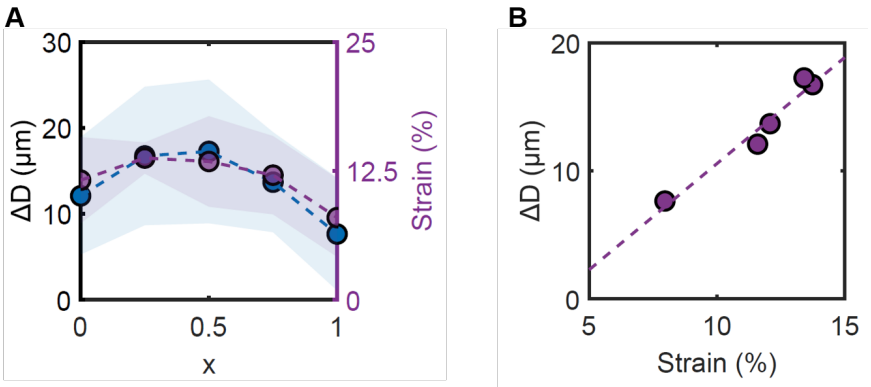

FIGURE 4.14: Increase in luminal diameter during the initial monolayer formation as a function of axial position. **A.** Increase in diameter ΔD (blue, N=28) and strain (purple) as a function of position. Dots are mean experimental values, shadows display the standard deviation among chips and dashed lines are guides for the eyes. **B.** Increase in diameter ΔD as a function of strain, with a linear fit (dashed line) to highlight the proportionality relationship. Dots are the different axial positions.

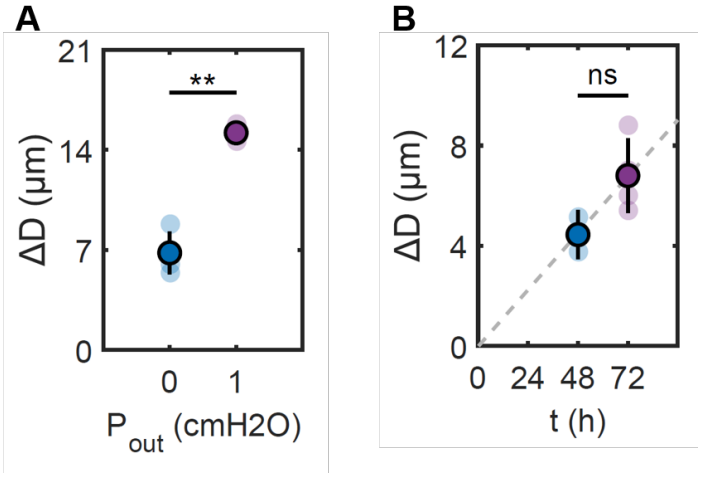

FIGURE 4.15: Increase in luminal diameter during the initial monolayer formation as a function of outlet pressure (**A**) and time (**B**), with a linear fit to highlight the increasing trend (**B**, dashed line).

which themselves had larger diameters than bare channels as already described. Further experiments showed that it is not the absolute culture time that determines the diameter but rather the time after the monolayer attains confluence, which can be varied by changing the initial seeding density. This observation was reproduced by Sara Barrasa-Ramos, another Ph.D. student in the group, who spent several weeks investigating the role of cell density on angiogenic events (see section 5.2.2) and saw the same effect. After 48 h of culture, channels seeded at high density (already confluent) had larger diameters than channels seeded at medium density (confluent after a day), which were in turn larger than channels seeded at low density (confluent after two days). This last group had diameters that matched those of bare channels.

4.2.6.2 Stretch experiments at high pressure

The results from the stretch experiments at high pressure had many similarities to those at low pressure. For instance, channel remodeling at high pressure also depended on the presence of a confluent endothelium. Bare channels and channels with subconfluent ECs did not increase in diameter, even under the highest pressure for 24 h. The low pressure

experiments actually contained all the clues to predict the response of the channels, which was an interesting realization for me. It highlighted the richness of information that can be present in an experiment beyond the intended outputs. By designing an experiment that had finer control over channel pressure, with the straws, I was able to address the hypotheses that emerged from the previous preliminary results: the pressure and time dependence.

Position dependence, i.e. pressure dependence Plotting the increase in channel diameter as a function of axial position showed different patterns between the flow-based (A) and the outlet pressure-based (B) stretches (Figure 4.16). In the flow-based stretch, the channel remodeling decreased linearly from inlet to outlet (Figure 4.16 A, purple); while in the outlet pressure-based stretch, the channel remodeling profile was flat (Figure 4.16 B). These two profiles were in accordance with the pressure profile under the two stretch conditions: in the flow-based approach, there was a large pressure gradient from inlet to outlet, while in the outlet pressure-based approach, the hydraulic gradient was small relative to the outlet pressure, so the channel pressure remained almost constant. This experiment confirmed that the remodeling during stretch experiments was pressure dependent.

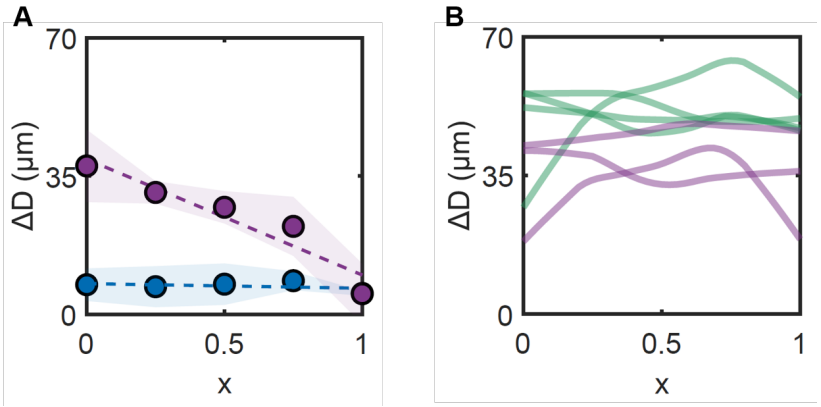

FIGURE 4.16: Increase in luminal diameter during stretch experiments as a function of axial position for a flow-based stretch (**A**) and a pressure-based stretch (**B**). **A.** Increase in diameter ΔD of control (blue) and stretched (purple) channels as a function of position, with a linear fit to highlight the decreasing trend. Dots are mean experimental values, and shadows denote the standard deviation. **B.** Increase in diameter ΔD as a function of position for outlet pressures of 4 (purple) and 8 (green) cmH_2O. Diameter was measured at 30 positions along the channel length, and the resulting curve was smoothed with a 5 points moving average (thick lines).

Pressure dependence The height of the fluid in the outlet straw determined the luminal pressure in a direct way, allowing a quantitative study of the channel remodeling as a function of luminal pressure. Channels under static stretch for 7 h with an outlet pressure of 8 cmH_2O (green) had higher diameters than their counterparts under half that pressure (purple) (Figure 4.16). Varying the outlet pressure with smaller increments showed that channel diameter increased linearly with luminal pressure (Figure 4.17), demonstrating once again that the remodeling was pressure driven. This effect could be seen in two different collagen batches (A & B) and for static stretches of 7 (blue) and 24 (purple) h (Figure 4.17).

Time dependence Channel diameter also depended on time, with microvessels subjected to 24 h of stretch having a larger diameter than those subjected to 7 h of stretch (Figure 4.17, blue vs purple). Channel remodeling increased on average by around 20 %. The time lapse experiment gave a higher temporal resolution of channel remodeling, revealing an exponential shape from 0 to 24 h (Figure 4.18). The confluence, pressure and time dependence were now clear, but the mechanistic model to explain the remodeling that would connect the three

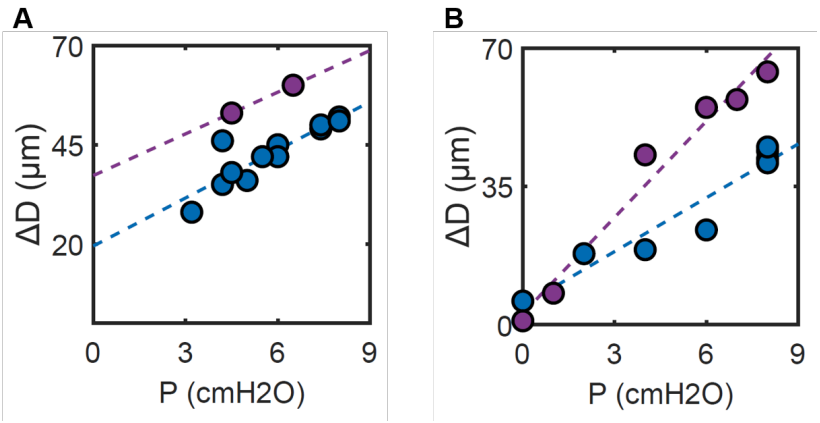

FIGURE 4.17: Average increase in luminal diameter as a function of pressure after 7 (blue) and 24 (purple) h of stretch for two collagen batches (**A, B**). Dots are mean diameter increase per channel, and the dashed line is a linear fit to highlight the increasing trend.

features together was still elusive and required further investigation.

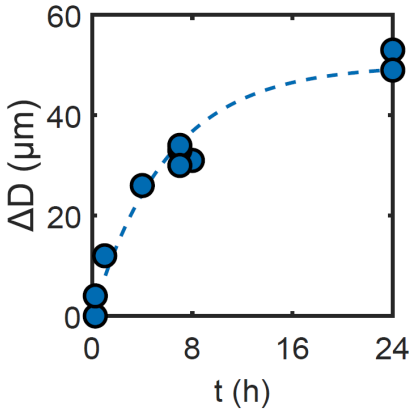

FIGURE 4.18: Increase in luminal diameter during static stretch experiments as a function of time. Dots are the mean diameter change in each channel, and the dashed line is an exponential fit.

4.2.6.3 Origin of the remodeling: cell activity?

As demonstrated in the previous paragraphs, cells were necessary for the observed increase in channel diameter. The underlying mechanism could be active, through a pressure-dependent biological activity, or passive, through a mechanical contribution. The characteristic time scale of hours to days would perfectly fit a biological process, whereas mechanical times would be expected to be considerably shorter, typically on the order of minutes or hours. This simple consideration oriented me first towards the hypothesis of cell activity.

Pressure-dependent MMP production For two years I was convinced, based on my experiments and the literature, that the diameter increase was due to cell activity. ECs are known to remodel their extracellular matrix by enzymatic activity. They secrete matrix metalloproteinases (MMPs) that digest the surrounding polymeric network, a process essential in angiogenesis. Papers with similar microvessel systems, where an endothelium lines a cylindrical channel in a natural hydrogel, report increased diameter after a couple of days of cell culture with VEGF. Additionally, one of the talks at the NAVBO conference in 2019 that I attended also presented data on lumen remodeling by vascular and lymphatic ECs in

a pressure dependent manner. I hypothesized that MMP production could be stimulated by pressure.

To test this hypothesis, I cultured the cells in the presence of GM6001, or ilomastat, a broad spectrum MMP inhibitor. The inhibitor was present from cell seeding to the end of the experiment. To my surprise, I saw no differences relative to the controls. Channel diameters still increased, slowly during the initial monolayer growth and dramatically during stretch experiments (Figure 4.19). I did not have time to validate the efficacy of the inhibitor, which would have required a Western blot to quantify MMP expression. However, Sara, who is studying angiogenesis in the same microvessel platform, has grown ECs in the presence of GM6001 and has observed total inhibition of sprouting, which suggests that the inhibitor does affect MMP expression.

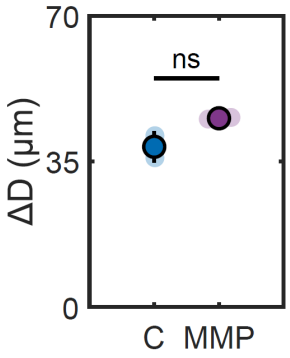

FIGURE 4.19: Average increase in channel diameter after 7 h of static stretch with (purple) and without the (blue) MMP inhibition.

4.2.6.4 A viscoelastic fluid inside a poroelasto-plastic solid?

Cell mechanical contribution, from a poroelastic to an elastic-like gel Following the observation that MMP activity does not appear to be the driving force behind remodeling of the gel, I began to formulate a new hypothesis by asking the following question: what does the endothelium change mechanically that could lead to a slow diameter increase and why does the remodeling occur only in the presence of a confluent endothelia? The main mechanical effect shown so far in my Ph.D. was the shielding effect (see Chapter 2), whereby the endothelial lining of the channel decreased the gel pressure, leading to an increased instantaneous deformation for a given luminal pressure (Figure 4.20, green and blue curve).

Monolayer and gel mechanics The endothelium also had an elastic contribution as a thin stiff layer. This contribution was impossible to measure as the control case, the bare channel deformation, was mostly affected by the poroelastic pressure effect. If I could increase the luminal pressure of bare channels without increasing their pore pressure, their deformation would be expected to be much higher (Figure 4.20, purple curve). The difference between the deformation of the elastic-like gel and the deformation measured in the presence of a monolayer, would correspond to the monolayer stiffness (Figure 4.20, red arrow).

If the gel maximum dilation is much higher and the cells are indeed the load bearing stiff layer, then the slow increase in diameter could be viewed as a progressive relaxation of the monolayer, until the equilibrium position of the gel is finally attained. In other words, during the stretch experiment, the system would start with cells being load bearing (point 1, green curve). The monolayer then progressively slackens (orange arrow), until the gel becomes the load bearing structure and stops the channel dilation (point 2, purple curve). The difference between the initial diameter just after strain application and the final diameter after the

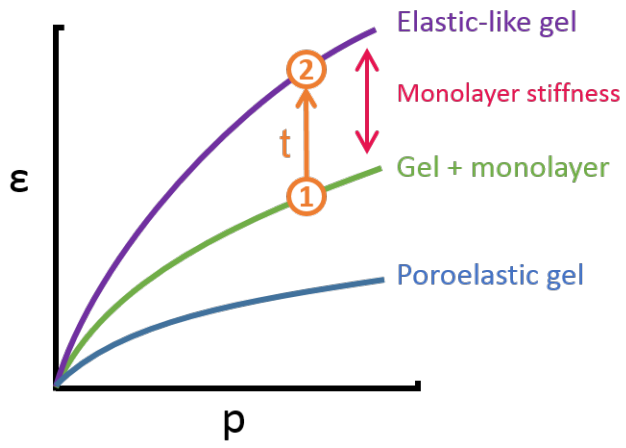

FIGURE 4.20: Schematics of the system mechanics, showing the three instantaneous deformation curves as a function of pressure for the bare channel (poroelastic gel, blue), the endothelialized channel (gel + monolayer, green) and the hypothetical bare channel without porous effects (elastic-like gel, purple). The contribution of the monolayer stiffness is indicated with the red arrow. The hypothesized time course of the diameter increase is shown in orange.

stretch experiment would then be the elastic contribution of the monolayer (Figure 4.20, red arrow).

Monolayer mechanics, a viscoelastic fluid? The hypothesis of monolayer relaxation is consistent with the curve of the increase in diameter (Figure 4.18). The shape of this curve is reminiscent of a viscoelastic fluid, a model that has been used to describe monolayer and tissue mechanics in the literature [160, 193]. Viscoelasticity usually comes from a tension (or strain) minimization process, through cell elongation and increased proliferation.

Gel mechanics, an elasto-plastic solid? If the gel were purely elastic, then the channel should relax back to its original diameter upon removal of the pressure. This was indeed observed for short time steps (see Chapter 2 & 3). However, in the stretch experiments, which are actually creep tests, the channel does not revert back to its initial diameter. Either something (the monolayer?) is preventing the gel from relaxing back or the gel has been plastically deformed. The former idea is unlikely: thin stiff films are strong under traction but perform poorly under compression where they simply buckle. The plastic deformation strikes me as a more plausible explanation. Elasto-plasticity has been reported in collagen hydrogels [154]. For a hydrogel at a collagen concentration of 1 mg/ml (six times lower than what I used), a plasticity of up to 0.6 (meaning the gel would only relax to 40% of its initial dimensions) has been reported after 15 min of a creep test. In my experiments, the creep test lasts for hours.

4.2.6.5 A thin viscoelastic fluid film encased in a soft poroelasto-plastic substrate?

Creep test, diameter decrease after load removal? If this theory is correct and the system can be considered as a thin viscoelastic fluid film encased in a soft poroelasto-plastic substrate, then the progressive diameter increase as the monolayer and/or the gel slackens would suggest that the system, including the monolayer, is under constant tension. To test this idea, I measured the difference in diameter of stretched channels before and after removing the load (decreasing luminal pressure to zero). The diameter under zero load corresponded to the resting length L_0. Any difference between the initial length L and L_0

would be indicative of tension ($L > L_0$) or compression in the monolayer ($L < L_0$). The magnitude of the stress would then be proportional to the length difference.

The results are shown in figure 4.21, with the instantaneous diameter change plotted as a function of outlet pressure in channels that were stretched for 7 (blue) and 24 (purple) h. When the load was removed, the channel diameter decreased, indicating that the channel was indeed still under tension ($L > L_0$). The diameter decrease was proportional to the initial load (dashed blue line), indicative of higher tension in monolayers under higher loads. This suggests that the remaining tension in the monolayer is in fact due to the luminal pressure and the applied traction stresses. Finally, the diameter decrease was smaller for channels that were stretched for 24 h (purple), showing that the tension was dissipated (by the gel and/or the monolayer) between 7 and 24 h.

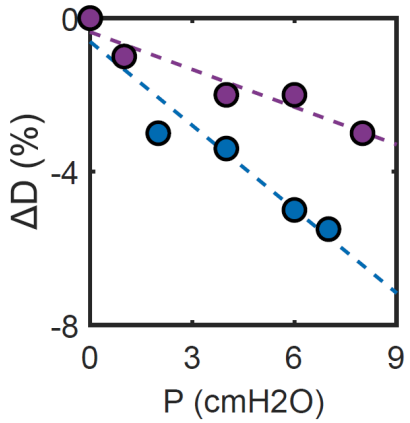

FIGURE 4.21: Luminal diameter change after pressure release as a function of pressure, after 7 (blue) and 24 (purple) h of static stretch. Dots are the mean diameter change in each channel, and dashed lines are linear fits to highlight the two different decreasing trends.

Working model My current hypothesis, which is purely a conjecture at this stage, is that the diameter increase involves a three-step process: (1) at the beginning, the monolayer is the load-bearing layer and limits the dilation of the channel; (2) subsequently there is a progressive extension of the monolayer until the channel reaches a dilation level corresponding to the pore pressure equilibrium in the gel; (3) at this point, the gel becomes the load-bearing structure, and the stretched monolayer behaves like a "floppy" thin film inside the gel lumen that has completely dissipated its tension. In the absence of definitive validation, I wanted to perform a rapid scaling analysis to check if the orders of magnitude were correct. The maximum dilation seems to be around 70 µm (Figure 4.18) for an outlet pressure of 8 cmH_2O. A quick numerical simulation estimates that the Young's modulus of a purely elastic solid yielding a dilation of 70 µm is 2 kPa, which matches the measured hydrogel elastic modulus, around 1 kPa. Finally, the best way to test this idea would be via laser ablation to assess monolayer tension at different time points, which I plan to do. I would also like to repeat the load release experiments at time points farther along in the experiment to see if the monolayer tension can be fully dissipated and if the diameter reaches a plateau at the gel maximum diameter.

4.2.6.6 Decoupling the contribution of the monolayer and of the gel

The three-step mechanical model outlined above is extremely complex and contains many rheological phenomena happening in parallel. To test it, I would need to decouple the contributions of the monolayer and of the gel. On the gel side, I plan on changing the width of the hydrogel, which determines the maximum dilation of the gel (see Chapter 2), without

changing its stiffness, thereby keeping the load distribution between the cells and the gel unchanged. If the characteristic exponential time is due to the cells, it should not change, while the final plateau diameter, determined by the gel, should be modified. To test the monolayer contribution, I plan on using acto-myosin inhibitors, such as blebbistatin, to decrease monolayer stiffness. The contribution of the monolayer to the dynamics of the diameter increase should be smaller, with a shorter characteristic exponential time, and elements due to the gel such as the plateau value should remain unchanged.

I can also change the mechanical contribution of the monolayer by disrupting cell-cell junctions. This should perturb the physical integrity of the tissue, analogous to having a stiffness of zero, while maintaining (partially) the flow shielding effect. The physical presence of a confluent layer of cells blocks the gel pores and should prevent most of the fluid from seeping into the gel. I expect (1) the characteristic exponential time to be close to zero, with the channel increasing rapidly to the gel maximum dilation, as the monolayer cannot act as a thin stiff film anymore; and (2) the final plateau to be unchanged, as it is determined by the gel properties and the luminal pressure. If the flow shielding effect is reduced by the increased permeability of a monolayer without junctions, the equilibrium diameter would be smaller due to increased pore pressure. The predicted curves of the diameter as a function of time, based on this very complex and hypothetical model, are shown in panel A.

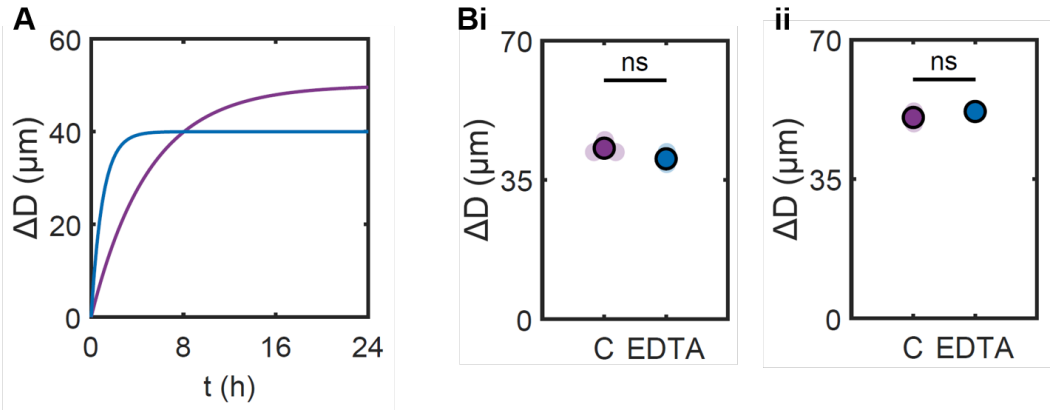

FIGURE 4.22: **A.** Schematics of the hypothetical increase in diameter as a function of time for the control (purple) and with cell-cell junction disruption (blue). **B.** Average increase in diameter after 7 h for an outlet pressure of 6 (**i**) and 8 (**ii**) cmH_2O of static stretch, with (blue, (A) N=2 and (B) N=1) and without (purple, N=3) EDTA.

I reanalyzed the images from the two EDTA experiments in order to compare them to the predicted curves. The final diameter of a creep test with an outlet pressure of 6 cmH_2O (**Bi**) and one with 8 cmH_2O (**Bii**) are shown in Figure 4.22. In both experiments, EDTA channels had similar diameters to the control channels, which would match the intersection point between the two predicted curves (**Bii**). I plan on redoing the EDTA experiments with the creep test format: I want to combine EDTA with the time lapse approach, to measure the diameter of the channels as a function of time before and after load removal. The comparison of the experimental curves with the predicted curves for the EDTA, blebbistatin and gel width experiments should provide enough information to test the validity of the current working model.

4.2.7 Underlying mechanism

4.2.7.1 Mechanical integrity: the tale of hand-holding reinforced Jell-O

Cytoskeletal reinforcement The most notable stretch-induced internal reorganization observed in ECs is that of the cytoskeleton, with the formation of thick central stress fibers in the tension direction. The theory of tension minimization predicts the exact opposite, with the tension direction being the most unfavorable as it maximizes tension in the stress fibers (see section 4.1). Another theory must therefore be formulated to explain the parallel alignment, and it needs to take into account the specificity of this stretch assay. The major difference between the literature and my microvessel is that in my system what I control and impose is the tensile stress and not the strain. As a result, the tension in the cytoskeleton is also imposed and thus cannot be minimized. The cells nonetheless can minimize their strain to prevent monolayer disruption or cell tearing, and this can be accomplished by stiffening in the tension direction via cytoskeletal reinforcement (formation of stress fibers), similar to reinforced Jell-O. The cytoskeletal reorientation can also be seen as necessary for active cell remodeling, as the cell shape is driven by the cytoskeleton. By elongating circumferentially, the cells redistribute their total area and reduce their tension in the stretch direction. It would be interesting to see how those two concepts fit in the context of the tensional homeostasis theory which postulates that cells tend to normalize their tension toward an equilibrium value after perturbation. The notions of strain and tension are notably delicate in active materials such as cells (see section 1.2). My hypothetical mechanism would require careful physical modeling to be definitively validated (see section 5.1).

Strengthening cell-cell junctions through focal adherens junction formation Cell-cell junctions are likely to be the mechanical weakest link in a monolayer, as they are extremely thin structures, and they rely on VE-cadherin dimers for physical strength. AJs have been shown to be dynamically remodeled into FAJs under tension (see section 1.3) [10]. As part of their response to tensile stresses in my microvessel, ECs displayed both linear AJs and FAJs (Figure 4.23). Linear AJs were found almost exclusively in the circumferential direction, along the tension direction, whereas FAJs tended to be orthogonal to the tension, i.e. longitudinally. Junctions oriented longitudinally were under high normal forces, with the tensional stresses working to tear the junctions open. Part of the mechanism to protect physical integrity of a monolayer under tension seems to be the transformation of linear AJs into FAJs to increase junctional strength.

Transcellular actin belt Another advantage of forming FAJs orthogonal to the tension direction is their ability to enable transendothelial actin cables running through these FAJs [9]. Immunostaining in the microvessel post-stretch showed stress fibers that seem to be continuous through the FAJ jagged teeth. FAJs appear to enable stress fibers to run across several cells, with one seemingly continuous cable spanning four or five cells (Figure 4.24). The cytoskeleton of the adjacent cell in the monolayer can be described as a network of transcellular actin belts that encircle the channel, with an obvious analogy to the metal bands encircling wine barrels to hold the tensile stresses. This description reinforces the previous hypothesis of strain minimization and monolayer integrity protection. Future investigation of the transcellular actin belts might require revisiting the idea of unfolding whole channel Z-stacks (see section 4.2.8) to visualize long belt-like fibers that quickly go out of focus due to the cylindrical geometry and their circumferential orientation.

4.2.7.2 Adherens junction dependence

Single cells Most of the strain EC literature has focused on single cells. The few reports on confluent ECs seem to indicate a different behavior. Therefore, I wanted to clarify the role of

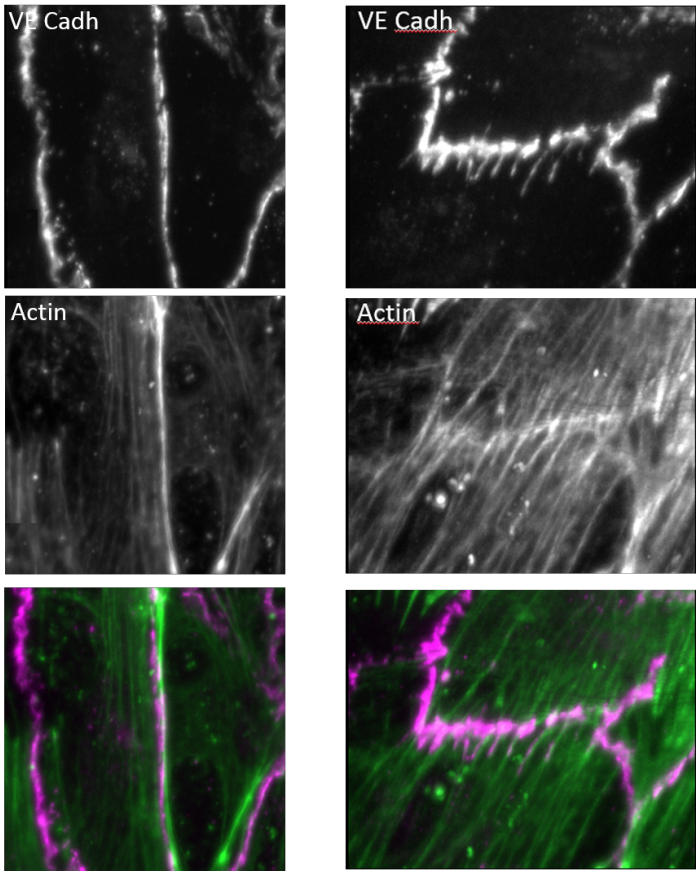

FIGURE 4.23: Representative images of linear (left) and jagged (right) junctions, with VE-cadherin (top) and actin (middle) staining. Co-localization of actin (green) and VE-cadherin (pink) can be noted in the composite image (bottom).

cell-cell junctions in my microvessel. Stretching channels with subconfluent cells resulted in an absence of cell reorganization, with no particular orientation detectable. Furthermore, in one confluent channel that had a subconfluent region in the channel center, where cells were broadly aligned axially, similar to control channels at low density, while the confluent cells located upstream of this area where circumferentially aligned. These preliminary experiments already point toward cell-cell junctions as being important for sensing and responding to tensile stresses.

Junction disruption To separate the role of cell-cell junctions from that of cell density, I decided to disrupt adherens junction using the calcium chelator EDTA (see section 4.2.4). Stretch failed to elicit the expected response in the EDTA-treated endothelium. After 7 h, ECs were still randomly oriented and did not elongate, with an aspect ratio close to 1. Their cytoskeleton was also randomly organized with no preferential direction of fiber alignment (Figure 4.25). Interestingly, the cytoskeleton was still remodeled into very thick stress fiber bundles, suggesting that cells were still partially under mechanical stress.

In an experiment in which EDTA concentration fell below the threshold for complete AJ disruption but was sufficiently high to perturb the junctions, interesting results were observed. More specifically, although still present, AJs did not remodel into FAJs which probably require higher calcium levels to form, and the cells also showed less pronounced alignment after 7 h of stretch (Figure 4.25). This modified response in the absence of FAJs suggests a crucial role for these structures in cell tension sensing, acting as a possible mechanosensor (see paragraph below) and/or as a possible organizing complex for the actin belt in the remodeling process

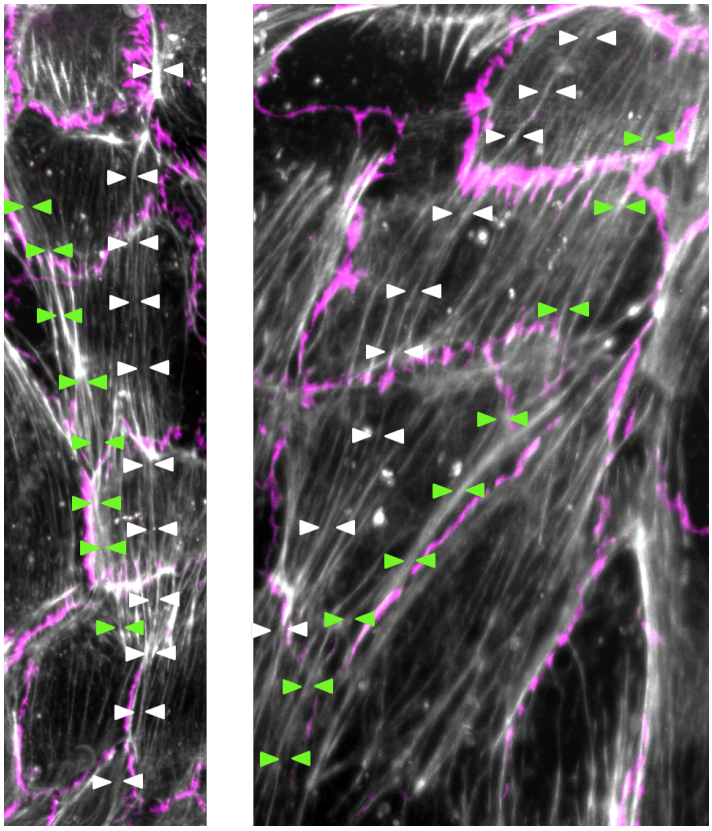

FIGURE 4.24: Representative MIP composite images of actin (gray) and adherens junctions (pink) in a channel after 7 h of stretch showing transcellular actin fibers. Continuous filaments running through 4-6 cells are delineated with the white and green arrowhead pairs.

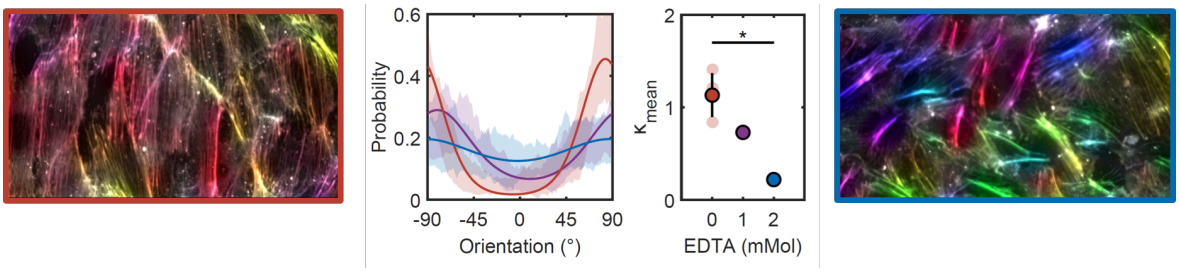

FIGURE 4.25: Inhibition of the cytoskeletal response to stretch by EDTA, which disrupts cell-cell junctions. Representative 40X MIP images of phalloidin staining of a control (red) and EDTA-treated (blue) channel, color coded for stress fiber orientation, show the lack of circumferential alignment of the stress fibers. Von Mises distribution fits (solid line) for the control (red), 1 mM (purple) and 2 mM (blue) EDTA conditions are shown in the left graph, with the standard deviation of all the axial positions (shadows). Channel-averaged concentration parameter K as a function of EDTA concentration is shown in the right graph.

(see paragraph above). This accidental experiment would need to be reproduced in the future by inhibiting FAJs in a controlled manner. The use of an alpha-catenin mutant EC line, which prevents FAJ formation, is thus planned for future experiments in collaboration with Dr Stephan Huveneers' laboratory (see section 5.2.2).

4.2.7.3 Mechanosensors

One interesting pathway towards elucidating the mechanisms underlying stretch responsiveness is the identification of the mechanosensors involved in tension sensing. A multitude of

proteins have been shown to be mechanosensitive in ECs (see section 1.4), and I have decided to focus on those associated with FAs and junctions. A third group of proteins that could be pertinent would be stretch-activated ion channels, such as piezzo-1, that I did not have the time to investigate during my Ph.D.

Focal adhesions Integrins, and more generally FAs, are well known mechanosensors of strain and stretch. How important are they in my microvessel where cells are confluent and live on a soft substrate? In fact, both confluence and substrate stiffness regulate FAs: FAs have been shown to be downregulated by both substrate softness and adherens junctions in confluent endothelium [194–196]. I observed a similar effect in the channel with very small and sparse FAs, whereas FAs in single ECs plated on glass substrates are much bigger and more dense. FAs were identified as dotted vinculin patterns, located at the tips of an actin stress fibers. It is still unclear if FAs play a role in the process described in this chapter. I plan on disrupting FAs to validate the hypothesis that FAs are not necessary for EC elongation and alignment. This hypothesis is in line with the junction disruption experiment, where EDTA-treated ECs, whose FAs should in principle be unaffected, did not exhibit responsiveness to stretch.

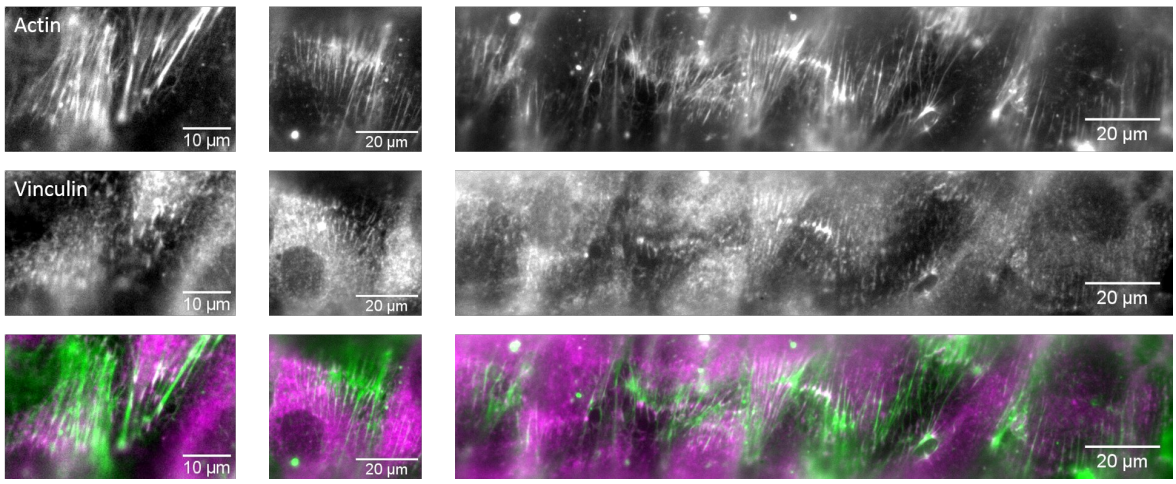

FIGURE 4.26: Representative 40X images of actin (top) and vinculin (middle) staining of stretched channels. FAs are visible in the composite image (bottom) as the white spots where the actin (green) and vinculin (pink) co-localize.

The staining of FAs with vinculin revealed an exotic structure, with a scar-like morphology (Figure 4.26, right panel). A double line of FAs was present in the centerline of the "actin scar", with an array of actin stress fibers on either side. Anchored on only one side to the FAs at the scar center, no other FAs at the other end of the stress fibers were visible. The actin cables seemed to run through the FAs and to be continuous from one side to the other. The FAs in that case would be in the filament center, which would have two free ends. I have never observed such structures in the literature. The closest actin organization to this are the actin asters, where actin bundles are organized radially from a FA. The scar may thus be an anisotropic version of the aster due to the anisotropic tension. In fact, all "actin scars" were oriented along the channel axis, so the stress fibers were oriented circumferentially. Interestingly, the actin filaments were regularly spaced, similar to the spacing found in FAJs. The spacing and the orientation in the tension direction suggest this structure is formed to reinforce the monolayer and hold the tension. Unlike the transcellular actin cables that rely on FAJs, these "actin scars" rely only on FAs and are confined inside the cells, with very short actin bundles.

Junctional mechanosensors To explore the potential mechanosensors responsible for tensile stress detection, I used immunostaining of the usual suspect proteins suggested in the literature to be involved in such processes. I focused on vinculin, which often associates with FAs but can also be part of the FAJ complex when junctions are under tension [10], and zyxin, which can associate with FAs, damaged stress fibers and junctions [197–200]. Both vinculin and zyxin showed strong co-localization with adherens junctions (Figure 4.27). Zyxin did not associate with other visible structures in the cells: it was prominently present at junctions but was diffuse, with low fluorescence intensity, within the rest of the cell. Vinculin localization was more complex: it showed intense fluorescence staining in linear junctions and weaker, but clearly visible, presence at FAs while also being diffuse in the rest of the cell. I did not observe vinculin co-localization with FAJs, despite being a hallmark of these structures according to the literature [10]. There is the possibility that the intensity of vinculin localization at these very small and thin teeth was too low to be detectable relative to the strong diffuse background signal. Overall, these two co-localizations were clues pointing toward a role for junctions as potential mechanosensors of tensional stresses.

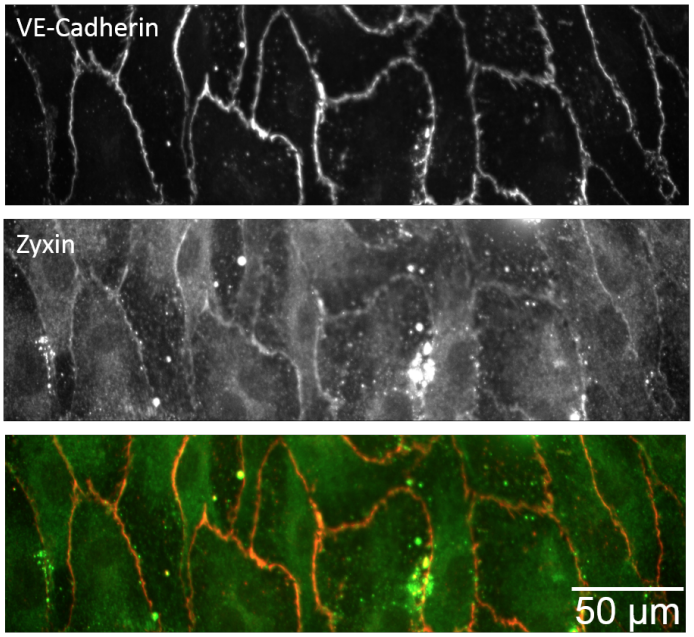

FIGURE 4.27: Representative 40X MIP image of VE-cadherin (top) and zyxin (middle) staining of a stretched channel. Co-localization of zyxin (green) to cell-cell junctions (VE-cadherin, red) can be seen in the composite image (bottom).

4.2.7.4 Redefining our understanding of adherens junctions

Confronting my results against the literature Several papers have described vinculin association with the VE-cadherin complex when under tension, through a conformational change of alpha-catenin [160]. The strong co-localization at linear circumferential junctions would thus suggest that these junctions are under high tension [10], which is logical considering their orientation in the stretch direction. The fact that vinculin has never been reported to associate with linear junctions may be attributable to the fact that previous in vitro systems could not subject cells to tensile stresses directly and that the tension was created by inflammatory agents such as thrombin. An inflammatory reaction would create isotropic tension, always exerted orthogonal to the junction direction, creating the FAJs. My system is the first platform to apply anisotropic tensile stresses on cell-cell junctions, thus subjecting

linear junctions to tension in the junction direction, which may trigger vinculin recruitment.

Tension direction Another important characteristic of FAJs according to the literature is the actin direction, orthogonal to the cell-cell junction, which clearly separates them from linear junctions that have actin filaments running tangent to the cell-cell junction [9, 10]. In various illustrations, the actin filaments are shown as extensions of the VE-cadherin dimer in the case of FAJs. Careful observation of the localization of actin filaments in my microvessel after stretching revealed that (1) the actin is indeed parallel to the linear junctions, but (2) although it is perpendicular to the cell-cell interface at the FAJs, it is still parallel to the adherens junctions themselves at the teeth level (Figure 4.23).

Having a tangent direction for the actin in all types of junctions would make sense in terms of mechanical considerations. Let us first consider intrinsic stresses, generated by the acto-myosin contractility. If actin filaments were perpendicular to the adherens junction, they would exert tension on the cadherin complex and lead to cadherin dissociation and opening of the junction. However, if actin filaments were tangent to the adherens junction, then they would exert a shearing force that would not affect cadherins that can then move freely within the membrane.

Now let us consider the case of extrinsic stresses such as the tensile forces present in my system. To understand how the junctions remodel to hold the tension, we need to differentiate the directions of the cell-cell interface, the AJ and the VE-cadherin dimer. When the cell-cell interface is oriented circumferentially, the tension is along the interface. A simple linear AJ would work: the tension would be parallel to the AJ and will be borne by the tangent actin cables (Figure 4.28 A). When the cell-cell interface is oriented longitudinally, the tension is perpendicular to the interface. In that case, the AJs remodel into FAJs, so that locally the tension is in the direction of the adherens junctions, at the level of each tooth of the FAJs; therefore the tension would once again be borne by the tangent actin cables (Figure 4.28 B).

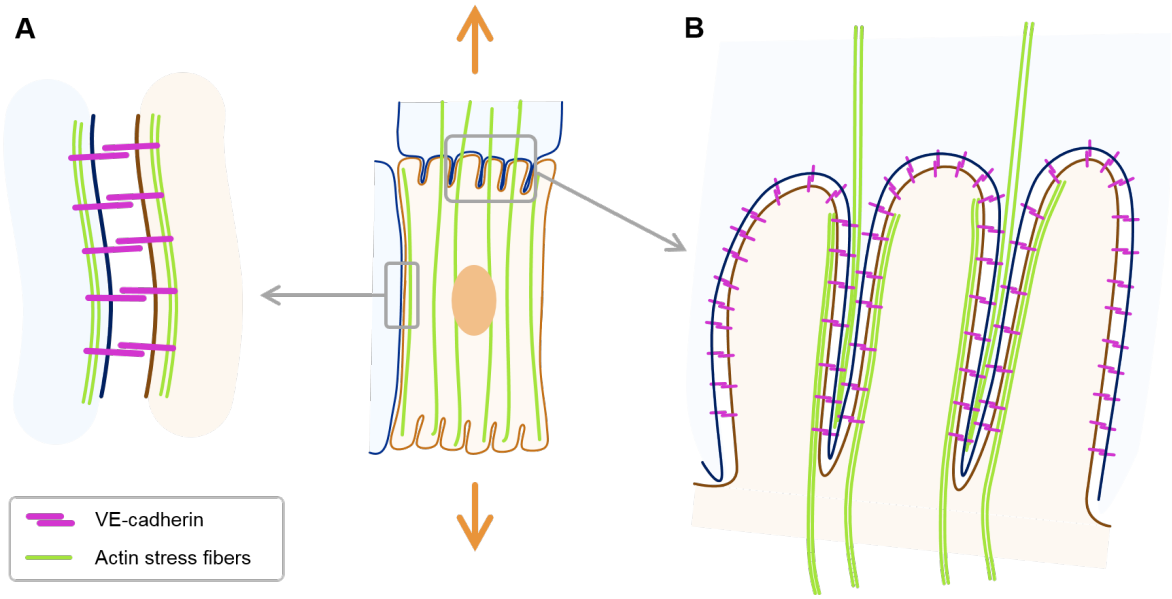

FIGURE 4.28: Schematics of the structure of the cell-cell junctions for the case of a linear AJ (**A**) and for the case of a FAJ (**B**) under tension (orange arrow). VE-cadherin dimers are represented in purple and actin stress fibers in green.

Proposed concept One can think of an AJ as a velcro tape, each VE-cadherin monomer being a hook of the velcro that can bind to a loop from the opposing side, and the tissue holding the hook is the actin cytoskeleton. Velcro provides minimal resistance to normal

opening forces but is very strong against tangential forces, or tension, thanks to the tissue with the hooks. When the cell-cell interface is in the tension direction, the cells use one long velcro in the interface direction to attach to one another. But when the cell-cell interface is perpendicular to the tension direction, the cells use several parallel short velcros in the tension direction.

Based on all these considerations, I would like to propose a new concept for the various forms of adherens junctions, where FAJs would simply be a meta-structure of short linear junctions. AJs would always be linear and parallel to the tension direction, with tangent actin cables, but could be orthogonal to the cell-cell junction direction, thanks to the meta-structure. The meta-structure could either be discontinuous, like the FAJs from the literature, or continuous, like those observed in my microvessel, with a connecting AJ orthogonal to the tension direction. Purely conjectural at this stage, this proposed concept requires further investigation. As we are neither equipped with the necessary tools nor experts in protein complex structure at our laboratory, I decided to contact Dr Stephan Huveneers to set up a collaboration on this project, which I hope will lead to exciting results in the future (see section 5.2.2).

4.2.7.5 Proliferation

The preliminary live cell imaging experiments of flow-based stretch showed that the cells shift from elongated to round during the second phase(after 10 h). The movies also showed an increased number of mitosis events, visible in brightfield, where cells rounded up, became bright and divided into daughter cells. Mechanistically, covering the same surface with more round and smaller cells requires a larger number of cells. Stretch is known to increase proliferation, notably through the YAP pathway (see section 4.1). The experimental data, area calculation and literature all pointed toward proliferation being increased during microvessel exposure to tensile stresses. This hypothesis also fits into the global theory of tension minimization: by increasing the amount of material available to hold the tension (through proliferation), the tension sustained by each cell would be decreased. To quantify the proliferation rates and validate the hypothesis, I tried an EdU incorporation assay, marking the cells that had divided during a given time window (see section 4.2.5). The outcome of both trials were not conclusive as even the control channels exhibited oddly low proliferation rates, probably due to an unusual EC phenotype (see section 4.3.8 below for details). I plan on repeating these experiments using "healthy" ECs in the coming months and to complement them with YAP staining in the hopes of unraveling the mechanobiological pathway responsible for the putative increased proliferation, an essential element for the dissipation of monolayer tension.

4.2.8 LifeAct

A couple of months before the end of my project, a colleague obtained two fluorescent EC lines from a team at College de France, one with fluorescent actin (LifeAct) and one VE-cadherin-GFP. I decided to test the stretch on the LifeAct ECs to (1) visualize the instantaenous initial strain effect on the actin cytoskeleton and (2) record the actin dynamics during cell remodeling.

Imaging LifeAct cells As described in the Methods section, imaging inside the microvessel requires a balance between resolution and the size of the field of view, while at the same time dealing with the additional difficulty of focus drift for live movies due to the small vertical displacement of the channel. The fluorescent signal from LifeAct was much weaker than the one from phalloidin staining, and imaging the cells with a 10X or a 20X objective barely allowed detection of stress fibers. I therefore opted to use a 40X water immersion objective,

which had to be used with a Z-scan on the CREST system to reduce noise from out-of-focus planes and enable a correct MIP (Figure 4.29). Consequently, long duration time-lapse imaging was particularly difficult because of focus drift and photobleaching. The longest time-lapse that I succeeded to record was a few hours.

Instantaneous strain Comparing the actin orientation before and after the pressure step confirmed that the actin cytoskeleton is subjected to strain. As a reminder, the strain are around 5% so the strained configuration will be similar to the initial configuration. Nevertheless I could still detect by eye elongation of the cells in the stretch direction and small changes in the fiber orientation map (Figure 4.29, white arrowheads). Indeed, fibers at a certain angle are stretched only in the circumferential direction and not in the axial direction, which changes the fiber direction. An interesting possibility would be to compute a map of this initial strain, based on image cross-correlation, similar to the PIV method. The strain field could potentially be linked to local heterogeneity in the cellular monolayer. Indeed, the local strain could be affected by the actin cytoskeleton of cells, with initial stress fibers in the stretch direction reducing the strain.

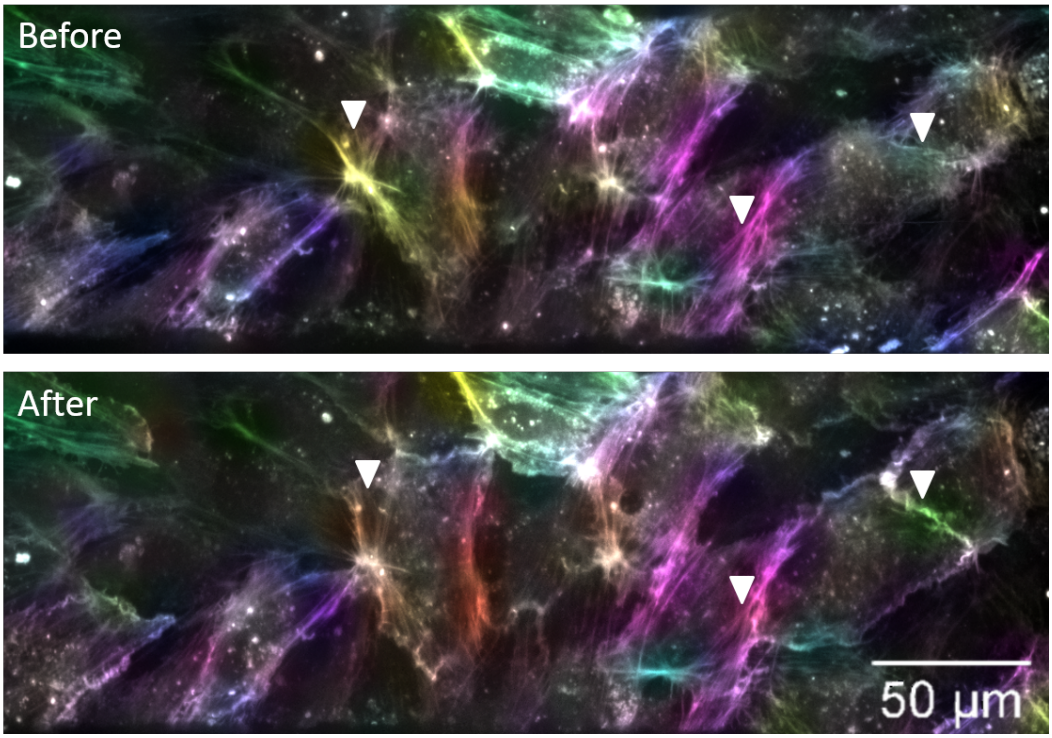

FIGURE 4.29: Snapshots of the actin cytoskeleton in LifeAct cells right before (top) and just after (stretch) a pressure step, color coded for stress fiber orientation. Slight fiber circumferential reorientation by the initial strain is visible in a couple of cells (arrowhead), such as the yellow fiber (top) turning orange (bottom).

Breaking the actin cytoskeleton with excessive strain In one of the stretch experiments, I accidentally increased the pressure level to twice the usual maximum, to 15 cmH_2O. I observed a very striking and surprising phenomenon: the fluorescent structures that should be akin to thin straight filaments characteristic of an actin staining were instead short and wavy and showed strong thermal agitation (Figure 4.30 B). These "wiggly worms" were predominantly located close to the nuclei. This type of structure reminded me of a mitochondria staining, and I first thought the LifeAct transfection was of poor quality and had stained mitochondria.

I therefore repeated the experiments, this time imaging the cells right before and just after the excessive strain. A close-up of the actin network right before (top) and just after (bottom) pressure application in one cell is shown in panel A of figure 4.30. A formerly straight thick actin bundle can be seen to curl after the stretch, reminiscent of an elastic fiber under tension whose ends are suddenly released. This could suggest a rupture of the attachment of the actin to FAs or AJs, or even multiple tears in the actin network itself. I have never seen reports of such events in the literature, and further exploration of the dynamics and potential rupture of the actin cytoskeleton under high tensile stresses are necessary.

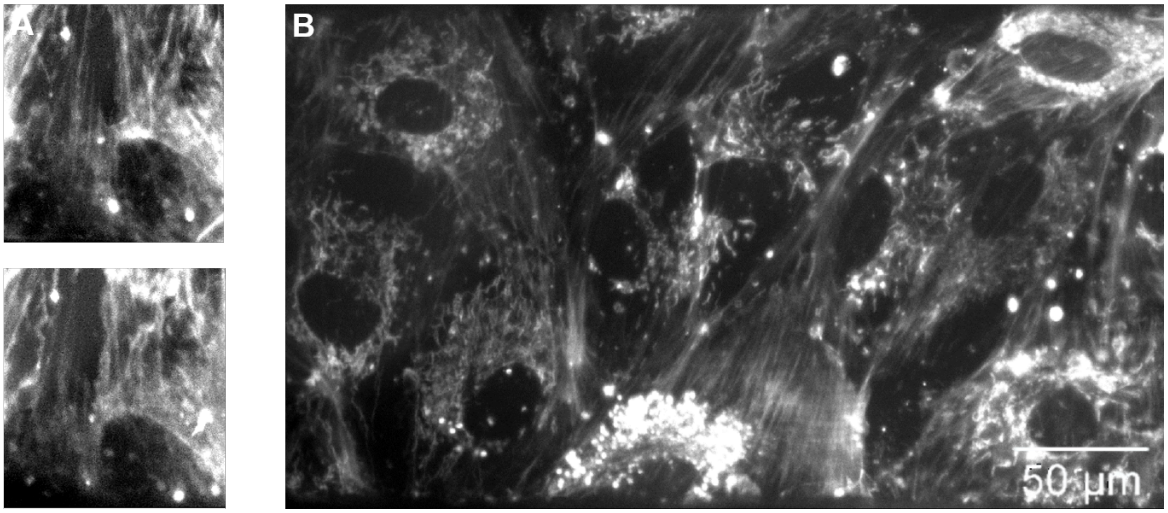

FIGURE 4.30: Actin cytoskeleton damage by excessive strain. **A.** Snapshots of the actin cytoskeleton in LifeAct cells right before (top) and just after (bottom) a pressure step leading to 15 % strain. Straight actin fibers become wiggly, similar to a detached filament under tension. **B.** Representative 40X MIP image of actin in LifeAct cells just after a static 15 % strain, showing wavy actin in most cells, instead of the straight long fibers seen in control cells.

LifeAct ECs were also used to perform laser ablation experiments, presented in the next section, in order to directly address the question of fiber tension pre- and post-stretch.

4.2.9 Laser ablation to measure tension

One of the most direct ways to assess the tension in actin stress fibers is through laser ablation. The concept is simple: the fiber is severed with a laser beam, and fiber recoil is tracked. The dynamics of a viscoelastic fiber's recoil after the cut depends on the initial tension in the fiber. The experiment is more complex and requires cells with fluorescent actin (see section 4.2.2) and a 2-photon microscope in order to focus the light on a single fiber. I found out that the Optics and Bioscience Laboratory at Ecole Polytechnique had a laser ablation setup and the necessary expertise, and I collaborated with Arthur Boutillon, a Ph.D. student under the supervision of Dr. Nicolas David on these studies. The quantification of tension is not absolute but relative, as the properties of stress fibers, namely elasticity and viscosity, are unknown. The tension in the viscoelastic fiber is proportional to the difference between the resting length after the cut and the initial length as well as to the peak retraction velocity of the fiber ends [201, 202].

4.2.9.1 2D proof of concept

Arthur was using laser ablation in zebrafish embryos to ablate several cells at the same time in multiple z planes. We therefore had to adapt the ablation to my geometry, where the target of ablation is a single stress fiber inside a cell on the surface of a channel inside a gel. This necessitated imaging at a much higher spatial resolution, a single Z-plane and on a curved surface. It also meant that the laser beam had to traverse hundreds of microns of hydrogel. We decided to first test stress fiber ablation in a 2D setting in order to verify the feasibility of the experiment and to figure out the correct parameter range.

Interestingly, ablation in cells plated directly on a glass surface led to a highly variable and extreme outcome with cells being either unaffected or obliterated. Despite exploring several parameters, we were unable to find a stable condition. In contrast, ablation in cells plated on a thin layer of hydrogel on top of a glass surface led to very robust and precise stress fiber ablation. Our current hypothesis is that the gel acts as a diffuser and reduces the probability of cell damage by excessive laser power. The optimal parameters are detailed in Section 4.2.6. The ablation was very sensitive to the Z plane focus, with out-of-focus fibers getting bleached and not cut. The recoil of both ends of the cut fiber was clearly visible in the recorded images, confirming the feasibility of laser ablation on cells plated on a hydrogel with this setup.

4.2.9.2 Preliminary results in the microvessel

Experimental setup After the successful stress fiber ablation in 2D, we tried ablation in the microvessel. Because the microscope was upright, the sample had to be inverted, which was especially delicate for my system with the straws serving as reservoirs. The microvessel-on-chip was placed upside down in a petri dish. For the control condition, we made sure that the PDMS reservoirs were in contact with the liquid in the dish to prevent pressure fluctuations by the hanging drop. These fluctuations created large vertical motions of the channel, moving the target cell out of focus during ablation. For the high pressure condition, straws ended up being very practical as we used their bending section to create a 180°turn to keep most of the reservoir length upright, while the part connected to the chip was inverted. The pressure imposed in the channel is defined by the height between the chip and the free surface in the reservoir, similar to the working principle of a gas tank siphon.

Ablation The major difficulty when switching from 2D to the microvessel was the channel curvature. Only the cells at the channel bottom and top could be imaged in a single Z plane. Their stress fibers were relatively in plane and could be ablated and their recoil tracked (Figure 4.31). When plotting the half distance between the fiber ends, I was able to observe the expected exponential shape, characteristic of a Kelvin-Voigt fiber.

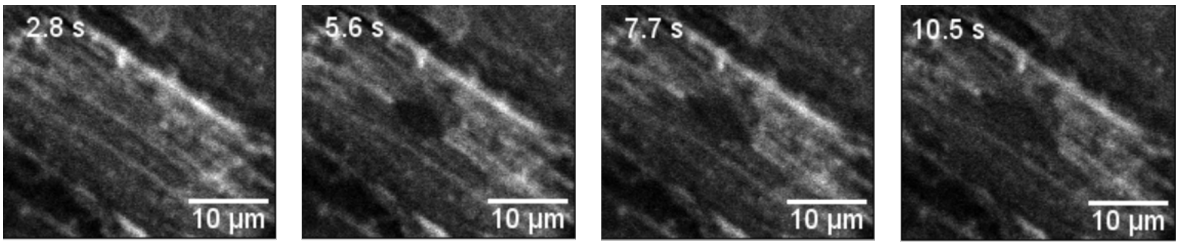

FIGURE 4.31: Time lapse of the actin cytoskeleton of a LifeAct EC after laser ablation of one stress fiber. Both ends of the cut fiber can be seen to retract with time, reflecting the initial fiber tension.

4.2.9.3 Planned experiments

The preliminary tests proved the experimental feasibility of laser ablation in the microvessel. To my knowledge, this technique is the most suited for inferring fiber tension. I have identified tensile stresses as the core of this story, both for the stimulus and the cell response. I therefore plan on using laser ablation as a standard test in future experiments to determine tension under various conditions.

Stress fiber ablation The first planned experiment will be to quantify fiber recoil in a control channel (with thin cortical actin), a stretched channel tested under high pressure (with tense stress fibers) and a stretched channel tested under low pressure (with loose stress fibers). Next, I would like to compare the tension of fibers in stretched channels under medium and high pressure and expect them to show different tension levels. I also plan on quantifying tension in channels with perturbed responses, for instance by disrupting junctions. In this condition, I expect the tension to be lower as it cannot propagate from one cell to another through FAJs, which would provide a clue as to the mechanism underlying the EC response.

Junction ablation Finally, I would like to test the ablation of junctions in GFP-VE-cadherin ECs. Although ablation of junctions has been reported on epithelial cells, demonstrating epithelial junctions are under high tension due to the cortical actin distribution [202, 203], the experiment has not been done on ECs to the best of my knowledge. I would like to ablate junctions in round and randomly oriented cells, which I expect would exhibit constant isotropic tension in their junctions as well as in stretched cells, which should exhibit variable anisotropic tension in their junctions. Indeed, I anticipate that the vertical linear junctions would be under high tension and show rapid recoil, while the horizontal FAJs would be under low tension and show no recoil in the junction direction. Ablation of FAJs might even lead to recoil of both adjacent cells in the vertical direction, as the junction is a tension holder. Combined with a quantification of linear vs. FAJ direction, this experiment would demonstrate the anisotropy of the tension distribution.

4.2.10 Variability

Complex in vitro platforms have definite advantages (see section 1.4), but they also come with several drawbacks. In my opinion, the biggest drawback is experimental variability. When an experiment requires numerous fabrication steps, encompasses multiple materials, requires cell culture for days, the odds of one or more steps failing are non-negligible. Even when the entire process is successfully completed, each step introduces a potential source of chip-to-chip variability. I would like to discuss here the two principal sources of experimental variability in my microvessel-on-chip, namely collagen structure and EC phenotype.

4.2.10.1 Collagen batch

Batch-to-batch variability of collagen has already been discussed in the characterization section in Chapter 2, and it has been identified as a factor that can, for instance, double the strain in the microvessel. Collagen variability is also important for the mechanobiological response of cells in at least two ways: 1) altering the imposed stimulus and 2) changing the cell phenotype. Collagen homogeneity impacts the gel's Young's modulus and its porosity, both of which are critical for imposing the tensile stresses on the endothelium because they change the relative stiffness of the two layers (gel and endothelium) and they alter the transmural pressure difference due to porous medium flow.

The collagen microstructure also changes EC behavior in various ways that remain incompletely understood. The most obvious effect is on the number of FAs present on the basal surface of ECs. Images of vinculin staining from two channels fabricated using two different

collagen batches revealed large differences in the number and size of FAs. Another possible effect is on cell-cell junctional integrity. Indeed, monolayers grown using different collagen batches exhibited differences in these junctions. This is especially important in light of the hypothesized role of cell-cell junctions in responsiveness to stretch.

Comparing the results from experiments on different collagen batches introduces an additional layer of complexity and unknown parameters. As concluded in Chapter 2, the only viable option for reliable conclusions is to compare results from microvessels made with the same batch of collagen, which requires careful experimental planning and collagen stock management.

4.2.10.2 EC phenotype

Experimental difficulties The importance of EC phenotype only became apparent during the last two months of my experiments, when we experienced multiple technical problems concomitantly. To list a few, the CO2 probe of one of the the incubators had a hidden dysfunction, the culture medium's pH was altered, at that point in time we did not know the probe had a problem, we only saw that cells had stopped their normal proliferation rate, so we started using gelatin coating in the culture flasks. Then the culture medium delivery took many weeks, so we used expired medium. Multiple contaminations happened over a couple of weeks in the cell culture room, and we also realized the humidity control in the incubators was variable. During this crisis, ECs exhibited an unusual phenotype, the cause of which could be related to any of the problems listed above, it did highlight the well known issue of cell variability in experimental biology once again. I will briefly describe a series of observations on odd EC behavior, which led me to believe that some EC batches had trans-differentiated into a more fibroblast-like phenotype, affecting their response to stretch. Although uncontrolled and accidental, the results of the experiments with these cells are worth reporting as they suggest a couple of interesting clues as to cell response to tensile stresses.

Phenotypic description The atypical behavior was first observed in culture flasks where ECs were seen to have rough edges and lower proliferation rates, with some cells having a spindle-like shape. When seeded into the channel, the monolayer appeared discontinuous, even at confluent densities, with jagged edges between cells. Immunostaining of actin, adherens junctions and nuclei of control channels revealed a very different monolayer and cell structure (Figure 4.32). Cell-cell junctions were rarely linear and were more discontinuous, reminiscent of the punctate junctions found in inflamed endothelium [10] (Figure 4.32 A). The endothelial monolayer also had large holes between cells (Figure 4.32 A).

The actin cytoskeleton was also unusual, with central stress fibers present in all cells with low fluorescence intensity. A significant fraction of cells had a bilayered actin network, with criss-cross orthogonal fibers at 0 and 90 °(Figure 4.32 B). The absence of cortical actin, which is normally found in healthy confluent endothelia and epithelia, may have been linked to the poor junctional integrity. A criss-cross actin organization has been described in the literature in smooth muscle cells plated on curved substrates [204]. Together, the low junctional staining and predominant central stress fibers suggest a fibroblast-like phenotype. Finally, nuclei were strongly deformed and often polylobate, or even ruptured, often with a small pouch of DNA separated from the main nucleus (Figure 4.32 C). Nuclear deformation of this magnitude is usually associated with nuclear and DNA damage.

Effect on the response to stretch The response of these cells to stretch was broadly similar to that of normal ECs but with some distinct differences. The fibroblast-like cells did not form FAJs as frequently, and the very few FAJs that did form did not have clear teeth-like structures and were rarely associated with actin stress fibers. The actin stress fibers were

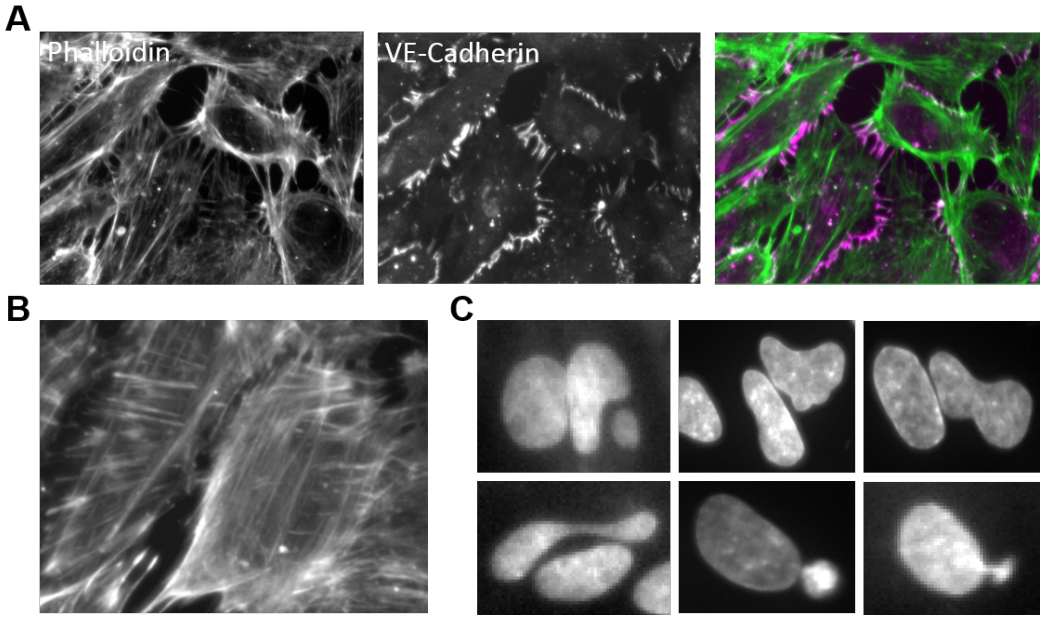

FIGURE 4.32: Characteristics of the atypical phenotype. **A.** Representative immunostaining of phalloidin (left, green) and VE-cadherin (center, pink) showing gaps between cells and poor junctions (right). **B.** Criss-cross actin organization visualized with phalloidin staining. **C.** Highly deformed nuclei, stained with DAPI.

also generally shorter, and transcellular cables were not visible. Taken together with the discontinuous junctions in the control monolayer, these two observations suggest that strong cell-cell junctions are necessary to form both FAJs and the actin belt holding the monolayer tension. The frequency of the "actin scars" was drastically increased in the fibroblast-like cells and constituted the main cytoskeletal structure in these cells. This anchoring of actin stress fibers to FAs could be a mechanism to compensate for the low anchoring on AJs and the absence of transcellular cables. The effect of these modifications on monolayer physical integrity remain unclear.

4.3 Future steps

The future experiments that I hope to perform in the coming months after my defense have been presented in the Results section. I will summarize here a couple of the more important ones and present a few more ambitious future steps that constitute for me the natural extension of this chapter. Overall, these steps can be divided into three parts: a mechanical model to infer stress distribution in the system, a model for the monolayer's active mechanics linked to cellular behavior, and the study of AJ mechanobiology.

4.3.1 Mechanical model of the monolayer and the gel

After the various experiments presented in the Results section, it became abundantly clear that cells respond to tensile stresses. Stresses are much more difficult to measure than strains and need to be inferred from the strain and the constitutive properties of the material. Poroelasticity itself is poorly understood, and computation of stresses inside hydrogels is complex. These stresses depend strongly on the flow shielding effect of the monolayer described in Chapter 2. Because of the flow shielding effect, the elasticity of the monolayer, an essential component of the mechanical model, is completely hidden. Furthermore, the mechanics of an active monolayer and the plasticity of hydrogels over long time points need to also be taken

into account. The result is an intricate mix of many rheologies. The title of my working model illustrates this perfectly : "a thin viscoelastic fluid film encased in a soft poroelasto-plastic substrate". A careful modeling of the various components, at both short and long times, would be useful to test hypotheses and validate the current theory. Building a numerical twin of the microvessel-on-chip under tensile stresses is, in my opinion, a possible future direction for this project. The collaboration with Inria (see Chapter 5) to model the fluid and poroelastic gel has that aim, with the idea of adding the cells as an elastic semi-permeable membrane. This would work for short terms mechanics, when the cells behave as passive materials. Whether it can be adapted to include the cell activity, possibly with a strain-dissipating property, is an open question.

4.3.2 Combining the mechanical model and the cellular mechanisms

More effort also needs to be dedicated towards connecting the mechanical model to the cellular behavior to link the active cells to the monolayer mechanics. I summarize here my current ideas and suggest possible models.

4.3.2.1 Strain minimization

A key idea in my theory is that cells aim to minimize their strain with the goal of protecting the physical integrity of the monolayer and attaining a new homeostatic tension level. Three different strategies are used by the cells: stress fiber formation in the tension direction, elongation in the tension direction, and oriented division and increased proliferation. By forming thick stress fibers in the tension direction, the cells increase their stiffness in that direction and presumably reduce further extension by the continuous tension, thus minimizing their strain. By elongating in the tension direction or dividing along the tension direction, each cell increases its resting length L_0. When strain, i.e. the final length L, is imposed, a higher L_0 leads to reduced tension. But when the tension is imposed (as is the case here), a higher L_0 causes a higher L to keep the tension constant. An interesting future possibility would be to model cell behavior through energy minimization, as energy depends on the product of strain and tension.

4.3.2.2 Long term monolayer mechanics

The collective consequence of strain minimization depends on whether or not the hydrogel has a mechanical contribution and participates in bearing the load. In the scenario where the gel does not contribute, we can imagine the vessel as a free monolayer with a constant luminal pressure. If all the cells decrease their strain (higher L_0), then the imposed tension would stretch the cells further (higher L). This would increase the tissue length in the stretch direction, causing the diameter of the microvessel to increase. As the tension in a thin tube at a fixed pressure increases with tube diameter, the tension in the monolayer would actually increase. This process can then start again, so that the monolayer becomes trapped in a loop and would tend to extend continuously, behaving like a viscoelastic fluid, as long as the pressure is maintained. A model that could potentially be explored in the future is one based on game theory, where individual agent decision based on minimization of a parameter can lead to collective effect with opposite effects on that parameter. In the scenario where the gel contributes, the tension in the monolayer is decreased, reducing further extension and allowing a steady length to be reached. Cells can then minimize their tension, as the strain (or length) is fixed by the gel. The reality in the case of my experiments is probably a combination of both scenarii, with first the free monolayer and second the gel contribution once the monolayer has extended sufficiently.

4.3.3 Mechanobiology & EC mutants

Finally, the possibility of applying tensile stresses and constant load on an endothelium offers many new avenues in EC mechanobiology. The study of AJ remodeling under tension that started a few years ago by using inflammatory agents to generate tension is limited because of the available techniques. The hypotheses I formulated in the Results section, such as tangent actin organization in all AJs and the proposed concept of AJ meta-structures, require deeper investigation to gain in substance. Imaging the dynamics of AJs and the cytoskeleton in live cells would be an exciting new direction. The objective of the collaboration with Dr. Huveneers' laboratory (see Chapter 5) is to tackle these issues and more broadly study AJ mechanobiology, principally by exploiting EC mutants and expertise in molecular biology.

4.4 Conclusions

4.4.1 EC response to tension

The results presented in this chapter showed a striking response of ECs to tension, marked by dynamic remodeling of the individual cells and the overall monolayer. Cells reoriented and elongated in the stretch direction, while their actin cytoskeleton was reorganized into thick actin stress fibers aligned with the tension. The formation of FAJs at longitudinal cell-cell junctions enabled the stress fibers to be mechanically connected between cells, creating transcellular actin cables, or an "actin belt". Disruption of adherens junctions with EDTA abrogated the cell and cytoskeletal alignment. At the monolayer level, this translated into a progressive increase in channel diameter, possibly through an increased and oriented proliferation. The diameter increase was not MMP dependent but was pressure dependent. In this work, I describe a novel collective behavior of ECs in response to tensile stresses, which points towards new directions in endothelial mechanics and mechanobiology.

4.4.2 Importance of tensile stresses for ECs

Although rarely investigated, tensile stresses are essential forces in the vasculature. Circumferential tension is created by the pulsatile blood pressure while longitudinal tension can be created by the movement of the surrounding tissue, such as in the lung, heart or muscles. Indeed, vessels in muscles are oriented longitudinally, leading to significant extension and compression of the vascular wall.

Except in the smallest capillaries, vessels have mural cells embedded in the wall, and one of the main functions of these support cells is to resist the blood pressure. This mechanical function is in line with their circumferential orientation: the contraction of the acto-myosin cytoskeleton of these cells would counteract the tensile stresses in the hoop direction. If the mural cells are the load-bearing layer, the inner endothelium would not be subjected to tension and can align longitudinally in response to the circumferential strain and the longitudinal shear stress. In capillaries, where mural cells are scarce or absent, ECs are thought to be the load bearing structure. In physiological situations, the pressure in the capillary bed should match the homeostatic tension of the capillary EC to create a steady state. However, in pathological situations, such as aging-induced vessel stiffening or hypertension, blood pressure can increase. ECs in the capillaries would be subjected to pathological pressures that could cause remodeling, as suggested by the results presented in this chapter.

4.4.3 Concluding remarks

I particularly appreciated this part of the project, where I actually used the microvessel I had developed to investigate the response of cells to forces never tested previously. The

variety of approaches that had to be deployed, such as monolayer dynamics, tissue mechanics, cellular mechanisms and mechanobiology, to construct the complete picture was an exciting challenge. The data presented in this chapter were a never ending source of surprises that pushed me to exclude certain hypotheses and to formulate new ones almost daily. As evident from the Results section, this work is not finished and needs to be validated and extended. I ventured to only present ideas with their supporting preliminary results and to list the necessary experiments to test the validity of these ideas. I therefore remind the reader of this uncertainty level and hope that he/she has found an interest in taking a walk through my thought process.

Chapter 5

Conclusions & Future work

> Now this is not the end. It is not even the beginning of the end. But it is, perhaps, the end of the beginning.
>
> *Winston Churchill - 1942*

5.1 Conclusions

ECs lining the inner surfaces of blood vessels sense and respond to numerous mechanical forces present in the microvascular environment. Although the influence of wall shear stress, stiffness and curvature has been thoroughly investigated, the role of strain remains less clear, and virtually nothing is known about the response of confluent cell monolayers to tensile stresses. In vitro platforms, such as organ-on-chips, are ideal systems to investigate EC mechanobiology as they offer a controllable and well defined set of mechanical stimuli. During my Ph.D., I developed a microvessel-on-chip that can subject cells to wall tension. I characterized the mechanical behavior of this system in detail and used it to investigate the response of cells to tensile stresses, revealing a novel form of collective behavior.

5.1.1 System development

I started my Ph.D. by developing a hydrogel-based microvessel-on-chip that encompasses both shear stress and circumferential strain in a pulsatile manner. In my system, ECs line the walls of a cylindrical channel with a diameter of 120 microns, templated inside a soft collagen hydrogel. The cells are therefore subjected to physiologically relevant curvature and a physiological substrate stiffness. The microvessel-on-chip relies on luminal flow actuation to generate both the shear stress and the circumferential strain. Luminal flow actuation is a method that has not been employed in other microfluidic systems. The concept is the following: by imposing a given flow rate inside the channel, the luminal pressure is increased due to the channel's hydraulic resistance, which dilates the vessel. A programmable syringe pump can impose a sinusoidal flow rate, leading to pulsatile shear and strain.

After ensuring that the chip fabrication process was robust and after the channels were successfully endothelialized, I conducted an extensive characterization of the mechanical behavior of the system. I measured the range of average shear stresses and strains attainable and documented their variations along the channel axis due to the hydraulic pressure gradient. Because both stresses derive from the luminal pressure, shear and strain in the microvessel-on-chip are tightly coupled. To enable independent control of each stress, I explored three

strategies: (1) adding a hydraulic resistance of variable length at the channel output to increase the luminal pressure while maintaining the shear stress constant; (2) changing the width of the hydrogel, which alters both the strain (through the gel stiffness) and the shear stress (through the gel's hydraulic resistance); and (3) tuning the hydrogel concentration, which also alters both the strain (through the gel's Young's modulus) and the shear stress (through the gel permeability). Finally, I recorded the dynamics of the shear stress and the strain as a function of the sinusoidal waveform, sinusoidal frequency and axial position.

I also demonstrated that the endothelial monolayer has an effect of flow shielding. Because of its low permeability, the endothelium prevents fluid seepage from the lumen into the gel, thereby reducing gel pressure. As the hydrogel is a poroelastic material, i.e. the pore pressure is linked to deformation, reduced gel pressure meant reduced gel swelling and therefore larger channel dilation. The presence of the EC monolayer, despite its stiffness, actually increased channel dilation for a given luminal pressure because of poroelastic considerations. Porous medium flow and the monolayer contribution were modeled with a simple analytical theory based on the analogy to an equivalent electrical circuit. Thanks to this model, I was able to extract permeability values for the hydrogel, a parameter otherwise hard to measure experimentally.

5.1.2 Poroelasticity mechanics

The second part of my Ph.D. was devoted to the study of the dynamics of the poroelastic gel. I started this part by developing a small project to estimate hydrogel stiffness with a simple homemade method. This was done by Elvire Fauchet, a student intern that I supervised. The project led to a perfect example of frugal science and to surprisingly robust Young's modulus values. The values were around 1 kPa, in the correct range for collagen hydrogels.

The luminal flow actuation in the microvessel-on-chip can also be viewed as a hydraulic compression assay. It is, to the best of my knowledge, the first experimental system that exerts a double boundary load onto a poroelastic material, with the pressure applied both on the solid and the fluid. This leads to complex dynamic behavior that I was able to exploit to independently derive the important poroelastic parameters, most notably the Young's modulus and the permeability. The three main observed responses were the dynamics of the channel dilation after a pressure step, the strain distribution in the hydrogel and wave propagation.

5.1.3 Cellular response

The third and final part of my Ph.D. was focused on the investigation of the response of EC monolayers to tensile stresses. To identify what feature was due to stretch, I started with a careful investigation of the control conditions. The initial monolayer state was highly dependent on cell density. Furthermore, the presence of residual tensile stresses determined if the monolayer had a longitudinal or helicoidal alignment. In the latter case, the helicoidal pattern was chiral, with a systematic clockwise direction.

Two methods were then used to apply stretch, either flow-based (low pressure magnitude and large axial pressure gradient) or outlet pressure-based (high pressure magnitudes and virtually constant pressure axially). In both cases, ECs showed prominent reorganization, aligning their overall shape, cytoskeleton and nuclei in the stretch direction. The dynamics were slightly different, with a shared first phase of elongation and alignment, followed by a second phase of rounding up in the case of the flow-based method. The intensity of the orientation was dependent on the pressure magnitude. The initial density dependence influenced the response dynamics, with dense monolayers that have round cells and smaller area showing the most prominent and most rapid response.

Along with the monolayer reorganization came a significant increase in vessel diameter with time. The increase in diameter was proportional to the applied pressure and required the presence of ECs. Because MMP inhibition did not appear to play a role, the monolayer contribution to the diameter increase was more likely a result of the flow shielding effect. In the presence of cells, the gel deforms significantly more, behaving like an elastic material (because the pore pressure is maintained low, there is no poroelastic swelling of the gel). During the first phase of the diameter increase, the stiff monolayer is the load-bearing layer and behaves like a viscoelastic fluid. This behavior appears to stem from cell elongation and increased proliferation, a dual mechanism employed by cells to reduce their strain. As a high tissue tension is maintained by the fixed luminal pressure, the tissue is progressively stretched further, increasing in length to compensate for the strain reduction by the cells. During the second phase of the diameter increase, the diameter reaches a value close to the maximum dilation of the elastic gel, and the gel becomes the load-bearing layer. The diameter then attains a plateau. Finally, the gel was shown to behave like an elasto-plastic solid where the diameter did not revert back to its original value upon load removal. To sum up, the monolayer is a viscoelastic fluid that slackens progressively due to cellular mechanisms for strain minimization. This viscoelastic fluid is encased inside an elasto-plastic gel whose porosity plays a relatively minor role in the presence of cells due to the flow shielding effect of the monolayer.

In addition to the reorientation of the cells and their cytoskeleton, the monolayer was shown to manifest mechanical reinforcement. AJs were remodeled into FAJs, a specialized structure that forms under tension and connects actin cables from adjacent cells. The cortical network of actin filaments also remodeled into thick bundles of central stress fibers. The association of the stress fibers and the FAJs enabled the formation of transendothelial actin cables, oriented circumferentially and spanning several cells. AJ disruption using EDTA abrogated the EC response to stretch, underscoring the central role of AJs as mechanosensors and/or mechanoeffectors. Furthermore, two other candidate mechanosensors, namely vinculin and zyxin, showed pronounced co-localization with cell-cell junctions.

5.1.4 Concluding remarks

I succeeded in developing a novel flow-actuated microvessel-on-chip, which ended up being a versatile platform with numerous applications in various fields. I used this chip to explore the dynamics of poroelasticity in hydrogels as a novel form of mechanical test, the hydraulic compression assay. I also discovered a new monolayer response to tensile stresses, formulated a hypothesis for the underlying tissue-level mechanism and explored the intracellular mechanism through junctional and cytoskeletal remodeling.

In the three main projects of my Ph.D. research, the close combination of mechanics and biology was essential to grasp the phenomena at play, which was exactly what I was looking for when I started this project. During these three years I had the opportunity to do experimental work, numerical simulations and theoretical analysis. The experiments were extremely varied, from platform development and debugging to mechanical testing and characterization of a biomaterial, and including cell culture and imaging. Because the subject of my thesis is multidisciplinary, I had to make connections and imagine links among multiple fields and to learn and teach myself new concepts constantly. It was challenging, exciting and an incredible opportunity to grow as a researcher.

5.2 Ongoing collaborations

5.2.1 Improving numerical models of poroelasticity

When I first observed the overshoot in the bare channel dilation and started to wonder if this could be explained through poroelasticity, I decided to contact experts in poroelastic behavior to validate my naive hypotheses. I met with Dr Dominique Chapelle and Dr Philippe Moireau from MEDISIM, a joint research team between Inria and the Laboratoire de Mécanique des Solides (LMS) located on campus. They have experience in developing theoretical frameworks of poroelasticity and their numerical implementation to model biological tissues such as the heart [205–207]. After my presentation to them of the principal experimental observations, they confirmed my intuition that poroelasticity may explain the observations, and they were open to the idea of collaborating. My experimental platform offers a simple geometry in a finely controlled configuration. With a battery of measurements and characterizations already performed, this platform provided an excellent combination for testing and validation of their theoretical predictions. Their model was likewise the tool I needed to infer unknown gel properties such as permeability from an inverse problem analysis, demonstrating that poroelasticity could explain most of the gel's dynamic behavior.

A couple of months after my presentation to the MEDISIM colleagues, they hired Mathieu Barré for an internship on the poroelastic modeling of biological tissues, and the collaboration was officially launched at that point. Mathieu has since then been awarded a Ph.D. fellowship to continue his work on the same project under the supervision of Dr Philippe Moireau and Dr Celine Grandmont. We have been in close interaction over the past year, and we have been collaborating on the modeling of the hydrogel in the microvessel-on-chip with their poroelastic framework. The bulk of the initial work has been to add the coupling of fluid-poroelastic-solid-interaction to the free fluid flow in the channel. Mathieu is currently finalizing the implementation of the coupling, and we should soon be in position to start comparing the numerical and experimental results in order to validate the model and infer interesting parameters. An advantage their approach offers is the possibility to investigate the dynamics of the gel, including the overshoot, strain rate dependency and wave propagation, both in the channel and in the gel.

The next step will be to add the cell monolayer into the model, either as a continuous poroelastic material or as a thin poroelastic membrane at the channel wall. This improved version of the model would enable us to infer the elastic contribution of the monolayer, which is currently concealed by our inability to model gel deformation as a function of applied pressure and pore pressure, both of which depend on the monolayer presence through the shielding effect (see Chapter 2).

This collaboration has been a rich experience for me. I discovered how applied mathematicians build new frameworks by literally creating equations that faithfully describe a physical reality. I also had the first hand experience of seeing*in vitro* systems used as tools for model validation or parameter inference. Mathieu's final goal is to model the poroelastic behavior of lungs in a complex geometry and over a wide range of values for each parameter. He also benefits largely from our collaboration because he is able to confront his results with experiments for a simple case study, allowing him to improve his model and be more confident in the output before targeting more challenging *in vivo* situations.

5.2.2 The microvessel as a mechanical testing platform

Another interesting experience for me was setting up a collaboration with Suzette Lust, a Ph.D. student in Prof. Eileen Gentleman's laboratory at King's College London. I met Suzette at an online conference. She works on the study of the effect of interstitial flow-

derived shear stresses on SMCs, and the role that these stresses play in the development of aneurysms. She has developed a hydrogel-based bioreactor with SMCs embedded in a polyethylene glycol- (PEG-) based gel. A pressure difference across the gel drives the porous flow through it, generating interstitial flow on the cells. A key parameter to model the flow in her system is the gel permeability which, as discussed in Chapter 3, is extremely difficult to measure directly for soft materials such as hydrogels. After our discussion, we concluded that it would be interesting to use the microvessel-on-chip as a mechanical testing platform in order to measure the permeability of her gel. We can indeed compute the permeability by measuring the flow loss for different luminal pressures and flow rates, either with the simple analytical model (see Chapter 2) or with numerical simulations (see Chapter 3). Although in its early stages, this collaboration already illustrates the potential of using microfluidic systems such as the one I developed not only as biological mimics but also as mechanical testing platforms for micromechanical measurements.

5.2.3 Tensile stresses and focal adherens junction structure

The last and most recent collaboration is more on the biology side, with Dr. Stefan Huveneers, a PI investigating endothelial cell-cell junctions. He is interested in vascular integrity and in the regulation of cell-cell junctions and adhesions by cytoskeletal and external forces. I first contacted him to discuss the formation of FAJs under tensile stresses in my system and the similarities and differences I observed in their structure. During the discussion, the possibility of collaborating was mentioned, both in the short term with him sharing genetically modified ECs, and in the longer term with my microvessel used in their projects. I am particularly interested in two of their cell lines for the follow-up of my project. The first is a double fluorescent line expressing GFP-VE-cadherin and mCherry-LifeAct, and the second expresses a mutant of alpha-catenin that prevents the binding of vinculin and thus the formation of FAJs [10]. I plan on using both of these constructs in the coming months to tackle the open questions identified in Chapter 4 and validate my hypotheses. Images from my microvessel-on-chip preprint (Chapter 2) have been included in a grant proposal written by Dr Huveneers to investigate the role of various proteins in the FAJ complex formation in response to tensile stresses.

5.3 Future projects

The microvessel-on-chip that I have developed has caught the attention of a number of biologists who have expressed interest in adopting the platform for their studies on vascular mechanobiology. During my Ph.D., I carried out a few exploratory experiments to test ideas on what would be the natural continuation of my work and to validate their feasibility. They are currently the subject of two Ph.D. projects carried out by Clara Ramon-Lozano and Sara Barrasa-Ramos. I am actively involved in both projects which I present briefly in the following two sections. I will conclude this chapter with a brief opening on other non-vascular applications.

5.3.1 Complexifying the microvessel: adding mural cells

As presented in Chapter 1, blood vessels are composed of multiple cell types including mural cells. Mural cells are essential for many vascular functions in blood vessels of all sizes including the smallest capillaries where pericytes wrap around the vessel. During the literature review I undertook at the beginning of my Ph.D., I realized that pericytes were an understudied cell type, especially compared to ECs or even SMCs. Pericyte response to their mechanical microenvironment remains largely unexplored. However, in my literature review, I was able

to connect some hidden clues in studies from different fields which used various approaches. I felt that a clear and centralized picture of the state-of-the-art on pericyte mechanics and mechanobiology was missing and decided to write a review on the subject and present the connections I made to the pericyte community [208]. This community received my review very well and invited me to give a junior researcher talk at the symposium on vascular mural cells, as part of the Europhysiology meeting.

Similar microvessel-on-chip studies have successfully co-cultured pericytes with ECs, with the pericytes localizing abluminally through self organization. Including pericytes in my microvessel would certainly create a more physiologically relevant environment and would allow us to study at least two different phenomena: the impact of pericytes on EC responses to mechanical stresses and the effect of mechanical stresses on the pericytes themselves.

For instance, one of my experiments in the microvessel with only pericytes cultured at high density showed a strong longitudinal alignment of pericytes under low flow conditions and with no stretch. Pericytes had a spindle-like morphology and were extremely elongated and perfectly aligned at 0°. This observation raises two interesting hypotheses: pericytes may have a lower sensitivity threshold to shear stress and may be capable of fully sensing magnitudes as low as 0.01 Pa; or pericytes might be very sensitive to curvature, with their longer bodies integrating bending stresses over larger distances. This subject is now part of Clara's work.

5.3.2 Breaking the quiescence: EC angiogenesis

All the work presented so far has focused on quiescent endothelia, meaning ECs that divide minimally once they attain confluence and stay in plane. In the non-quiescent (active) state, ECs migrate collectively out of the vessel wall into the surrounding matrix and form dead-ended tubes. This process is known as angiogenesis and leads to the formation of new capillary networks after the newly formed tubes connect to target vessels. Mechanical forces are known to regulate angiogenesis, but the precise contribution of each force remains unclear. Sara's Ph.D. work will investigate this process in the microvessel-on-chip, exploring all the different forces at play, both solid- and fluid-derived.

Sara and I had the opportunity to write a review article on the regulatory role of mechanical forces in the early phases of angiogenesis. This manuscript will be submitted soon. It was a very different experience from the two previous reviews I wrote. For this one, I used my own experience to mentor Sara through the process of defining the scope, building an outline, selecting references, synthesizing data, structuring a central message and adding personal hypotheses and opinions. This experience gave me a preview of the different skills involved in supervising and editing someone else's writing, and it was overall an excellent learning opportunity.

5.3.3 Beyond the vasculature: tensile stresses in epithelia

To close this chapter, I will give an example of the wider impact that my microvessel-on-chip can have if pushed beyond the vascular field. Indeed, epithelial cells have already been cultured inside similar templated microchannels [155]. By culturing epithelial cells in the channel, this system can become a lung-on-chip or a gut-on-chip. Tensile stresses in these organs due to breathing or digestion are omnipresent and extremely important. Tensile stresses are also crucial in the field of morphogenesis, where collective cell movement and tension distribution shape the embryo. This chip offers the ability to subject these cells to a controlled level of unidirectional tensile stress in a well-defined microenvironment.

Another example I can mention is the replication of the scaling law found between apical stress fibers and cell size in developing drosophila [209]. The defined cylindrical geometry,

imaging resolution, microenvironment tuning, and cell line control are all features of this chip that would unlock several follow-up studies to push this intriguing result further and unravel the underlying mechanisms. Tensile stresses are universal forces present in most living systems, and the microvessel-on-chip I developed is one of the first in vitro systems that applies tensile stresses on the cells directly. I believe the biophysics and mechanobiology communities will appreciate the added value of this system and will use it to address many challenging questions.

Appendix A

Review on EC mechanobiology

communications biology

REVIEW ARTICLE

https://doi.org/10.1038/s42003-021-02285-w OPEN

Integration of substrate- and flow-derived stresses in endothelial cell mechanobiology

Claire A. Dessalles[1,2], Claire Leclech[1,2], Alessia Castagnino[1] & Abdul I. Barakat[1✉]

Endothelial cells (ECs) lining all blood vessels are subjected to large mechanical stresses that regulate their structure and function in health and disease. Here, we review EC responses to substrate-derived biophysical cues, namely topography, curvature, and stiffness, as well as to flow-derived stresses, notably shear stress, pressure, and tensile stresses. Because these mechanical cues in vivo are coupled and are exerted simultaneously on ECs, we also review the effects of multiple cues and describe burgeoning in vitro approaches for elucidating how ECs integrate and interpret various mechanical stimuli. We conclude by highlighting key open questions and upcoming challenges in the field of EC mechanobiology.

Research over the past two decades has established that mechanical forces are potent regulators of cellular structure and function in both health and disease. While all cells in our tissues experience physical forces, mechanical stimulation plays a particularly prominent role in the vascular system. By virtue of its strategic location at the interface between the bloodstream and the vascular wall, the endothelium is constantly subjected to a complex set of mechanical stresses that are often highly dynamic in nature. The ability of the endothelium to sense these biomechanical stimuli and to integrate information from different types of biophysical cues is essential for regulating vascular function.

The mechanical environment of the endothelium consists of a collection of intertwined stresses, which can be broadly divided into two categories (Fig. 1): contact stresses emanating from physical features of the underlying substrate and fluid-derived stresses due to blood flow. The contact stresses act on the endothelial cell (EC) basal surface and are principally due to substrate topography, curvature, and stiffness. The fluid-derived stresses consist of the shear stress on the EC apical surface due to the flow of viscous blood, the compressive blood pressure, and the circumferential and axial tensile stresses due respectively to the transmural pressure difference and tissue movement. All these stresses are dynamic in nature, albeit with considerably different time scales. While substrate physical properties at a given vascular location remain globally constant at short time scales, shear, pressure, and tensile forces are highly dynamic and vary cyclically due to blood flow pulsatility. In addition, the nature and magnitude of all these mechanical cues vary with location in the vasculature and across organs.

EC sensing and responsiveness to mechanical forces are critical for vascular homeostasis. How mechanical stimuli exerted on the EC surface are converted into intracellular biochemical responses has been reviewed elsewhere[1–3] and will therefore not be detailed here. We can nevertheless mention that the various candidate mechanosensors in ECs can be categorized based on their cellular location. Apical mechanosensors include mechanosensitive ion channels[4–7], primary cilia[8,9], the glycocalyx[10], GTP-binding proteins[9,11], and caveole[12]. At cell–cell junctions, platelet endothelial adhesion molecule-1, vascular endothelial-cadherin, and vascular endothelial growth factor receptors have been shown to form an elaborate mechanosensory complex[13–15]. Integrins, the principal mechanosensors on the EC basal surface, provide

[1] LadHyX, CNRS, Ecole polytechnique, Institut polytechnique de Paris, Palaiseau, France. [2] These authors contributed equally: Claire A. Dessalles, Claire Leclech. ✉email: abdul.barakat@polytechnique.edu

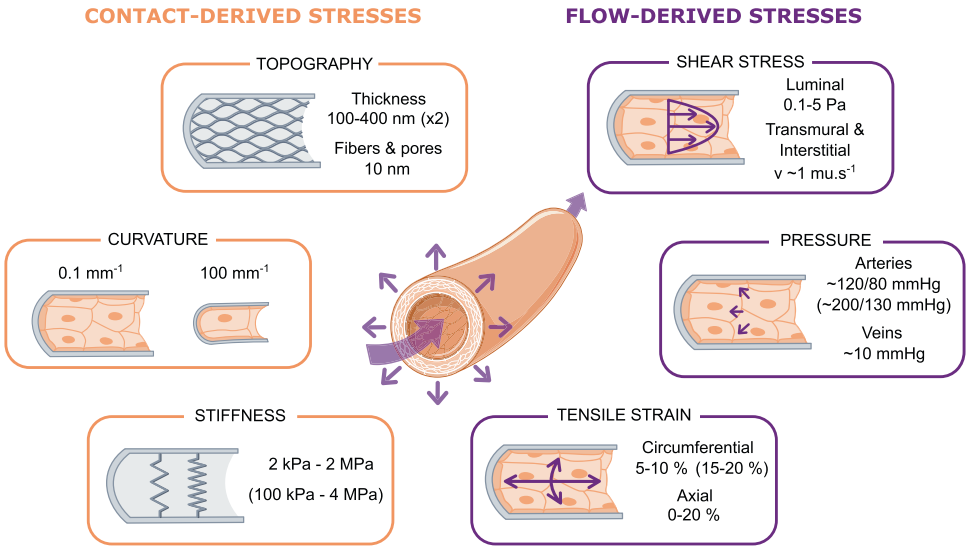

Fig. 1 Summary of the biophysical forces present within the vasculature. Endothelial cells (ECs) within blood vessels are subjected to various mechanical cues, from the substrate (orange, left panels) or from the blood flow (purple, right panels). Physiological (or pathological in parentheses) ranges of values are provided for each type of cue.

a direct link between the actin cytoskeleton and the extracellular matrix (ECM)[16,17] and are involved in the response to both substrate- and flow-derived cues[15].

EC mechanobiology has been the subject of several excellent recent reviews, each with a specific focus: mechanotransduction events and governing mechanisms[2,3], experimental platforms to mechanically stimulate ECs[3,18], angiogenesis and vascular development[19], mechanobiology of vascular diseases[20], and physical/mechanical considerations[21,22]. Here we review EC responses to the different types of contact- and fluid-derived mechanical stresses present in the vasculature. We identify key features of each one of these biophysical cues and discuss how they affect EC morphology, intracellular organization, and overall function. We pay special attention to the interplay among these stresses and how ECs integrate multiple mechanical signals. Throughout the review, we focus on in vitro studies that have greatly advanced our understanding of EC mechanics and assess their physiological relevance and ability to mimic pathological conditions. We conclude by highlighting open questions and describing how recent technological advances promise to offer new avenues in the field of EC mechanobiology.

Substrate-derived biophysical cues

In vivo, the vascular endothelium responds to various biophysical cues derived from the underlying vascular wall structure, most notably the topography of the vascular basement membrane (BM), the curvature of the tubular vessel wall, and the stiffness arising from the mechanical properties of the BM and adjacent cellular and connective layers (Fig. 1).

Topography. Vascular ECs are anchored to a BM that is a few hundred nanometers thick and whose topography takes the form of intermingled fibers and pores[23,24]. The BM thus presents ECs with an isotropic topographical environment at the nanoscale, whereas at the microscale, the topography appears more anisotropic, formed by the organization of nanoscale structures and/or by tissue undulations[23,25].

Influence of topography architecture: anisotropic vs. isotropic substrates. Several types of engineered substrates have been developed to mimic the anisotropy found in some native extracellular environments. Despite being highly idealized configurations that differ considerably from physiological BM topographies, unidirectional grooved substrates consisting of parallel arrays of rectangular grooves and ridges have been widely used because their layout and dimensions can be precisely controlled, thereby providing well characterized biophysical cues to cells (Fig. 2a). Studies on these ridge/groove systems have provided crucial information about fundamental EC responses to anisotropic topographies. For instance, ECs have been shown to migrate, align, and elongate in the direction of grooved substrates[26–33], reproducing EC morphologies encountered in vivo. Cell alignment and elongation are reflected intracellularly by the alignment of actin filaments[26,28,31–33], microtubules[32], and focal adhesions (FAs)[26,29,31]. Additionally, anisotropic grooved surfaces lead to stronger EC adhesion, more oriented migration, and greater migration speeds compared to isotropic surfaces (such as arrays of pillars or holes)[34,35].

To assess the effect of the nanoscale BM roughness found in vivo, different types of rough substrates have been developed[36–38] and have been shown to promote EC adhesion and growth relative to smooth surfaces[36] (Fig. 2a). On these substrates, ECs are typically more elongated than on smooth flat surfaces but less so than on grooved substrates, and they migrate faster than on untreated surfaces[37].

Fibrous networks are attractive model substrates as they resemble the physiological structure and composition of native BMs (Fig. 2a). Aligned (and thus anisotropic) fibers at both the nano- and microscale induce higher levels of cell and cytoskeletal alignment and elongation compared to random fibers[39–42], as well as increased migration directionality[43,44]. From a more functional perspective, ECs on both aligned fibrous scaffolds[39,40] and grooved substrates[30,40,45,46] appear to adopt an anti-inflammatory and antiatherogenic phenotype.

Influence of topography dimensions: micro- vs. nanoscale cues. In vivo, the endothelial BM is a multi-scale topographic surface with both nanoscale fibers and microscale aligned or anisotropic topographies. Most studies suggest that decreasing groove width from the micron to the nanometer scale increases cell elongation, alignment, adhesion, proliferation, and FA size

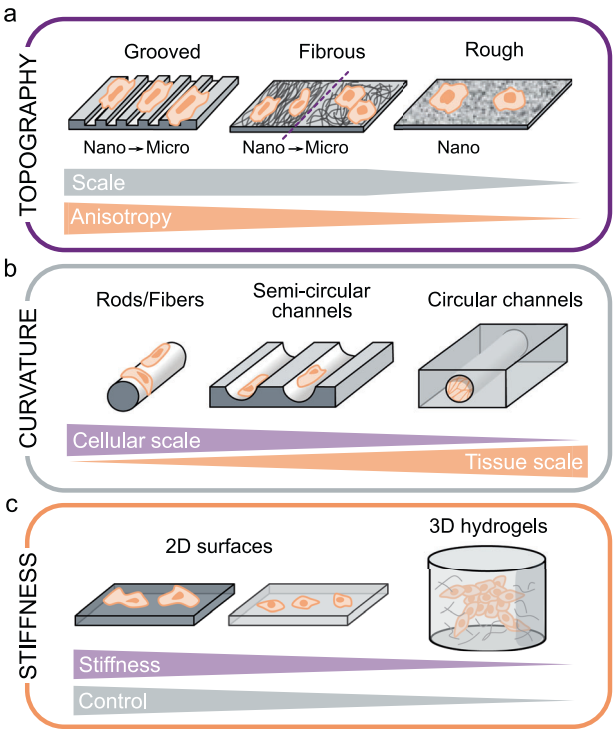

Fig. 2 Substrate-derived cues experienced by endothelial cells and associated experimental model systems. a Substrate topography can be mimicked in vitro with grooved, fibrous, or rough surfaces. Each of these systems can provide a different level of anisotropy at different scales (nano- or micro-scale). **b** Substrate curvature can be mimicked in vitro with microscale rods or fibers, semicircular channels, or full circular channels. These systems provide curvature ranging from the cellular scale to the tissue (monolayer) scale. **c** Substrate stiffness can be tuned in either 2D surfaces (where increased cell spreading is observed on stiffer substrates) or 3D hydrogels (where smaller stiffness values can be attained but at the expense of more limited control of the extracellular environment).

and stability[28,32,33]. In contrast, a similar decrease in groove depth decreases EC alignment and elongation[29,31]. On fibrous substrates, microscale fibers have been reported to induce both decreased[41] and increased[42] EC alignment and elongation relative to nanoscale fibers. This apparent contradiction may be explained by differences in pore sizes between the two studies, with cells capable of spreading over multiple fibers in the first study but not the second.

As cells usually encounter micro- and nano-cues simultaneously, combining both scales provides a more physiologically relevant environment. In a study that focused on this issue, nanofibers aligned in the same direction as microscale grooves were shown to have a synergistic effect, amplifying EC elongation and alignment, whereas an orthogonal orientation between nanofibers and microgrooves had an antagonistic effect[47], demonstrating that ECs can integrate topographical cues of different scales.

Influence of EC type and cell density. ECs in vivo possess great phenotypic variability depending on the vascular bed and organs. Whether substrate topography induces different responses in different EC types remains unknown but is an important question given the differences in BM structure between arteries and veins[23,25]. A comparison of arterial, venous, and stem cell-derived ECs on grooves shows that while their morphological responses are similar, different phenotypic responses are observed: both primary cell lines preferentially adopt a venous phenotype, while grooves promote an arterial phenotype in stem cell-derived ECs[48]. The effect of groove size on the alignment and migration of ECs has also been shown to depend on EC type[34], which may explain the discrepancies reported in the literature regarding the optimal topographic feature size for cell alignment.

An understudied aspect is EC response to topography in pathological settings. A recent study reveals that diabetic ECs are generally less responsive to topography than healthy ECs in terms of angiogenic capacity and monolayer integrity[49]. Similarly, ECs from older donors exhibit decreased cell speed but higher directionality along grooves compared to those from younger donors[50].

ECs in vivo form continuous monolayers, while many of the previously mentioned in vitro studies focus on individual cells. Single ECs and EC monolayers exhibit broadly the same response to topography: they align and elongate along anisotropic substrates such as grooves or aligned fibrous scaffolds[30,32,35,39,40,45,51]. One study reported that EC alignment on grooved substrates decreased near confluence[31], suggesting that ECs in monolayers are nevertheless less responsive to topographical cues than individual cells.

Curvature. The impact of substrate curvature on cells has only recently been investigated and is now recognized as a critical cue regulating cell behavior[52]. In the vasculature, ECs encounter curvature at the subcellular, cellular, and tissue (monolayer) scales.

Subcellular curvature is due to the curvature of BM fibers and is typically studied using nano- to microscale wavy surfaces (sinusoidal grooves); however, only a few studies have so far used these types of substrates on ECs. In general, ECs align and elongate in the direction of sinusoidal grooves as they do on rectangular grooves, but they exhibit lower migration speeds[53]. EC alignment decreases progressively with increasing wavelength (i.e., decreasing curvature) until it disappears at a wavelength of ~50 μm[53–55], a dimension comparable to EC size.

The curved vascular wall subjects ECs to cell- to monolayer-scale curvature. The diameter of human blood vessels ranges from ~5 μm in capillaries to more than 1 cm in large arteries, which translates to curvatures ranging from 0.1 to 100 mm^{-1}, spanning four orders of magnitude. Starting with simple, non-perfused systems of semicircular channels, it was observed that ECs form confluent monolayers that conform to the curved substrate[56–58] (Fig. 2b), orient along the longitudinal axis, and have fewer actin stress fibers compared to adjacent flat regions[56]. More recently, many "vessel-on-chip" systems have been developed where ECs are cultured in closed, perfused channels of physiological diameters (Fig. 2b)[59–61], but the impact of substrate curvature on the cells in these systems has not yet been investigated.

The most informative studies on the impact of curvature on ECs arise from the use of microfibers over which ECs are cultured, mimicking the high curvature found in smaller vessels such as capillaries (Fig. 2b). While endothelial colony forming cells (ECFCs) were observed to orient in the direction of fibers with diameters of 5–11 μm[62], human umbilical vein ECs (HUVECs) were reported to exhibit a circumferential orientation and ring-like actin organization on 5–20 μm PCL fibers[62,63] but a longitudinal orientation on 14 μm glass rods[64]. In this last study, human brain microvascular ECs (HBMECs) retained a random orientation regardless of rod curvature. The authors hypothesized that this resistance to curvature might be an organ-specific behavior, allowing brain ECs to minimize the length of cell–cell junctions and hence to maintain very low permeability levels[64]. Interestingly, the combination of cell-scale curvature with nanoscale topography reveals competing effects:

while nanotopography orientation appears to drive ECFC orientation, the orientation of the secreted ECM is driven by the cell-scale curvature[65].

Stiffness. An elastic material's bulk deformability is characterized by its Young's modulus, an intrinsic property defined as the ratio of stress to strain (SI units of Pa). Although the term "stiffness" is commonly used to indicate if a material is "soft" or "hard", its technical definition is the ratio of an applied force to the elongation in the direction of the force (SI units of N/m). Stiffness thus depends on the material's dimensions. In this review, the term "stiffness" corresponds to its common language usage. As such, the material stiffness values are actually Young's moduli. It should be noted that in the literature, a clear distinction between stiffness and Young's modulus is not always made.

Atomic force microscopy (AFM) measurements on excised adult BMs suggest that their elastic modulus is in the 1–4 MPa range[25]. A wide range of vessel wall stiffnesses has been reported, from ~10 kPa[66,67] to 1.5 MPa[68]. It is important to emphasize that stiffnesses measured ex vivo in excised vessels differ from those in pressurized vessels in vivo[69,70] due to the strain-stiffening behavior of extracellular matrices. Additionally, vessel wall stiffness changes with anatomical location and increases with age[71,72] as well as with cardiovascular pathologies such as hypertension[73] or atherosclerosis. The effective stiffness that ECs perceive in vivo is difficult to determine. Reports of the distance over which cells feel stiffness vary from a couple of microns to tens of microns[74,75]. By using soft gels on glass substrates, it has been shown that this distance depends both on the substrate's Young's modulus and the gel thickness[74–76]. Based on these studies, we can assume that large vessel ECs in vivo sense a combination of the stiffnesses of the BM and the underlying medial and adventitial layers, whereas ECs in small vessels might even sense the stiffness of adjacent tissues.

Influence of 2D substrate stiffness on EC morphological and functional responses. Varying substrate stiffness in vitro has a clear impact on EC morphology, with cells being more round and less spread on soft substrates (1–5 kPa) than on stiff substrates (20 kPa–2 MPa)[77–81] (Fig. 2c). In terms of intracellular organization, ECs on softer substrates are associated with fewer FAs[79,80,82–84] and actin stress fibers[77,80,82,85–88]. Furthermore, ECs on stiff substrates are more contractile and exhibit larger traction forces, both as single cells[81] and in monolayers, as assessed by traction force microscopy[85,88,89]. The stresses within the monolayer are lower but are also more homogeneously distributed on soft substrates[80].

Various studies have shown that monolayer and cell–cell junction integrity decrease with increasing substrate stiffness[79,80,85,89–91], with important functional consequences for monolayer permeability and inflammation[89,92]. ECs in vivo can also encounter cell-scale heterogeneities in BM stiffness[66]. In vitro, gaps in EC monolayers were observed with increasing matrix stiffness heterogeneity, and tended to localize at matrix stiffness interfaces[84], suggesting that stiffness gradients regulate EC structure and function.

Influence of EC type and cell density. Interestingly, although observed in both individual cells and monolayers, stiffness-related morphological and cytoskeletal modifications are considerably smaller in the case of monolayers[78,86]. This may reflect preferential force redistribution towards cell–cell junctions within monolayers. Although veins have softer walls than arteries[93], it remains unknown if venous and arterial ECs respond differently to substrate stiffness. However, the switch to a venous phenotype observed for arterial ECs cultured on soft matrices (0.5 kPa) suggests that endothelial morphology and function are principally determined by the biomechanical properties of the ECM environment rather than intrinsic differences between arterial and venous ECs[83].

Influence of 3D substrate stiffness on EC network formation. To better simulate the native extracellular environment, recent efforts have focused on developing 3D culture systems. Although the vascular endothelium can be viewed as an essentially 2D structure, 3D environments are particularly relevant in the context of angiogenesis, where new microvessels sprout from existing vessels in all directions (Fig. 2c). Studies using hydrogels of varying stiffnesses in the range of 0.1–10 kPa show enhanced EC vascular network formation in softer matrices[87,94–98]. Consequently, ECs migrate longer distances[99] and are more spread in soft gels[94], the opposite effect to that on 2D substrates. Importantly, tuning collagen gel stiffness by controlling the cross-linking rather than altering gel density and structure (as in the previous studies) yields the opposite effect: stiffer (500 Pa) collagen gels lead to increased spreading, number, length, and branching of angiogenic sprouts[90,100]. This observation highlights the importance and intrinsic difficulty of independently tuning the detailed features of the environmental cues, mainly stiffness and topography, in 3D culture systems. Using colloidal gels where stiffness and topography can be independently controlled, a recent study concluded that there is an optimal structure of tenuous strands and spacious voids for EC network formation, irrespective of matrix stiffness[97]. The magnitudes of the 3D substrate stiffnesses eliciting the aforementioned effects are approximately an order of magnitude lower than the 2D substrate stiffnesses, suggesting that matrix dimensionality modulates matrix stiffness effects. In any case, the apparent stiffness perceived by cells is hard to evaluate, as illustrated by the different morphologies of vascular networks seen in floating and constrained collagen gels that are otherwise identical[96]. In addition, while most of the different gels used in 3D studies possess purely elastic properties, the extracellular environment and its components in vivo exhibit viscoelastic and strain-stiffening behavior that are rarely reproduced in vitro, creating an additional layer of complexity for the physiological relevance of these models.

Flow-derived mechanical cues

The endothelium experiences multiple mechanical stresses due to the flow of viscous blood. These include fluid dynamic shear (or frictional) stress, compressive pressure, and tensile (or hoop) stresses due to the transmural pressure difference (Fig. 1).

Flow shear stress. Fluid shear stress is the tangential frictional force per unit area experienced by the endothelium as a result of blood flow. Blood is a complex non-Newtonian fluid composed principally of plasma and red blood cells. At sufficiently low shear rates (below ~100 s^{-1}), blood exhibits shear-thinning behavior. Therefore, the non-Newtonian of blood strongly affects the shear stress on the EC surface within low shear regions[101–103]. In the microvasculature, blood can no longer be considered a homogeneous fluid but rather a suspension of deformable active particles[104–106]. Recent results indicate that in those vessels, the presence of blood cells can significantly alter the near-wall flow field, thereby impacting the shear stress on the EC surface[106]. Most of the in vitro studies discussed here document EC responses to physiological values of shear stress that are generated using more simple Newtonian fluids. Those investigations have revealed that shear stress regulates major EC functions including angiogenesis, vessel remodeling, and cell fate[19]. In vivo, the time-

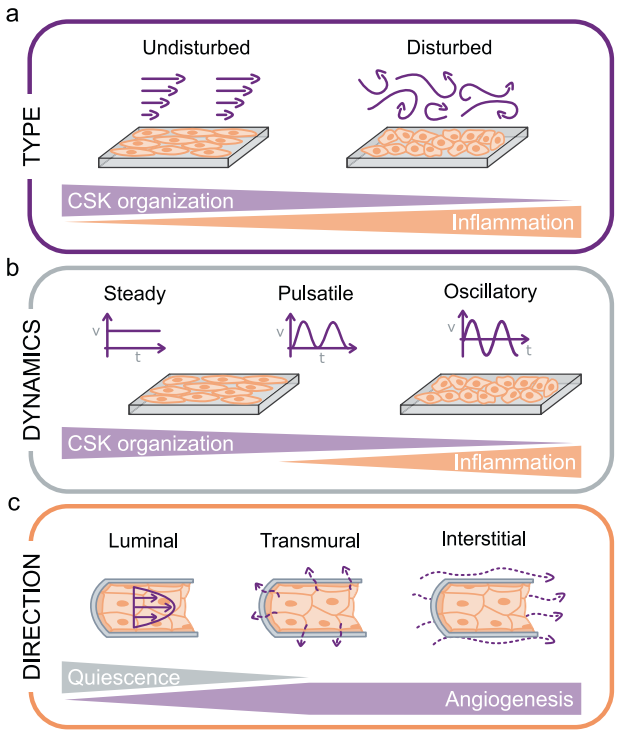

Fig. 3 Features of flow-induced shear stress experienced by endothelial cells (ECs). a ECs experience either undisturbed or disturbed flow, which have different effects on cytoskeletal (CSK) organization and the inflammatory state of the cells. **b** ECs can experience steady, pulsatile, or oscillatory flow. The flow dynamics influence cytoskeletal organization and the inflammatory state of the cells. **c** ECs experience flow in the luminal direction (parallel to cells, on the apical side), transmural (across the endothelium, on cell–cell junctions), or interstitial (in the vessel wall or parenchymal tissue, on the basal side). The direction of the flow influences EC quiescence and/or angiogenesis.

averaged wall shear stress is ~1 Pa in the aorta, ~5 Pa in small arterioles[1,107], ~2 Pa in venules, and ~0.1 Pa in the vena cava[107–110]. Furthermore, within the same vessel, shear stress levels and profiles can vary significantly due to geometric features including vessel curvature and branching.

Steady flow: undisturbed vs. disturbed. Vascular flows can be broadly classified as either "undisturbed" or "disturbed". Undisturbed flows are most typically uniaxial and laminar flows; whereas disturbed flows include turbulent flows and laminar flows with spatial shear stress gradients and/or secondary flows. In relatively straight vascular segments, flow streamlines are largely undisturbed and remain mostly parallel to the vascular wall[111] (Fig. 3a). In contrast, flow in areas of vascular curvature, branching, and bifurcation becomes highly disturbed with regions of flow separation and recirculation (Fig. 3a). Interestingly, these zones of flow disturbance correlate with the localization of vascular diseases including atherosclerosis[112,113], aortic valve calcification[114,115], and inflammation and thrombosis in veins[115,116].

In vivo, ECs in undisturbed flow zones are elongated and aligned in the direction of blood flow[117,118]. In contrast, ECs in disturbed flow areas are more cuboidal (round) and randomly oriented[119,120]. In vitro, steady flow systems are able to reproduce these observations, with undisturbed shear stress elongating ECs and aligning them parallel to the flow direction[4,121–125] and disturbed shear stress leading to round EC shapes and random cellular orientation[121,126,127]. At the cytoskeletal level, undisturbed flow leads to prominent actin stress fibers that are aligned in the direction of flow[128–131], whereas ECs subjected to disturbed flow exhibit shorter and randomly oriented actin filaments[4,121,123,130]. Shear-induced cytoskeletal reorganization is initiated within 1 h after flow onset[132], even though complete cytoskeletal remodeling and cellular shape changes require significantly longer times[120].

EC morphological and alignment responses to steady flow depend not only on the type of applied shear stress but also on shear stress magnitude. Although increasing shear stress level generally increases the extent of cell elongation and alignment[120,133,134], there seems to be an optimal value of shear stress above which the response decreases[112]. Interestingly, several recent studies have challenged the consensus of EC alignment in the direction of steady flow, with reports of perpendicular alignment at both low shear (0.3 Pa)[135] and high shear (>10 Pa)[136,137]. The alignment response may be dynamic, with a switch from perpendicular to parallel orientation after 72 h of flow[138].

In addition to its effect on EC shape and cytoskeletal organization, steady unidirectional flow elicits higher EC migration speeds than disturbed flow[127,139], leading to more efficient wound healing. This effect is dependent on shear stress magnitude[140] and on the direction of cell migration, with ECs along the downstream wound edge migrating more slowly than ECs along the upstream edge[140]. ECs also appear to retain a level of shear stress memory, with pre-sheared ECs exhibiting accelerated wound closure[141,142]. Moreover, steady unidirectional flow promotes an anti-inflammatory and antithrombotic EC phenotype with reduced cell apoptosis and proliferation[143,144] while disturbed flow has the opposite effect[126].

Two additional and important features of disturbed flow that affect EC behavior are spatial shear stress gradients and secondary flows. Shear stress gradients inhibit EC alignment in the direction of the shear in vitro[138,145,146]. The alignment response can be restored, however, by supra physiological levels of shear stress[147] whose value depends on the gradient magnitude[148]. EC alignment is also restored by switching from a positive to a negative gradient, underscoring the importance of gradient direction[149]. In a new type of "impinging flow device", ECs were surprisingly observed to align perpendicular to high shear stress gradients[136], emphasizing our incomplete comprehension of EC response to shear gradients.

Secondary flows associated with disturbed flow zones in regions of branching and curvature arise from streamline curvature. A key consequence of secondary flows for ECs is the generation of transverse shear stresses that act orthogonal to the axial shear stress due to the primary flow[150,151]. Interestingly, the localization of atherosclerotic plaques has recently been correlated with transverse flow rather than with disturbed axial flow[152]. The response of ECs to these secondary flows remains unclear with some reports of alignment loss in orbital shakers[153–155]. However, the transverse shear stresses in most of these systems are also accompanied by shear stress gradients and in some cases oscillatory shear forces[156], thus complicating the isolation of individual effects and underscoring the need for the development of novel in vitro platforms that allow decoupling of these various phenomena. Recently, a unique system of spiral microvessels was developed in which physiological torsion and curvature enable the generation of physiological secondary flows[157]. This new generation of systems will certainly enhance our understanding of complex flow patterns and their influence on ECs.

Pulsatile flow: non-reversing vs. reversing vs. oscillatory. A key feature of blood flow in larger vessels is its pulsatility due to the

rhythmic heartbeat. Within the microvasculature, this pulsatility is significantly dampened, and blood flow becomes quasi-steady. Thus, the shear stress profile on the EC surface depends on the vascular location. In undisturbed flow regions in medium and large vessels, the endothelium experiences non-reversing pulsatile flow, whereas in disturbed flow zones, the shear stress exhibits periodic directional reversal and oscillation.

ECs in vitro are able to discriminate among steady, non-reversing pulsatile, reversing pulsatile, and oscillatory (zero net) flow (Fig. 3b)[158–160]. For instance, while both steady and non-reversing pulsatile flow induce EC elongation and alignment in the flow direction[161,162] as already mentioned, they do so with different dynamics[158]. The recruitment of apical stress fibers and the high migration persistence observed under steady flow disappear under non-reversing pulsatile flow[161]. Prolonged exposure to either reversing pulsatile flow or oscillatory flow fails to elicit EC elongation, orientation, and cytoskeletal remodeling[158,159,163]. Contrary to steady flow, oscillatory flow disrupts cell–cell junctions[125] and elicits a pro-inflammatory and atherogenic EC phenotype[164–166]. These results underscore the need for understanding the links between the exact flow waveform and the resulting EC responses.

Luminal vs. transmural vs. interstitial flow. ECs in vivo are subjected to a combination of luminal, transmural, and interstitial flow (Fig. 3c). Luminal blood flow exerts a shear stress on the apical EC surface. The pressure difference across the vascular wall generates a transmural flow, particularly prominent in the microvasculature with typical flow velocities of ~1 μm/sec[167,168]. Transmural shear forces are exerted most directly on endothelial cell–cell junctions. Interstitial flow arises from fluid movement within the tissue surrounding the ECs, shearing ECs on their basal side. For large vessels, interstitial flow can originate from transmural flow currents as well as from other sources such as fluid leakage from the vaso vasora. In the microvasculature, interstitial flow stems from porous medium flow in the surrounding parenchyma.

In vitro, physiological levels of transmural flow increase endothelial sprouting[169] both in the cases of outward[170,171] and inward flow[172,173], with more filopodial protrusions under inward flow[169]. Transmural flow is also necessary for sustained sprout elongation[170]. In a microfluidic branching model, transmural flow was shown to restore sprouting after inhibition by luminal shear stress[174]. Interestingly, the shear stress threshold for triggering angiogenesis is conserved between luminal and transmural flow, at ~1 Pa[170].

Because interstitial flow can have multiple sources, its intensity is highly variable across the vasculature and is difficult to measure in vivo, with the few reported velocities varying between 0.1 and 4 μm/sec[168,175]. In vitro, interstitial flow around ECs embedded within a 3D matrix stimulates network formation[176–178]. Vascular tubes align in the flow direction[179], with vascular sprouts elongating against the flow direction[176,180].

Influence of EC type and cell density. Arterial and venous ECs exhibit different responses to flow-induced shear stress. For instance, arterial ECs become more polarized[181] and exhibit more prominent actin stress fibers in the direction of flow than venous ECs[131,182,183]. It is also notable that certain types of ECs such as aortic valve ECs or lymphatic ECs behave differently with alignment orthogonal to the direction of flow[184,185]. Similarly, brain microvascular ECs subjected to a steady shear stress of 1.6 Pa do not elongate or align and continue to exhibit a randomly oriented cytoskeleton[186,187].

Although EC responses to flow have been investigated at both the single cell and monolayer levels, very few studies have specifically tackled the influence of cell density on EC flow responses. One study reported that only confluent ECs aligned in response to a 2 Pa shear stress[188]. Cell density also influences EC migration: while low density ECs migrate in the direction of the flow, ECs in dense monolayers move against the flow direction[136].

Compressive stresses from blood pressure

Blood pressure exerts a normal force that compresses the EC apical surface. Blood pressure varies drastically along the vasculature, from ~1.3 kPa (10 mmHg) in veins up to ~16 kPa (120 mmHg) in the human aorta during systole. Severe hypertension may lead to pressures as high as ~27 kPa (200 mmHg). Blood pressure is highly pulsatile on the arterial side, but these oscillations are progressively dampened by the vessel elasticity until they virtually disappear in capillaries.

Hydrostatic pressure applied to ECs in vitro influences cell shape, cytoskeletal organization, and various aspects of vascular function. Bovine aortic ECs (BAECs) under both physiological (5–20 kPa) and low pressure (0.1–1 kPa)[189,190] elongate while maintaining a random orientation. They also have a smaller area and less smooth cell contours[191–194]. However, some studies applying similar pressures reported no elongation in BAECs[163,195,196]. Interestingly, HUVECs under physiological pressure also have a reduced cell area but do not exhibit the elongation and tortuosity responses[197,198], suggesting that pressure-induced changes in cell shape are specific to arterial ECs. The morphological changes are mirrored by cytoskeletal reorganization, with the formation of central stress fibers and remodeling of FAs under both physiological[163,192,194] and low pressure values[189,190,199]. Pressure-induced cytoskeletal reorganization follows a two-step dynamic: increased cytoskeletal tension through actomyosin-mediated contraction after 1 h followed by increased cortical actin density through actin polymerization and assembly of stress fibers[198,200].

Hydrostatic pressure at both physiological[197] and sub-physiological levels[199] increases EC proliferation, consistent with reports of increased angiogenesis and tubulogenesis in these situations[198,201]. For low and physiological ranges of pressure, the rate of proliferation correlates with the magnitude of the applied pressure[189,193], while pathological pressures (20–25 kPa) induce EC degeneration and apoptosis[202,203].

One hypothesis put forward to explain pressure-induced EC proliferation is the disruption of adherens junctions[192,204], leading to a multilayer EC structure in vitro[189–192]. Indeed, the formation of VE-cadherin-based junctions normally inhibits proliferation within confluent monolayers[205,206]. The multilayer structure is not observed in subconfluent ECs under pressure[193], which confirms that it originates from an excessive proliferation of confluent ECs. Physiological pressure further alters endothelial function by increasing intercellular gaps[197], inducing a reversible loss of monolayer integrity[191,207], loss of barrier function[200], and increased permeability[204]. In contrast, low pressure was shown to protect pulmonary endothelial monolayer integrity against inflammatory agents[208].

Unlike constant pressure, the effect of pulsatile pressure on ECs in vitro has received little attention. Similar to constant pressure, a magnitude-dependent effect of pulsatile pressure on proliferation was reported, with physiological pressure values increasing proliferation and pathological values decreasing it[196,201]. Application of pulsatile pressure also leads to a magnitude-dependent decrease in peripheral actin and relocalization of ZO-1 junctions associated with decreased permeability[209].

Tensile stresses. Tensile stresses in the vasculature can be axial, due to tissue growth or movement, or circumferential (hoop), due to the transmural pressure difference which dilates the vessels

cyclically. In vivo measurements report a wide range of axial strain magnitudes across the vasculature: ~20% in the lungs[210], 5% in coronary arteries[211], and 5–15% in leg arteries[212–214]. Hoop strains due to diameter changes during the cardiac cycle are in the range of 0–15%[213,215–218]. In most in vitro studies, 5–10% strains are considered physiological while 15–20% strains are viewed as pathological.

General cell response: alignment, elongation, and activation. In vitro studies that have examined the effect of stretch on ECs all report EC elongation and alignment orthogonal to the strain direction[219–221]. This result is in line with the longitudinal alignment of ECs in vivo, orthogonal to the direction of circumferential strain. This behavior is highly dynamic: when the direction of the strain is changed during the experiment, ECs reorient orthogonal to the new strain direction[220]. The cell morphological changes are reflected intracellularly by orthogonal alignment of actin filaments and an increased number of stress fibers[222,223]. At the onset of stretch, stress fibers disassemble[224,225] with vanishing traction forces[226], then stress fibers reassemble in the transverse direction within minutes[222,224,227,228] with recovery of the transverse traction forces, and finally the entire cell reorients within hours[221,226]. Stretching the substrate upon which cells adhere increases tension in the actin cytoskeleton[229], increasing cell stiffness[230,231].

Another major effect of strain is EC activation: low strains (5–10%) inhibit apoptosis and increase proliferation, while large strains (15–20%) have the opposite effect[232–235]. The stretch-induced proliferation requires cell–cell junctions[236–239]. An intermediate level of strain (10%) is also able to increase endothelial motility and migration[240,241], tubulogenesis, and endothelial sprouting[235,242] and aligns the newly formed sprouts orthogonal to the strain[243,244]. The stimulation of angiogenesis is observed for both static and cyclic tensile strains.

Stretch direction: free uniaxial, pure uniaxial, and biaxial. Beyond the general observation of EC alignment orthogonal to strain, variations in the exact orientation angle have been reported. These apparent discrepancies are reconciled when viewed through the lens that ECs align in the direction of minimal strain[221,223]. Three major forms of stretching can be applied to cells: free uniaxial, pure uniaxial, and biaxial (Fig. 4a). In free uniaxial stretching, the substrate on which the cells are cultured is elongated actively along one axis but undergoes slight retraction in the orthogonal direction due to the positive Poisson's ratio exhibited by most materials. In pure uniaxial stretching, the sample is constrained orthogonal to the uniaxial stretch in order to prevent the orthogonal (transverse) retraction strain. In biaxial stretching, the sample is stretched in two orthogonal directions via two unidirectional stretches of a rectangular sample, radial stretching of a circular sample, or by inflation of a circular membrane.

The first experiments with pure uniaxial stretching were conducted in the late 1990s[221], with a follow-up study that specifically explored the variation of cell orientation among the three types of stretchers[223]. Cells were found to orient in the minimal strain direction (90° for pure uniaxial stretching[220,223,245] and ~70° for free uniaxial stretching[223,246]), which is determined by the balance between the longitudinal tensile strain and the transverse compressive strain[228]. ECs were also found to avoid pure compressive strains, albeit with slower dynamics[247].

In the biaxial stretch configuration, cells are subjected to two different minimum strain directions, leading to a cuboidal morphology[223,245,248]. These platforms are mostly used to investigate functional responses to stretch, such as cell proliferation or changes in gene expression. Inflation of circular membranes generates equiaxial strain at the center, where cells are seen to be randomly oriented, and a gradient of anisotropic biaxial strain in the peripheral areas which complicates interpretation of cell orientation responses[249,250]. In contrast, radial stretching of circular membranes leads to uniform equiaxial strains[248].

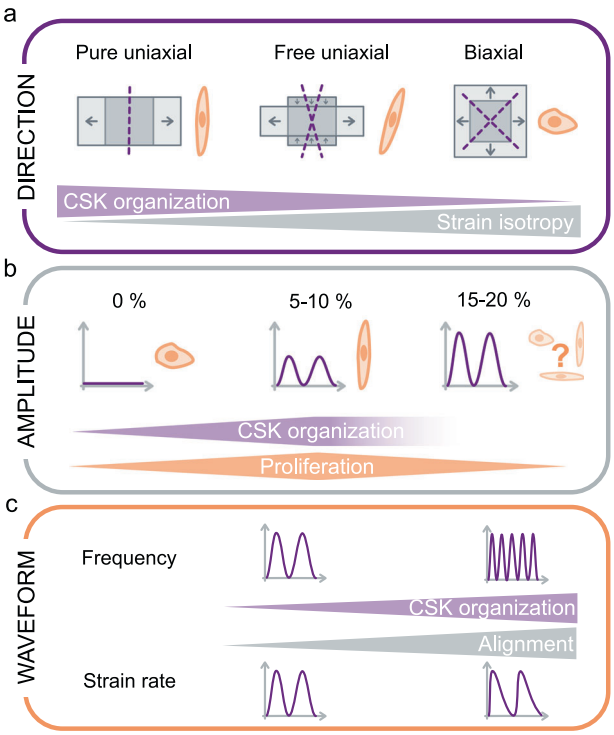

Fig. 4 Features of tensile stresses experienced by endothelial cells. a Strain direction can be purely uniaxial, free uniaxial (with an additional lateral compression), or biaxial (isotropic). Purple dotted lines indicate minimum strain direction. Strain direction influences cytoskeletal (CSK) organization. **b** Strain amplitude influences cytoskeletal organization and cell proliferation, which are maximized for intermediate strain amplitudes. **c** Strain frequency and strain rate influence cytoskeletal organization and cell alignment.

Stretch pattern: amplitude, frequency, and waveform. EC response to cyclic stretch loading is modulated by the stretch pattern, most notably its frequency, amplitude, and precise waveform (Fig. 4b, c). Increasing the frequency towards the physiological value of 1 Hz amplifies cell response, leading to more elongated cells with an orientation angle closer to the minimum strain direction[251] and with a faster response[252]. A minimum frequency of 0.1 Hz for cyclic strain is necessary to induce a response[251,253,254]. Similarly, the stretch amplitude has a strong influence on EC mechano-response. Large physiological strains (~10%), induce a final orientation that is closer to the "minimum strain direction"[228,247,255], reduced orientation dispersion[220], and accelerated dynamics[252] relative to smaller strains (~5%). For pathological strains, above 15%, the results are less clear, with reports of both orthogonal[252,256] and longitudinal alignment[250]. Possible explanations are differences in cell type (venous vs. arterial ECs) or in stretching profiles (free uniaxial vs. biaxial). Finally, physiological waveforms, i.e. faster extension and slower relaxation, lead to more intense responses with faster

dynamics[252,257], as ECs are more responsive to tensile strain rate than to compressive strain rate[258].

Influence of EC type and cell density. Single cells align in the direction of a 2% compressive strain while confluent monolayers align in the direction of the true minimum strain[259]. Cell confluency also modulates the response to strain amplitudes, suggesting an important role for cell–cell junctions[259]. The previously described switch of endothelial orientation from orthogonal to parallel to the stretch direction under pathological strain levels is lost when cell–cell junction formation is inhibited via blocking antibodies[250]. This collective orientation switch is hypothesized to be key for preserving monolayer integrity, which can be damaged under pathological strains[260].

An additional layer of complexity is mechanical preconditioning. EC confluent monolayers grown under cyclic strain withstand deformation while their static counterparts are less compliant and detach from the substrate under strain[224]. Interestingly, the denudation zones correlate with areas of initial higher density, which is known to modulate cytoskeletal tension and substrate adhesion[205], two key components of the strain sensing mechanism. Lastly, as strain levels vary along the vascular tree, EC type (arterial, capillary, or venous) is likely to modulate its mechano-response. One study tackled this question and found that only venous ECs reorient while only arterial ECs exhibit increased proliferation in response to stretch[222]. The dependence of the stretch response on EC type merits further investigation in light of the fact that most of the other studies reviewed in this section have reported orthogonal alignment despite using arterial ECs, and a number of studies using venous ECs have reported increased proliferation[235,236,244].

Combined cues

While the study of individual substrate- and flow-derived mechanical cues on ECs has greatly improved our understanding of the fundamental mechanobiology of these cells, ECs in vivo experience a complex combination of all these cues. The recent development of experimental platforms integrating multiple mechanical stimuli has begun to address this issue. Depending on their respective magnitudes, waveforms, directionality, and the cellular processes they regulate, multiple cues may have synergistic or antagonistic effects when they regulate the same cellular process (es), or one cue may modulate the effect of another on a cellular response that it does not directly regulate on its own.

Flow and substrate cues

Flow and topography. How apical flow-derived shear stress and basal contact stresses due to BM topography cooperate or compete to modulate EC responses is a central question, for optimizing the design and surface properties of endovascular devices. When flow and anisotropic topographies in the form of ridges/grooves are oriented in the same direction, synergistic effects on ECs are observed. For instance, EC orientation and elongation are more pronounced for the combination of both cues than for either one alone[137,261]. ECs on grooves under flow also exhibit increased adhesion forces[51,262], leading to higher resistance to detachment[41] and a protective effect on monolayer integrity[51,137]. They also show enhanced counterflow migration[263,264] and thus more efficient wound healing[263].

When the flow and anisotropic topography cues are oriented orthogonal to one another, most studies report that ECs align and elongate in the direction of the topography rather than the flow[261,265]. However, this conclusion depends on both the groove dimensions, with micron-scale grooves counteracting the effect of flow more effectively than nanoscale grooves[261], and the magnitude of shear stress, with ECs aligning perpendicular to the grooves for sufficiently high shear stress levels[266].

In vivo, ECs that are elongated and aligned in the direction of blood flow exhibit an anti-inflammatory, atheroprotective phenotype whereas ECs in disturbed flow zones are largely cuboidal and have a pro-inflammatory and atheroprone profile[267]. An interesting question is whether the differences in inflammation phenotype are driven directly by the differences in cell morphology which can also be modulated by the underlying topography. Studies on ECs on grooved substrates in the absence of flow[30,39,268] suggest that cell morphology regulates phenotype independently of flow. Nevertheless, a cooperative effect of the two types of cues has also been reported, with aligned collagen fibers reducing EC inflammation under disturbed flow[265].

Flow and substrate stiffness. How vascular wall stiffening with age or with vascular disease affects EC responses to blood flow has motivated studies of the combination of different substrate stiffnesses with flow-induced shear stress. As an isotropic biophysical cue, substrate stiffness appears to modulate other directional cues. For instance, higher shear stresses (2.2 vs. 0.6 Pa) are required to align ECs on very soft substrates (elastic modulus of 100 Pa) compared to stiffer substrates (10 kPa)[269]. Kohn et al. nicely demonstrated that stiffness values characteristic of healthy vessel walls (2.5 kPa) promote the atheroprotective signals induced by fluid shear stress compared to stiffer substrates[270]. Thus, it appears that both exceedingly soft and pathologically stiff substrates decrease EC sensitivity to flow.

Stretch and substrate cues

Stretch and substrate cues. The interaction between stretch and substrate cues has mostly been investigated on cell types other than ECs such as fibroblasts or cells derived from mesenchymal stem cells. As these studies reveal interesting combined effects, we review the broad findings that should guide future studies on ECs.

Stretch and substrate topography. For adhesion-based substrate cues, cell elongation and orientation are driven by the pattern anisotropy, despite the competing strain[271–273]. When strain competes with anisotropic substrate topography cues, the dominant cue depends on the characteristic size of the topography: for microgrooves, cells align with the topography[274,275], whereas for nanogrooves[276] or cell-scale micropillars[277], the strain dictates cellular orientation. Interestingly, it appears that while the basal actin and cell shape follow the contact guidance of elliptical micropillars, the apical actin and nucleus orientation are dictated by the strain[278], underscoring the complexity of the competition between topography and stretch. When topography and stretch are configured to reinforce one another, they have a synergistic effect as illustrated by the amplification of fibroblast alignment on grooved substrates in the presence of orthogonal stretch[279].

Stretch and substrate stiffness. Substrate stiffness alters cellular responses to stretch, with soft substrates either attenuating cell alignment[280] or even changing the alignment direction from orthogonal to parallel to the stretch direction[281]. Conversely, stretch rescues the impaired cell spreading observed on soft substrates[280,282]. Both substrate stiffness and stretch modify cytoskeletal tension, suggesting the following possible mechanism to explain these results: stretch restores cytoskeletal tension, allowing cell spreading on soft substrates, and soft substrates decrease cytoskeletal tension allowing cells to withstand the additional tension due to alignment parallel to stretch. One study cultured lung ECs on a stretchable membrane of physiological stiffness to mimic the native soft lung matrix and respiration-induced strains[283]. In this system, a synergistic effect of stiffness

and stretch was observed, protecting the cells against inflammatory thrombin.

Finally, stretch and substrate stiffness are tightly coupled, with stiffness determining the level of strain for a given stress and substrate stiffness being affected by stretch. In fibrous matrices (such as collagen) that exhibit strain-stiffening behavior[284], uniaxial stretching leads to anisotropic stiffening which aligns cells in the stiffer direction, i.e., the strain direction[281,285]. Interestingly, cells already aligned by anisotropic stiffness exhibit enhanced alignment in response to cyclic stretch, indicative of a synergistic effect of stiffness anisotropy and stretch[281].

Shear stress and stretch. Shear stress and circumferential stretch both arise from blood hemodynamics and are therefore naturally coupled both in vivo and in vitro. As already described, ECs align parallel to shear stress and perpendicular to stretch; thus, axial shear stress and circumferential strain are expected to reinforce one another while shear stress and axial stretch would be expected to counteract one another. ECs subjected to strain orthogonal to an applied shear stress (either steady or pulsatile) indeed exhibit more pronounced[286,287] and faster[288] alignment as well as more prominent actin stress fibers[289]. In contrast, stretch parallel to shear stress leads to competition between the two stimuli, with the aggregate effect depending on the relative magnitudes of the cues. More specifically, a shear stress of 0.5 Pa dominates the effect of strain (even for strains of 15%), whereas a shear stress of 0.08 Pa is dominated by the strain[245]. Owatverot et al. introduced the notion of "equipotent stimuli": the levels of stresses needed to elicit similar responses in terms of amplitude and dynamics[288]. They showed that equipotent shear and cyclic stretch cancel one another when applied in counteracting configurations. Interestingly, if the angle between the shear stress and the strain is intermediate (30°–60°), both stimuli influence the response[245].

In vivo, pulsatile shear stress and cyclic hoop stretch are not synchronized, exhibiting a phase shift whose magnitude varies across the vascular tree. This phase shift was demonstrated to attenuate the synergistic effect, with an altered production of vasodilators[290] and an increased expression of atherogenic genes when both stimuli are perfectly out of phase[291].

Conclusions and future directions

In this review, we have described how different forms of mechanical stimulation regulate vascular EC structure and function. Engineered in vitro systems have shed light onto fundamental EC responses to individual mechanical cues, such as cell alignment in the direction of either an applied shear stress or an anisotropic substrate topography and orthogonal to an applied strain. We have also touched upon the need to better characterize possible mechanobiological differences among ECs derived from different vascular beds as well as between single cells and cellular monolayers.

To design and implement systems and experiments that address physiologically relevant questions in mechanobiology, it is essential to carefully characterize the detailed nature of the forces at play. This includes the direction of the forces (isotropic or anisotropic for topography, axial or radial for flow or strain), the dimension/magnitude of the forces (scale of topography, values of strain, shear stress, or stiffness), and, when applicable, the time-dependent pattern of the force (waveform and frequency of strain or flow profile, for instance). Much work is needed to better understand the effect of multiple mechanical cues on ECs and to elucidate the mechanisms by which ECs integrate and decipher multiple environmental signals, as discussed in the last section. In this regard, the notion of "equipotent stimuli" provides an attractive framework for translating the effects of different types of cues into a common "language" that the cell uses to integrate multiple mechanical cues exerted simultaneously. Applying this framework to both physiological and pathological conditions would define the normal "equilibrium" values of the individual stimuli and how pathologies that alter one or more of the biophysical cues would perturb this equilibrium. Synergistic effects are also reported for almost all combinations of cues, which highlights the robustness of the vascular system, as well as potential compensatory mechanisms to maintain homeostasis to the extent possible in pathological settings.

It should be noted that the different mechanical cues are often interdependent, underscoring the need for careful decoupling of their respective contributions. For instance, the topography of the substrate and the waviness of the EC surface modify the shear stress that the cells perceive[292–294]. Similarly, substrate stiffness changes the effective strain applied on the cells[281]. In a pathological context, BM thickening (up to twofold) in pathologies such as diabetes[295,296] or atherosclerosis[297,298] is expected to change both the topography and stiffness sensed by ECs and consequently the strain that ECs undergo. All of these aspects should therefore be carefully taken into account in the design of experimental systems and in the interpretation of the obtained results.

Cellular mechanobiology is an active field of research that nicely complements the more traditional biochemically-centered view of most biological processes. As we have highlighted throughout this review, mechanical forces are particularly diverse, dynamic, and multifaceted in the vascular system, and these forces play a critical role in regulating vascular physiology and pathology. In light of the fact that many of these forces are borne most directly by the endothelium, elucidating the mechanisms governing EC mechanobiology will enhance our understanding of the etiology of various vascular diseases including atherosclerosis, thrombosis, aneurysm formation, and diabetes. Furthermore, understanding how substrate- and flow-derived stresses regulate EC structure and function promises to inform the design and development of next generation implantable endovascular devices including stents, valves, and grafts.

One of the principal challenges in mechanobiology in the coming years is certainly technological. Two recent developments provide unique opportunities for devising novel in vitro systems that promise to greatly enhance our understanding of endothelial mechanobiology. The first development is the democratization of previously complex and expensive techniques, leading to better integration of mechanical cues. An example is the field of microfabrication where techniques such as micropatterning and microfluidics have become much more widely available in the past decade. Another example is the advent of DIY technologies such as Lego-based stretchers[299] or paper-based compression-flow devices[300]. As a result, mechanical platforms can be more readily adapted to investigate particular diseases, as illustrated by a recent study modeling atherosclerosis on a chip[60]. The second development entails technological advances that allow the fabrication of innovative in vitro platforms, thus enabling new combinations of mechanical cues[301]. For instance, the topographical patterning of hydrogels[302–304], or hydrogel laser carving, recently enabled the production of perfusable endothelialized capillaries inside a soft hydrogel[305]. Future systems promise to better recapitulate the complexity of the native vascular environment and to provide finer control over the detailed magnitudes, directions, and waveforms of the applied biophysical stimuli, thereby furthering our understanding of EC responses to mechanical forces.

Received: 2 January 2021; Accepted: 2 June 2021;
Published online: 21 June 2021

References

1. Givens, C. & Tzima, E. Endothelial mechanosignaling: does one sensor fit all? *Antioxid. Redox Signal* **25**, 373–388 (2016).
2. Charbonier, F. W., Zamani, M. & Huang, N. F. Endothelial cell mechanotransduction in the dynamic vascular environment. *Adv. Biosyst.* **3**, 1800252 (2019).
3. Gordon, E., Schimmel, L. & Frye, M. The importance of mechanical forces for in vitro endothelial cell biology. *Front. Physiol.* **11**, 684 (2020).
4. Barakat, A. I., Leaver, E. V., Pappone, P. A. & Davies, P. F. A flow-activated chloride-selective membrane current in vascular endothelial cells. *Circ. Res.* **85**, 820–828 (1999).
5. Yamamoto, K., Korenaga, R., Kamiya, A. & Ando, J. Fluid shear stress activates Ca^{2+} influx into human endothelial cells via P2X4 purinoceptors. *Circ. Res.* **87**, 385–391 (2000).
6. Wang, S. et al. Endothelial cation channel PIEZO1 controls blood pressure by mediating flow-induced ATP release. *J. Clin. Invest.* **126**, 4527–4536 (2016).
7. Ranade, S. S. et al. Piezo1, a mechanically activated ion channel, is required for vascular development in mice. *Proc. Natl Acad. Sci. USA* **111**, 10347–10352 (2014).
8. Hierck, B. P. et al. Primary cilia sensitize endothelial cells for fluid shear stress. *Dev. Dyn.* **237**, 725–735 (2008).
9. Iomini, C., Tejada, K., Mo, W., Vaananen, H. & Piperno, G. Primary cilia of human endothelial cells disassemble under laminar shear stress. *J. Cell Biol.* **164**, 811–817 (2004).
10. Weinbaum, S., Zhang, X., Han, Y., Vink, H. & Cowin, S. C. Mechanotransduction and flow across the endothelial glycocalyx. *Proc. Natl Acad. Sci. USA* **100**, 7988–7995 (2003).
11. Gudi, S. et al. Rapid activation of Ras by fluid flow is mediated by $G\alpha_q$ and Gβγ subunits of heterotrimeric G proteins in human endothelial cells. *Arterioscler. Thromb. Vasc. Biol.* **23**, 994–1000 (2003).
12. Boyd, N. L. et al. Chronic shear induces caveolae formation and alters ERK and Akt responses in endothelial cells. *Am. J. Physiol. Circ. Physiol.* **285**, H1113–H1122 (2003).
13. Osawa, M., Masuda, M., Kusano, K. & Fujiwara, K. Evidence for a role of platelet endothelial cell adhesion molecule-1 in endothelial cell mechanosignal transduction. *J. Cell Biol.* **158**, 773–785 (2002).
14. Chiu, Y.-J., McBeath, E. & Fujiwara, K. Mechanotransduction in an extracted cell model: Fyn drives stretch- and flow-elicited PECAM-1 phosphorylation. *J. Cell Biol.* **182**, 753–763 (2008).
15. Tzima, E. et al. A mechanosensory complex that mediates the endothelial cell response to fluid shear stress. *Nature* **437**, 426–431 (2005).
16. Eyckmans, J., Boudou, T., Yu, X. & Chen, C. S. A hitchhiker's guide to mechanobiology. *Dev. Cell* **21**, 35–47 (2011).
17. Geiger, B., Spatz, J. P. & Bershadsky, A. D. Environmental sensing through focal adhesions. *Nat. Rev. Mol. Cell Biol.* **10**, 21–33 (2009).
18. Gray, K. M. & Stroka, K. M. Vascular endothelial cell mechanosensing: new insights gained from biomimetic microfluidic models. *Semin. Cell Dev. Biol.* **71**, 106–117 (2017).
19. Campinho, P., Vilfan, A. & Vermot, J. Blood flow forces in shaping the vascular system: a focus on endothelial cell behavior. *Front. Physiol.* **11**, 552 (2020).
20. Jufri, N. F., Mohamedali, A., Avolio, A. & Baker, M. S. Mechanical stretch: physiological and pathological implications for human vascular endothelial cells. *Vasc. Cell* **7**, 8 (2015).
21. Kaunas, R. Good advice for endothelial cells: get in line, relax tension, and go with the flow. *APL Bioeng.* **4**, 010905 (2020).
22. Roux, E., Bougaran, P., Dufourcq, P. & Couffinhal, T. Fluid shear stress sensing by the endothelial layer. *Front. Physiol.* **11**, 861 (2020).
23. Liliensiek, S. J., Nealey, P. & Murphy, C. J. Characterization of endothelial basement membrane nanotopography in rhesus macaque as a guide for vessel tissue engineering. *Tissue Eng. Part A* **15**, 2643–2651 (2009).
24. Brody, S. et al. Characterizing nanoscale topography of the aortic heart valve basement membrane for tissue engineering heart valve scaffold design. *Tissue Eng.* **12**, 413–421 (2006).
25. Leclech, C., Natale, C. F. & Barakat, A. I. The basement membrane as a structured surface - role in vascular health and disease. *J. Cell Sci.* **133**, jcs239889 (2020).
26. Natale, C. F., Lafaurie-Janvore, J., Ventre, M., Babataheri, A. & Barakat, A. I. Focal adhesion clustering drives endothelial cell morphology on patterned surfaces. *J. R. Soc. Interface* **16**, 20190263 (2019).
27. Biela, S. A., Su, Y., Spatz, J. P. & Kemkemer, R. Different sensitivity of human endothelial cells, smooth muscle cells and fibroblasts to topography in the nano-micro range. *Acta Biomater.* **5**, 2460–2466 (2009).
28. Sales, A., Holle, A. W. & Kemkemer, R. Initial contact guidance during cell spreading is contractility-independent. *Soft Matter* **13**, 5158–5167 (2017).
29. Franco, D. et al. Control of initial endothelial spreading by topographic activation of focal adhesion kinase. *Soft Matter* **7**, 7313–7324 (2011).
30. Song, K. H., Kwon, K. W., Song, S., Suh, K. Y. & Doh, J. Dynamics of T cells on endothelial layers aligned by nanostructured surfaces. *Biomaterials* https://doi.org/10.1016/j.brat.2013.05.014 (2012).
31. Uttayarat, P., Toworfe, G. K., Dietrich, F., Lelkes, P. I. & Composto, R. J. Topographic guidance of endothelial cells on silicone surfaces with micro- to nanogrooves: orientation of actin filaments and focal adhesions. *J. Biomed. Mater. Res. Part A* **75**, 668–680 (2005).
32. Antonini, S. et al. Sub-micron lateral topography affects endothelial migration by modulation of focal adhesion dynamics. *Biomed. Mater.* https://doi.org/10.1088/1748-6041/10/3/035010 (2015).
33. Vandrangi, P., Gott, S. C., Kozaka, R., Rodgers, V. G. J. & Rao, M. P. Comparative endothelial cell response on topographically patterned titanium and silicon substrates with micrometer to sub-micrometer feature sizes. *PLoS ONE* **9**, e111465 (2014).
34. Liliensiek, S. J. et al. Modulation of human vascular endothelial cell behaviors by nanotopographic cues. *Biomaterials* **31**, 5418–5426 (2010).
35. Kukumberg, M. et al. Evaluation of the topographical influence on the cellular behavior of human umbilical vein endothelial cells. *Adv. Biosyst.* https://doi.org/10.1002/adbi.201700217 (2018).
36. Chung, T. W., Liu, D. Z., Wang, S. Y. & Wang, S. S. Enhancement of the growth of human endothelial cells by surface roughness at nanometer scale. *Biomaterials* **24**, 4655–4661 (2003).
37. Brammer, K. S., Oh, S., Gallagher, J. O. & Jin, S. Enhanced cellular mobility guided by TiO2 nanotube surfaces. *Nano Lett.* **8**, 786–793 (2008).
38. Ranjan, A. & Webster, T. J. Increased endothelial cell adhesion and elongation on micron-patterned nano-rough poly(dimethylsiloxane) films. *Nanotechnology* https://doi.org/10.1088/0957-4484/20/30/305102 (2009).
39. Huang, N. F. et al. The modulation of endothelial cell morphology, function, and survival using anisotropic nanofibrillar collagen scaffolds. *Biomaterials* https://doi.org/10.1016/j.biomaterials.2013.02.036 (2013).
40. Huang, N. F. et al. Spatial patterning of endothelium modulates cell morphology, adhesiveness and transcriptional signature. *Biomaterials* **34**, 2928–2937 (2013).
41. Whited, B. M. & Rylander, M. N. The influence of electrospun scaffold topography on endothelial cell morphology, alignment, and adhesion in response to fluid flow. *Biotechnol. Bioeng.* **111**, 184–195 (2014).
42. Li, X. et al. Effects of aligned and random fibers with different diameter on cell behaviors. *Colloids Surf. B Biointerfaces* **171**, 461–467 (2018).
43. Bouta, E. M. et al. Biomaterial guides for lymphatic endothelial cell alignment and migration. *Acta Biomater.* **7**, 1104–1113 (2011).
44. Lai, E. S., Huang, N. F., Cooke, J. P. & Fuller, G. G. Aligned nanofibrillar collagen regulates endothelial organization and migration. *Regen. Med.* **7**, 649–661 (2012).
45. Jeon, H. et al. Combined effects of substrate topography and stiffness on endothelial cytokine and chemokine secretion. *ACS Appl. Mater. Interfaces* **7**, 4525–4532 (2015).
46. Di Rienzo, C. et al. Unveiling LOX-1 receptor interplay with nanotopography: mechanotransduction and atherosclerosis onset. *Sci. Rep.* https://doi.org/10.1038/srep01141 (2013).
47. Moffa, M., Sciancalepore, A. G., Passione, L. G. & Pisignano, D. Combined nano- and micro-scale topographic cues for engineered vascular constructs by electrospinning and imprinted micro-patterns. *Small* **10**, 2439–2450 (2014).
48. Arora, S., Lin, S., Cheung, C., Yim, E. K. F. & Toh, Y. C. Topography elicits distinct phenotypes and functions in human primary and stem cell derived endothelial cells. *Biomaterials* **234**, 119747 (2020).
49. Cutiongco, M. F. A., Chua, B. M. X., Neo, D. J. H., Rizwan, M. & Yim, E. K. F. Functional differences between healthy and diabetic endothelial cells on topographical cues. *Biomaterials* **153**, 70–84 (2018).
50. Sales, A., Picart, C. & Kemkemer, R. Age-dependent migratory behavior of human endothelial cells revealed by substrate microtopography. *Exp. Cell Res.* https://doi.org/10.1016/j.yexcr.2018.10.008 (2019).
51. Stefopoulos, G., Giampietro, C., Falk, V., Poulikakos, D. & Ferrari, A. Facile endothelium protection from TNF-α inflammatory insult with surface topography. *Biomaterials* **138**, 131–141 (2017).
52. Baptista, D., Teixeira, L., van Blitterswijk, C., Giselbrecht, S. & Truckenmüller, R. Overlooked? Underestimated? Effects of substrate curvature on cell behavior. *Trends Biotechnol.* **37**, 838–854 (2019).
53. Cheng, D. et al. Studies of 3D directed cell migration enabled by direct laser writing of curved wave topography. *Biofabrication* **11**, 021001 (2019).
54. Bettinger, C. J., Orrick, B., Misra, A., Langer, R. & Borenstein, J. T. Microfabrication of poly (glycerol-sebacate) for contact guidance applications. *Biomaterials* https://doi.org/10.1016/j.biomaterials.2005.11.029 (2006).
55. Sun, B., Xie, K., Chen, T.-H. & Lam, R. H. W. Preferred cell alignment along concave microgrooves. *RSC Adv.* https://doi.org/10.1039/c6ra26545f (2017).
56. Frame, M. D. & Sarelius, I. H. Flow-induced cytoskeletal changes in endothelial cells growing on curved surfaces. *Microcirculation* **7**, 419–427 (2000).

57. Esch, M. B., Post, D. J., Shuler, M. L. & Stokol, T. Characterization of in vitro endothelial linings grown within microfluidic channels. *Tissue Eng. Part A* **17**, 2965–2971 (2011).
58. Choi, J. S., Piao, Y. & Seo, T. S. Fabrication of a circular PDMS microchannel for constructing a three-dimensional endothelial cell layer. *Bioprocess Biosyst. Eng.* **36**, 1871–1878 (2013).
59. Polacheck, W. J., Kutys, M. L., Tefft, J. B. & Chen, C. S. Microfabricated blood vessels for modeling the vascular transport barrier. *Nat. Protoc.* **14**, 1425–1454 (2019).
60. Zhang, X. et al. Modeling early stage atherosclerosis in a primary human vascular microphysiological system. *Nat. Commun.* **11**, 5426 (2020).
61. Alimperti, S. et al. Three-dimensional biomimetic vascular model reveals a RhoA, Rac1, and N-cadherin balance in mural cell–endothelial cell-regulated barrier function. *Proc. Natl Acad. Sci. USA* **114**, 8758–8763 (2017).
62. Fioretta, E. S., Simonet, M., Smits, A. I. P. M., Baaijens, F. P. T. & Bouten, C. V. C. Differential response of endothelial and endothelial colony forming cells on electrospun scaffolds with distinct microfiber diameters. *Biomacromolecules* **15**, 821–829 (2014).
63. Jones, D. et al. Actin grips: circular actin-rich cytoskeletal structures that mediate the wrapping of polymeric microfibers by endothelial cells. *Biomaterials* **52**, 395–406 (2015).
64. Ye, M. et al. Brain microvascular endothelial cells resist elongation due to curvature and shear stress. *Sci. Rep.* **4**, 4681 (2014).
65. Barreto-Ortiz, S. F., Zhang, S., Davenport, M., Fradkin, J. & Ginn, B. A novel in vitro model for microvasculature reveals regulation of circumferential ECM organization by curvature. *PLoS ONE* **8**, 81061 (2013).
66. Peloquin, J., Huynh, J., Williams, R. M. & Reinhart-King, C. A. Indentation measurements of the subendothelial matrix in bovine carotid arteries. *J. Biomech.* **44**, 815–821 (2011).
67. Engler, A. J., Richert, L., Wong, J. Y., Picart, C. & Discher, D. E. Surface probe measurements of the elasticity of sectioned tissue, thin gels and polyelectrolyte multilayer films: Correlations between substrate stiffness and cell adhesion. *Surf. Sci.* **570**, 142–154 (2004).
68. Khanafer, K. et al. Determination of the elastic modulus of ascending thoracic aortic aneurysm at different ranges of pressure using uniaxial tensile testing. *J. Thorac. Cardiovasc. Surg.* **142**, 682–686 (2011).
69. Jansen, K. A. et al. The role of network architecture in collagen mechanics. *Biophys. J.* **114**, 2665–2678 (2018).
70. Humphrey, J. D. *Cardiovascular Solid Mechanics* (Springer 2002).10.1007/978-0-387-21576-1
71. Redfield, M. M., Jacobsen, S. J., Borlaug, B. A., Rodeheffer, R. J. & Kass, D. A. Age- and gender-related ventricular-vascular stiffening: aa community-based study. *Circulation* **112**, 2254–2262 (2005).
72. Haskett, D., Johnson, G., Zhou, A., Utzinger, U. & Vande Geest, J. Microstructural and biomechanical alterations of the human aorta as a function of age and location. *Biomech. Model. Mechanobiol.* **9**, 725–736 (2010).
73. Laurent, S. & Boutouyrie, P. Recent advances in arterial stiffness and wave reflection in human hypertension. *Hypertension* **49**, 1202–1206 (2007).
74. Sen, S., Engler, A. J. & Discher, D. E. Matrix strains induced by cells: computing how far cells can feel. *Cell. Mol. Bioeng.* **2**, 39–48 (2009).
75. Tusan, C. G. et al. Collective cell behavior in mechanosensing of substrate thickness. *Biophys. J.* **114**, 2743–2755 (2018).
76. Banerjee, S. & Marchetti, M. C. Contractile stresses in cohesive cell layers on finite-thickness substrates. *Phys. Rev. Lett.* **109**, 108101 (2012).
77. Yeh, Y.-T. et al. Matrix stiffness regulates endothelial cell proliferation through septin 9. *PLoS ONE* **7**, e46889 (2012).
78. Yeung, T. et al. Effects of substrate stiffness on cell morphology, cytoskeletal structure, and adhesion. *Cell Motil. Cytoskeleton* **60**, 24–34 (2005).
79. Casillo, S. M., Peredo, A. P., Perry, S. J., Chung, H. H. & Gaborski, T. R. Membrane pore spacing can modulate endothelial cell-substrate and cell-cell interactions. *ACS Biomater. Sci. Eng.* **3**, 243–248 (2017).
80. Andresen Eguiluz, R. C., Kaylan, K. B., Underhill, G. H. & Leckband, D. E. Substrate stiffness and VE-cadherin mechano-transduction coordinate to regulate endothelial monolayer integrity. *Biomaterials* **140**, 45–57 (2017).
81. Califano, J. P. & Reinhart-King, C. A. Substrate stiffness and cell area predict cellular traction stresses in single cells and cells in contact. *Cell. Mol. Bioeng.* **3**, 68–75 (2010).
82. Fioretta, E. S., Fledderus, J. O., Baaijens, F. P. T. & Bouten, C. V. C. Influence of substrate stiffness on circulating progenitor cell fate. *J. Biomech.* **45**, 736–744 (2012).
83. Van Geemen, D. et al. F-actin-anchored focal adhesions distinguish endothelial phenotypes of human arteries and veins. *Arterioscler. Thromb. Vasc. Biol.* **34**, 2059–2067 (2014).
84. Lampi, M. C., Guvendiren, M., Burdick, J. A. & Reinhart-King, C. A. Photopatterned hydrogels to investigate the endothelial cell response to matrix stiffness heterogeneity. *ACS Biomater. Sci. Eng.* **3**, 3007–3016 (2017).
85. Krishnan, R. et al. Substrate stiffening promotes endothelial monolayer disruption through enhanced physical forces. *Am. J. Physiol. Cell Physiol.* **300**, C146–C154 (2011).
86. Birukova, A. A. et al. Endothelial barrier disruption and recovery is controlled by substrate stiffness. *Microvasc. Res.* **87**, 50–57 (2013).
87. Byfield, F. J., Reen, R. K., Shentu, T. P., Levitan, I. & Gooch, K. J. Endothelial actin and cell stiffness is modulated by substrate stiffness in 2D and 3D. *J. Biomech.* **42**, 1114–1119 (2009).
88. Bastounis, E. E., Yeh, Y. T. & Theriot, J. A. Subendothelial stiffness alters endothelial cell traction force generation while exerting a minimal effect on the transcriptome. *Sci. Rep.* **9**, 18209 (2019).
89. Huynh, J. et al. Age-related intimal stiffening enhances endothelial permeability and leukocyte transmigration. *Sci. Transl. Med.* **3**, 112ra122 (2011).
90. Bordeleau, F. et al. Matrix stiffening promotes a tumor vasculature phenotype. *Proc. Natl Acad. Sci. USA* **114**, 492–497 (2017).
91. Canver, A. C., Ngo, O., Urbano, R. L. & Clyne, A. M. Endothelial directed collective migration depends on substrate stiffness via localized myosin contractility and cell-matrix interactions. *J. Biomech.* **49**, 1369–1380 (2016).
92. Stroka, K. M. & Aranda-Espinoza, H. Endothelial cell substrate stiffness influences neutrophil transmigration via myosin light chain kinase-dependent cell contraction. *Blood* **118**, 1632–1640 (2011).
93. Gauvin, R. et al. Mechanical properties of tissue-engineered vascular constructs produced using arterial or venous cells. *Tissue Eng. Part A* **17**, 2049–2059 (2011).
94. Schweller, R. M. & West, J. L. Encoding hydrogel mechanics via network cross-linking structure. *ACS Biomater. Sci. Eng.* **1**, 335–344 (2015).
95. Chwalek, K., Tsurkan, M. V., Freudenberg, U. & Werner, C. Glycosaminoglycan-based hydrogels to modulate heterocellular communication in in vitro angiogenesis models. *Sci. Rep.* **4**, 1–8 (2014).
96. Sieminski, A. L., Hebbel, R. P. & Gooch, K. J. The relative magnitudes of endothelial force generation and matrix stiffness modulate capillary morphogenesis in vitro. *Exp. Cell Res.* **297**, 574–584 (2004).
97. Nair, S. K. et al. Colloidal gels with tunable mechanomorphology regulate endothelial morphogenesis. *Sci. Rep.* **9**, 1–17 (2019).
98. Sieminski, A. L., Was, A. S., Kim, G., Gong, H. & Kamm, R. D. The stiffness of three-dimensional ionic self-assembling peptide gels affects the extent of capillary-like network formation. *Cell Biochem. Biophys.* **49**, 73–83 (2007).
99. Duan, Y. et al. Migration of endothelial cells and mesenchymal stem cells into hyaluronic acid hydrogels with different moduli under induction of pro-inflammatory macrophages. *J. Mater. Chem. B* **7**, 5478–5489 (2019).
100. Mason, B. N., Starchenko, A., Williams, R. M., Bonassar, L. J. & Reinhart-King, C. A. Tuning three-dimensional collagen matrix stiffness independently of collagen concentration modulates endothelial cell behavior. *Acta Biomater.* **9**, 4635–4644 (2013).
101. Liu, B. & Tang, D. Influence of non-Newtonian properties of blood on the wall shear stress in human atherosclerotic right coronary arteries. *MCB* **8**, 73–90 (2011).
102. Sriram, K., Intaglietta, M. & Tartakovsky, D. M. Non-Newtonian flow of blood in arterioles: consequences for wall shear stress measurements. *Microcirculation* **21**, 628–639 (2014).
103. Cherry, E. M. & Eaton, J. K. Shear thinning effects on blood flow in straight and curved tubes. *Phys. Fluids* **25**, 073104 (2013).
104. Secomb, T. W., Hsu, R. & Pries, A. R. Motion of red blood cells in a capillary with an endothelial surface layer: effect of flow velocity. *Am. J. Physiol. Circ. Physiol.* **281**, H629–H636 (2001).
105. Freund, J. B. & Vermot, J. The wall-stress footprint of blood cells flowing in microvessels. *Biophys. J.* **106**, 752–762 (2014).
106. Hogan, B., Shen, Z., Zhang, H., Misbah, C. & Barakat, A. I. Shear stress in the microvasculature: influence of red blood cell morphology and endothelial wall undulation. *Biomech. Model. Mechanobiol.* **18**, 1095–1109 (2019).
107. Papaioannou, T. Vascular wall shear stress: basic principles and methods. *Hell. J. Cardiol.* **46**, 9–15 (2005).
108. Lipowsky, H. H., Kovalcheck, S. & Zweifach, B. W. The distribution of blood rheological parameters in the microvasculature of cat mesentery. **43**, 738–749 (1978).
109. Natarajan, M., Aravindan, N., Sprague, A. & Mohan, S. Hemodynamic flow-induced mechanotransduction signaling influences the radiation response of the vascular endothelium. **186**, 175–188 (2016).
110. Chatterjee, S. Endothelial mechanotransduction, redox signaling and the regulation of vascular inflammatory. *Pathways* **9**, 1–16 (2018).
111. Hahn, C. & Schwartz, M. A. Mechanotransduction in vascular physiology and atherogenesis. *Nat. Rev. Mol. Cell Biol.* https://doi.org/10.1038/nrm2596 (2009).
112. Baeyens, N. et al. Vascular remodeling is governed by a VEGFR3-dependent fluid shear stress set point. *eLife* https://doi.org/10.7554/eLife.04645 (2015).
113. Baratchi, S. et al. Molecular sensors of blood flow in endothelial cells. *Trends Mol. Med.* **23**, 850–868 (2017).

114. Davies, P. F. Hemodynamic shear stress and the endothelium in cardiovascular pathophysiology. *Nat. Clin. Pract. Cardiovasc. Med.* **6**, 16–26 (2009).
115. Chiu, J.-J. & Chien, S. Effects of disturbed flow on vascular endothelium: pathophysiological basis and clinical perspectives. *Physiol. Rev.* **91**, 327–387 (2011).
116. Bergan, J. J. et al. Chronic venous disease. *N. Engl. J. Med* **355**, 488–498 (2006).
117. Flaherty, J. T. et al. Endothelial nuclear patterns in the canine arterial tree with particular reference to hemodynamic events. *Circ. Res.* **30**, 23–33 (1972).
118. Silkworth, J. B., Stehbens, W. E. & Phil, D. The shape of endothelial cells in en face preparations of rabbit blood vessels. *Angiology* **26**, 474–487 (1975).
119. Langille, B. L. & Adamson, S. L. E. E. Relationship between blood flow direction and endothelial cell orientation at arterial branch sites in rabbits and mice. *Circ. Res.* **48**, 481–488 (1981).
120. Levesque, M. & Nerem, R. M. The elongation and orientation of cultured endothelial cells in response to shear stress. *J. Biomech. Eng.* **107**, 341–347 (1985).
121. Estrada, R., Giridharan, G. A. & Nguyen, M. Microfluidic endothelial cell culture model to replicate disturbed flow conditions seen in atherosclerosis susceptible regions. *Biomicrofluidics* **5**, 32006–3200611 (2011).
122. Malek, A. M. & Izumo, S. Mechanism of endothelial cell shape change and cytoskeletal remodeling in response to fluid shear stress. **726**, 713–726 (1996).
123. Chiu, J.-J., Wang, D. L., Chien, S., Skalak, R. & Usami, S. Effects of disturbed flow on endothelial cells. *J. Biomech. Eng.* **120**, 2–8 (1998).
124. Dewey, C. F., Bussolari, S. R., Gimbrone, M. A. & Davies, P. F. The dynamic response of vascular endothelial cells to fluid shear stress. *J. Biomech. Eng.* **103**, 177–185 (1981).
125. Miao, H. et al. Effects of flow patterns on the localization and expression of VE-cadherin at vascular endothelial cell junctions: in vivo and in vitro investigations. *J. Vasc. Res.* **42**, 77–89 (2005).
126. Davies, P. F., Remuzzi, A., Gordon, E. J., Dewey, C. F. & Gimbrone, M. A. Turbulent fluid shear stress induces vascular endothelial cell turnover in vitro. *Proc. Natl. Acad. Sci. USA* https://doi.org/10.1073/pnas.83.7.2114 (1986).
127. Li, S., Huang, N. F. & Hsu, S. Mechanotransduction in endothelial cell migration. *J. Cell Biochem.* **96**, 1110–1126 (2005).
128. Inglebert, M. et al. The effect of shear stress reduction on endothelial cells: A microfluidic study of the actin cytoskeleton. Biomicrofluidics **14**, 024115 (2020).
129. Noria, S. et al. Assembly and reorientation of stress fibers drives morphological changes to endothelial cells exposed to shear stress. *Am. J. Pathol.* **164**, 1211–1223 (2004).
130. Galbraith, C. G., Skalak, R. & Chien, S. Shear stress induces spatial reorganization of the endothelial cell. *Cytoskeleton* **330**, 317–330 (1998).
131. Franke, R.-P. et al. Induction of human vascular endothelial stress fibres by fluid shear stress. *Nature* **307**, 648–649 (1984).
132. Steward, R. et al. Fluid shear, intercellular stress, and endothelial cell alignment. *Am. J. Physiol. Cell Physiol.* **308**, C657–C664 (2015).
133. Hur, S. S. et al. Roles of cell confluency and fluid shear in 3-dimensional intracellular forces in endothelial cells. *Proc. Natl Acad. Sci. USA* **109**, 11110–11115 (2012).
134. Metaxa, E. et al. Nitric oxide-dependent stimulation of endothelial cell proliferation by sustained high flow. *Am. J. Physiol. Hear. Circ. Physiol.* **295**, 736–742 (2008).
135. Tovar-lopez, F., Thurgood, P., Gilliam, C. & Nguyen, N. A microfluidic system for studying the effects of disturbed flow on endothelial cells. *Front. Bioeng. Biotechnol.* **7**, 1–7 (2019).
136. Ostrowski, M. A. et al. Microvascular endothelial cells migrate upstream and align against the shear stress field created by impinging flow. *Biophys. J.* **106**, 366–374 (2014).
137. Robotti, F. et al. The influence of surface micro-structure on endothelialization under supraphysiological wall shear stress. *Biomaterials* https://doi.org/10.1016/j.biomaterials.2014.06.046 (2014).
138. Sato, M., Saito, N., Sakamoto, N. & Ohashi, T. High wall shear stress gradient suppress morphological responses of endothelial cells to fluid flow. In *World Congress on Medical Physics and Biomedical Engineering, September 7 - 12, 2009, Munich, Germany. IFMBE Proceedings* (eds. Dössel, O. & Schlegel W. C.)312–313 (Springer, Berlin, Heidelberg, 2009). https://doi.org/10.1007/978-3-642-03882-2_82.
139. Hsu, P. et al. Effects of flow patterns on endothelial cell migration into a zone of mechanical denudation. *Biochem. Biophys. Res Commun.* **285**, 751–759 (2001).
140. Gojova, A., Barakat, A. I. & Barakat, A. I. Vascular endothelial wound closure under shear stress: role of membrane fluidity and flow-sensitive ion channels. **95616**, 2355–2362 (2005).
141. Albuquerque, M. L. C. & Flozak, A. S. Lamellipodial motility in wounded endothelial cells exposed to physiologic flow is associated with different patterns of b 1 -integrin and vinculin localization. *J. Cell. Physiol.* **60**, 50–60 (2003).
142. Albuquerque, M. L. C., Waters, C. M., Savla, U., Schnaper, H. W. & Flozak, A. S. Shear stress enhances human endothelial cell wound closure in vitro. *Am. J. Physiol. Circ. Physiol.* **279**, H293–302 (2000).
143. Ciechanowska, A., Ladyzynski, P., Hoser, G. & Sabalinska, S. Human endothelial cells hollow fiber membrane bioreactor as a model of the blood vessel for in vitro studies. *J. Artif. Organs* https://doi.org/10.1007/s10047-016-0902-0 (2016).
144. Akimoto, S., Mitsumata, M., Sasaguri, T. & Yoshida, Y. Laminar shear stress inhibits vascular endothelial cell proliferation by inducing cyclin-dependent kinase inhibitor p21. *Circ. Res.* **86**, 185–190 (2000).
145. DePaola, N., Gimbrone, M. A., Davies, P. F. & Dewey, C. F. Vascular endothelium responds to fluid shear stress gradients. *Arterioscler. Thromb.* **12**, 1254–1257 (1992).
146. Sakamoto, N., Saito, N., Han, X., Ohashi, T. & Sato, M. Effect of spatial gradient in fluid shear stress on morphological changes in endothelial cells in response to flow. *Biochem. Biophys. Res. Commun.* **395**, 264–269 (2010).
147. Szymanski, M. P., Metaxa, E., Meng, H. & Kolega, J. Endothelial cell layer subjected to impinging flow mimicking the apex of an arterial bifurcation. *Ann. Biomed. Eng.* **36**, 1681–1689 (2008).
148. Yoshino, D., Sakamoto, N. & Sato, M. Integrative biology fluid shear stress combined with shear stress spatial gradients regulates vascular endothelial. *Integr. Biol.* https://doi.org/10.1039/c7ib00065k (2017).
149. Dolan, J. M., Meng, H., Singh, S., Paluch, R. & Kolega, J. High fluid shear stress and spatial shear stress gradients affect endothelial proliferation, survival, and alignment. *Ann. Biomed. Eng.* **39**, 1620–1631 (2011).
150. Peiffer, V., Sherwin, S. J. & Weinberg, P. D. Computation in the rabbit aorta of a new metric - the transverse wall shear stress - to quantify the multidirectional character of disturbed blood flow. *J. Biomech.* **46**, 2651–2658 (2013).
151. Frydrychowicz, A. et al. Interdependencies of aortic arch secondary flow patterns, geometry, and age analysed by 4-dimensional phase contrast magnetic resonance imaging at 3 Tesla. *Eur. Radiol.* https://doi.org/10.1007/s00330-011-2353-6 (2012).
152. Mohamied, Y., Sherwin, S. J. & Weinberg, P. D. Understanding the fluid mechanics behind transverse wall shear stress. *J. Biomech.* **50**, 102–109 (2017).
153. Chakraborty, A. et al. Impact of bi-axial shear on atherogenic gene expression by endothelial cells. *Ann. Biomed. Eng.* **44**, 3032–3045 (2016).
154. Potter, C. M. F. et al. Role of shear stress in endothelial cell morphology and expression of cyclooxygenase isoforms. *Arter. Thromb. Vasc. Biol.* **31**, 384–391 (2011).
155. Dardik, A. et al. Differential effects of orbital and laminar shear stress on endothelial cells. *J. Vasc. Surg.* **41**, 869–880 (2005).
156. Warboys, C. M., Ghim, M. & Weinberg, P. D. Understanding mechanobiology in cultured endothelium: a review of the orbital shaker method. *Atherosclerosis* **285**, 170–177 (2019).
157. Mandrycky, C., Hadland, B. & Zheng, Y. 3D curvature-instructed endothelial flow response and tissue vascularization. *Sci. Adv.* **6**, 3629–3645 (2020).
158. Helmlinger, G., Geiger, R. V., Schreck, S. & Nerem, R. M. Effects of pulsatile flow on cultured vascular endothelial cell morphology. *J. Biomech. Eng.* **113**, 123–131 (1991).
159. Lum, R. M., Wiley, L. M. & Barakat, A. I. Influence of different forms of fluid shear stress on vascular endothelial TGF-beta1 mRNA expression. *Int. J. Mol. Med.* https://doi.org/10.1088/1755-1315/117/1/012035 (2000).
160. Helmlinger, G., Berk, B. C. & Nerem, R. M. Calcium responses of endothelial cell monolayers subjected to pulsatile and steady laminar flow differ. *Am. J. Physiol. Physiol.* **269**, C367–C375 (1995).
161. Blackman, B. R. & Gimbrone, M. A. A new in vitro model to evaluate differential responses of endothelial cells to simulated arterial shear stress waveforms. *J. Biomech. Eng.* **124**, 397–407 (2002).
162. Uzarski, J. S., Scott, E. W. & Mcfetridge, P. S. Adaptation of endothelial cells to physiologically- modeled, variable shear. *Stress* **8**, 17–19 (2013).
163. Thoumine, O., Nerem, R. M. & Girard, F. R. Oscillatory shear stress and hydrostatic pressure modulate cell-matrix attachment proteins in cultured endothelial cells. *Vitr. Cell. Dev. Biol. Anim.* https://doi.org/10.1007/BF02631337 (1995).
164. Sampath, R. et al. Shear stress-mediated changes in the expression of leukocyte adhesion receptors on human umbilical vein endothelial cells in vitro. **23**, 247–256 (1995).
165. Ohno, M., Cooke, J. P., Dzau, V. J. & Gibbons, G. H. Fluid shear stress induces endothelial transforming growth factor beta-1 transcription and production modulation by potassium channel blockade. **95**, 1363–1369 (1995).
166. Jiang, Z., Berceli, S. A., Pfahnl, C. L. & Wu, L. Wall shear modulation of cytokines in early vein grafts. *J. Vasc. Surg.* **40**, 345–350 (2004).
167. Chang, C., Seibel, A. J. & Song, J. W. Application of microscale culture technologies for studying lymphatic vessel biology. *Microcirculation* **26**, e12547 (2019).

168. Chary, S. R. & Jain, R. K. Direct measurement of interstitial convection and diffusion of albumin in normal and neoplastic tissues by fluorescence photobleaching. *Proc. Natl Acad. Sci. USA* **86**, 5385–5389 (1989).
169. Song, J. W. & Munn, L. L. Fluid forces control endothelial sprouting. *Proc. Natl Acad. Sci. USA* **108**, 15342–15347 (2011).
170. Galie, P. A. et al. Fluid shear stress threshold regulates angiogenic sprouting. *Proc. Natl Acad. Sci. USA* **111**, 7968–7973 (2014).
171. Hernández Vera, R. et al. Interstitial fluid flow intensity modulates endothelial sprouting in restricted Src-activated cell clusters during capillary morphogenesis. *Tissue Eng. Part A* **15**, 175–185 (2009).
172. Abe, Y. et al. Balance of interstitial flow magnitude and vascular endothelial growth factor concentration modulates three-dimensional microvascular network formation. *APL Bioeng.* **3**, 36102 (2019).
173. Vickerman, V. & Kamm, R. D. Mechanism of a flow-gated angiogenesis switch: early signaling events at cell-matrix and cell-cell junctions. *Integr. Biol.* **4**, 863–874 (2012).
174. Akbari, E., Spychalski, G. B., Rangharajan, K. K., Prakash, S. & Song, J. W. Competing fluid forces control endothelial sprouting in a 3-D microfluidic vessel bifurcation model. *Micromachines* **10**, 451 (2019).
175. Dafni, H. & Israely, T. Overexpression of vascular endothelial growth factor 165 drives peritumor interstitial convection and induces lymphatic drain: magnetic resonance imaging, confocal microscopy, and histological tracking of triple-labeled albumin. *Cancer Res.* **62**, 6731–6739 (2002).
176. Kim, S., Chung, M., Ahn, J., Lee, S. & Jeon, N. L. Interstitial flow regulates the angiogenic response and phenotype of endothelial cells in a 3D culture model. *Lab Chip* **16**, 4189–4199 (2016).
177. Figarol, A. et al. Biochemical and Biophysical Research Communications Interstitial flow regulates in vitro three-dimensional self-organized brain micro-vessels. *Biochem. Biophys. Res. Commun.* https://doi.org/10.1016/j.bbrc.2020.09.061 (2020).
178. Ng, C. P., Helm, C. L. E. & Swartz, M. A. Interstitial flow differentially stimulates blood and lymphatic endothelial cell morphogenesis in vitro. *Microvasc. Res.* **68**, 258–264 (2004).
179. Hsu, Y. H. et al. Full range physiological mass transport control in 3D tissue cultures. *Lab Chip* **13**, 81–89 (2013).
180. Shirure, V. S., Lezia, A., Tao, A., Alonzo, L. F. & George, S. C. Low levels of physiological interstitial flow eliminate morphogen gradients and guide angiogenesis. *Angiogenesis* **20**, 493–504 (2017).
181. Kwon, H. et al. In vivo modulation of endothelial polarization by Apelin receptor signalling. *Nat. Commun.* https://doi.org/10.1038/ncomms11805 (2016).
182. Krüger-genge, A., Blocki, A., Franke, R. & Jung, F. Vascular endothelial cell biology: an update. *Int J. Mol. Sci.* **20**, 4411 (2019).
183. Drenckhahn, D. & Wagner, J. Stress fibers in the splenic sinus endothelium in situ: molecular structure, relationship to the extracellular matrix and contractility . *J. Cell Biol.* **102**, 1738–1747 (1986).
184. Butcher, J. T. & Penrod, A. M. Unique morphology and focal adhesion development of valvular endothelial cells in static and fluid flow environments. *Arter. Thromb. Vasc. Biol.* **24**, 1429–1434 (2004).
185. Michalaki, E., Surya, V. N., Fuller, G. G. & Dunn, A. R. Perpendicular alignment of lymphatic endothelial cells in response to spatial gradients in wall shear stress. *Commun. Biol.* **3**, 57 (2020).
186. Reinitz, A., DeStefano, J., Ye, M., Wong, A. D. & Searson, P. C. Human brain microvascular endothelial cells resist elongation due to shear stress. *Microvasc. Res.* https://doi.org/10.1016/j.mvr.2015.02.008 (2015).
187. Destefano, J. G., Xu, Z. S., Williams, A. J., Yimam, N. & Searson, P. C. Effect of shear stress on iPSC - derived human brain microvascular endothelial cells (dhBMECs). *Fluids Barriers CNS* https://doi.org/10.1186/s12987-017-0068-z (2017).
188. Ohta, S., Inasawa, S. & Yamaguchi, Y. Alignment of vascular endothelial cells as a collective response to shear flow. *J. Phys. D. Appl. Phys.* **48**, 245401 (2015).
189. Acevedo, A. D., Bowser, S. S., Gerritsen, M. E. & Bizios, R. Morphological and proliferative responses of endothelial cells to hydrostatic pressure: role of fibroblast growth factor. *J. Cell. Physiol.* **157**, 603–614 (1993).
190. Salwen, S. A., Szarowski, D. H., Turner, J. N. & Bizios, R. Three-dimensional changes of the cytoskeleton of vascular endothelial cells exposed to sustained hydrostatic pressure. *Med. Biol. Eng. Comput.* **36**, 520–527 (1998).
191. Ohashi, T., Sugaya, Y., Sakamoto, N. & Sato, M. Relative contribution of physiological hydrostatic pressure and fluid shear stress to endothelial monolayer integrity. *Biomed. Eng. Lett.* **6**, 31–38 (2016).
192. Ohashi, T., Sugaya, Y., Sakamoto, N. & Sato, M. Hydrostatic pressure influences morphology and expression of VE-cadherin of vascular endothelial cells. *J. Biomech.* **40**, 2399–2405 (2007).
193. Sumpio, B. E., Widmann, M. D., Ricotta, J., Awolesi, M. A. & Watase, M. Increased ambient pressure stimulates proliferation and morphologic changes in cultured endothelial cells. *J. Cell. Physiol.* **158**, 133–139 (1994).
194. Sugaya, Y., Sakamoto, N., Ohashi, T. & Sato, M. Elongation and random orientation of bovine endothelial cells in response to hydrostatic pressure: comparison with response to shear stress. *JSME Int. J. Ser. C* **46**, 1248–1255 (2003).
195. Tworkoski, E., Glucksberg, M. R. & Johnson, M. The effect of the rate of hydrostatic pressure depressurization on cells in culture. *PLoS ONE* **13**, e0189890 (2018).
196. Vouyouka, A. G. et al. Ambient pulsatile pressure modulates endothelial cell proliferation. *J. Mol. Cell. Cardiol.* **30**, 609–615 (1998).
197. Yoshino, D., Sato, K. & Sato, M. Endothelial cell response under hydrostatic pressure condition mimicking pressure therapy. *Cell. Mol. Bioeng.* **8**, 296–303 (2015).
198. Yoshino, D. & Sato, M. Early-stage dynamics in vascular endothelial cells exposed to hydrostatic pressure. *J. Biomech. Eng.* **141**, 091006 (2019).
199. Schwartz, E. A., Bizios, R., Medow, M. S. & Gerritsen, M. E. Exposure of human vascular endothelial cells to sustained hydrostatic pressure stimulates proliferation. *Circ. Res.* **84**, 315–322 (1999).
200. Prystopiuk, V. et al. A two-phase response of endothelial cells to hydrostatic pressure. *J. Cell Sci.* **131**, jcs206920 (2018).
201. Shin, H. Y., Gerritsen, M. E. & Bizios, R. Regulation of endothelial cell proliferation and apoptosis by cyclic pressure. *Ann. Biomed. Eng.* **30**, 297–304 (2002).
202. Hasel, C. et al. Pathologically elevated cyclic hydrostatic pressure induces CD95-mediated apoptotic cell death in vascular endothelial cells. *Am. J. Physiol. Physiol.* **289**, C312–C322 (2005).
203. Tokunaga, O. & Watanabe, T. Properties of endothelial cell and smooth muscle cell cultured in ambient pressure. *In Vitr. Cell. Dev. Biol.* **23**, 528–534 (1987).
204. Friedrich, E. E. et al. Endothelial cell Piezo1 mediates pressure-induced lung vascular hyperpermeability via disruption of adherens junctions. *Proc. Natl Acad. Sci. USA* **116**, 12980–12985 (2019).
205. Nelson, C. M., Pirone, D. M., Tan, J. L. & Chen, C. S. Vascular endothelial-cadherin regulates cytoskeletal tension, cell spreading, and focal adhesions by stimulating RhoA. *Mol. Biol. Cell* **15**, 2943–2953 (2004).
206. Giannotta, M., Trani, M. & Dejana, E. VE-Cadherin and endothelial adherens junctions: active guardians of vascular integrity. *Dev. Cell* **26**, 441–454 (2013).
207. Kiyoumarsioskouei, A., Saidi, M. S., Mosadegh, B. & Firoozabadi, B. A portable culture chamber for studying the effects of hydrostatic pressure on cellular monolayers. *Proc. Inst. Mech. Eng. Part C J. Mech. Eng. Sci.* **233**, 807–816 (2019).
208. Müller-Marschhausen, K., Waschke, J. & Drenckhahn, D. Physiological hydrostatic pressure protects endothelial monolayer integrity. *Am. J. Physiol. Physiol.* **294**, C324–C332 (2008).
209. Shin, H. Y., Bizios, R. & Gerritsen, M. E. Cyclic pressure modulates endothelial barrier function. *Endothelium* **10**, 179–187 (2003).
210. Tschumperlin, D. J., Oswari, J. & Margulies, S. S. Deformation-induced injury of alveolar epithelial cells: effect of frequency, duration, and amplitude.*Am. J. Respir. Crit. Care Med.* **162**, 357–362 (2000).
211. Ding, Z. & Friedman, M. H. Quantification of 3-D coronary arterial motion using clinical biplane cineangiograms. *Int. J. Card. Imaging* **16**, 331–346 (2000).
212. Cheng, C. P., Wilson, N. M., Hallett, R. L., Herfkens, R. J. & Taylor, C. A. In vivo MR angiographic quantification of axial and twisting deformations of the superficial femoral artery resulting from maximum hip and knee flexion. *J. Vasc. Interv. Radiol.* **17**, 979–987 (2006).
213. Choi, G., Shin, L. K., Taylor, C. A. & Cheng, C. P. In vivo deformation of the human abdominal aorta and common iliac arteries with hip and knee flexion: implications for the design of stent-grafts. *J. Endovasc. Ther.* **16**, 531–538 (2009).
214. Klein, A. J. et al. Quantitative assessment of the conformational change in the femoropopliteal artery with leg movement. *Catheter. Cardiovasc. Interv.* **74**, 787–798 (2009).
215. Wedding, K. L. et al. Measurement of vessel wall strain using cine phase contrast MRI. *J. Magn. Reson. Imaging* **15**, 418–428 (2002).
216. Morrison, T. M., Choi, G., Zarins, C. K. & Taylor, C. A. Circumferential and longitudinal cyclic strain of the human thoracic aorta: age-related changes. *J. Vasc. Surg.* **49**, 1029–1036 (2009).
217. Wittek, A. et al. Cyclic three-dimensional wall motion of the human ascending and abdominal aorta characterized by time-resolved three-dimensional ultrasound speckle tracking. *Biomech. Model. Mechanobiol.* **15**, 1375–1388 (2016).
218. Dobrin, P. B. Mechanical properties of arteries. *Physiol. Rev.* **58**, 397–460 (1978).
219. Ives, C. L., Eskin, S. G. & McIntire, L. V. Mechanical effects on endothelial cell morphology: In vitro assessment. *Vitr. Cell. Dev. Biol.* **22**, 500–507 (1986).
220. Kaunas, R., Usami, S. & Chien, S. Regulation of stretch-induced JNK activation by stress fiber orientation. *Cell. Signal.* **18**, 1924–1931 (2006).
221. Wang, J. H.-C., Goldschmidt-Clermont, P. & Yin, F. C.-P. Contractility affects stress fiber remodeling and reorientation of endothelial cells subjected to cyclic mechanical stretching. *Ann. Biomed. Eng.* **28**, 1165–1171 (2000).

222. Iba, T. & Sumpio, B. E. Morphological response of human endothelial cells subjected to cyclic strain in vitro. *Microvasc. Res.* **42**, 245–254 (1991).
223. Wang, J. H. C., Goldschmidt-Clermont, P., Wille, J. & Yin, F. C. P. Specificity of endothelial cell reorientation in response to cyclic mechanical stretching. *J. Biomech.* https://doi.org/10.1016/S0021-9290(01)00150-6 (2001).
224. Shirinsky, V. P. et al. Mechano-chemical control of human endothelium orientation and size. *J. Cell Biol.* **109**, 331–339 (1989).
225. Hayakawa, K., Sato, N. & Obinata, T. Dynamic reorientation of cultured cells and stress fibers under mechanical stress from periodic stretching. *Exp. Cell Res.* **268**, 104–114 (2001).
226. Krishnan, R. et al. Fluidization, resolidification, and reorientation of the endothelial cell in response to slow tidal stretches. *Am. J. Physiol. Cell Physiol.* **303**, C368–C375 (2012).
227. Sokabe, M. et al. Mechanotransduction and intracellular signaling mechanisms of stretch-induced remodeling in endothelial cells. *Heart Vessels* Suppl. 12, 191–193 (1997).
228. Takemasa, T., Sugimoto, K. & Yamashita, K. Amplitude-dependent stress fiber reorientation in early response to cyclic strain. *Exp. Cell Res.* **230**, 407–410 (1997).
229. Pourati, J. et al. Is cytoskeletal tension a major determinant of cell deformability in adherent endothelial cells? *Am. J. Physiol.* **274**, C1283–C1289 (1998).
230. Hatami, J., Tafazzoli-Shadpour, M., Haghighipour, N., Shokrgozar, M. A. & Janmaleki, M. Influence of cyclic stretch on mechanical properties of endothelial cells. *Exp. Mech.* **53**, 1291–1298 (2013).
231. Wang, N. et al. Cell prestress. I. Stiffness and prestress are closely associated in adherent contractile cells. *Am. J. Physiol. Cell Physiol.* **282**, C606–C616 (2002).
232. Sumpio, B. E., Banes, A. J., Levin, L. G. & Johnson, G. Mechanical stress stimulates aortic endothelial cells to proliferate. *J. Vasc. Surg.* **6**, 252–256 (1987).
233. Liu, X., Ensenat, D., Wang, H., Schafer, A. I. & Durante, W. Physiologic cyclic stretch inhibits apoptosis in vascular endothelium. *FEBS Lett.* **541**, 52–56 (2003).
234. Li, W. & Sumpio, B. E. Strain-induced vascular endothelial cell proliferation requires PI3K-dependent mTOR-4E-BP1 signal pathway. *Am. J. Physiol. Heart Circ. Physiol.* **288**, H1591–H1597 (2005).
235. Kou, B., Zhang, J. & Singer, D. R. J. Effects of cyclic strain on endothelial cell apoptosis and tubulogenesis are dependent on ROS production via NAD(P)H subunit p22phox. *Microvasc. Res.* **77**, 125–133 (2009).
236. Neto, F. et al. YAP and TAZ regulate adherens junction dynamics and endothelial cell distribution during vascular development. *Elife* **7**, e31037 (2018).
237. Huveneers, S. & de Rooij, J. Mechanosensitive systems at the cadherin-f-actin interface. *J. Cell Sci.* **126**, 403–413 (2013).
238. Abiko, H. et al. Rho guanine nucleotide exchange factors involved in cyclic-stretch-induced reorientation of vascular endothelial cells. *J. Cell Sci.* **128**, 1683–1695 (2015).
239. Liu, W. F., Nelson, C. M., Tan, J. L. & Chen, C. S. Cadherins, RhoA, and Rac1 are differentially required for stretch-mediated proliferation in endothelial versus smooth muscle cells. *Circ. Res.* **101**, e44–e52 (2007).
240. Von Offenberg Sweeney, N. et al. Cyclic strain-mediated regulation of vascular endothelial cell migration and tube formation. *Biochem. Biophys. Res. Commun.* **329**, 573–582 (2005).
241. Yano, Y., Geibel, J. & Sumpio, B. E. Tyrosine phosphorylation of pp125(FAK) and paxillin in aortic endothelial cells induced by mechanical strain. *Am. J. Physiol.* **271**, C635–C649 (1996).
242. Zeiger, A. S. et al. Static mechanical strain induces capillary endothelial cell cycle re-entry and sprouting. *Phys. Biol.* **13**, 46006 (2016).
243. Joung, I. S., Iwamoto, M. N., Shiu, Y. T. & Quam, C. T. Cyclic strain modulates tubulogenesis of endothelial cells in a 3D tissue culture model. *Microvasc. Res.* **71**, 1–11 (2006).
244. Matsumoto, T. et al. Mechanical strain regulates endothelial cell patterning in vitro. *Tissue Eng.* **13**, 207–217 (2007).
245. Sinha, R. et al. Endothelial cell alignment as a result of anisotropic strain and flow induced shear stress combinations. *Sci. Rep.* **6**, 29510 (2016).
246. Moretti, M., Prina-Mello, A., Reid, A. J., Barron, V. & Prendergast, P. J. Endothelial cell alignment on cyclically-stretched silicone surfaces. *J. Mater. Sci. Mater. Med.* **15**, 1159–1164 (2004).
247. Wille, J. J., Ambrosi, C. M. & Yin, F. C. P. Comparison of the effects of cyclic stretching and compression on endothelial cell morphological responses. *J. Biomech. Eng.* **126**, 545–551 (2004).
248. Meza, D., Abejar, L., Rubenstein, D. A. & Yin, W. A Shearing-stretching device that can apply physiological fluid shear stress and cyclic stretch concurrently to endothelial cells. *J. Biomech. Eng.* **138**, 4032550 (2016).
249. Awolesi, M. A., Sessa, W. C. & Sumpio, B. E. Cyclic strain upregulates nitric oxide synthase in cultured bovine aortic endothelial cells. *J. Clin. Invest.* **96**, 1449–1454 (1995).
250. Bernardi, L. et al. Adaptive reorientation of endothelial collectives in response to strain. *Integr. Biol.* **10**, 527–538 (2018).
251. Hsu, H.-J., Lee, C.-F. & Kaunas, R. A dynamic stochastic model of frequency-dependent stress fiber alignment induced by cyclic stretch. *PLoS ONE* **4**, e4853 (2009).
252. Haghighipour, N. et al. Topological remodeling of cultured endothelial cells by characterized cyclic strains. *Mol. Cell Biomech.* **4**, 189–199 (2007).
253. Greiner, A. M., Biela, S. A., Chen, H., Spatz, J. P. & Kemkemer, R. Featured article: temporal responses of human endothelial and smooth muscle cells exposed to uniaxial cyclic tensile strain. *Exp. Biol. Med.* **240**, 1298–1309 (2015).
254. Lee, C. F., Haase, C., Deguchi, S. & Kaunas, R. Cyclic stretch-induced stress fiber dynamics - Dependence on strain rate, Rho-kinase and MLCK. *Biochem. Biophys. Res. Commun.* **401**, 344–349 (2010).
255. Takemasa, T., Yamaguchi, T., Yamamoto, Y., Sugimoto, K. & Yamashita, K. Oblique alignment of stress fibers in cells reduces the mechanical stress in cyclically deforming fields. *Eur. J. Cell Biol.* **77**, 91–99 (1998).
256. Birukov, K. G. et al. Magnitude-dependent regulation of pulmonary endothelial cell barrier function by cyclic stretch. *Am. J. Physiol. Lung Cell. Mol. Physiol.* **285**, L785–L797(2003).
257. Haghighipour, N., Tafazzoli-Shadpour, M., Shokrgozar, M. A. & Amini, S. Effects of cyclic stretch waveform on endothelial cell morphology using fractal analysis. *Artif. Organs* **34**, 481–490 (2010).
258. Tondon, A., Hsu, H. J. & Kaunas, R. Dependence of cyclic stretch-induced stress fiber reorientation on stretch waveform. *J. Biomech.* **45**, 728–735 (2012).
259. Yamada, H. & Ando, H. Orientation of apical and basal actin stress fibers in isolated and subconfluent endothelial cells as an early response to cyclic stretching. *Mol. Cell. Biomech.* **4**, 1–12 (2007).
260. Birukova, A. A. et al. Differential regulation of pulmonary endothelial monolayer integrity by varying degrees of cyclic stretch. *Am. J. Pathol.* **168**, 1749–1761 (2006).
261. Morgan, J. T. et al. Integration of basal topographic cues and apical shear stress in vascular endothelial cells. *Biomaterials* **33**, 4126–4135 (2012).
262. Hwang, S. Y. et al. Adhesion assays of endothelial cells on nanopatterned surfaces within a microfluidic channel. *Anal. Chem.* https://doi.org/10.1021/ac100107z (2010).
263. Franco, D. et al. Accelerated endothelial wound healing on microstructured substrates under flow. *Biomaterials* **34**, 1488–1497 (2012).
264. Potthoff, E. et al. Toward a rational design of surface textures promoting endothelialization. *Nano Lett.* **14**, 1069–1079 (2014).
265. Nakayama, K. H. et al. Nanoscale patterning of extracellular matrix alters endothelial function under shear stress. *Nano Lett.* **16**, 410–419 (2016).
266. Uttayarat, P. et al. Microtopography and flow modulate the direction of endothelial cell migration. *Am. J. Physiol. Heart Circ. Physiol.* **294**, H1027–H1035 (2008).
267. Davies, P. F. Flow-mediated endothelial mechanotransduction. *Physiol. Rev.* **75**, 519–560 (1995).
268. Vartanian, K. B., Berny, M. A., Mccarty, O. J. T., Hanson, S. R. & Hinds, M. T. Cytoskeletal structure regulates endothelial cell immunogenicity independent of fluid shear stress. *Am. J. Physiol. Cell Physiol.* **298**, 333–341 (2010).
269. Galie, P. A., Van Oosten, A., Chen, C. S. & Janmey, P. A. Application of multiple levels of fluid shear stress to endothelial cells plated on polyacrylamide gels. *Lab Chip* **15**, 1205–1212 (2015).
270. Kohn, J. C. et al. Cooperative effects of matrix stiffness and fluid shear stress on endothelial cell behavior. *Biophys. J.* **108**, 471–478 (2015).
271. Balachandran, K. et al. Cyclic strain induces dual-mode endothelialmesenchymal transformation of the cardiac valve. *Proc. Natl Acad. Sci. USA* **108**, 19943–19948 (2011).
272. Greiner, A. M. et al. Stable biochemically micro-patterned hydrogel layers control specific cell adhesion and allow long term cyclic tensile strain experiments. *Macromol. Biosci.* **14**, 1547–1555 (2014).
273. Ahmed, W. W. et al. Myoblast morphology and organization on biochemically micro-patterned hydrogel coatings under cyclic mechanical strain. *Biomaterials* **31**, 250–258 (2010).
274. Wang, J. H. C., Grood, E. S., Florer, J. & Wenstrup, R. Alignment and proliferation of MC3T3-E1 osteoblasts in microgrooved silicone substrata subjected to cyclic stretching. *J. Biomech.* **33**, 729–735 (2000).
275. Wang, J. H. C. & Grood, E. S. The strain magnitude and contact guidance determine orientation response of fibroblasts to cyclic substrate strains. *Connect. Tissue Res.* **41**, 29–36 (2000).
276. Prodanov, L. et al. The interaction between nanoscale surface features and mechanical loading and its effect on osteoblast-like cells behavior. *Biomaterials* **31**, 7758–7765 (2010).
277. Doroudian, G., Curtis, M. W., Gang, A. & Russell, B. Cyclic strain dominates over microtopography in regulating cytoskeletal and focal adhesion remodeling of human mesenchymal stem cells. *Biochem. Biophys. Res. Commun.* **430**, 1040–1046 (2013).

278. Tamiello, C. et al. Cellular strain avoidance is mediated by a functional actin cap - observations in an Lmna-deficient cell model. *J. Cell Sci.* **130**, 779–790 (2017).
279. Loesberg, W. A. et al. The threshold at which substrate nanogroove dimensions may influence fibroblast alignment and adhesion. *Biomaterials* **28**, 3944–3951 (2007).
280. Quinlan, A. M. T., Sierad, L. N., Capulli, A. K., Firstenberg, L. E. & Billiar, K. L. Combining dynamic stretch and tunable stiffness to probe cell mechanobiology in vitro. *PLoS ONE* **6**, e23272 (2011).
281. Tondon, A. & Kaunas, R. The direction of stretch-induced cell and stress fiber orientation depends on collagen matrix stress. *PLoS One* **9**, e89592 (2014).
282. Cui, Y. et al. Cyclic stretching of soft substrates induces spreading and growth. *Nat. Commun.* **6**, 1–8 (2015).
283. Dan, A., Huang, R. B. & Leckband, D. E. Dynamic imaging reveals coordinate effects of cyclic stretch and substrate stiffness on endothelial integrity. *Ann. Biomed. Eng.* **44**, 3655–3667 (2016).
284. Gavara, N., Roca-Cusachs, P., Sunyer, R., Farré, R. & Navajas, D. Mapping cell-matrix stresses during stretch reveals inelastic reorganization of the cytoskeleton. *Biophys. J.* **95**, 464–471 (2008).
285. Korff, T. & Augustin, H. Tensional forces in fibrillar extracellular matrices control directional capillary sprouting. *J. Cell Sci.* **112**, 3249–3258 (1999).
286. Moore, J. E. et al. A device for subjecting vascular endothelial cells to both fluid shear stress and circumferential cyclic stretch. *Ann. Biomed. Eng.* **22**, 416–422 (1994).
287. Zheng, W. et al. A microfluidic flow-stretch chip for investigating blood vessel biomechanics. *Lab Chip* **12**, 3441–3450 (2012).
288. Owatverot, T. B., Oswald, S. J., Chen, Y., Wille, J. J. & Yin, F. C. P. Effect of combined cyclic stretch and fluid shear stress on endothelial cell morphological responses. *J. Biomech. Eng.* **127**, 374–382 (2005).
289. Zhao, S. et al. Synergistic effects of fluid shear stress and cyclic circumferential stretch on vascular endothelial cell morphology and cytoskeleton. *Arterioscler. Thromb. Vasc. Biol.* **15**, 1781–1786 (1995).
290. Qiu, Y. & Tarbell, J. M. Interaction between wall shear stress and circumferential strain affects endothelial cell biochemical production. *J. Vasc. Res.* **37**, 147–157 (2000).
291. Amaya, R., Pierides, A. & Tarbell, J. M. The interaction between fluid wall shear stress and solid circumferential strain affects endothelial gene expression. *PLoS ONE* **10**, e0129952 (2015).
292. Brown, A., Burke, G. & Meenan, B. J. Modeling of shear stress experienced by endothelial cells cultured on microstructured polymer substrates in a parallel plate flow chamber. *Biotechnol. Bioeng.* **108**, 1148–1158 (2011).
293. Barbee, K. A., Mundel, T., Lal, R. & Davies, P. F. Subcellular distribution of shear stress at the surface of flow-aligned and nonaligned endothelial monolayers. *Am. J. Physiol.* **268**, H1765–H1772 (1995).
294. Lafaurie-Janvore, J., Antoine, E. E., Perkins, S. J., Babataheri, A. & Barakat, A. I. A simple microfluidic device to study cell-scale endothelial mechanotransduction. *Biomed. Microdevices* https://doi.org/10.1007/s10544-016-0090-y (2016).
295. Siperstein, M. D., Unger, R. H. & Madison, L. L. Studies of muscle capillary basement membranes in normal subjects, diabetic, and prediabetic patients. *J. Clin. Invest.* **47**, 1973–1999 (1968).
296. Feingoldf, K. R., Browner, W. S. & Siperstein, M. D. Prospective studies of muscle capillary basement membrane width in prediabetics. *J. Clin. Endocrinol. Metab.* **69**, 784–789 (1989).
297. Begieneman, M. P. V. et al. The basement membrane of intramyocardial capillaries is thickened in patients with acute myocardial infarction. *J. Vasc. Res.* **47**, 54–60 (2009).
298. Nielsen, S. H. et al. Markers of basement membrane remodeling are associated with higher mortality in patients with known atherosclerosis. *J. Am. Heart Assoc.* **7**, e009193 (2018).
299. Boulter, E., Tissot, F. S., Dilly, J., Pisano, S. & Féral, C. C. Cyclic uniaxial mechanical stretching of cells using a LEGO®parts-based mechanical stretcher system. *J. Cell Sci.* **133**, jcs234666 (2020).
300. Kaarj, K., Madias, M., Akarapipad, P., Cho, S. & Yoon, J. Y. Paper-based in vitro tissue chip for delivering programmed mechanical stimuli of local compression and shear flow. *J. Biol. Eng.* **14**, 20 (2020).
301. Shemesh, J. et al. Flow-induced stress on adherent cells in microfluidic devices. *Lab a Chip* **15**, 4114–4127 (2015).
302. Cutiongco, M. F. A. et al. Planar and tubular patterning of micro and nano-topographies on poly(vinyl alcohol) hydrogel for improved endothelial cell responses. *Biomaterials* https://doi.org/10.1016/j.biomaterials.2016.01.036 (2016).
303. Munoz-Robles, B. G., Kopyeva, I. & DeForest, C. A. Surface patterning of hydrogel biomaterials to probe and direct cell–matrix interactions. *Adv. Mater. Interfaces* **7**, 2001198 (2020).
304. Rizwan, M. et al. Sequentially-crosslinked bioactive hydrogels as nano-patterned substrates with customizable stiffness and degradation for corneal tissue engineering applications. *Biomaterials* **120**, 139–154 (2017).
305. Arakawa, C. et al. Biophysical and biomolecular interactions of malaria-infected erythrocytes in engineered human capillaries. *Sci. Adv.* **6**, eaay7243 (2020).

Acknowledgements

This work was funded in part by an endowment in Cardiovascular Bioengineering from the AXA Research Fund (to A.I.B.), a doctoral fellowship from Ecole Polytechnique (to C. A.D.), a postdoctoral fellowship from the Lefoulon-Dellalande Foundation (to C.L.). A.C. was supported by a research grant from the LaSIPS Laboratory of Excellence (to A.I.B.).

Author contributions

C.A.D., C.L., A.C., and A.I.B. wrote, reviewed, and edited the manuscript.

Competing interests

The authors declare no competing interests.

Additional information

Correspondence and requests for materials should be addressed to A.I.B.

Peer review information *Communications Biology* thanks the anonymous reviewers for their contribution to the peer review of this work.

Reprints and permission information is available at http://www.nature.com/reprintsPrimary Handling Editors: Marco Fritzsche and Christina Karlsson Rosenthal.

Appendix B

Complement to Chapter 2

B.1 Iterative process to attain a robust fabrication protocol

After careful consideration, I decided to use the templating technique to fabricate the chip. More specifically, liquid hydrogel is poured in a PDMS housing around a channel template, which is then removed to create a hollow cylindrical channel [61, 63]. I will present here the iterative process I went through before reaching a functional robust system and the reasons underlying each decision made during the process. The details of the final fabrication protocol are described in the Methods section of the paper (see next section).

B.1.1 Microvessel fabrication

The PDMS housing's principal role is to contain the hydrogel, but it also serves as a hub for all the microfluidic connectors used for flow and cell seeding in the channel. PDMS housings are usually cast on custom molds, made either using classic soft lithography techniques or micro-drilling. I wanted a wide and deep chamber in order to make sure that there were several hundred microns of gel between the cells and the stiff walls. Housings found in other published work in similar setups often have narrow and shallow hydrogel chambers. ECs are known to sense stiff walls up to a hundred microns (see Section 1.4). This initial consideration on geometrical constraints later proved crucial in the generation of large strains(see next section).

I chose micro-drilling, which produces robust molds compatible with micron- and millimeer-scale structures. The molds were fabricated in brass by Caroline Frot, an engineer at LadHyX, based on my drawings (Figure B.1). The mold I ended up using for my experiments was the one made after tweaking the design three times; the dimensions are detailed in the supplementary section of the paper (Figure B.1A,B). The first mold excluded in the process had a chamber that was too long for the needle length and the second mold's chamber was too big and used too much of the collagen stock. This process taught me a great deal about the reality of experimental work, where iteration is key: one can neither predict if a design will work before testing it nor imagine the perfect design on the first try. It was an important first lesson that ultimately guided the way I tackled the rest of my thesis, through trial and error, by constantly confronting the idea to the reality and improving it step-by-step.

B.1.2 Channel template

Once I had the perfect housing, I needed to choose an object to template the channel. The surface of the object had to be smooth, to minimize gel sticking and subsequent tearing of the polymerized gel. It also had to be cylindrical, straight, long and available in different diameters. The length was another difference between my envisioned design and those in the

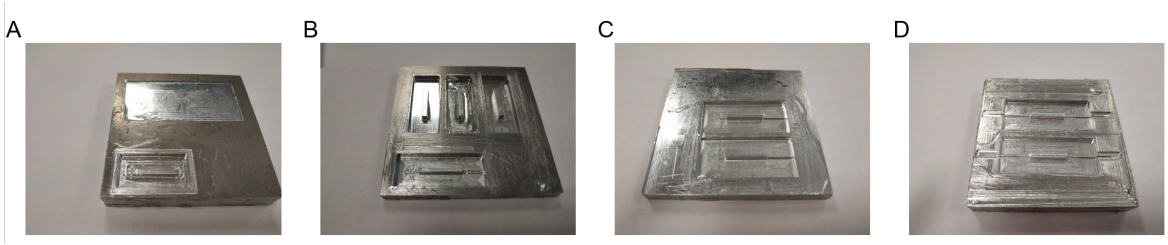

FIGURE B.1: Pictures of the various brass molds made during the iteration process. **A.** First successful mold with the use of nylon thread. **B.** First successful mold with the use of acupuncture needles. **C.** Design with varying hydrogel chamber width. **D.** Clara's design with needles pre-positioned in the mold.

literature. I realized that statistically significant quantification would necessitate analyzing hundreds of cells, whilst the perimeter of the narrow microvessel contains only around a dozen cells. As a consequence, I designed the hydrogel chamber to be a hundred times longer than the channel diameter to have enough cells for robust quantification.

Fishing line My first idea was to use fishing lines. They are cheap and nylon-based (a nontoxic smooth material), can be cut to any desired length, and exist in several diameters, down to 50 µm. The diameter I targeted was 50 µm, typically cited as the smallest diameter in which cell seeding is possible [210]. When the diameter falls below this threshold, suspended cells, whose size becomes comparable to the channel diameter, clog the channel during seeding. I originally considered the pliability of the fishing lines an advantage in that I could thread them through the vertical inlet/outlet ports into the horizontal hydrogel chamber. I later realized, however, that this led to wavy channels and frequent tearing of the polymerized gel (see next paragraph).

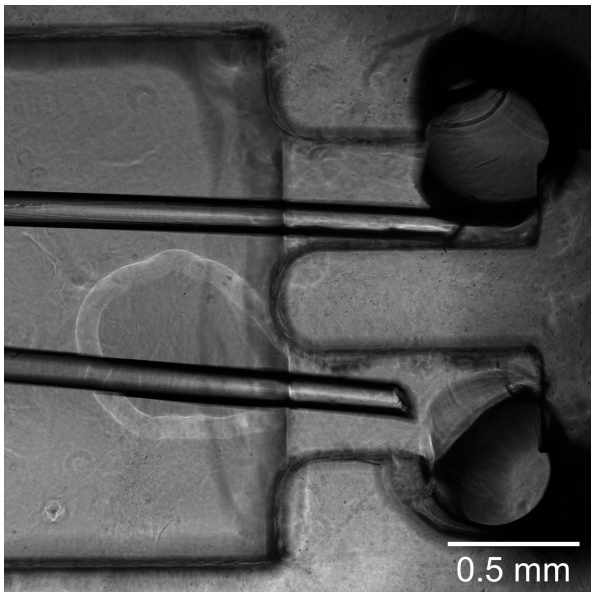

FIGURE B.2: Brightfield image of the channel outlet showing the two nylon thread ends, the two punched outlets and the two large rectangular fingers filled with collagen.

In my design, the chamber had two finger-like extensions at each end to guide the fishing line into position (Figure B.2). The line was suspended between the two ends of the chamber; the distance from the suspended line (and thus the channel once the line was removed) to the bottom glass slide was defined by the depth of these finger-like extensions holding the line in position. This detail was important when the channel was dilated in a pulsatile manner

(see next section) and live imaged (see section 4.2.8). Because these finger-like structures were slightly wider than the fishing line, the liquid collagen would flow by capillarity from the hydrogel chamber into the fingers and the inlet/outlet, creating a "collagen sock" (Figure B.2). This collagen sock provoked gel detachment or clogging during the removal of the fishing line (by the reversal of the collagen sock). To eliminate this problem and to glue the fishing line in place, a small drop of liquid PDMS was carefully placed with a needle on top of the line secured in the finger-like extensions at the inlet and outlet. I managed to have several perfusable channels using this method, and I was able to visualize the flow with fluorescent beads, but the success rate was below 30%.

Needle Fishing lines are available in different diameters, but the waviness of the resulting channel and recurrent damaging of the channel edges by the tip of the lines led me to seek an alternative solution. In the microfabrication literature, the most commonly used material for templating microchannels are acupuncture needles. They are cheap, available in different diameters (down to 120 µm), stiff, smooth and sterile. Switching to needles entailed a small design modification; the needles could not be thread through the vertical inlet/outlet ports. Instead, two horizontal tunnels in the continuation of the channel were added to the PDMS housing, one of them longer and open at the end so the needle could come out on the side (Figure B.1B,C) while the other was short and closed and only served to hold the needle at that end. The open access tunnel could be sealed with vacuum grease after needle removal.

Channel diameter To facilitate cell seeding and ensure a high cell count per channel, I decided to start with needles of 200 µm in diameter. My first confluent endothelium was obtained in these channels and exhibited excellent junctional staining. The issue that appeared quickly thereafter, however, was the volume of medium necessary to maintain a physiological level of shear stress on the cells over several hours. These shear stress magnitudes are on the order of 0.5 to 5 Pa. The corresponding flow rate can be computed from the following equation for steady laminar flow in cylindrical channels:

$$\tau = \frac{4\mu Q}{\pi R^3} \tag{B.1}$$

where τ is the wall shear stress, μ the fluid dynamic viscosity, Q the volumetric flow rate and R the channel radius. The calculated flow rates range from 25 to 250 µL min^{-1}, i.e. 36 to 360 mL per day. Because the microvessel-on-chip does not permit recirculation of the medium, this volume was needed for each chip and required multiple refillings of syringes during the course of the experiment. Finally, these volumes prohibit running several chips in parallel multiple times per week as the price of the total volume of medium used would be prohibitive.

Wall shear stress scales inversely with the radius to the power three, as seen in the previous equation. In other words, a small change in diameter leads to a large variation in shear stress. Switching from a 200 µm-diameter needle to a 120 µm-diameter needle reduces the necessary medium by a factor of five! After the first couple of endothelialized 200 µm channels, all subsequent channels were made with 120 µm needles.

B.1.3 Delamination at the PDMS-gel interface

One recurrent issue was the delamination of the collagen hydrogel from the PDMS housing at the inlet/outlet ports. This occurred either during needle removal or with increased flow rate. The first cause of delamination was the gel sticking rather strongly to the needle, so when the needle was removed, the whole gel block was pulled away from the walls of the PDMS chamber. I realized that the metal tweezers I used to handle the needles were scratching the needle's surface, creating roughness and rendering them more prone to gel sticking. I

resolved this issue by handling needles more carefully and holding them with the tweezers only at their ends, which were not in contact with the gel. This careful manipulation also solved issues of wavy and scratched channel edges, also due to the gel sticking to the needle.

Avoiding the delamination due to pressure increase required stronger binding of the gel to the PDMS housing. The liquid PDMS used to glue the needle in place creates a smooth surface compared to the PDMS that is peeled out of a metal mold and has some roughness. This reduces collagen adhesion at the inlet and outlet of the channel; the resulting concave or convex interfaces also contribute to delamination. In the improved design developed by Clara Ramon-Lozano, another Ph.D. student working on the microvessel (Figure B.1D), two needles are placed in the metal mold and held on the ends of the central chamber before the PDMS is cast around them. These needles are then removed, leaving two dead-end channels in the PDMS housing whose tips are cut open with a biopsy punch, creating a straight and rough interface between the PDMS channels and the central chamber, ideal for strong collagen binding.

B.2 Channel endothelialization

In a microvessel-on-chip, a confluent endothelium lines the walls of the channel. The typical technique for seeding cells in channels is to suspend and push the cells inside the channel using a micropipette, let them sediment and adhere for 15 minutes, and then flush out the floating (non-adherent) cells. I could not use this method because the volume of my microchannel was below one microliter, and the high concentration of cells that would have been needed to have enough cells in the channel would have caused cell aggregation and clogging of the channel. Instead, I decided to infuse the cells at the inlet and to then use a small hydrostatic pressure difference to flow them slowly into the channel. By adjusting the height of the inlet/outlet reservoirs by a couple of microliters, the flow rate in the channel can be tuned to control the amount of cells being flown in and their velocity, which determines the attachment probability. Because the channel diameter is small, suspended cells attached to the bottom as well as the top and sides of the channel. Cell seeding is therefore done under the microscope, to visualize the flow during the process and adjust it accordingly. As a result, the final density of cells seeded in the channel was not proportional to the concentration of the cell suspension and depended highly on the seeding process. The cell density was therefore controlled visually and adjusted to the level that led to a confluent endothelium after 24 hours. This optimal density was found empirically, and typical examples of low, optimal, high and extremely high density are depicted in Figure B.3. Finally, the flow had to be initiated less than an hour after cell seeding in order to prevent cell detachment and apoptosis.

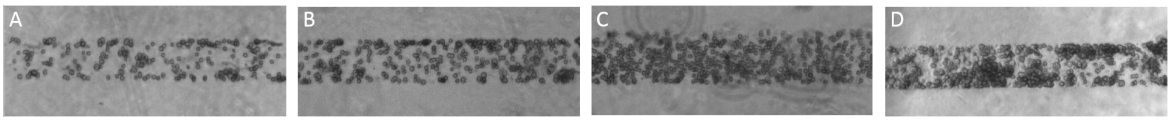

FIGURE B.3: Brightfield representative images of different cell densities during seeding, showing low (**A**), optimal (**B**), high (**C**) and extremely high (**D**) densities.

B.3 Generating capillary-sized vessels

B.3.1 Motivation

At the very beginning of my Ph.D., I wanted to have vessels on the chip with diameters similar to the capillaries found *in vivo*, down to four microns. As mentioned before, cell seeding in

a lumen of this size is impossible. Fabrication of capillaries in hydrogels involves taking advantage of one of two natural processes for the *de novo* vessel formation: angiogenesis or vasculogenesis. Angiogenesis refers to the sprouting of capillaries from a mother vessel, whereas vasculogenesis refers to the spontaneous formation of lumenized tubes by single ECs embedded in a biodegradable matrix. The chip should contain two parallel channels, separated by a few hundred microns, lined with ECs, and capillaries would be formed in between through angiogenesis or vasculogenesis. The channels perfused with microfluidic techniques would facilitate anastomosis, and the smaller lumens would mimic the native vascular bed.

B.3.2 Implementation

To develop this ambitious vascular-network-on-a-chip, two main technical challenges were identified and tackled separately: the double channel design and capillary formation. I worked on the former, while supervising an intern, Clara Ramon-Lozano (who then stayed on as a Ph.D. student, see section 5.2.2), who worked on the latter.

Double channel design To develop a double channel chip, I altered the PDMS mold to have two finger-like extensions on each side of the hydrogel chamber, separated by 350 µm, to guide the needles and keep them in position (Figure B.2 & Figure B.4). The rest of the process was identical to the one for the single channel configuration. The bigger challenge in scaling from one to two templated channels was the fragility of the hydrogel layer separating the two. The smaller the distance between the two channels, the faster sprouts can anastomose to both sides; however, the thinner the gel layer, the more prone it is to tearing during needle removal. A 350 µm distance was found to be a good compromise, leading to a high success rate of needle removal without gel damage. This distance could be adjusted later on, depending on the outcome of the second challenge, the capillary bed formation. Each channel is perfused individually, enabling separate shear stress and strain conditions on each channel, or even the formation of species gradients between the two channels.

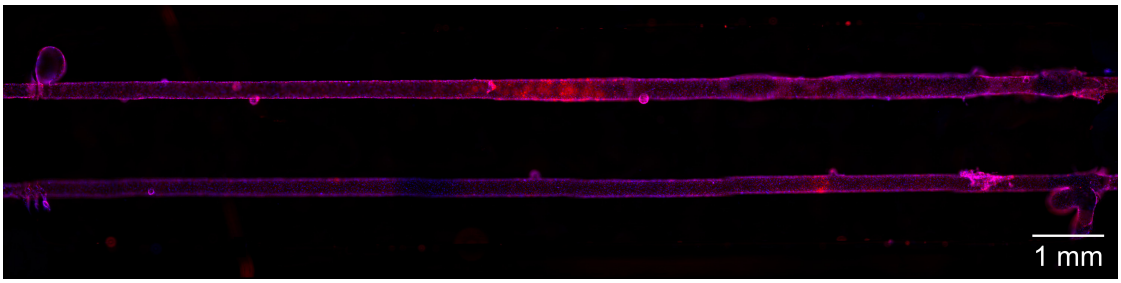

FIGURE B.4: Image of the double channel design in fluorescence with cell-cell junctions in red (VE-cadherin) and nuclei in blue (DAPI).

Vasculogenesis Sprouts formed by angiogenesis progress slowly in the surrounding matrix, no faster than a hundred microns per day [70, 75, 211]. For a sprout emanating from one channel to reach another channel 350 µm away would thus require several days, increasing the duration of the experiment. Excessively long experiments have increased likelihood of failure and contamination and lead to a smaller number of possible experiments. It is based on these considerations that I selected vasculogenesis as the process with the best odds of success. The details of these experiments can be found in the master's thesis of Clara, I will briefly summarize our approach hereafter.

Pericytes are known to increase sprout number and length, so I decided to include them in the vasculogenesis experiment. I identified from the literature a cocktail of growth factors likely to promote sprout formation by cells suspended in a collagen matrix, a mixture

of vascular endothelial growth factor (VEGF), platelet-derived growth factor (PDGF) and ascorbic acid. ECs and pericytes were suspended in the liquid collagen mix before being poured into the PDMS housing and over the needle. Cells were cultured with EC growth medium (EGM-2), supplemented with the growth factor cocktail as commonly done in co-culture experiments. In collagen gels with a concentration above $4\,\mathrm{mg\,mL^{-1}}$, cells stayed round and became apoptotic. In the gels with lower concentrations, cells could spread and form trains of several cells, with visible lumens. However, these trains were sparsely distributed and never anastomosed together to form a connected network, even after four days of culture. Higher flow rates seemed to slightly improve this process but failed to generate capillary-like structures.

After these initial observations, I contacted colleagues in other laboratories who routinely generate networks using vasculogenesis, and it became clear that this process depends strongly on the primary cell line. They told me that some batches of cells never formed any tubes, and their experiments were based on a single cell line. The use of ECs derived from induced pluripotent stem cells might be a way forward to generate cells with reproducible and defined phenotype, compared to primary cell lines purchased commercially. Based on these results, I concluded that vasculogenesis required too much optimization and development to be a viable option for my Ph.D. at this stage. The study of angiogenesis to generate capillaries using this microvessel-on-chip is now the topic of another Ph.D. project by Sara Barrasa-Ramos (see section 5.2.2).

Appendix C

Methods for Chapter 4

C.1 Device fabrication

The microvessel-on-chip used in this study is the one presented and characterized in detail in Chapter 2, with a few modifications. First, the collagen housing was slightly altered to improve collagen adhesion at the channel ends and thus minimize the risk of delamination. This was accomplished by replacing the flat interface between the PDMS and the collagen gel with a curved interface (see Figure C.1). This interface was created with a 2 mm biopsy punch, whose cutting tip was ground to obtain a half-cylinder. Second, the height of the outlet reservoir was increased to the same level as the inlet reservoir (around 1 cm), to enable a tight seal for the straws used for the stretch experiments (see below). To maintain the outlet pressure close to zero during monolayer growth, a side hole was punctured on the side of the outlet reservoir. This hole was sealed with vacuum grease just before straw insertion in the reservoirs.

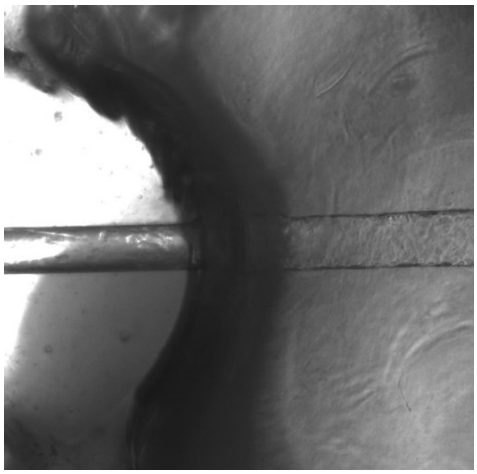

FIGURE C.1: Brightfield image of the channel inlet, showing the curved PDMS-gel interface.

C.2 Cell culture

Cell seeding and culture were performed using the protocols described in Chapter 2. Three cell lines were used in the present study: HUVECs, LifeAct-HUVECs and VE-cadherin-GFP-HUVECs. The two fluorescently-tagged cell lines were a generous gift from Dr Laurent Muller (Collège de France). The cell culture protocols were the same for the three cell lines, with the exception that fluorescent HUVECs were cultured on gelatin coated flasks and kept for two additional passages.

C.3 Stretch

Two different strategies were used to generate stretch in the microvessel, the "flow-based" strategy for the preliminary study and the "outlet pressure-based" strategy for the main study. Although both options are based on gel compression from the luminal pressure, they enable different levels of control of the luminal pressure and have different limitations.

C.3.1 Flow-based stretch

The flow-based stretch approach was the one used in all the experiments in Chapters 2 and 3, whose details were described in Chapter 2. Briefly, by imposing the flow rate within the microvessel, large axial pressure gradient was created throughout the narrow channel. The elevated luminal pressure compresses the gel, dilates the channel and stretches the cell layer lining the wall. As a consequence, the amount of stretch applied to the cells was coupled to the wall shear stress and decreased significantly along the length. Although this approach was compatible with pulsatility, the analysis of the cell response was complicated by the axial variations. The interpretation of the collected data was difficult because of the coupling among the various stresses (see Introduction, section EC mechanobiology).

To generate the luminal pressure in the microvessel, the flow rate imposed at the syringe pump was set to $10\,\mu L\,min^{-1}$ (instead of the $2\,\mu L\,min^{-1}$ used for monolayer growth). After a couple of tests, the protocol described in Chapter 2, where the tubing was connected directly into the inlet, was modified to avoid bubbles and vibration issues.

Bubbles In long term experiments (over several hours), very small bubbles in the syringe coalesce into larger ones. Although bubbles are a recurrent problem in microfluidics, "Bubble trouble", they are particularly harmful in cell-covered channels and soft channels. When the tubing was connected directly to the inlet, a bubble would get pushed into the microvessel and detach the cells or even destroy the channel (surface tension-derived forces are sufficiently large to delaminate or plastically deform the soft collagen gel) (Figure C.2).

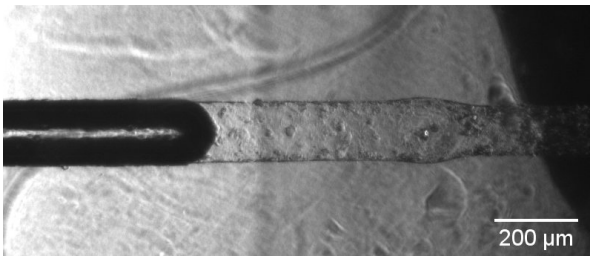

FIGURE C.2: Brightfield image of a channel with an air bubble lodged inside, showing the plastic deformation of the channel by the bubble.

Vibrations The microvessel was by design highly deformable in order to attain large strains and tensile stresses for small luminal pressures. As a result, it is prone to abrupt dilations of large amplitude when pressure shock waves emanating from the tubing propagate into the channel. When the tubing was connected directly to the inlet, the mere act of touching the tubing was sufficient to elicit large diameter oscillations in the channel, up to 50 %, sufficiently elevated to damage or rupture the cell monolayer. While being extra careful and changing the experimental set-up to minimize external perturbations was possible, it complicated the scale-up to the case of several chips in parallel, necessary to maximize data collection.

Solution: straws To solve both issues, the connection of the tubing to the inlet port was replaced by a connection to a reservoir out of which flow was driven into the microvessel via hydrostatic pressure, similar to the way flow was imposed during initial monolayer growth (see Chapter 2). The free surface of the reservoir breaks the pressure shock waves and allow air bubbles to rise to the reservoir free surface rather than enter the microvessel. The height necessary to drive a flow of $10\,\mu L\,min^{-1}$ was 10 cm. To increase the reservoir height, a straw (5 mm in diameter) was inserted into the PDMS reservoir hole (with a slightly smaller diameter), establishing a tight seal (both the PDMS and the straw are slightly deformable). The end of the tubing was then simply placed inside the straw to constantly refill the straw at the imposed flow rate, ensuring a constant height in the inlet reservoir. Straws were chosen because they are stiff, easy to sterilize and their length is easily adjustable.

C.3.2 Outlet pressure-based stretch

The second approach, based on controlling the outlet pressure, addressed the two major limitations of the flow-based approach, namely stretch-shear coupling and the axially non-uniform stretch. When I began my experiments on stretch, it became rapidly clear that the flow rates necessary to attain the desired strains (above 10 %) with the flow-based approach were modifying the response of the cells through wall shear stress (see Results section below). Additionally, only the cells in the first half of the channel were subjected to large strains, limiting the type of quantification I could perform. I decided to change the flow actuation strategy to a pressure actuation strategy, i.e. directly controlling the channel pressure by increasing the outlet pressure.

The simplest manner to impose a given pressure was through a hydrostatic head using a water column, as long as the pressure magnitudes were on the order of hundreds of pascals. Otherwise the height of the water column would have been impractical. For example, to impose a pressure of 100 mmHg, the average pressure in the aorta, I would need a water column of 1.3 m! Here, the order of magnitude I targeted was achievable with a 10 cm-long plastic straw. The channel pressures were then increased by the same amount as the outlet pressure. The desired outlet pressure was obtained by cutting the straw to a set height (Figure C.3 A). Furthermore, when the flow rate was small, the pressure gradient created by the flow was small compared to the outlet pressure, leading to a quasi-uniform channel pressure and thus axially uniform stretch. To guarantee that the shear stress would not vary, the flow rate was increased slightly (from $2\,\mu L\,min^{-1}$ to $3\,\mu L\,min^{-1}$) to compensate for the increase in diameter due to stretch (Figure C.3 B). The main drawback of this approach is that it is incompatible with pulsatile flow.

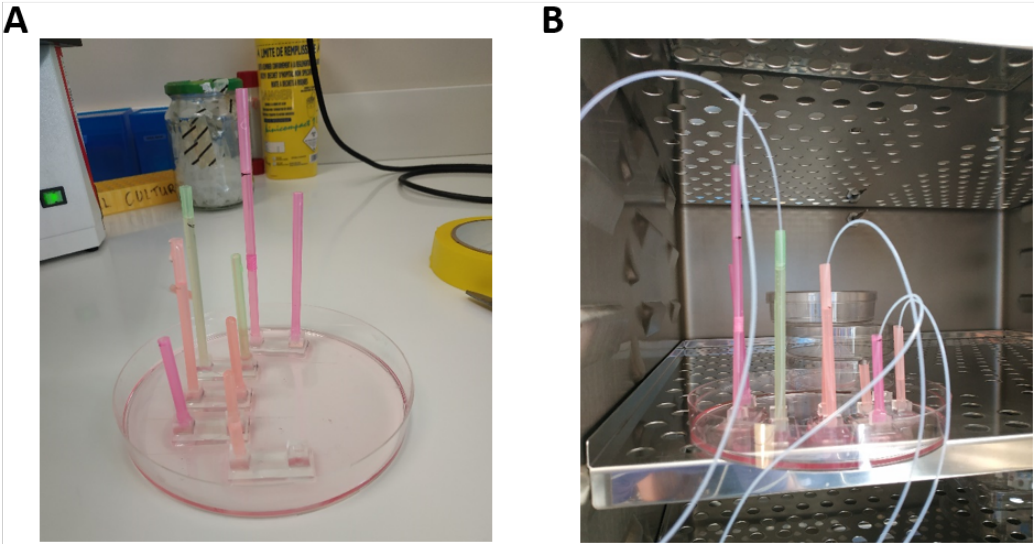

FIGURE C.3: Photos of the outlet pressure-based experimental setup. **A.** Five chips of different outlet pressures, imposed by the varying the outlet straw heights (right), with the intlet straw being a couple of centimeters higher (left). **B.** The same five chips in the incubator showing the tubing that refills the inlet straw at the desired flow rate.

To summarize, the stretch magnitude was set through the outlet straw height, and the flow rate and shear stress were set by the syringe pump that fills the inlet straw. The height of the medium in the inlet straw stabilized at a few centimeters above that of the outlet straw. This hydrostatic pressure difference led to flow in the microvessel, maintained constant by the refilling of the inlet straw with the a syringe pump. The flow exiting the microchannel

entered the outlet straw and was allowed to overflow as the outlet straw remained constantly full.

C.4 Adherens junction disruption

To disrupt adherens junctions, the chelating agent ethylenediaminetetraacetic acid (EDTA) was added to the cell culture medium at 2 mM. The medium was changed to EDTA-containing medium two hours prior to stretch application, and the EDTA was maintained during the stretch. Immunofluorescence assays confirmed adherens junction disruption at this concentration with no visible cell toxicity (Figure C.4). EDTA is a calcium and magnesium chelator that acts in a non-specific manner and affects several aspects of cell function, most notably adherens junction formation, which requires calcium, and cell-substrate adhesion, which primarily requires magnesium [212]. High concentrations of EDTA are known to lead to cell detachment and are routinely used in many protocols as a substitute for trypsin.

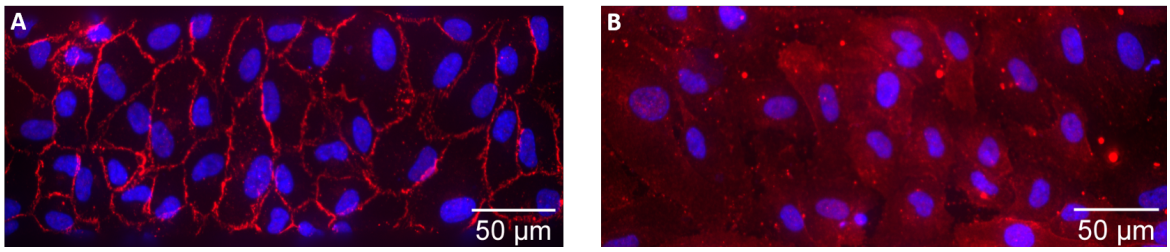

FIGURE C.4: Disruption of adherens junctions by EDTA (2 mM). VE-cadherin immunofluorescence staining for a control (**A**) and EDTA-treated (**B**) HUVEC monolayer . The EDTA-treated cells show no visible cell-cell junctions; the staining appears to be distributed homogeneously within the cells.

C.5 Proliferation assay

To assess EC proliferation, EdU was added to the cell medium at a concentration of 10 µM. Cells were maintained in EdU-containing culture medium for 18 h after which they were fixed and stained for only DAPI and EdU-positive nuclei. The azide-based click chemistry used to reveal EdU-positive nuclei prevents phalloidin or VE-cadherin immunostaining. EdU gets incorporated in cell DNA during DNA replication, a major step in the process of cell mitosis. All the cells that exhibit EdU staining have undergone mitosis during the 18 h window. The fraction of EdU-positive to EdU-negative nuclei (stained with only DAPI) provides a measure of the proliferation rate.

C.6 Laser ablation

Laser ablation of actin stress fibers was performed using the TriM Scope II microscope (La Vision Biotech) equipped with a femtosecond Mai Tai HP DeepSee laser (Spectra Physics) and an Insight DeepSee (Spectra Physics) laser. Cells were imaged with a 25X water immersion objective at 1.44 Hz. LifeAct was excited by the Mai Tai laser set to 820 nm wavelength. Ablations were performed with the Mai Tai laser at 820 nm and exit power at 300 mW. The region to be ablated was defined as an XY ROI and selectively illuminated using an Electro Optic Modulator. The selected exit power allowed efficient ablation with good spatial resolution. Efficiency of the ablation was assessed by the absence of mCherry fluorescence as

well as cellular debris and was confirmed in the following seconds by the recoil of actin stress fibers. Cells were imaged at 1.44 Hz with 5 frames before ablation and for 60-120 seconds following ablation.

C.7 Immunostaining

Immunostaining was performed according to the protocols described in Chapter 2. The following primary antibodies were used: VE-cadherin (rabbit, 1:400), vinculin (mouse, 1:300), paxillin (mouse, 1:200), zyxin (mouse, 1:200), beta-catenin (mouse, 1:200) and fibronectin (mouse, 1:200). Secondary antibodies were all used at a 1:400 dilution.

C.8 Imaging

Most of the measurements and analyses in this project are based on image analysis. Therefore, imaging required some thinking, planning and a clear protocol in order to guarantee robust, precise, unbiased and informative data.

C.8.1 Constraints imposed by the microvessel structure

Although 2D glass petri dishes have many limitatons as *in vitro* platforms, they do have the advantage of providing ecellent conditions for imaging. 3D hydrogel-based microfluidic systems certainly open exciting new avenues as *in vitro* platforms; however, they suffer from imaging limitations. Usually, the more realistic and complex a system is, the more limited the imaging is. In the case of the present microvessel-on-chip, the transparency of the different layers in the light path (glass, hydrogel, cells, medium) was very high and did not interfere with either brightfield (DIC or phase contrast) or fluorescence imaging. Rather, the three major difficulties were the channel position, its horizontality and its curvature.

Channel position The position of the channel relative to the bottom coverslip determined the combination of microscope objective and working distance that I could use. In the present configuration of the system, the channel was positioned intentionally at 400 µm from the bottom in order to provide a thick volume of hydrogel between the channel and the stiff glass bottom, which necessary for large channel dilation (see Chapter 2). Moreover, the channel was around 140 µm in diameter, so the cells on the top surface of the channel were even further from the bottom. Although the 140 µm might not seem significant, comparing it to the thickness of the bottom coverslip, 170 µm, shows that this distance cannot be neglected. As a result, the choice of the objectives was limited to relatively low magnification (up to 20X), with the exception of one extra-long working distance 40X objective we have in the laboratory.

Channel horizontality The templated channel was never perfectly straight and flat because of needle bending and very small differences in height between the two sides of the needle housing. Consequently, the microvessel was slightly tortuous, and although the variations in the XY plane were not an issue, variations in the Z direction strongly affected imaging by not having the entire length of the channel within the the same focal plane. For large structures, such as a 15 mm-long channel, the traditional approach is to use an automated grid scanning followed by stitching of the positions; However, in the case of the microvessel, this led to blurry images as each XY position had a different Z (focal plane).

Channel curvature The EC monolayer lining the microvessel adopted the high curvature cylindrical shape of the channel: one focal plane could not capture the entire channel (or

even half the channel). Different imaging strategies were possible and are detailed in the next section.

C.8.2 Imaging protocol

Field of view, spatial resolution and focus depth To choose the best objective, a balance between the size of field of view, the spatial resolution and focus depth had to be struck. Bigger fields of view, found in low magnification objectives, enabled rapid acquisition of numerous cells, essential for statistical analysis of the cellular response. High spatial resolution, possible using high magnification objectives, was necessary for the identification of small structures (such as focal adhesions) and precise visualization of thin structures and thus for accurate co-localization analysis. Low magnification objectives offer large focus depth, where structures from different Z planes are in focus simultaneously, which provides optimal conditions for acquisitions in a single plane.

Based on this analysis, the 4X and 20X objectives were excluded. A 4X objective did not offer sufficiently high spatial resolution to visualize thin structures such as cell-cell junctions or actin stress fibers, the principle structures of interest in this study. Although a 20X objective had a good field of view and spatial resolution, its depth of focus was too narrow for single plane acquisition (only a quarter of the channel width was in focus) but yet too thick for Z-stack imaging, leading to blurry projection imaging and poor 3D reconstruction.

Systematic imaging for robust quantification 10X objectives have a large focus depth, a good spatial resolution (enough to visualize actin stress fibers) and a large field of view (around 1mm wide), and were thus selected for the rapid whole channel single plane scanning (Figure C.5). Every channel was systematically scanned with the 10X objective with one focal plane along the channel bottom surface and one along the channel top surface, either in brightfield (overall cell shape) or in triple fluorescence (nuclei, actin and adherens junction). The generated data were the basis for automated quantification of cellular response.

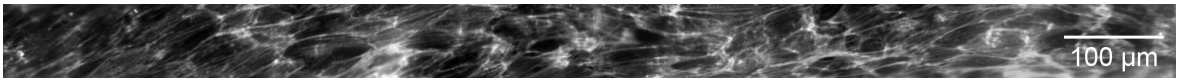

FIGURE C.5: Illustration of a typical image of a phalloidin staining obtained with a 10X objective, showing well resolved actin stress fibers.

Live imaging for cell dynamics quantification The 10X objective was also used for live imaging of cells in brightfield. The same axial scanning, with focal planes along the bottom and top surfaces, was repeated on channels at 15-min intervals for up to 24 h. One challenge I faced while live imaging was the drying of the hydrogel due to the open top of the microvessel. Indeed, when the water fraction changed, the gel swelled or shrank, which shifted the channel either up or down, thus moving the top and bottom surfaces out of focus. Additionally, the quality of the hydrogel-air interface at the hydrogel top was essential for phase-contrast imaging, which was needed for visualizing cell-cell junctions. The change in water fraction had different sources. The humidity of the incubator chamber of the microscope stage was not at 100%, leading to slow drying of the gel. In the case of high flow rate, the excessive fluid volume pushed into the gel resulted in a pool of liquid on top of the hydrogel. To prevent this pool from forming, a paper tissue was placed to aspirate the liquid progressively. The balance between drying and refilling was difficult to control precisely, and the focus often had to be readjusted during image acquisition.

Sampled imaging for qualitative description and validation A 40X objective with a narrow focus depth and excellent spatial resolution was selected for sampled Z-stack imaging of the channel (Figure C.6). The small field of view and small Z step, necessary for good reconstruction or projection, led to long acquisition and prevented systematic scanning. A whole channel stack with a Z step of 0.4 µm to scan a 140 µm thick structure, requires more than 300 Z positions. Sharp reconstructions and projections could only be obtained by using the CREST system (a semi-confocal with one pinhole disk on the emission light-path) which reduces fluorescence noise from out-of-focus planes. However, because the pinhole reduces the amount of light that passes through, the CREST system could only be used with high numerical aperture objectives (in my case a water immersion objective), and exposure times had to be increased to several hundreds of milliseconds. As a result, a whole channel stack in triple fluorescence required 45 min, an excessive duration for a systematic acquisition protocol. A good compromise between amount of data and the time spent acquiring it was scanning only a quarter of the channel periphery, either along the bottom or top surfaces. As these surfaces were almost horizontal, a wider area remained in focus, maximizing the amount of data acquired in one Z plane. Because the structures of interest were also almost horizontal, the Z step could be increased to 1 µm without significant loss of image quality. Overall, a stack of around 35 Z-positions was sufficient to obtain a high quality reconstruction and needed only 2 min. This combination was selected as a systematic imaging protocol, usually repeated on three to five positions per channel, mostly along the bottom surface where fluorescence intensity was higher.

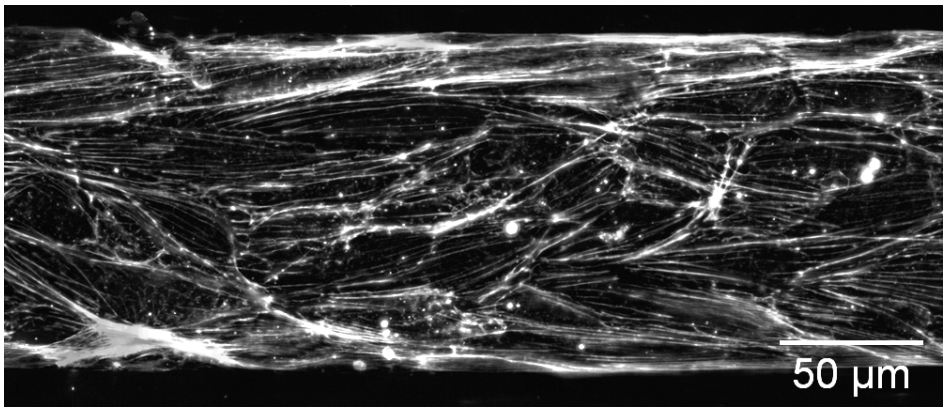

FIGURE C.6: Illustration of a typical maximum intensity projection (MIP) image of a Z-stack of a phalloidin staining obtained with a water immersion 40X objective, showing well resolved actin stress fibers.

C.8.3 Post-processing: channel curvature

The channel's high curvature created significant image distortion on the channel sides when the images were projected onto a single flat plane. The distortion was present not only in the maximum intensity projection of the 40X Z-stack but also in the 10X single plane images. For Z-stacks, three post-processing options were possible to account for the distortion: unwrapping, projection stretching or reducing the region-of-interest (ROI). For single plane images, only the last two were applicable.

Unwrapping is the most accurate approach as it maps a curved 2D plane onto a flat 2D plane by unfolding the cylinder. An open source MATLAB code for this complex mathematical mapping is available on the Searson's group website, included in a rather recent publication, in which they used the code to unwrap EC images acquired on a cylindrical

shape [213]. The process requires a sharp Z-stack, i.e. acquired with the CREST system and a small Z step. Although the algorithm worked quite well, it was time consuming: stacks had to be processed one-by-one manually, and the code running time was around 5 min. This option was the only one capable of extracting data from the channel sides, but I decided it was best used only occasionally and opted to also explore a more rapid and systematic approach.

Projection stretching is an approximation of the unwrapping technique whereby the distorted 2D flat projection is mapped onto a new 2D flat surface to reduce distortion. The mapping algorithm is equivalent to a non-uniform stretching of the initial surface where the center is left as is and the sides are stretched to the maximum. Although some information is lost during the projection and cannot be recovered, this algorithm corrects for the distortion and restores native structure orientation. A MATLAB code implementing this process was developed by Clara Ramon-Lozano, my colleague who is also working on the microvessel-on-chip. The small benefit of the increased precision of adding this stretching step was negated by the added processing step and extra computational time.

ROI reduction involves simply cropping the image to a narrower band where only pseudo-horizontal cells remained. Distortion was therefore minimal and could be neglected. As long as this band was sufficiently wide to have a significant amount of quantifiable structures, this approach was both the fastest and relatively precise. Quantification of actin orientation from images obtained with the most precise method, the unwrapping, and the ROI reduction approach revealed minimal differences in actin orientation (Figure C.7). This simplest and quickest method was therefore selected for all subsequent systematic quantification.

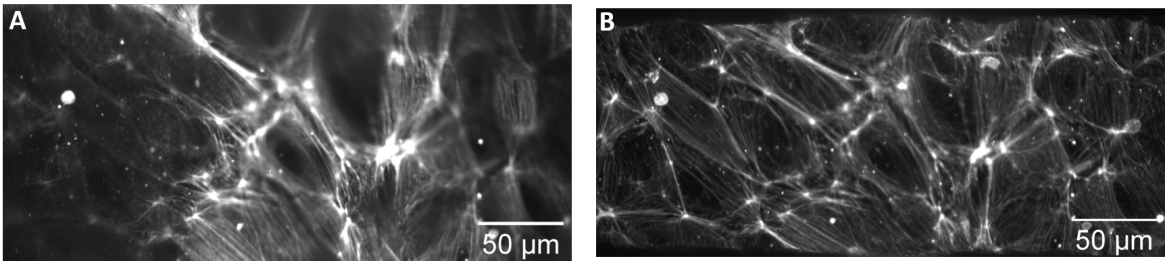

FIGURE C.7: Comparison of the final image obtained by unwrapping (**A**) and MIP (**B**) of the same Z-stack of a phalloidin staining. The resolution of the MIP image (**B**) is higher, and the distortion of the image edges compared to that in the unwrapping case (**B**) is acceptable.

C.9 Automated orientation analysis

One of the principal responses of cells, in particular ECs, to directional stresses such as shear and tensile stresses is cellular reorientation. This reorganization can be seen at the whole cell as well as at the subcellular level, with cytoskeletal and nuclear reorientation.

C.9.1 Detection of actin cytoskeleton orientation

Although the cytoskeleton is composed of three networks, namely actin filaments, microtubules and intermediate filaments, the actin cytoskeleton is often regarded as the major player in mechanical responses (see Chapter 1). As the actin cytoskeleton is composed of fibers, it is a perfect candidate for using the OrientationJ plugin in ImageJ, which detects the orientation of an ROI from a local gradient structure tensor. The user-defined parameters

are the gradient computation method and the local window size. Here, the chosen gradient computation method was the cubic-spline. The local window size is the size of the elementary unit of analysis that has one uniform orientation. If the window size is too large, the image is undersampled, and the resulting orientation does not capture the local orientation of actin stress fibers. On the other hand, if the window size is too small, the image is oversampled, and the resulting orientation is noisy (Figure C.8). The optimal window size was found to be *sim* 3 µm, corresponding to 5 pixels on a 10X image and 20 pixels on a 40X image. This was validated visually by overlaying the colored map of orientations on the original actin image (Figure C.8). Two plugins were used in this study: OrientationJ Analysis, to obtain the color coded images, and OrientationJ Distribution, to obtain the table of distribution of orientations for each pixel.

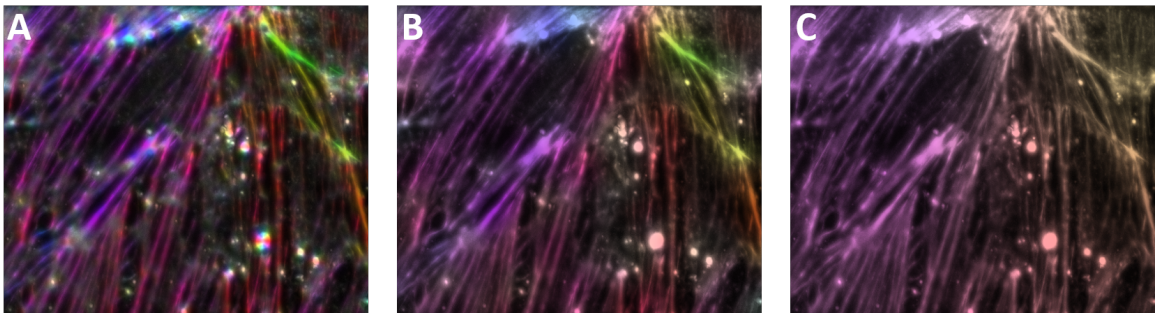

FIGURE C.8: Illustration of the optimization process to determine the optimal OrientationJ parameters, showing the resulting analysis for window sizes of 3 (**A**), 20 (**B**) and 50 (**C**) pixels. **A** shows oversampling, with a noisy color map, while **C** shows undersampling, with fibers of different orientation being averaged together. **B** shows the output.

C.9.2 Detection of cell orientation

Whole cell segmentation Most of the cell shape analysis found in the literature is based on cell segmentation. The contour of a cell is detected, defining the area inside that closed contour as one object. Properties of interest associated with that object can then be computed, such as the perimeter, area, and shape index, or even elongation and orientation, by fitting an ellipse to the object. The segmentation algorithm of cell outline obtained with the ImageJ plugin Tissue Analyzer was developed in MATLAB and successfully identified each cell (Figure C.9). However, whole cell detection requires a closed contour. As evident from the technique's name, it requires the whole cell to be in the field of view. In this study, the channel geometry and chosen imaging strategy led to a narrow stripe of imaged ECs, with often only a couple of whole cells across the image width and most of the cells cut out by the image edge (Figure C.9). This issue was exacerbated by the circumferential alignment found under certain mechanical stimuli, making whole cell detection unsuited for my purposes.

Detection of junction orientation Another way to access cell orientation is through cell-cell junction orientation. Instead of detecting the whole cell contour, cell borders were directly analysed for their orientation. The orientation distribution of the borders of a round cell would be flat, while the distribution of the borders of an oriented cell would have a peak at the cell orientation angle, whose height and sharpness depend on cell elongation.

For a cell monolayer, the orientation distribution depends on both the elongation of the individual cells as well as the order parameter of the monolayer, a measure of the homogeneity of the cell orientation distribution. A flat orientation distribution would indicate a monolayer of round cells or a monolayer of highly elongated cells that are randomly oriented.

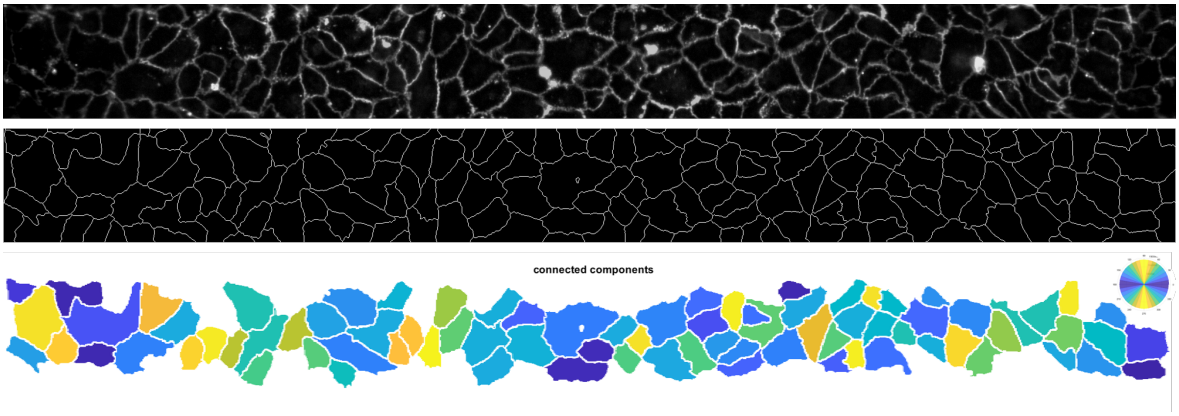

FIGURE C.9: Illustration of the segmentation process. VE-cadherin staining (top) is pre-processed to enhance contrast and then binarized (middle). The segmentation algorithm is run on the resulting image (bottom). The output image shows individual segmented cells, color coded by their orientation as defined by the major axis of a best-fit ellipse (bottom).

Similarly, while an orientation distribution with a peak indicates an average orientation in that particular direction, it can be either a monolayer of slightly elongated cells uniformly aligned in that direction or a monolayer of highly elongated cells distributed around that direction with higher levels of noise. The order parameter, which can be computed from the orientation map, can be used to distinguish between the two scenarios. Of note, confluent ECs exhibit strong collective behavior and tend to have high order parameters with their orientation strongly influenced by their neighbors. To sum up, although the junction orientation analysis is less rich than whole cell segmentation, it provides a reliable and rapid method to compute average cell orientation in monolayers.

VE-cadherin staining vs. brightfield images The easiest method to image cell-cell junctions is by immunostaining of junctional proteins such as VE-cadherin, the major component of adherens junctions in ECs. As junctions are anisotropic linear structures, the OrientationJ plugin efficiently detects their orientation, with the same set of parameters as for the actin stress fiber network (Figure C.10 top). Immunostaining is, however, incompatible with live cell imaging. An alternative option is to use phase contrast images, where cell-cell junctions of confluent monolayers appear as white lines between grey cell bodies. OrientationJ detects the orientation of these cell-cell junctions, with the same set of parameters (Figure C.10 bottom). A comparison of the orientation distribution of a whole channel between VE-cadherin-based and brightfield-based detection revealed similar results, validating the brightfield-based detection as a good method for live cell orientation analysis.

C.9.3 Nucleus segmentation

Nuclei are oblong structures, and although they are anisotropic, they are not thin slender structures and as such their orientation is poorly detected by OrientationJ. Their fluorescence signal is always very bright and has an excellent signal-to-noise ratio, optimal for automated segmentation. Whole nuclear segmentation has the additional advantage of measuring more parameters than orientation including area and shape index. Since nuclei are smaller objects than whole cells, the issue faced during whole cell segmentation, i.e. being cut by the narrow image borders, does not apply. A custom MATLAB code was used for nucleus segmentation. The code I used was based on a version developed by Thévy Lok, a former Ph.D. student in our group. After binarizing the DAPI staining image, the MATLAB connected component

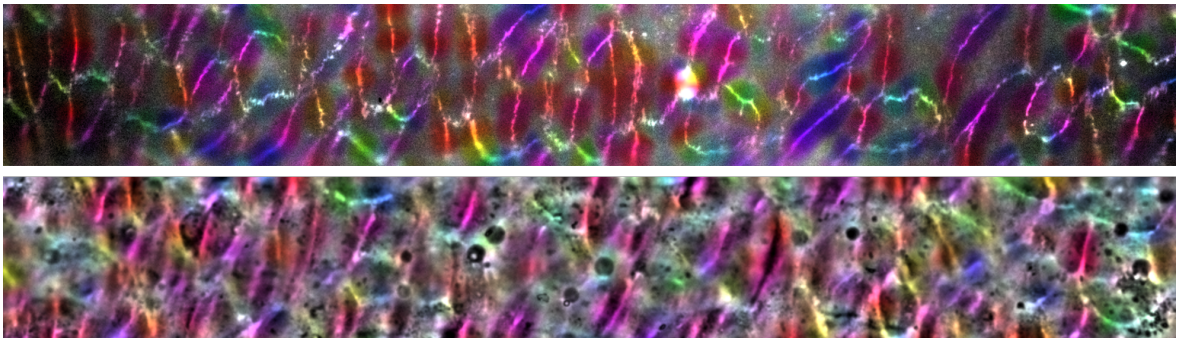

FIGURE C.10: Illustration of the output of the OrientationJ analysis on a fluorescence image of cell-cell junctions stained for VE-cadherin (top) and on a brightfield image (bottom). Colors indicate the computed orientation of the local segment, with warm colors closer to the vertical direction and cooler colors closer to the horizontal direction.

algorithm was run to detect individual objects (Figure C.11). In this algorithm, a bandpass filter is applied to keep only objects of reasonable size (area between 100 and 400 µm2), and partial objects located at the image border are deleted. The main limitations of this algorithm is with two adjacent nuclei that sometimes touch and may be thus detected as a single large object with an inaccurate assessment of orientation.

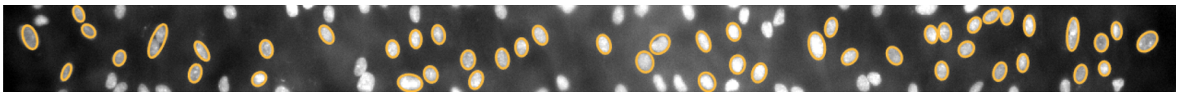

FIGURE C.11: Illustration of the nucleus segmentation algorithm, with the ellipses fitted to the segmented objects (yellow contours) overlayed on the original DAPI image (gray).

C.9.4 Orientation analysis

Post-processing The output of each orientation analysis method was a table of binned angles. For each bin, the table indicated the number of elements whose orientation falls within that angle range. To recreate a probability density function from this table, I normalized it by the sum of all elements multiplied by the bin size in radians. A graphical representation was then plotted from the table of orientation distribution with a MATLAB code, either for a single XY position or for the entire channel. For a channel, the code averaged the normalized distributions of all the XY positions, with the distribution from the images of the channel top being flipped to account for the cylindrical geometry.

Curve fitting to a von Mises distribution An effective approach to quantitatively compare different distributions is to fit them to a known distribution, defined with a couple of parameters and to then compare the values of these parameters. Orientation distributions are actually periodic angular distributions and are therefore best fitted with a von Mises distribution. Von Mises distributions are the periodic equivalent of a Gaussian distribution wrapped on a circle and are described by only two parameters, the location μ and the concentration K. The location μ indicates the angle of the distribution peak, around which most of the data is distributed (Figure C.12 A). The concentration K is a measure of the "sharpness" of the distribution: a large K denotes a distribution with a high and narrow peak, whereas a small K indicates a distribution that is fairly flat (Figure C.12 B). In fact, 1/K is the analogue of the variance σ^2 in a Gaussian distribution. Practically, K measures the intensity of

orientation of the considered elements. As discussed above, in the case of the cell orientation distribution, K is affected by both the orientation and the elongation of the cells.

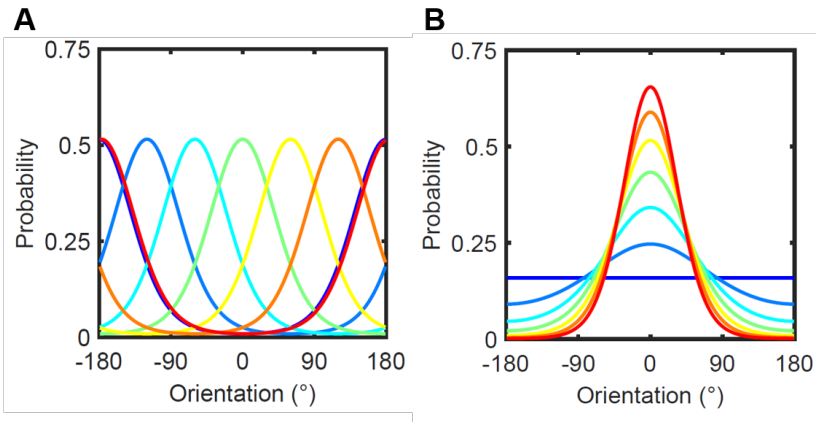

FIGURE C.12: Illustration of the influence of the location (**A**), from -180°(blue) to 180°(red) and concentration (**B**), from 0 (blue) to 3 (red) on the shape of the von Mises distribution.

For the algorithm implementation in MATLAB, I used a circular probability toolbox that contains the von Mises fitting functions [214]. Both the local orientation distributions (**i,ii**) and the channel average distribution (**iii**) were well described by the von Mises distribution (Figure C.13). One important element to note is the fact that von Mises distributions are defined on a 2π period, whereas my data was π periodic. Indeed, a horizontal filament, the nucleus, a junction or a cell, are all apolar, and can be seen as similarly oriented at either 0 or 180°. I therefore stretched the experimental data linearly onto a 2π-long interval, computed the location and concentration parameters and then plotted the fitting von Mises distribution back on a π-long interval.

C.10 Diameter measurement

Two different approaches were used, sometimes concomitantly, to measure channel diameter.

Whole channel The first approach was to image the entire channel at the end of the experiment, after immunostaining, with a 10X grid acquisition focused on the channel's centerline. These images were typically acquired in the actin staining channel because it was usually the brightest apart from the punctate DAPI staining. The fact that the channel was not perfectly flat often blurred both ends of the scan, but a majority of the length remained in focus. Channel diameter was then manually measured in ImageJ at around 30 regularly spaced axial positions. The average channel diameter was computed and the diameter profile plotted, allowing easy visualization of axial variations.

Dynamics with pressure The second approach was to image a given XY position during pressure variation to measure instantaneous and long term changes in channel diameter with high precision. To facilitate imaging during long term experiments, where chips had numerous straws and attached tubing, and being kept in the incubator, the images were acquired with the microscope from the culture room. The imaging was performed using a 20X objective by manually placing the channel in the correct XY position each time (with the help of visual markers). Channel diameter was calculated as the average of seven diameters manually measured in ImageJ at different positions regularly spaced across the image.

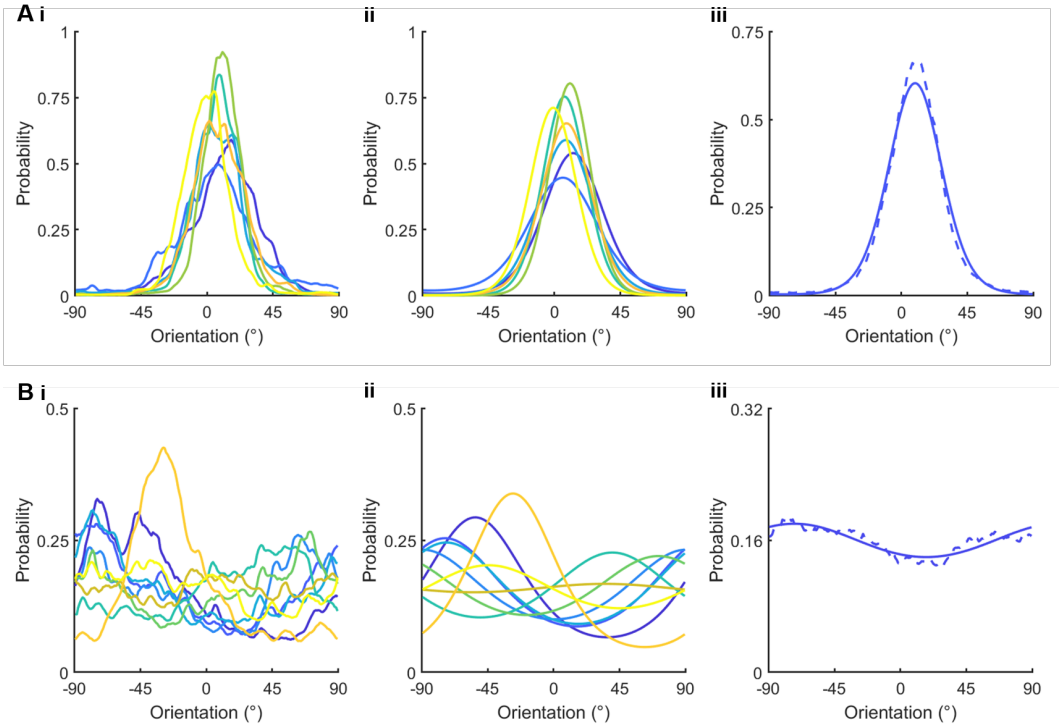

FIGURE C.13: Illustration of the curve fitting by von Mises distribution for a channel with elongated and aligned cells (**A**) and a channel with round and randomly oriented cells (**B**). The experimental orientation distribution for each axial position (**i**) is each fitted to a von Mises distribution (**ii**). Colors denote the axial position from inlet (blue) to outlet (yellow). The average channel distribution (**iii** dashed line), computed as the mean of all axial distributions, can also be fitted to a von Mises distribution (**iii** solid line).

Bibliography

[1] W. C. Aird, *Endothelial biomedicine*. Cambridge University Press, 1 2007.

[2] C. Leclech, C. F. Natale, and A. I. Barakat, "The basement membrane as a structured surface – role in vascular health and disease," 9 2021.

[3] S. Fleischer, D. N. Tavakol, and G. Vunjak-Novakovic, "From Arteries to Capillaries: Approaches to Engineering Human Vasculature," 9 2020.

[4] G. Letort, H. Ennomani, L. Gressin, M. Théry, and L. Blanchoin, "Dynamic reorganization of the actin cytoskeleton," *F1000Research*, vol. 4, 10 2015.

[5] K. Burridge and E. S. Wittchen, "The tension mounts: Stress fibers as force-generating mechanotransducers," 1 2013.

[6] W. Lewis and M. Lewis, "Behavior of cells in tissue cultures.," *General Cytology.*, pp. 385–447, 1924.

[7] A. J. Wong, T. D. Pollard, and I. M. Herman, "Actin filament stress fibers in vascular endothelial cells in vivo," *Science*, vol. 219, no. 4586, pp. 867–869, 1983.

[8] G. E. White, M. A. Gimbrone, and K. Fujiwara, "Factors influencing the expression of stress fibers in vascular endothelial cells in situ.," *Journal of Cell Biology*, vol. 97, 8 1983.

[9] J. Millán, R. J. Cain, N. Reglero-Real, C. Bigarella, B. Marcos-Ramiro, L. Fernández-Martín, I. Correas, and A. J. Ridley, "Adherens junctions connect stress fibres between adjacent endothelial cells," *BMC Biology*, vol. 8, pp. 1–13, 8 2010.

[10] S. Huveneers and J. de Rooij, "Mechanosensitive systems at the cadherin-f-actin interface," 1 2013.

[11] L. Fernández-Martín, B. Marcos-Ramiro, C. L. Bigarella, M. Graupera, R. J. Cain, N. Reglero-Real, A. Jiménez, E. Cernuda-Morollón, I. Correas, S. Cox, A. J. Ridley, and J. Millán, "Crosstalk between reticular adherens junctions and platelet endothelial cell adhesion molecule-1 regulates endothelial barrier function," *Arteriosclerosis, Thrombosis, and Vascular Biology*, vol. 32, 8 2012.

[12] X. Cong and W. Kong, "Endothelial tight junctions and their regulatory signaling pathways in vascular homeostasis and disease," 2 2020.

[13] S. Citi, "The mechanobiology of tight junctions," 10 2019.

[14] C. O. Lizama and A. C. Zovein, "Polarizing pathways: Balancing endothelial polarity, permeability, and lumen formation," 5 2013.

[15] S. McCue, D. Dajnowiec, F. Xu, M. Zhang, M. R. Jackson, and B. L. Langille, "Shear stress regulates forward and reverse planar cell polarity of vascular endothelium in vivo and in vitro," *Circulation Research*, vol. 98, pp. 939–946, 4 2006.

[16] G. Zeng, S. M. Taylor, J. R. McColm, N. C. Kappas, J. B. Kearney, L. H. Williams, M. E. Hartnett, and V. L. Bautch, "Orientation of endothelial cell division is regulated by VEGF signaling during blood vessel formation," in *Blood*, vol. 109, pp. 1345–1352, Blood, 2 2007.

[17] J. L. Heuslein, J. K. Meisner, X. Li, J. Song, H. Vincentelli, R. J. Leiphart, E. G. Ames, B. R. Blackman, and R. J. Price, "Mechanisms of Amplified Arteriogenesis in Collateral Artery Segments Exposed to Reversed Flow Direction," *Arteriosclerosis, Thrombosis, and Vascular Biology*, vol. 35, pp. 2354–2365, 11 2015.

[18] J. A. Dawson, "An experimental study of an amicronucleate Oxytricha. II. The formation of double animals or 'twins'," *Journal of Experimental Zoology*, vol. 30, 1 1920.

[19] M. Inaki, T. Sasamura, and K. Matsuno, "Cell chirality drives left-right asymmetric morphogenesis," 4 2018.

[20] L. Q. Wan, A. S. Chin, K. E. Worley, and P. Ray, "Cell chirality: Emergence of asymmetry from cell culture," 12 2016.

[21] T. Rahman, H. Zhang, J. Fan, and L. Q. Wan, "Cell chirality in cardiovascular development and disease," 9 2020.

[22] J. Fan, P. Ray, Y. Lu, G. Kaur, J. J. Schwarz, and L. Q. Wan, "Cell chirality regulates intercellular junctions and endothelial permeability," *Science Advances*, vol. 4, p. eaat2111, 10 2018.

[23] S. Jalal, S. Shi, V. Acharya, R. Y.-J. Huang, V. Viasnoff, A. Bershadsky, and Y. H. Tee, "Actin cytoskeleton self-organization in single epithelial cells and fibroblasts under isotropic confinement," *Journal of Cell Science*, 1 2019.

[24] M. Inaki, J. Liu, and K. Matsuno, "Cell chirality: Its origin and roles in left-right asymmetric development," 12 2016.

[25] Y. H. Tee, W. J. Goh, X. Yong, H. T. Ong, J. Hu, I. Y. Y. Tay, S. Shi, S. Jalal, S. F. H. Barnett, P. Kanchanawong, W. Huang, J. Yan, V. Thiagarajan, and A. D. Bershadsky, "Actin polymerization and crosslinking drive left-right asymmetry in single cell and cell collectives," *bioRxiv*, p. 2021.04.22.440942, 1 2021.

[26] E. E. Friedrich, Z. Hong, S. Xiong, M. Zhong, A. Di, J. Rehman, Y. A. Komarova, and A. B. Malik, "Endothelial cell Piezo1 mediates pressure-induced lung vascular hyperpermeability via disruption of adherens junctions," *Proceedings of the National Academy of Sciences of the United States of America*, vol. 116, pp. 12980–12985, 6 2019.

[27] T. J. Kirby and J. Lammerding, "Emerging views of the nucleus as a cellular mechanosensor," 4 2018.

[28] S. Budday, T. C. Ovaert, G. A. Holzapfel, P. Steinmann, and E. Kuhl, "Fifty Shades of Brain: A Review on the Mechanical Testing and Modeling of Brain Tissue," *Archives of Computational Methods in Engineering*, vol. 27, pp. 1187–1230, 7 2019.

[29] P. H. Wu, D. R. B. Aroush, A. Asnacios, W. C. Chen, M. E. Dokukin, B. L. Doss, P. Durand-Smet, A. Ekpenyong, J. Guck, N. V. Guz, P. A. Janmey, J. S. Lee, N. M. Moore, A. Ott, Y. C. Poh, R. Ros, M. Sander, I. Sokolov, J. R. Staunton, N. Wang, G. Whyte, and D. Wirtz, "A comparison of methods to assess cell mechanical properties," *Nature Methods*, vol. 15, p. 491, 6 2018.

[30] P. Kollmannsberger and B. Fabry, "Linear and nonlinear rheology of living cells," *Annual Review of Materials Research*, vol. 41, pp. 75–97, 8 2011.

[31] R. Varol, S. Omeroglu, Z. Karavelioglu, G. Aydemir, A. Karadag, H. E. Meco, G. C. Kocal, M. E. Oruc, G. B. Esmer, Y. Basbinar, and H. Uvet, "Holographic Cell Stiffness Mapping Using Acoustic Stimulation," 2 2021.

[32] G. Scarcelli, W. J. Polacheck, H. T. Nia, K. Patel, A. J. Grodzinsky, R. D. Kamm, and S. H. Yun, "Noncontact three-dimensional mapping of intracellular hydromechanical properties by Brillouin microscopy," *Nature Methods*, vol. 12, pp. 1132–1134, 12 2015.

[33] K. Elsayad, S. Werner, M. Gallemí, J. Kong, E. R. Guajardo, L. Zhang, Y. Jaillais, T. Greb, and Y. Belkhadir, "Mapping the subcellular mechanical properties of live cells in tissues with fluorescence emission-Brillouin imaging," *Science Signaling*, vol. 9, pp. rs5–rs5, 7 2016.

[34] E. Evans and A. Yeung, "Apparent viscosity and cortical tension of blood granulocytes determined by micropipet aspiration," tech. rep., 1989.

[35] O. Otto, P. Rosendahl, A. Mietke, S. Golfier, C. Herold, D. Klaue, S. Girardo, S. Pagliara, A. Ekpenyong, A. Jacobi, M. Wobus, N. Töpfner, U. F. Keyser, J. Mansfeld, E. Fischer-Friedrich, and J. Guck, "Real-time deformability cytometry: On-the-fly cell mechanical phenotyping," *Nature Methods*, vol. 12, pp. 199–202, 2 2015.

[36] M. Jedrzejczak-Silicka, "History of Cell Culture," in *New Insights into Cell Culture Technology*, InTech, 5 2017.

[37] R. L. Nachman and E. A. Jaffe, "Endothelial cell culture: Beginnings of modern vascular biology," 2004.

[38] S. R. Caliari and J. A. Burdick, "A practical guide to hydrogels for cell culture," 5 2016.

[39] S. J. Buwalda, K. W. Boere, P. J. Dijkstra, J. Feijen, T. Vermonden, and W. E. Hennink, "Hydrogels in a historical perspective: From simple networks to smart materials," 9 2014.

[40] O. W. Petersen, L. Ronnov-Jessen, A. R. Howlett, and M. J. Bissell, "Interaction with basement membrane serves to rapidly distinguish growth and differentiation pattern of normal and malignant human breast epithelial cells," *Proceedings of the National Academy of Sciences of the United States of America*, vol. 89, no. 19, pp. 9064–9068, 1992.

[41] C. F. Dewey, S. R. Bussolari, M. A. Gimbrone, and P. F. Davies, "The dynamic response of vascular endothelial cells to fluid shear stress," *Journal of Biomechanical Engineering*, vol. 103, pp. 177–185, 8 1981.

[42] S. R. Bussolari, C. F. Dewey, and M. A. Gimbrone, "Apparatus for subjecting living cells to fluid shear stress," *Review of Scientific Instruments*, vol. 53, pp. 1851–1854, 6 1982.

[43] R. P. Franke, M. Gräfe, H. Schnittler, D. Seiffge, C. Mittermayer, and D. Drenckhahn, "Induction of human vascular endothelial stress fibres by fluid shear stress," *Nature*, vol. 307, no. 5952, pp. 648–649, 1984.

[44] P. F. Davies, A. Remuzzitt, E. J. Gordon, C. F. Dewey, and M. A. Gimbrone, "Turbulent fluid shear stress induces vascular endothelial cell turnover in vitro (hemodynamic forces/endothelial growth control/atherosclerosis)," tech. rep., 1986.

[45] J. Ando, H. Nomura, and A. Kamiya, "The effect of fluid shear stress on the migration and proliferation of cultured endothelial cells," *Microvascular Research*, vol. 33, pp. 62–70, 1 1987.

[46] M. J. Levesque and R. M. Nerem, "The elongation and orientation of cultured endothelial cells in response to shear stress," *Journal of Biomechanical Engineering*, vol. 107, pp. 341–347, 11 1985.

[47] W. J. Polacheck, R. Li, S. G. M. Uzel, and R. D. Kamm, "Microfluidic platforms for mechanobiology," *Lab on a Chip*, vol. 13, no. 12, p. 2252, 2013.

[48] C. L. Thompson, S. Fu, M. M. Knight, and S. D. Thorpe, "Mechanical Stimulation: A Crucial Element of Organ-on-Chip Models," 12 2020.

[49] D. Huh, B. D. Matthews, A. Mammoto, M. Montoya-Zavala, H. Y. Hsin, and D. E. Ingber, "Reconstituting Organ-Level Lung Functions on a Chip," *Science*, vol. 328, 6 2010.

[50] D. T. T. Phan, X. Wang, B. M. Craver, A. Sobrino, D. Zhao, J. C. Chen, L. Y. N. Lee, S. C. George, A. P. Lee, and C. C. W. Hughes, "A vascularized and perfused organ-on-a-chip platform for large-scale drug screening applications," *Lab on a Chip*, vol. 17, no. 3, pp. 511–520, 2017.

[51] I. Maschmeyer, A. K. Lorenz, K. Schimek, T. Hasenberg, A. P. Ramme, J. Hübner, M. Lindner, C. Drewell, S. Bauer, A. Thomas, N. S. Sambo, F. Sonntag, R. Lauster, and U. Marx, "A four-organ-chip for interconnected long-term co-culture of human intestine, liver, skin and kidney equivalents," *Lab on a Chip*, vol. 15, pp. 2688–2699, 6 2015.

[52] Q. Ramadan and M. Zourob, "Organ-on-a-chip engineering: Toward bridging the gap between lab and industry," 7 2020.

[53] L. Si, H. Bai, M. Rodas, W. Cao, C. Y. Oh, A. Jiang, R. Moller, D. Hoagland, K. Oishi, S. Horiuchi, S. Uhl, D. Blanco-Melo, R. A. Albrecht, W. C. Liu, T. Jordan, B. E. Nilsson-Payant, I. Golynker, J. Frere, J. Logue, R. Haupt, M. McGrath, S. Weston, T. Zhang, R. Plebani, M. Soong, A. Nurani, S. M. Kim, D. Y. Zhu, K. H. Benam, G. Goyal, S. E. Gilpin, R. Prantil-Baun, S. P. Gygi, R. K. Powers, K. E. Carlson, M. Frieman, B. R. tenOever, and D. E. Ingber, "A human-airway-on-a-chip for the rapid identification of candidate antiviral therapeutics and prophylactics," *Nature Biomedical Engineering*, pp. 1–15, 5 2021.

[54] L. A. Low, C. Mummery, B. R. Berridge, C. P. Austin, and D. A. Tagle, "Organs-on-chips: into the next decade," 5 2021.

[55] A. Herland, B. M. Maoz, D. Das, M. R. Somayaji, R. Prantil-Baun, R. Novak, M. Cronce, T. Huffstater, S. S. F. Jeanty, M. Ingram, A. Chalkiadaki, D. Benson Chou, S. Marquez, A. Delahanty, S. Jalili-Firoozinezhad, Y. Milton, A. Sontheimer-Phelps, B. Swenor, O. Levy, K. K. Parker, A. Przekwas, and D. E. Ingber, "Quantitative prediction of human pharmacokinetic responses to drugs via fluidically coupled vascularized organ chips," *Nature Biomedical Engineering*, vol. 4, 4 2020.

[56] R. Novak, M. Ingram, S. Marquez, D. Das, A. Delahanty, A. Herland, B. M. Maoz, S. S. F. Jeanty, M. R. Somayaji, M. Burt, E. Calamari, A. Chalkiadaki, A. Cho, Y. Choe, D. B. Chou, M. Cronce, S. Dauth, T. Divic, J. Fernandez-Alcon, T. Ferrante, J. Ferrier, E. A. FitzGerald, R. Fleming, S. Jalili-Firoozinezhad, T. Grevesse, J. A. Goss, T. Hamkins-Indik, O. Henry, C. Hinojosa, T. Huffstater, K.-J. Jang, V. Kujala, L. Leng, R. Mannix, Y. Milton, J. Nawroth, B. A. Nestor, C. F. Ng, B. O'Connor, T.-E. Park, H. Sanchez, J. Sliz, A. Sontheimer-Phelps, B. Swenor, G. Thompson, G. J. Touloumes, Z. Tranchemontagne, N. Wen, M. Yadid, A. Bahinski, G. A. Hamilton, D. Levner, O. Levy, A. Przekwas, R. Prantil-Baun, K. K. Parker, and D. E. Ingber, "Robotic fluidic coupling and interrogation of multiple vascularized organ chips," *Nature Biomedical Engineering*, vol. 4, 4 2020.

[57] A. Cochrane, H. J. Albers, R. Passier, C. L. Mummery, A. van den Berg, V. V. Orlova, and A. D. van der Meer, "Advanced in vitro models of vascular biology: Human induced pluripotent stem cells and organ-on-chip technology," *Advanced Drug Delivery Reviews*, vol. 140, pp. 68–77, 2 2019.

[58] K. Haase and R. D. Kamm, "Advances in on-chip vascularization," *Regenerative Medicine*, vol. 12, pp. 285–302, 4 2017.

[59] B. M. Maoz, A. Herland, E. A. FitzGerald, T. Grevesse, C. Vidoudez, A. R. Pacheco, S. P. Sheehy, T.-E. Park, S. Dauth, R. Mannix, N. Budnik, K. Shores, A. Cho, J. C. Nawroth, D. Segrè, B. Budnik, D. E. Ingber, and K. K. Parker, "A linked organ-on-chip model of the human neurovascular unit reveals the metabolic coupling of endothelial and neuronal cells," *Nature Biotechnology*, no. August, 2018.

[60] A. Jain, A. D. van der Meer, A.-L. Papa, R. Barrile, A. Lai, B. L. Schlechter, M. A. Otieno, C. S. Louden, G. A. Hamilton, A. D. Michelson, A. L. Frelinger, and D. E. Ingber, "Assessment of whole blood thrombosis in a microfluidic device lined by fixed human endothelium," *Biomedical Microdevices*, vol. 18, p. 73, 8 2016.

[61] K. M. Chrobak, D. R. Potter, and J. Tien, "Formation of perfused, functional microvascular tubes in vitro," *Microvascular Research*, vol. 71, no. 3, pp. 185–196, 2006.

[62] J. S. Miller, K. R. Stevens, M. T. Yang, B. M. Baker, D. H. T. Nguyen, D. M. Cohen, E. Toro, A. A. Chen, P. A. Galie, X. Yu, R. Chaturvedi, S. N. Bhatia, and C. S. Chen, "Rapid casting of patterned vascular networks for perfusable engineered three-dimensional tissues," *Nature Materials*, vol. 11, pp. 768–774, 7 2012.

[63] W. J. Polacheck, M. L. Kutys, J. B. Tefft, and C. S. Chen, *Microfabricated blood vessels for modeling the vascular transport barrier*, vol. 14. Springer US, 2019.

[64] G. M. Price and J. Tien, "Subtractive Methods for Forming Microfluidic Gels of Extracellular Matrix Proteins," *Methods in Bioengineering: Microdevices in Biology and Medicine*, pp. 235–248, 2009.

[65] D.-H. T. Nguyen, S. C. Stapleton, M. T. Yang, S. S. Cha, C. K. Choi, P. A. Galie, and C. S. Chen, "Biomimetic model to reconstitute angiogenic sprouting morphogenesis in vitro," *Proceedings of the National Academy of Sciences*, vol. 110, no. 17, pp. 6712–6717, 2013.

[66] D. Tsvirkun, A. Grichine, A. Duperray, C. Misbah, and L. Bureau, "Microvasculature on a chip: Study of the Endothelial Surface Layer and the flow structure of Red Blood Cells," *Scientific Reports*, vol. 7, pp. 1–11, 3 2017.

[67] R. G. Mannino, D. R. Myers, B. Ahn, Y. Wang, Margo Rollins, H. Gole, A. S. Lin, R. E. Guldberg, D. P. Giddens, L. H. Timmins, and W. A. Lam, "Do-it-yourself in vitro vasculature that recapitulates in vivo geometries for investigating endothelial-blood cell interactions," *Scientific Reports*, vol. 5, p. 12401, 7 2015.

[68] Y. Zheng, J. Chen, M. Craven, N. W. Choi, S. Totorica, A. Diaz-Santana, P. Kermani, B. Hempstead, C. Fischbach-Teschl, J. A. Lopez, and A. D. Stroock, "In vitro microvessels for the study of angiogenesis and thrombosis," *Proceedings of the National Academy of Sciences*, vol. 109, no. 24, pp. 9342–9347, 2012.

[69] W. F. Hynes, M. Pepona, C. Robertson, J. Alvarado, K. Dubbin, M. Triplett, J. J. Adorno, A. Randles, and M. L. Moya, "Examining metastatic behavior within 3D bioprinted vasculature for the validation of a 3D computational flow model," *Science Advances*, vol. 6, p. eabb3308, 8 2020.

[70] S. Kim, H. Lee, M. Chung, and N. L. Jeon, "Engineering of functional, perfusable 3D microvascular networks on a chip," *Lab on a Chip*, vol. 13, no. 8, pp. 1489–1500, 2013.

[71] J. Kim, M. Chung, S. Kim, D. H. Jo, J. H. Kim, and N. L. Jeon, "Engineering of a biomimetic pericyte-covered 3D microvascular network," *PLoS ONE*, vol. 10, 7 2015.

[72] G. Offeddu, C. Hajal, C. Foley, Z. Wan, L. Ibrahim, M. Coughlin, and R. Kamm, "Glycocalyx-Mediated Vascular Dissemination of Circulating Tumor Cells," *bioRxiv*, p. 2020.04.28.066746, 4 2020.

[73] N. C. A. van Engeland, A. M. A. O. Pollet, J. M. J. den Toonder, C. V. C. Bouten, O. M. J. A. Stassen, and C. M. Sahlgren, "A biomimetic microfluidic model to study signalling between endothelial and vascular smooth muscle cells under hemodynamic conditions," *Lab on a Chip*, vol. 18, no. 11, pp. 1607–1620, 2018.

[74] S. Alimperti, T. Mirabella, V. Bajaj, W. Polacheck, D. M. Pirone, J. Duffield, J. Eyckmans, R. K. Assoian, and C. S. Chen, "Three-dimensional biomimetic vascular model reveals a RhoA, Rac1, and N-cadherin balance in mural cell–endothelial cell-regulated barrier function," *Proceedings of the National Academy of Sciences of the United States of America*, vol. 114, no. 33, pp. 8758–8763, 2017.

[75] E. Lee, H. Takahashi, J. Pauty, M. Kobayashi, K. Kato, M. Kabara, J. I. Kawabe, and Y. T. Matsunaga, "A 3D in vitro pericyte-supported microvessel model: Visualisation and quantitative characterisation of multistep angiogenesis," *Journal of Materials Chemistry B*, vol. 6, no. 7, pp. 1085–1094, 2018.

[76] A. Tan, K. Fujisawa, Y. Yukawa, and Y. T. Matsunaga, "Bottom-up fabrication of artery-mimicking tubular co-cultures in collagen-based microchannel scaffolds," *Biomaterials Science*, vol. 4, no. 10, pp. 1503–1514, 2016.

[77] S. Pradhan, O. A. Banda, C. J. Farino, J. L. Sperduto, K. A. Keller, R. Taitano, and J. H. Slater, "Biofabrication Strategies and Engineered In Vitro Systems for Vascular Mechanobiology," *Advanced Healthcare Materials*, p. 1901255, 2 2020.

[78] R. Gharleghi, C. A. Dessalles, R. Lal, S. McCraith, K. Sarathy, N. Jepson, J. Otton, A. I. Barakat, and S. Beier, "3D Printing for Cardiovascular Applications: From End-to-End Processes to Emerging Developments," *Annals of Biomedical Engineering*, pp. 1–21, 5 2021.

[79] Y.-J. Seol, H.-W. Kang, S. J. Lee, A. Atala, and J. J. Yoo, "Bioprinting technology and its applications.," *European journal of cardio-thoracic surgery : official journal of the European Association for Cardio-thoracic Surgery*, vol. 46, pp. 342–8, 9 2014.

[80] S. V. Murphy and A. Atala, "3D bioprinting of tissues and organs," 2014.

[81] T. G. Papaioannou, D. Manolesou, E. Dimakakos, G. Tsoucalas, M. Vavuranakis, and D. Tousoulis, "3D bioprinting methods and techniques: Applications on artificial blood vessel fabrication," *Acta Cardiologica Sinica*, vol. 35, pp. 284–289, 5 2019.

[82] P. Sasmal, P. Datta, Y. Wu, and I. T. Ozbolat, "3D bioprinting for modelling vasculature," *Microphysiological Systems*, vol. 1, pp. 1–1, 11 2018.

[83] M. D. Sarker, S. Naghieh, N. K. Sharma, L. Ning, and X. Chen, "Bioprinting of Vascularized Tissue Scaffolds: Influence of Biopolymer, Cells, Growth Factors, and Gene Delivery," *Journal of Healthcare Engineering*, vol. 2019, 2019.

[84] E. S. Bishop, S. Mostafa, M. Pakvasa, H. H. Luu, M. J. Lee, J. M. Wolf, G. A. Ameer, T. C. He, and R. R. Reid, "3-D bioprinting technologies in tissue engineering and regenerative medicine: Current and future trends," 12 2017.

[85] Y. S. Zhang, F. Davoudi, P. Walch, A. Manbachi, X. Luo, V. Dell'Erba, A. K. Miri, H. Albadawi, A. Arneri, X. Li, X. Wang, M. R. Dokmeci, A. Khademhosseini, and R. Oklu, "Bioprinted thrombosis-on-a-chip," *Lab on a Chip*, vol. 16, pp. 4097–4105, 10 2016.

[86] L. E. Bertassoni, M. Cecconi, V. Manoharan, M. Nikkhah, J. Hjortnaes, A. L. Cristino, G. Barabaschi, D. Demarchi, M. R. Dokmeci, Y. Yang, and A. Khademhosseini, "Hydrogel bioprinted microchannel networks for vascularization of tissue engineering constructs," *Lab on a Chip*, vol. 14, pp. 2202–2211, 7 2014.

[87] D. B. Kolesky, R. L. Truby, A. S. Gladman, T. A. Busbee, K. A. Homan, and J. A. Lewis, "3D Bioprinting of Vascularized, Heterogeneous Cell-Laden Tissue Constructs," *Advanced Materials*, vol. 26, pp. 3124–3130, 5 2014.

[88] K. Christensen, C. Xu, W. Chai, Z. Zhang, J. Fu, and Y. Huang, "Freeform inkjet printing of cellular structures with bifurcations," *Biotechnology and Bioengineering*, vol. 112, pp. 1047–1055, 5 2015.

[89] C. Xu, W. Chai, Y. Huang, and R. R. Markwald, "Scaffold-free inkjet printing of three-dimensional zigzag cellular tubes," *Biotechnology and Bioengineering*, vol. 109, pp. 3152–3160, 12 2012.

[90] P. K. Wu and B. R. Ringeisen, "Development of human umbilical vein endothelial cell (HUVEC) and human umbilical vein smooth muscle cell (HUVSMC) branch/stem structures on hydrogel layers via biological laser printing (BioLP)," *Biofabrication*, vol. 2, p. 014111, 3 2010.

[91] O. Kérourédan, J. M. Bourget, M. Rémy, S. Crauste-Manciet, J. Kalisky, S. Catros, N. B. Thébaud, and R. Devillard, "Micropatterning of endothelial cells to create a capillary-like network with defined architecture by laser-assisted bioprinting," *Journal of Materials Science: Materials in Medicine*, vol. 30, p. 28, 2 2019.

[92] S. Vanaei, M. Parizi, S. Vanaei, F. Salemizadehparizi, and H. Vanaei, "An Overview on Materials and Techniques in 3D Bioprinting Toward Biomedical Application," *Engineered Regeneration*, vol. 2, pp. 1–18, 1 2021.

[93] M. I. Bogorad, J. DeStefano, J. Karlsson, A. D. Wong, S. Gerecht, and P. C. Searson, "Review: In vitro microvessel models," *Lab on a Chip*, vol. 15, no. 22, pp. 4242–4255, 2015.

[94] S. W. L. Lee, M. Campisi, T. Osaki, L. Possenti, C. Mattu, G. Adriani, R. D. Kamm, and V. Chiono, "Modeling Nanocarrier Transport across a 3D In Vitro Human Blood-Brain–Barrier Microvasculature," *Advanced Healthcare Materials*, vol. 9, p. 1901486, 4 2020.

[95] E. E. Antoine, F. P. Cornat, and A. I. Barakat, "The stentable in vitro artery: An instrumented platform for endovascular device development and optimization," *Journal of the Royal Society Interface*, vol. 13, 12 2016.

[96] E. E. Antoine, P. P. Vlachos, and M. N. Rylander, "Review of Collagen I Hydrogels for Bioengineered Tissue Microenvironments: Characterization of Mechanics, Structure, and Transport," *Tissue Engineering Part B: Reviews*, vol. 20, pp. 683–696, 12 2014.

[97] J. S. Miller, K. R. Stevens, M. T. Yang, B. M. Baker, D. H. T. Nguyen, D. M. Cohen, E. Toro, A. A. Chen, P. A. Galie, X. Yu, R. Chaturvedi, S. N. Bhatia, and C. S. Chen, "Rapid casting of patterned vascular networks for perfusable engineered three-dimensional tissues," *Nature Materials*, vol. 11, no. 9, pp. 768–774, 2012.

[98] B. Prabhakarpandian, M.-C. Shen, K. Pant, and M. F. Kiani, "Microfluidic devices for modeling cell-cell and particle-cell interactions in the microvasculature.," *Microvascular research*, vol. 82, pp. 210–20, 11 2011.

[99] J. M. Rosano, N. Tousi, R. C. Scott, B. Krynska, V. Rizzo, B. Prabhakarpandian, K. Pant, S. Sundaram, and M. F. Kiani, "A physiologically realistic in vitro model of microvascular networks," *Biomedical Microdevices*, vol. 11, pp. 1051–1057, 10 2009.

[100] J. T. Borenstein, M. M. Tupper, P. J. MacK, E. J. Weinberg, A. S. Khalil, J. Hsiao, and G. García-Cardeña, "Functional endothelialized microvascular networks with circular cross-sections in a tissue culture substrate," *Biomedical Microdevices*, vol. 12, pp. 71–79, 2 2010.

[101] J. W. Nichol, S. T. Koshy, H. Bae, C. M. Hwang, S. Yamanlar, and A. Khademhosseini, "Cell-laden microengineered gelatin methacrylate hydrogels," *Biomaterials*, vol. 31, pp. 5536–5544, 7 2010.

[102] M. Nikkhah, N. Eshak, P. Zorlutuna, N. Annabi, M. Castello, K. Kim, A. Dolatshahi-Pirouz, F. Edalat, H. Bae, Y. Yang, and A. Khademhosseini, "Directed endothelial cell morphogenesis in micropatterned gelatin methacrylate hydrogels," *Biomaterials*, vol. 33, pp. 9009–9018, 12 2012.

[103] N. W. Choi, M. Cabodi, B. Held, J. P. Gleghorn, L. J. Bonassar, and A. D. Stroock, "Microfluidic scaffolds for tissue engineering," *Nature Materials*, vol. 6, pp. 908–915, 9 2007.

[104] Y. Zheng, P. W. Henderson, N. W. Choi, L. J. Bonassar, J. A. Spector, and A. D. Stroock, "Microstructured templates for directed growth and vascularization of soft tissue in vivo," *Biomaterials*, vol. 32, pp. 5391–5401, 8 2011.

[105] Y. Zheng, J. Chen, M. Craven, N. W. Choi, S. Totorica, A. Diaz-Santana, P. Kermani, B. Hempstead, C. Fischbach-Teschl, J. A. López, and A. D. Stroock, "In vitro microvessels for the study of angiogenesis and thrombosis," *Proceedings of the National Academy of Sciences of the United States of America*, vol. 109, pp. 9342–9347, 6 2012.

[106] W. Jia, P. S. Gungor-Ozkerim, Y. S. Zhang, K. Yue, K. Zhu, W. Liu, Q. Pi, B. Byambaa, M. R. Dokmeci, S. R. Shin, and A. Khademhosseini, "Direct 3D bioprinting of perfusable vascular constructs using a blend bioink," *Biomaterials*, vol. 106, pp. 58–68, 11 2016.

[107] Y. Zhang, Y. Yu, H. Chen, and I. T. Ozbolat, "Characterization of printable cellular microfluidic channels for tissue engineering," *Biofabrication*, vol. 5, p. 025004, 3 2013.

[108] R. Attalla, C. Ling, and P. Selvaganapathy, "Fabrication and characterization of gels with integrated channels using 3D printing with microfluidic nozzle for tissue engineering applications," *Biomedical Microdevices*, vol. 18, pp. 1–12, 2 2016.

[109] V. K. Lee, D. Y. Kim, H. Ngo, Y. Lee, L. Seo, S. S. Yoo, P. A. Vincent, and G. Dai, "Creating perfused functional vascular channels using 3D bio-printing technology," *Biomaterials*, vol. 35, pp. 8092–8102, 9 2014.

[110] S. V. Murphy, P. De Coppi, and A. Atala, "Opportunities and challenges of translational 3D bioprinting," *Nature Biomedical Engineering*, vol. 4, pp. 370–380, 4 2019.

[111] C. Norotte, F. S. Marga, L. E. Niklason, and G. Forgacs, "Scaffold-free vascular tissue engineering using bioprinting," *Biomaterials*, vol. 30, pp. 5910–5917, 10 2009.

[112] M. Itoh, K. Nakayama, R. Noguchi, K. Kamohara, K. Furukawa, K. Uchihashi, S. Toda, J. I. Oyama, K. Node, and S. Morita, "Scaffold-free tubular tissues created by a bio-3D printer undergo remodeling and endothelialization when implanted in rat aortae," *PLoS ONE*, vol. 10, p. e0136681, 9 2015.

[113] K. C. Hribar, K. Meggs, J. Liu, W. Zhu, X. Qu, and S. Chen, "Three-dimensional direct cell patterning in collagen hydrogels with near-infrared femtosecond laser," *Scientific Reports*, vol. 5, pp. 1–7, 11 2015.

[114] C. Arakawa, C. Gunnarsson, C. Howard, M. Bernabeu, K. Phong, E. Yang, C. A. DeForest, J. D. Smith, and Y. Zheng, "Biophysical and biomolecular interactions of malaria-infected erythrocytes in engineered human capillaries," *Science Advances*, vol. 6, p. eaay7243, 1 2020.

[115] M. Albanna, K. W. Binder, S. V. Murphy, J. Kim, S. A. Qasem, W. Zhao, J. Tan, I. B. El-Amin, D. D. Dice, J. Marco, J. Green, T. Xu, A. Skardal, J. H. Holmes, J. D. Jackson, A. Atala, and J. J. Yoo, "In Situ Bioprinting of Autologous Skin Cells Accelerates Wound Healing of Extensive Excisional Full-Thickness Wounds," *Scientific Reports*, vol. 9, pp. 1–15, 12 2019.

[116] E. Gordon, L. Schimmel, and M. Frye, "The Importance of Mechanical Forces for in vitro Endothelial Cell Biology," *Frontiers in Physiology*, vol. 11, 6 2020.

[117] P. C. Dartsch and E. Betz, "Response of cultured endothelial cells to mechanical stimulation," *Basic Research in Cardiology*, vol. 84, pp. 268–281, 5 1989.

[118] K. Chen, A. Vigliotti, M. Bacca, R. M. McMeeking, V. S. Deshpande, and J. W. Holmes, "Role of boundary conditions in determining cell alignment in response to stretch," *Proceedings of the National Academy of Sciences of the United States of America*, vol. 115, pp. 986–991, 1 2018.

[119] Y. Wang, X. Tang, X. Feng, C. Liu, P. Chen, D. Chen, and B. F. Liu, "A microfluidic digital single-cell assay for the evaluation of anticancer drugs," *Analytical and Bioanalytical Chemistry*, vol. 407, pp. 1139–1148, 1 2015.

[120] Y. Nagai, H. Yokoi, K. Kaihara, and K. Naruse, "The mechanical stimulation of cells in 3D culture within a self-assembling peptide hydrogel," *Biomaterials*, vol. 33, pp. 1044–1051, 2 2012.

[121] A. M. Throm Quinlan, L. N. Sierad, A. K. Capulli, L. E. Firstenberg, and K. L. Billiar, "Combining Dynamic Stretch and Tunable Stiffness to Probe Cell Mechanobiology In Vitro," *PLoS ONE*, vol. 6, p. e23272, 8 2011.

[122] W. Zhang, G. Huang, and F. Xu, "Engineering Biomaterials and Approaches for Mechanical Stretching of Cells in Three Dimensions," *Frontiers in Bioengineering and Biotechnology*, vol. 8, 10 2020.

[123] B. Kou, J. Zhang, and D. R. Singer, "Effects of cyclic strain on endothelial cell apoptosis and tubulogenesis are dependent on ROS production via NAD(P)H subunit p22phox," *Microvascular Research*, vol. 77, pp. 125–133, 3 2009.

[124] A. S. Zeiger, F. D. Liu, J. T. Durham, A. Jagielska, R. Mahmoodian, K. J. Van Vliet, and I. M. Herman, "Static mechanical strain induces capillary endothelial cell cycle re-entry and sprouting," *Physical Biology*, vol. 13, p. 046006, 8 2016.

[125] T. Matsumoto, Y. C. Yung, C. Fischbach, H. J. Kong, R. Nakaoka, and D. J. Mooney, "Mechanical strain regulates endothelial cell patterning in vitro," in *Tissue Engineering*, vol. 13, pp. 207–217, Tissue Eng, 1 2007.

[126] D. Kah, A. Winterl, M. Přechová, U. Schöler, W. Schneider, O. Friedrich, M. Gregor, and B. Fabry, "A low-cost uniaxial cell stretcher for six parallel wells," *HardwareX*, vol. 9, p. e00162, 4 2021.

[127] D. J. Shiwarski, J. W. Tashman, A. F. Eaton, G. Apodaca, and A. W. Feinberg, "3D printed biaxial stretcher compatible with live fluorescence microscopy," *HardwareX*, vol. 7, p. e00095, 4 2020.

[128] T. Iba and B. E. Sumpio, "Morphological response of human endothelial cells subjected to cyclic strain in vitro," *Microvascular Research*, vol. 42, pp. 245–254, 11 1991.

[129] L. Bernardi, C. Giampietro, V. Marina, M. Genta, E. Mazza, and A. Ferrari, "Adaptive reorientation of endothelial collectives in response to strain," *Integrative Biology (United Kingdom)*, vol. 10, pp. 527–538, 9 2018.

[130] H. Kamble, M. J. Barton, M. Jun, S. Park, and N.-T. Nguyen, "Cell stretching devices as research tools: engineering and biological considerations," *Lab on a Chip*, vol. 16, no. 17, pp. 3193–3203, 2016.

[131] J. E. Moore, E. Bürki, A. Suciu, S. Zhao, M. Burnier, H. R. Brunner, and J.-J. Meister, "A device for subjecting vascular endothelial cells to both fluid shear stress and circumferential cyclic stretch," *Annals of Biomedical Engineering*, vol. 22, pp. 416–422, 7 1994.

[132] A. Benbrahim, G. J. L'Italien, B. B. Milinazzo, D. F. Warnock, S. Dhara, J. P. Gertler, R. W. Orkin, and W. M. Abbott, "A compliant tubular device to study the influences of wall strain and fluid shear stress on cells of the vascular wall," *Journal of Vascular Surgery*, vol. 20, pp. 184–194, 8 1994.

[133] Y. Qiu and J. M. Tarbell, "Interaction between Wall Shear Stress and Circumferential Strain Affects Endothelial Cell Biochemical Production," *Journal of Vascular Research*, vol. 37, no. 3, pp. 147–157, 2000.

[134] H. Guo, J. D. Humphrey, and M. J. Davis, "Effects of biaxial stretch on arteriolar function in vitro," *American Journal of Physiology-Heart and Circulatory Physiology*, vol. 292, pp. H2378–H2386, 5 2007.

[135] Z. H. Syedain, L. A. Meier, J. W. Bjork, A. Lee, and R. T. Tranquillo, "Implantable arterial grafts from human fibroblasts and fibrin using a multi-graft pulsed flow-stretch bioreactor with noninvasive strength monitoring," *Biomaterials*, vol. 32, pp. 714–722, 1 2011.

[136] E. E. van Haaften, T. B. Wissing, M. C. Rutten, J. A. Bulsink, K. Gashi, M. A. van Kelle, A. I. Smits, C. V. Bouten, and N. A. Kurniawan, "Decoupling the Effect of Shear Stress and Stretch on Tissue Growth and Remodeling in a Vascular Graft," *Tissue Engineering Part C: Methods*, vol. 24, pp. 418–429, 7 2018.

[137] G. Helmlinger, R. V. Geiger, S. Schreck, and R. M. Nerem, "Effects of pulsatile flow on cultured vascular endothelial cell morphology," *Journal of Biomechanical Engineering*, vol. 113, pp. 123–131, 5 1991.

[138] N. Caille, Y. Tardy, and J. J. Meister, "Assessment of Strain Field in Endothelial Cells Subjected to Uniaxial Deformation of Their Substrate," *Annals of Biomedical Engineering*, vol. 26, pp. 409–416, 5 1998.

[139] A. S. Zeiger, F. D. Liu, J. T. Durham, A. Jagielska, R. Mahmoodian, K. J. Van Vliet, and I. M. Herman, "Static mechanical strain induces capillary endothelial cell cycle re-entry and sprouting," *Physical Biology*, vol. 13, p. 046006, 8 2016.

[140] W. Zheng, B. Jiang, D. Wang, W. Zhang, Z. Wang, and X. Jiang, "A microfluidic flow-stretch chip for investigating blood vessel biomechanics," *Lab on a Chip*, vol. 12, pp. 3441–3450, 9 2012.

[141] R. Sinha, S. Le Gac, N. Verdonschot, A. van den Berg, B. Koopman, and J. Rouwkema, "Endothelial cell alignment as a result of anisotropic strain and flow induced shear stress combinations," *Scientific Reports*, vol. 6, p. 29510, 7 2016.

[142] D. Meza, B. Musmacker, E. Steadman, T. Stransky, D. A. Rubenstein, and W. Yin, "Endothelial Cell Biomechanical Responses are Dependent on Both Fluid Shear Stress and Tensile Strain," *Cellular and Molecular Bioengineering*, vol. 12, pp. 311–325, 8 2019.

[143] D. Meza, L. Abejar, D. A. Rubenstein, and W. Yin, "A Shearing-Stretching Device That Can Apply Physiological Fluid Shear Stress and Cyclic Stretch Concurrently to Endothelial Cells," *Journal of Biomechanical Engineering*, vol. 138, 3 2016.

[144] L. Bernardi, C. Giampietro, V. Marina, M. Genta, E. Mazza, and A. Ferrari, "Adaptive reorientation of endothelial collectives in response to strain," *Integrative Biology*, vol. 10, no. 9, pp. 527–538, 2018.

[145] K. Sato, M. Nitta, and A. Ogawa, "A Microfluidic Cell Stretch Device to Investigate the Effects of Stretching Stress on Artery Smooth Muscle Cell Proliferation in Pulmonary Arterial Hypertension," *Inventions*, vol. 4, p. 1, 12 2018.

[146] L. Yahia, "History and Applications of Hydrogels," *Journal of Biomedical Sciencies*, vol. 04, no. 02, 2015.

[147] E. E. Antoine, P. P. Vlachos, and M. N. Rylander, "Tunable Collagen I Hydrogels for Engineered Physiological Tissue Micro-Environments," *PLOS ONE*, vol. 10, p. e0122500, 3 2015.

[148] D. Caccavo, S. Cascone, G. Lamberti, and A. A. Barba, "Hydrogels: experimental characterization and mathematical modelling of their mechanical and diffusive behaviour," *Chemical Society Reviews*, vol. 47, no. 7, pp. 2357–2373, 2018.

[149] Q.-M. Wang, A. C. Mohan, M. L. Oyen, and X.-H. Zhao, "Separating viscoelasticity and poroelasticity of gels with different length and time scales," *Acta Mechanica Sinica*, vol. 30, pp. 20–27, 2 2014.

[150] S. Ramanujan, A. Pluen, T. D. McKee, E. B. Brown, Y. Boucher, and R. K. Jain, "Diffusion and convection in collagen gels: Implications for transport in the tumor interstitium," *Biophysical Journal*, vol. 83, no. 3, pp. 1650–1660, 2002.

[151] G. A. Busby, M. H. Grant, S. P. MacKay, and P. E. Riches, "Confined compression of collagen hydrogels," *Journal of Biomechanics*, vol. 46, pp. 837–840, 2 2013.

[152] Joshua Loessberg-Zahl, A. D. d. Meer, A. d. Berg, and J. C. T. Eijkel, "Flow focusing through gels as a tool to generate 3D concentration profiles in hydrogel-filled microfluidic chips," *Lab on a Chip*, vol. 19, pp. 206–213, 1 2019.

[153] J. Lubliner, *Plasticity theory*. Dover, 2008.

[154] S. Nam, J. Lee, D. G. Brownfield, and O. Chaudhuri, "Viscoplasticity Enables Mechanical Remodeling of Matrix by Cells," *Biophysical Journal*, vol. 111, pp. 2296–2308, 11 2016.

[155] D. Maity, Y. Li, Y. Chen, and S. X. Sun, "Response of collagen matrices under pressure and hydraulic resistance in hydrogels," *Soft Matter*, vol. 15, pp. 2617–2626, 3 2019.

[156] L. C. Auton and C. W. MacMinn, "From arteries to boreholes: Steady-state response of a poroelastic cylinder to fluid injection," *Proceedings of the Royal Society A: Mathematical, Physical and Engineering Sciences*, vol. 473, no. 2201, 2017.

[157] L. C. Auton and C. W. MacMinn, "Large poroelasto-plastic deformations due to radially outward fluid injection," *Journal of the Mechanics and Physics of Solids*, vol. 132, p. 103690, 2019.

[158] C. W. Macminn, E. R. Dufresne, and J. S. Wettlaufer, "Large Deformations of a Soft Porous Material," *Physical Review Applied*, vol. 5, p. 044020, 4 2016.

[159] J. Y. Tinevez, N. Perry, J. Schindelin, G. M. Hoopes, G. D. Reynolds, E. Laplantine, S. Y. Bednarek, S. L. Shorte, and K. W. Eliceiri, "TrackMate: An open and extensible platform for single-particle tracking," *Methods*, vol. 115, pp. 80–90, 2 2017.

[160] G. Charras and A. S. Yap, "Tensile Forces and Mechanotransduction at Cell–Cell Junctions," 4 2018.

[161] N. A. Shirwany and M.-h. Zou, "Arterial stiffness: a brief review," *Acta Pharmacologica Sinica*, vol. 31, pp. 1267–1276, 10 2010.

[162] P. Segers, E. R. Rietzschel, and J. A. Chirinos, "How to Measure Arterial Stiffness in Humans," *Arteriosclerosis, Thrombosis, and Vascular Biology*, vol. 40, pp. 1034–1043, 5 2020.

[163] T. Iba and B. E. Sumpio, "Morphological response of human endothelial cells subjected to cyclic strain in vitro," *Microvascular Research*, vol. 42, pp. 245–254, 11 1991.

[164] M. Sokabe, K. Naruse, S. Sai, T. Yamada, K. Kawakami, M. Inoue, K. Murase, and M. Miyazu, "Mechanotransduction and intracellular signaling mechanisms of stretch-induced remodeling in endothelial cells," in *Heart and Vessels*, vol. 12, pp. 191–193, 1 1997.

[165] V. P. Shirinsky, A. S. Antonov, K. G. Birukov, A. V. Sobolevsky, Y. A. Romanov, N. V. Kabaeva, G. N. Antonova, and V. N. Smirnov, "Mechano-chemical control of human endothelium orientation and size," *Journal of Cell Biology*, vol. 109, no. 1, pp. 331–339, 1989.

[166] T. Takemasa, K. Sugimoto, and K. Yamashita, "Amplitude-dependent stress fiber reorientation in early response to cyclic strain," *Experimental Cell Research*, vol. 230, pp. 407–410, 2 1997.

[167] J. H. Wang and E. S. Grood, "The strain magnitude and contact guidance determine orientation response of fibroblasts to cyclic substrate strains," *Connective Tissue Research*, vol. 41, no. 1, pp. 29–36, 2000.

[168] R. Krishnan, E. P. Canović, A. L. Iordan, K. Rajendran, G. Manomohan, A. P. Pirentis, M. L. Smith, J. P. Butler, J. J. Fredberg, and D. Stamenović, "Fluidization, resolidification, and reorientation of the endothelial cell in response to slow tidal stretches," *American Journal of Physiology - Cell Physiology*, vol. 303, p. C368, 8 2012.

[169] J. H. Wang, P. Goldschmidt-Clermont, and F. C. Yin, "Contractility affects stress fiber remodeling and reorientation of endothelial cells subjected to cyclic mechanical stretching," *Annals of Biomedical Engineering*, vol. 28, no. 10, pp. 1165–1171, 2000.

[170] K. Hayakawa, N. Sato, and T. Obinata, "Dynamic reorientation of cultured cells and stress fibers under mechanical stress from periodic stretching," *Experimental Cell Research*, vol. 268, pp. 104–114, 8 2001.

[171] C. K. Thodeti, B. Matthews, A. Ravi, A. Mammoto, K. Ghosh, A. L. Bracha, and D. E. Ingber, "TRPV4 channels mediate cyclic strain-induced endothelial cell reorientation through integrin-to-integrin signaling," *Circulation Research*, vol. 104, pp. 1123–1130, 5 2009.

[172] Y. Yano, Y. Saito, S. Narumiya, and B. E. Sumpio, "Involvement of rho p21 in cyclic strain-induced tyrosine phosphorylation of focal adhesion kinase (pp125(FAK)), morphological changes and migration of endothelial cells," *Biochemical and Biophysical Research Communications*, vol. 224, pp. 508–515, 7 1996.

[173] A. D. Bershadsky, N. Q. Balaban, and B. Geiger, "Adhesion-Dependent Cell Mechanosensitivity," in *Annual Review of Cell and Developmental Biology*, vol. 19, pp. 677–695, Annu Rev Cell Dev Biol, 2003.

[174] J. Pourati, A. Maniotis, D. Spiegel, J. L. Schaffer, J. P. Butler, J. J. Fredberg, D. E. Ingber, D. Stamenovic, and N. Wang, "Is cytoskeletal tension a major determinant of cell deformability in adherent endothelial cells?," *American Journal of Physiology - Cell Physiology*, vol. 274, no. 5 43-5, 1998.

[175] M. Chrzanowska-Wodnicka and K. Burridge, "Rho-stimulated contractility drives the formation of stress fibers and focal adhesions," *Journal of Cell Biology*, vol. 133, no. 6, pp. 1403–1415, 1996.

[176] J. Hatami, M. Tafazzoli-Shadpour, N. Haghighipour, M. A. Shokrgozar, and M. Janmaleki, "Influence of Cyclic Stretch on Mechanical Properties of Endothelial Cells," *Experimental Mechanics*, vol. 53, pp. 1291–1298, 10 2013.

[177] N. Wang, I. M. Toli-Nørrelykke, J. Chen, S. M. Mijailovich, J. P. Butler, J. J. Fredberg, and D. Stamenovi, "Cell prestress. I. Stiffness and prestress are closely associated in adherent contractile cells," *American Journal of Physiology - Cell Physiology*, vol. 282, no. 3 51-3, 2002.

[178] H. Yamada, T. Takemasa, and T. Yamaguchi, "Theoretical study of intracellular stress fiber orientation under cyclic deformation," *Journal of Biomechanics*, vol. 33, pp. 1501–1505, 11 2000.

[179] H. Yamada, H. Ando, and D. Morita, "Numerical simulation of the effects of actin binding and cellular deformation on the orientation of actin stress fibers under cyclic stretch," in *Biomechanics at Micro- and Nanoscale Levels*, vol. 2, pp. 149–160, World Scientific Publishing Co., 1 2006.

[180] H. Ngu, L. Lu, S. J. Oswald, S. Davis, S. Nag, and F. C.-P. Yin, "Strain-induced Orientation Response of Endothelial Cells: Effect of Substratum Adhesiveness and Actin-myosin Contractile Level," Tech. Rep. 1, 2008.

[181] A. Tondon, H. J. Hsu, and R. Kaunas, "Dependence of cyclic stretch-induced stress fiber reorientation on stretch waveform," *Journal of Biomechanics*, vol. 45, pp. 728–735, 3 2012.

[182] R. Kaunas, P. Nguyen, S. Usami, and S. Chien, "Cooperative effects of Rho and mechanical stretch on stress fiber organization," *Proceedings of the National Academy of Sciences of the United States of America*, vol. 102, pp. 15895–15900, 11 2005.

[183] B. Ladoux and R. M. Mège, "Mechanobiology of collective cell behaviours," *Nature Reviews Molecular Cell Biology*, vol. 18, pp. 743–757, 12 2017.

[184] A. Angulo-Urarte, T. van der Wal, and S. Huveneers, "Cell-cell junctions as sensors and transducers of mechanical forces," 9 2020.

[185] Z. Liu, J. L. Tan, D. M. Cohen, M. T. Yang, N. J. Sniadecki, S. A. Ruiz, C. M. Nelson, and C. S. Chen, "Mechanical tugging force regulates the size of cell-cell junctions," *Proceedings of the National Academy of Sciences of the United States of America*, vol. 107, pp. 9944–9949, 6 2010.

[186] W. Choi, B. R. Acharya, G. Peyret, M. A. Fardin, R. M. Mège, B. Ladoux, A. S. Yap, A. S. Fanning, and M. Peifer, "Remodeling the zonula adherens in response to tension and the role of afadin in this response," *Journal of Cell Biology*, vol. 213, pp. 243–260, 4 2016.

[187] A. R. Harris, L. Peter, J. Bellis, B. Baum, A. J. Kabla, and G. T. Charras, "Characterizing the mechanics of cultured cell monolayers," *Proceedings of the National Academy of Sciences of the United States of America*, vol. 109, pp. 16449–16454, 10 2012.

[188] A. R. Harris, A. Daeden, and G. T. Charras, "Formation of adherens junctions leads to the emergence of a tissue-level tension in epithelial monolayers," *Journal of Cell Science*, vol. 127, pp. 2507–2517, 6 2014.

[189] S. A. Gudipaty, J. Lindblom, P. D. Loftus, M. J. Redd, K. Edes, C. F. Davey, V. Krishnegowda, and J. Rosenblatt, "Mechanical stretch triggers rapid epithelial cell division through Piezo1," *Nature*, vol. 543, pp. 118–121, 3 2017.

[190] A. Nestor-Bergmann, G. A. Stooke-Vaughan, G. K. Goddard, T. Starborg, O. E. Jensen, and S. Woolner, "Decoupling the Roles of Cell Shape and Mechanical Stress in Orienting and Cueing Epithelial Mitosis," *Cell Reports*, vol. 26, pp. 2088–2100, 2 2019.

[191] P. Campinho, M. Behrndt, J. Ranft, T. Risler, N. Minc, and C. P. Heisenberg, "Tension-oriented cell divisions limit anisotropic tissue tension in epithelial spreading during zebrafish epiboly," *Nature Cell Biology*, vol. 15, pp. 1405–1414, 11 2013.

[192] A. R. Harris, J. Bellis, N. Khalilgharibi, T. Wyatt, B. Baum, A. J. Kabla, and G. T. Charras, "Generating suspended cell monolayers for mechanobiological studies," *Nature Protocols 2013 8:12*, vol. 8, pp. 2516–2530, 11 2013.

[193] N. I. Petridou and C. Heisenberg, "Tissue rheology in embryonic organization," *The EMBO Journal*, vol. 38, p. e102497, 10 2019.

[194] Y. K. Wang, Y. H. Wang, C. Z. Wang, J. M. Sung, W. T. Chiu, S. H. Lin, Y. H. Chang, and M. J. Tang, "Rigidity of collagen fibrils controls collagen gel-induced down-regulation of focal adhesion complex proteins mediated by $\alpha 2\beta 1$ integrin," *Journal of Biological Chemistry*, vol. 278, pp. 21886–21892, 6 2003.

[195] Y. C. Yeh, J. Y. Ling, W. C. Chen, H. H. Lin, and M. J. Tang, "Mechanotransduction of matrix stiffness in regulation of focal adhesion size and number: Reciprocal regulation of caveolin-1 and $\beta 1$ integrin," *Scientific Reports*, vol. 7, pp. 1–14, 12 2017.

[196] C. M. Nelson, D. M. Pirone, J. L. Tan, and C. S. Chen, "Vascular endothelial-cadherin regulates cytoskeletal tension, cell spreading, and focal adhesions by stimulating RhoA," *Molecular Biology of the Cell*, vol. 15, pp. 2943–2953, 6 2004.

[197] M. Yoshigi, L. M. Hoffman, C. C. Jensen, H. J. Yost, and M. C. Beckerle, "Mechanical force mobilizes zyxin from focal adhesions to actin filaments and regulates cytoskeletal reinforcement," *Journal of Cell Biology*, vol. 171, pp. 209–215, 10 2005.

[198] S. S. Babu, A. Wojtowicz, M. Freichel, L. Birnbaumer, M. Hecker, and M. Cattaruzza, "Mechanism of stretch-induced activation of the mechanotransducer zyxin in vascular cells," *Science Signaling*, vol. 5, pp. ra91–ra91, 12 2012.

[199] M. A. Smith, E. Blankman, M. L. Gardel, L. Luettjohann, C. M. Waterman, and M. C. Beckerle, "A Zyxin-mediated mechanism for actin stress fiber maintenance and repair," *Developmental Cell*, vol. 19, pp. 365–376, 9 2010.

[200] J. Oldenburg, G. Van Der Krogt, F. Twiss, A. Bongaarts, Y. Habani, J. A. Slotman, A. Houtsmuller, S. Huveneers, and J. De Rooij, "VASP, zyxin and TES are tension-dependent members of Focal Adherens Junctions independent of the α-catenin-vinculin module," *Scientific Reports*, vol. 5, p. 17225, 11 2015.

[201] E. Kassianidou, C. A. Brand, U. S. Schwarz, and S. Kumar, "Geometry and network connectivity govern the mechanics of stress fibers," *Proceedings of the National Academy of Sciences of the United States of America*, vol. 114, pp. 2622–2627, 3 2017.

[202] X. Liang, M. Michael, and G. Gomez, "Measurement of Mechanical Tension at cell-cell junctions using two-photon laser ablation," *BIO-PROTOCOL*, vol. 6, no. 24, 2016.

[203] S. Curran, C. Strandkvist, J. Bathmann, M. De Gennes, A. Kabla, and G. Salbreux, "Myosin II Controls Junction Fluctuations to Guide Epithelial Tissue Ordering," *Developmental Cell*, vol. 43, pp. 480–492, 2017.

[204] N. D. Bade, R. D. Kamien, R. K. Assoian, and K. J. Stebe, "Curvature and Rho activation differentially control the alignment of cells and stress fibers," *Science Advances*, vol. 3, no. 9, pp. 1–9, 2017.

[205] D. Chapelle and P. Moireau, "General coupling of porous flows and hyperelastic formulations - From thermodynamics principles to energy balance and compatible time schemes," *European Journal of Mechanics, B/Fluids*, vol. 46, pp. 82–96, 2014.

[206] B. Burtschell, D. Chapelle, and P. Moireau, "Effective and energy-preserving time discretization for a general nonlinear poromechanical formulation," *Computers and Structures*, vol. 182, pp. 313–324, 4 2017.

[207] B. Burtschell, P. Moireau, and D. Chapelle, "Numerical Analysis for an Energy-stable Total Discretization of a Poromechanics Model with Inf-sup Stability," *Acta Mathematicae Applicatae Sinica*, vol. 35, pp. 28–53, 1 2019.

[208] C. A. Dessalles, A. Babataheri, and A. I. Barakat, "Pericyte mechanics and mechanobiology," 3 2021.

[209] J. M. López-Gay, H. Nunley, M. Spencer, F. di Pietro, B. Guirao, F. Bosveld, O. Markova, I. Gaugue, S. Pelletier, D. K. Lubensky, and Y. Bellaïche, "Apical stress fibers enable a scaling between cell mechanical response and area in epithelial tissue," *Science*, vol. 370, 10 2020.

[210] R. M. Linville, N. F. Boland, G. Covarrubias, G. M. Price, and J. Tien, "Physical and Chemical Signals That Promote Vascularization of Capillary-Scale Channels," *Cellular and Molecular Bioengineering*, vol. 9, no. 1, pp. 73–84, 2016.

[211] J. Kim, M. Chung, S. Kim, D. H. Jo, J. H. Kim, and N. L. Jeon, "Engineering of a biomimetic pericyte-covered 3D microvascular network," *PLoS ONE*, vol. 10, no. 7, pp. 1–15, 2015.

[212] K. Zhang and J. F. Chen, "The regulation of integrin function by divalent cations," 2012.

[213] M. Ye, H. M. Sanchez, M. Hultz, Z. Yang, M. Bogorad, A. D. Wong, and P. C. Searson, "Brain microvascular endothelial cells resist elongation due to curvature and shear stress. SUPP MAT," *Scientific reports*, vol. 4, p. 4681, 2014.

[214] P. Berens, "CircStat : A MATLAB Toolbox for Circular Statistics ," *Journal of Statistical Software*, vol. 31, pp. 1–21, 9 2009.

ECOLE DOCTORALE

Titre : Forces dans un microvaisseau-sur-puce : développement du système, mécanique poroélastique et réponse cellulaire

Mots clés : biomécanique, biophysique, biomatériaux,organes-sur-puces, cellules endothéliales

Résumé : Les cellules endothéliales qui tapissent la paroi des vaisseaux sanguins sont capables de détecter et de répondre aux nombreuses forces mécaniques présentes dans le système vasculaire. Bien que l'influence des forces dues au cisaillement, à la rigidité et à la courbure soit bien étudiée, le rôle de l'étirement et donc la tension dans la paroi vasculaire demeurent peu compris. Les plateformes in vitro telles que les organes sur puce sont idéales pour l'étude de ces phénomènes, puisqu'elles présentent une panoplie de stimuli mécaniques contrôlables et caractérisables. Pendant ma thèse, j'ai tout d'abord développé un microvaisseau-sur-puce capable de soumettre les cellules à toutes les forces mécaniques pertinentes, dont la tension de la paroi vasculaire. J'ai ensuite caractérisé son comportement mécanique, avec une attention particulière portée aux aspects dynamiques de la déformation du gel sous compression hydraulique. Enfin, j'ai étudié la réponse des cellules à la tension, dévoilant un nouveau comportement collectif où les cellules s'alignent dans la direction de la tension.

Title : Forces in a microvessel-on-chip: system development, poroelasticity mechanics and cellular response

Keywords : biomechanics, biophysics, biomaterials, organ-on-chip, endothelial cells

Abstract : Endothelial cells lining the inner surfaces of blood vessels sense and respond to the numerous mechanical forces present in the vasculature. Although the influence of wall shear stress, stiffness and curvature has been thoroughly investigated, the role of strain and wall tension remains less clear. In vitro platforms such as organ-on-chips are ideal systems for investigating these phenomena as they offer a controllable and well-defined set of mechanical stimuli. During my Ph.D., I first developed a microvessel-on-chip that can subject cells to all the relevant mechanical forces including wall tension. I then characterized its mechanical behavior, with a focus on the dynamics of the gel deformation under hydraulic compression. Finally, I investigated the response of the cells to tension, revealing a novel collective behavior where cells align in the direction of tension.

Institut Polytechnique de Paris
91120 Palaiseau, France